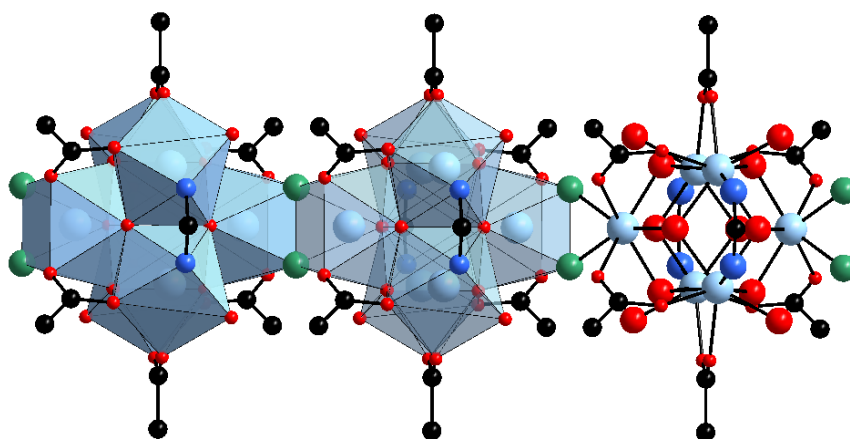


# Dissertation

## Entdeckung und Syntheseoptimierung von Zr-MOFs – Hochdurchsatzuntersuchungen und Reaktionen in Flussreaktoren



Zur Erlangung des Doktorgrades  
Der Mathematisch-Naturwissenschaftlichen Fakultät der  
Christian-Albrechts Universität zu Kiel

Vorgelegt von:  
M.Sc. Steve Waitschat

Ak Prof. Norbert Stock  
Institut für Anorganische Chemie  
Christian-Albrechts-Universität zu Kiel

Ostenfeld, August 2018



Gutachterseite

Erster Gutachter: Prof. Dr. Norbert Stock  
Zweiter Gutachter: Prof. Dr. Wolfgang Bensch

Tag der mündlichen Prüfung: 22.10.2018

Zum Druck genehmigt: 22.10.2018

Gez. Prof. Dr. Frank Kempken (Dekan)



**“Whatever your walk in life is,  
You pick what you want to be,  
Then go ahead and be the best one.”**

**CM Punk, Wrestler**



## Entdeckung und Syntheseoptimierung von Zr-MOFs –Hochdurchsatzuntersuchungen und Reaktionen in Flussreaktoren

Das Thema der hier vorliegenden Arbeit ist die Synthese und Charakterisierung von Zirkonium-basierten Metall-organischen Gerüstverbindungen (Zr-MOFs), insbesondere die Entdeckung und Syntheseoptimierung neuer Verbindungen mit stickstoffhaltigen Heterozyklen als Linkermoleküle und Flussreaktorsynthesen und die damit zusammenhängende Aufskalierung der Synthese bekannter MOFs. Im ersten Teil dieser Arbeit war es möglich mit den Linkermolekülen 2,5-Pyridindicarbonsäure (H<sub>2</sub>PDC), 2,5-Pyrazindicarbonsäure (H<sub>2</sub>PzDC) und Azopyridindicarbonsäure (H<sub>2</sub>APDC) jeweils die Verbindungen M-UiO-66-PDC ( $[M_6(O)_4(OH)_4(Cl)_{2x}(H_2O)_{2x}(PDC)_{6-x}]$ , mit M = Zr, Hf und Ce, CAU-22-PzDC ( $[Zr_6(\mu_3-O)_4(\mu_3-OH)_4(\mu-OH)_2(OH)_2(H_2O)_2(HCO_2)_2(PzDC)_3]$ ) und M-CAU-39-APDC ( $[M_{12}(\mu_3-O)_8(\mu_3-OH)_8(\mu_2-OH)_6(OH)_6(H_2O)_6(APDC)_3]$ ) mit M = Zr und Hf herzustellen. Für alle Verbindungen wurde eine wässrige Syntheseroute entwickelt, die sich nur marginal in der Menge an Additiven, Reaktionszeit und -temperatur unterscheiden. Die Strukturen der Verbindungen wurden mittels Rietfeld-Verfeinerung bestimmt. Hierbei sind insbesondere die anorganischen Baueinheiten (IBUs) der einzelnen MOFs hervorzuheben. Die IBU in der Kristallstruktur von UiO-66-PDC ist der bekannte hexanucleare  $\{Zr_6(O)_4(OH)_4\}$ -Cluster, dessen wässrige Synthese mit einem Pyridinderivat allerdings neu ist. Die IBU von CAU-22-PzDC ist bisher einmalig und besteht aus kondensierten hexanuclearen Zr-O-Clustern, die durch verbrückende OH<sup>-</sup>- Ionen eine Kette von  $\{Zr_6O_4(OH)_4(\mu-OH)_2\}$ -Clustern bilden. Die IBU von CAU-39 besteht aus kondensierten hexanuclearen Zr-O-Clustern, allerdings nur zu einem dodecanuclearen  $\{M_{12}(\mu_3-O)_8(\mu_3-OH)_8(\mu_2-OH)_6\}$ -Cluster. Neben einer vollständigen Charakterisierung unter Einsatz verschiedener Methoden - IR- und <sup>1</sup>H-NMR-Spektroskopie, Thermogravimetrie, Temperatur abhängige Pulverdiffraktometrie (VT-PXRD), N<sub>2</sub>-Gassorption - wurde Zr-UiO-66-PDC für den möglichen Einsatz in adsorptionsbasierten Kältemaschinen getestet. Eine erhöhte Hydrophilie der Verbindungen, verglichen mit UiO-66-BDC, konnte auf Grund einer früheren Adsorption von H<sub>2</sub>O bei geringeren relativen Drücken festgestellt werden. Um die Stabilität während des Adsorptionsprozesses zu testen, wurden zyklische Wasser- und die weltweit ersten zyklischen Methanolsorptionsmessungen durchgeführt. In beiden Fällen nimmt die Gesamtkapazität von Zr-UiO-66-PDC über mehrere Zyklen ab. Während diese Abnahme bei der Wassersorption auf eine Verringerung in der Fernordnung zurückzuführen ist, ist sie bei der Methanolsorption auf einen Austausch der Hydroxygruppen durch Methoxygruppen und die damit zusammenhängende Verkleinerung der Poren erklärbar.

Neben diesen Arbeiten, die in Autoklaven durchgeführt wurden, wurden zusätzlich zwei Flussreaktoren entwickelt, die sich hauptsächlich in der Reaktorgröße und der Förderpumpe unterscheiden. Beide Reaktoren bestehen aus einem gewickelten Teflonschlauch, wobei die kleine

## Zusammenfassung

Variante ein Volumen von ca. 15 ml aufweist (**Reaktor 1**, beheizt mit einem Ölbad) und der große Reaktor ein Volumen von ca. 1800 ml (**Reaktor 2**, beheizt in einem Umluftofen). Der **Reaktor 1** wird mit mehreren Spritzenpumpen betrieben, die mit den jeweiligen Eduktlösungen befüllt sind. Durch den enormen Anstieg des Reaktorvolumens ist es nicht möglich den **Reaktor 2** mit Spritzenpumpen zu betreiben, so dass nun mit einer Magnetmembranpumpe gearbeitet wird. Dies wiederum ermöglicht das vorherige Mischen der Edukte und auch das Arbeiten mit Suspensionen. Der Aufbau von **Reaktor 1** ist bewusst einfach und kostengünstig gehalten worden, sodass auf extra Ventile oder Ähnliches verzichtet wurde, wodurch nur unter Normaldruck und bei Temperaturen unterhalb des Siedepunktes des Lösungsmittels gearbeitet werden konnte. Nichtsdestotrotz konnten die Verbindungen UiO-66, CAU-13, Ga-TCP und Cd-STA-12 synthetisiert werden. Die ersten drei Verbindungen sind literaturbekannt, wurden abgesehen von UiO-66 aber das erste mal in einem Flussreaktor hergestellt. Cd-STA-12 hingegen ist eine neue Verbindung. Um zu zeigen, dass die Verbindungen die gleichen Eigenschaften aufweisen, wie die äquivalenten Verbindungen aus den Batchsynthesen wurde unter anderem die thermische Stabilität und die N<sub>2</sub>-Sorptionseigenschaften bestimmt und verglichen.

**Reaktor 2** wurde genutzt um zu zeigen, dass es nicht nur theoretisch möglich ist größere Mengen eines MOFs herzustellen, sondern dass auch real, größere Mengen erhalten werden können. Als Verbindungen wurden hierzu die bekannten UiO-66-Derivate mit Fumarsäure bzw. Aminoterephthalsäure als Linkermoleküle gewählt. Außerdem wurde die Homogenität der Produkte während der gesamten Reaktion untersucht. Hierzu wurde alle fünf Minuten ein Teil des Reaktionsproduktes isoliert und charakterisiert. Die Pulverdiffraktogramme der Proben zeigten nur marginale Unterschiede, wohingegen in den N<sub>2</sub>-Sorptionisothermen bei UiO-66-Fum im Gegensatz zu UiO-66-NH<sub>2</sub> große Unterschiede zu verzeichnen waren, was auf eine unzureichende Durchmischung der Edukte hindeutet.



## Discovery and synthesis optimization of Zr-MOFs - high-throughput methods and synthesis in flow reactors

The topic of this work is the synthesis of zirconium based metal-organic frameworks, on one hand the discovery and synthesis optimization of new Zr-MOFs with nitrogen containing heterocycles as linker molecules, on the other hand flow reactor syntheses for a possible synthesis upscaling of known MOFs.

In the first part 2,5-pyridinedicarboxylic acid ( $H_2PDC$ ), 2,5-pyrazinedicarboxylic acid ( $H_2PzDC$ ) and azopyridinedicarboxylic acid ( $H_2APDC$ ) were used as linker molecules to obtain the MOFs M-UiO-66-PDC ( $[M_6(O)_4(OH)_4(Cl)_{2x}(H_2O)_{2x}(PDC)_{6-x}]$ , with  $M = Zr, Hf$  and  $Ce$ ), CAU-22-PzDC ( $[Zr_6(\mu_3-O)_4(\mu_3-OH)_4(\mu-OH)_2(OH)_2(H_2O)_2(HCO_2)_2(PzDC)_3]$ ) and M-CAU-39-APDC ( $[M_{12}(\mu_3-O)_8(\mu_3-OH)_8(\mu_2-OH)_6(OH)_6(H_2O)_6(APDC)_3]$ ) with  $M = Zr$  and  $Hf$ , respectively. For all these compounds a water based synthesis route was established with only marginal differences in the amount of additives, reaction time and temperature. The inorganic building units (IBUs) of the MOFs are of particular interest. The IBU in the structure of UiO-66-PDC is the very well-known hexanuclear  $\{Zr_6(O)_4(OH)_4\}$ -cluster, for which a water based synthesis with pyridine-based linker molecules was unknown. The IBU of CAU-22-PzDC is unique and contains also the hexanuclear Zr-O-cluster, which is condensed via  $OH^-$  ions to an edge-sharing chain of  $\{Zr_6O_4(OH)_4(\mu-OH)_2\}$ -clusters. The IBU of CAU-39-APDC also exhibits a condensed form of the hexanuclear Zr-O-cluster, the dodecanuclear  $\{M_{12}(\mu_3-O)_8(\mu_3-OH)_8(\mu_2-OH)_6\}$ -cluster. A full characterization was carried out for all samples (IR- and  $^1H$ -NMR-spectroscopy, thermogravimetry, temperature dependent powder X-ray diffraction,  $N_2$ -adsorption). Additionally, Zr-UiO-66-PDC was tested as a material for heat transformation applications. Since, the start of the water adsorption is observed at lower relative pressure compared to UiO-66-BDC, this compound is more hydrophilic due to the incorporated  $PDC^{2-}$  linker molecules. For stability tests, cyclic water and the first ever cyclic methanol sorption experiments were carried out. In both cases the total uptake of the gases dropped after several cycles, which is explainable by a loss in the long range order and a decrease of the pore size due to an exchange of the hydroxyl ions by methoxy ions in the Zr-O-cluster, respectively.

In addition to the syntheses in batch-reactors, two flow-reactors were developed during this PhD-thesis. Both reactors are built of Teflon tubes; the main difference is the reactor volume with 15 ml (**reactor 1**, heated in an oil bath) and 1800 ml (**reactor 2**, heated in a conventional oven) and the transport medium. For **reactor 1** a set of syringe pumps, loaded with the precursor solutions, is used. Due to the increase of the reactor volume, it is not possible to work with syringe pumps for **reactor 2**, instead we employed a magnetic membrane pump, which also allows the use of suspensions of starting

## Abstract

materials. The setup of **reactor 1** is very simple and can be used for reaction temperatures below the boiling point of the solvent at ambient pressure. Nevertheless, we could synthesize the compounds UiO-66, CAU-13, Ga-TCPP and Cd-STA-12. The first three compounds are known from literature, but except for UiO-66 we established the flow reactor synthesis of these MOFs for the first time. Cd-STA-12 was observed and characterized the first time. The properties of the samples made in the flow reactor were compared to samples obtained via batch synthesis through detailed thermogravimetric and sorption measurements.

**Reactor 2** was used to show that it is not only theoretically possible to synthesize larger amounts of MOFs. To evaluate this, two known UiO-66-derivates with fumaric acid and aminoterephthalic acid as linker molecules were chosen. Additionally the homogeneity of the products during the whole synthesis was tested. Every five minutes a small sample was isolated and characterized by powder X-ray diffraction (PXRD) and N<sub>2</sub>-sorption. While the PXRD-patterns were almost identical the N<sub>2</sub>-sorption isotherms of UiO-66-Fum showed a variation in the uptake, which could be explained by incomplete mixing during the reaction. The samples of UiO-66-NH<sub>2</sub> did not show this problem and the different samples exhibit the same sorption properties.

## Danksagung

### Danksagung

Zu allererst möchte und muss ich natürlich meinen Doktorvater Prof. Norbert Stock danken. Ich konnte ihn jederzeit mit Fragen oder neuen Ideen behelligen und hatte viele Freiheiten während meiner Arbeit. Aber auch bei meiner Arbeit im JCF-Kiel und später als ich wegen meinem Sohn mehr und mehr von zu Hause gearbeitet habe, habe ich nur Unterstützung und Verständnis von Prof. Stock erhalten.

Als nächstes möchte ich Dr. Helge Reinsch und Dr. Michael Wharmby danken. Ohne euch beide hätte ich wahrscheinlich nie mit meiner Promotion angefangen und wäre der Forschung mit solcher Leidenschaft verfallen, aber auch während meiner Promotion wart ihr, so weit möglich, mir immer mit Rat und Tat zur Seite. Ich schätze nicht nur eure Unterstützung zu meiner Doktorarbeit, sondern auch eure Freundschaft im Allgemeinen.

Die Promotion ist eine harte Zeit und ohne verständnisvolle und tolle Kollegen nicht machbar. Namentlich möchte ich mich besonders bei Timo Rhauderwiek, Martin Albat und Achim Fölster bedanken.

Der NMR-spektroskopischen Abteilung der OC, der Analytik der AC, dem Arbeitskreis Stock, generell der AC und all meinen Kooperationspartnern sei natürlich auch gedankt.

Neben der wissenschaftlichen Unterstützung, gab es aber auch noch andere Menschen, allen voran möchte ich hier wie in allen anderen Arbeiten meinem Vater danken. Danke Papa, ohne dich wäre diese Arbeit nicht möglich gewesen!

Zudem möchte ich noch meiner Freundin Maike danken. Wir sind kurz nach dem Start meiner Promotion zusammen gekommen und haben viel zusammen durchgemacht. Nun sind wir Eltern und gehen stark in unsere gemeinsame Zukunft.

Natürlich danke ich auch meinem Sohn Lenny, der mir zum Schluss der Promotion gezeigt hat, dass es auch andere Dinge gibt, die wichtig sind.

Und zuletzt danke ich unserem Hund Marlon, wie viele Ideen, hatte ich während wir zusammen spazieren waren.

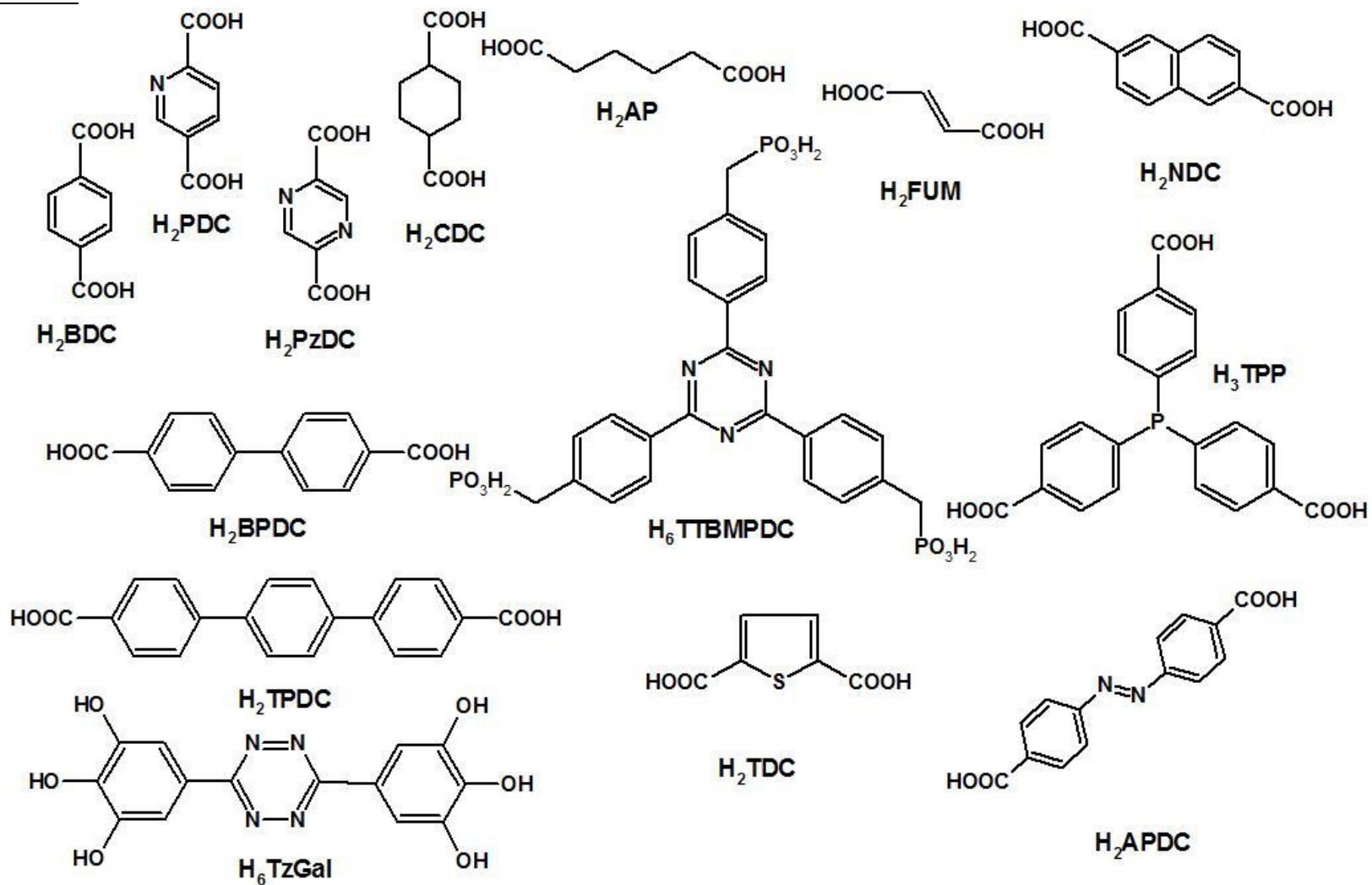
## Abkürzungsverzeichnis

### Abkürzungsverzeichnis

Abb.	Abbildung
BET	Brunauer-Emmett-Teller
BJH	Barret-Joyner-Halenda
EDX	energy-dispersive x-ray
engl	englisch
EXAFS	extended X-ray absorption fine structure
Gew. %	Gewichtsprozent
HD	Hochdurchsatz
HPLC	high performance liquid chromatography
IBU	inorganic building unit
IR	infrarot
IUPAC	International Union of Pure and Applied Chemistry
Kap	Kapazität
Lsgm.	Lösungsmittel
M	Metall
MO	Metall-Sauerstoff
MOF	metal-organic framework
PTFE	Polytetrafluorethylen
NMR	nuclear magnetic resonance
SEM	scanning electron microscope
Tab.	Tabelle
TEM	Transmissionselektronenmikroskopie
VT-PXRD	valuable temperature powder X-ray diffraction
XANES	X-ray absorption near-edge structure spectroscopy

Linker-Verzeichnis

Linker-Verzeichnis



## MOF-Verzeichnis

MOF-Verzeichnis

MOF	Name	Summenformel
Zr-UiO-66	Universität in Oslo	$[\text{Zr}_6(\text{O})_4(\text{OH})_4(\text{BDC})_6]$
Zr-UiO-67	Universität in Oslo	$[\text{Zr}_6(\text{O})_4(\text{OH})_4(\text{BPDC})_6]$
Zr-UiO-68	Universität in Oslo	$[\text{Zr}_6(\text{O})_4(\text{OH})_4(\text{TPDC})_6]$
DUT-69	Technische Universität Dresden	$[\text{Zr}_6(\text{O})_4(\text{OH})_4(\text{TDC})_5(\text{Ac})_2]$
DUT-67	Technische Universität Dresden	$[\text{Zr}_6(\text{O})_6(\text{OH})_2(\text{TDC})_4(\text{Ac})_2]$
DUT-84	Technische Universität Dresden	$[\text{Zr}_6(\text{O})_8(\text{NDC})_3(\text{Ac})_2]$
Zr-AP-2	---	$[\text{Zr}_6(\text{OH})_{12}(\text{SO}_4)_4(\text{AP})_2(\text{H}_2\text{O})_4]$
Zr-TPP	---	$[\text{Zr}_{12}\text{O}_8(\text{OH})_8(\text{Ac})_{18}(\text{TPP})_2]$
Zr-TPDC	---	$[\text{Zr}_{12}(\text{O})_8(\mu_3\text{-OH})_8(\mu_2\text{-OH})_6(\text{TPDC})_9]$
Zr-CAU-39	Christian-Albrechts Universität	$[\text{Zr}_{12}(\text{O})_8(\mu_3\text{-OH})_8(\mu_2\text{-OH})_6(\text{OH})_6(\text{H}_2\text{O})_6(\text{APDC})_6]$
CAU-22	Christian-Albrechts Universität	$[\text{Zr}_6(\mu_3\text{-O})_4(\mu_3\text{-OH})_4(\mu\text{-OH})_2(\text{OH})_2(\text{H}_2\text{O})_2(\text{HCO}_2)_2(\text{PzDC})_3]$
CAU-27	Christian-Albrechts Universität	$[\text{Zr}_5\text{O}_4(\text{OH})_4(\text{OAc})_4(\text{BDC})_2]$
MIL-140	Materiaux de l'institut lavoisier	$[\text{Zr}(\text{O})(\text{BDC})]$
MIL-163	Materiaux de l'institut lavoisier	$[\text{Zr}(\text{H}_2\text{-TzGal})]$
UPG-1	Universität Perugia	$[\text{Zr}(\text{H}_4\text{TTBMP})_2]$
Zr-CAU-30	Christian-Albrechts Universität	$[\text{Zr}_2(\text{Ni-H}_2\text{TPPP})(\text{OH}/\text{F})_2]$
PCN-221	Porous coordination network	$[\text{Zr}_8\text{O}_6(\text{TCPP})_3]$
Al-MIL-53	Materiaux de l'institut lavoisier	$[\text{Al}(\text{OH})\text{BDC}]$
HKUST-1	Hong Kong University of Science & Technology	$[\text{Cu}_3(\text{BTC})_2]$
ZIF-8	Zeolitic Imidazole Framework	$[\text{Zn}(\text{mim})_2]$
Basolite A250	BASF-MOF	$[\text{Al}(\text{OH})(\text{Fum})]$
Ni-CPO-27	Coordination Polymer Oslo	$[\text{Ni}_2(\text{DHTP})(\text{H}_2\text{O})_2]$
MIL-101	Materiaux de l'institut lavoisier	$[\text{Cr}_3(\text{O})\text{X}(\text{BDC})_3(\text{H}_2\text{O})_2]$ mit X = OH <sup>-</sup> oder F <sup>-</sup>
MIL-127	Materiaux de l'institut lavoisier	$[\text{Fe}_3\text{OF}(\text{ABTC})_{1.5}(\text{H}_2\text{O})_3]$
CAU-10	Christian-Albrechts Universität	$[\text{Al}(\text{OH})(\text{m-BDC})]$
NOTT-100	University of Nottingham	$[\text{Cu}_2(\text{H}_4\text{L})(\text{H}_2\text{O})_2]$
MIL-88	Materiaux de l'institut lavoisier	$[\text{Fe}_3\text{O}(\text{Fum})_3]$
MOF-14	Metal-organic framework	$[\text{Cu}_3(\text{BTB})_2(\text{H}_2\text{O})_3]$
MOF-5	Metal-organic framework	$[\text{Zn}_4\text{O}(\text{BDC})_3]$
IRMOF-3	Isorecticular metal-organic framework	$[\text{Zn}_4\text{O}(\text{ABDC})_3]$

## MOF-Verzeichnis

NOTT-400	University of Nottingham	$[\text{Sc}_2(\text{OH})_2(\text{BPTC})]$
CAU-13	Christian-Albrechts Universität	$[\text{Al}(\text{OH}(\text{CDC}))]$
STA-12	University of St. Andrews	$[\text{Cd}_2(\text{H}_2\text{O})_2\text{L}]$
Ga-PMOF	Porphyrin metal-organic framework	$[\text{Ga}_2(\text{OH})_2(\text{H}_2\text{TCPP})]$
MIL-100	Materiaux de l'institut lavoisier	$[\text{Fe}_3\text{X}_3(\text{BTB})_2]$ X = OH <sup>-</sup> oder F <sup>-</sup>

---

**Inhaltsverzeichnis**

Kurzzusammenfassung.....	V
Abstract.....	VII
Danksagung.....	IX
Abkürzungsverzeichnis.....	X
Linker-Verzeichnis.....	XI
MOF-Verzeichnis.....	XII
Inhaltsverzeichnis.....	XIV

**I. Allgemeiner Teil**

1. Einleitung.....	02
2. Präparative Methoden: Hochdurchsatzmethoden.....	04
3. Charakterisierungsmethoden: Gassorption.....	06

**II. Kumulativer Teil**

4.1 Zr-MOF

4.1.1. Einleitung.....	09
4.1.1.1 Zirkonium: Synthese, Eigenschaften und Anwendungen.....	09
4.1.1.2 Molekulare Zr-O-cluster.....	10
4.1.1.3 Zr-MOFs: IBU's, Strukturen und Synthesen.....	15
4.1.2. <u>Ergebnisse</u>	
4.1.2.1 Synthesis of M-UiO-66 (M = Zr, Ce or Hf) employing 2,5-pyridinedicarboxylic acid as linker: defect chemistry, framework hydrophilisation and sorption properties.....	25
4.1.2.2 Water-based synthesis and characterization of a new Zr-MOF with a unique inorganic building unit.....	37



## Inhaltsverzeichnis

4.1.2.3 Direct water-based synthesis and characterization of new Zr/Hf-MOFs with dodecanuclear clusters as IBU .....	44
<b>4.2 Flussreaktorsynthesen</b>	
4.2.1 Einleitung.....	50
4.2.1.1 Aufskalierung von MOFs? .....	50
4.2.1.2 Flussreaktoren: Grundlagen.....	50
4.2.1.3 Flussreaktoren: Einsatz in der MOF-Synthese.....	51
4.2.1.4 Beschreibungen der während dieser Arbeit entwickelten Flussreaktoren.....	55
4.2.2 <u>Ergebnisse</u>	
4.2.2.1 Flow-synthesis of carboxylate and phosphonate based metal–organic frameworks under non-solvothermal reaction conditions.....	58
4.2.2.2 Nanoscale Synthesis of Two Porphyrin-Based MOFs with Gallium and Indium.....	66
4.2.2.3 A Facile “Green” Route for Scalable Batch Production and Continuous Synthesis of Zirconium MOFs.....	76
5. Zusammenfassung.....	87
6. Ausblick.....	92
7. Anhang: Supporting Informations	
7.1 Synthesis of M-UiO-66 (M = Zr, Ce or Hf) employing 2,5-pyridinedicarboxylic acid as linker: defect chemistry, framework hydrophilisation and sorption properties.....	94
7.2 Water-based synthesis and characterization of a new Zr-MOF with a unique inorganic building unit.....	141
7.3 Direct water-based synthesis and characterization of new Zr/Hf-MOFs with dodecanuclear clusters as IBU.....	163
7.4 Flow-synthesis of carboxylate and phosphonate based metal–organic frameworks under non-solvothermal reaction conditions.....	182
7.5 Nanoscale Synthesis of Two Porphyrin-Based MOFs with Gallium and Indium.....	211

## Inhaltsverzeichnis

7.6 A Facile “Green” Route for Scalable Batch Production and Continuous Synthesis of Zirconium MOFs.....	230
8. Literaturverzeichnis.....	246
9. Publikationsliste und Konferenzbeiträge.....	251
Eidesstattliche Erklärung.....	252
Curriculum Vitae.....	253

# **I Allgemeiner Teil**

## 1. Einleitung

Der Wohlstand vieler Menschen auf unserer Erde wäre ohne die Fortschritte in der Chemie nicht denkbar. So ermöglicht erst das Haber-Bosch-Verfahren die heutige Großproduktion in der Landwirtschaft<sup>1,2</sup> oder das Cracken von Kohlenwasserstoffen wäre ohne Zeolithe nicht mehr vorstellbar.<sup>3</sup> All diese Fortschritte sind ohne die Grundlagenforschung an Universitäten nicht zu erreichen. Dazu gehört auch die Synthese und die Untersuchung potentieller Anwendungen der Verbindungsklasse der Metall-organischen Gerüstverbindungen (engl.: metal-organic framework, MOF).<sup>4</sup> Die IUPAC hat MOFs definiert als zwei oder drei dimensionale Gerüstverbindungen die aus Metallkationen oder Metall-Sauerstoff-Clustern, durch organische Linkermoleküle verbrückt werden und potentiell porös sind.<sup>5</sup> Aus dieser Definition lassen sich drei wichtige Punkte zu der Zusammensetzung von MOFs ableiten. Es handelt sich um Hybridverbindungen bestehend aus anorganischen Bausteinen (engl.: inorganig building unit, IBU) die über organische Moleküle, sogenannte Linker, verbrückt werden, wodurch potentiell zugängliche Hohlräume in den Verbindungen entstehen. Dadurch ist bereits zu erkennen, dass die Vielfalt möglicher Verbindungen schier unendlich ist. Es gibt verschiedenste IBUs von einfachen Metall-Sauerstoff-Clustern (MO),<sup>6,7</sup> über MO-Ketten<sup>8,9</sup> oder MO-Cluster-Ringen<sup>10</sup> um nur einige zu nennen, die je nach eingesetztem Metall und Linker unter bestimmten Reaktionsbedingungen bevorzugt entstehen (Abb. 1). Theoretisch ist es möglich mit jedem Metall einen MOF zu bilden, solange diese eine Koordinationsumgebung ermöglichen, mit der die Linkermoleküle ein Gerüst aufbauen können.

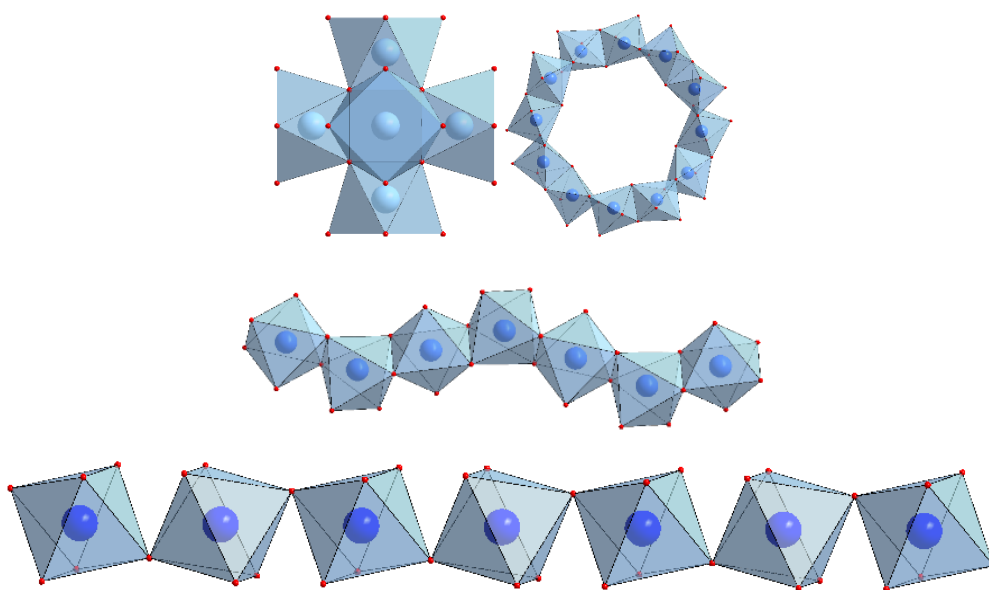


Abb. 1: Verschiedene IBUs die in MOFs möglich sind, wie MO-Cluster,<sup>6</sup> MO-Ketten<sup>8,9</sup> oder MO-Clusterringe.<sup>10</sup>

## Einleitung

Insbesondere die Metalle aus der Lanthanoid-,<sup>11-13</sup> Titan<sup>14-16</sup>- und Aluminiumgruppe<sup>8,17,18</sup> sowie die Metalle der vierten Periode<sup>19-21</sup> werden hierbei auf Grund Ihrer Eigenschaften vermehrt für die Synthese von MOFs eingesetzt. Es sind aber auch MOFs mit Erdalkalimetallen<sup>22-24</sup> oder den sehr schweren Metallen Blei<sup>25,26</sup> und Bismut<sup>27,28</sup> bekannt, eine Mischung von Metallen,<sup>29,30</sup> wodurch verschiedene Eigenschaften wie zum Beispiel Stabilität und katalytische Aktivität kombiniert werden können, ist auch möglich.<sup>30</sup> Um als Linker geeignet zu sein, müssen die organischen Moleküle zwei,<sup>6</sup> drei<sup>21</sup> oder mehr<sup>7</sup> funktionelle Gruppen wie Carbon-,<sup>10,13,30</sup> Phosphon-,<sup>31,32</sup> Sulfonsäuren<sup>33,34</sup> oder Hydroxidgruppen<sup>35</sup> aufweisen (Abb. 2). Weiterhin können aliphatische,<sup>17,36</sup> aromatische<sup>6,19</sup> oder zyklische<sup>18,37</sup> Reste an den funktionellen Gruppen gebunden sein.

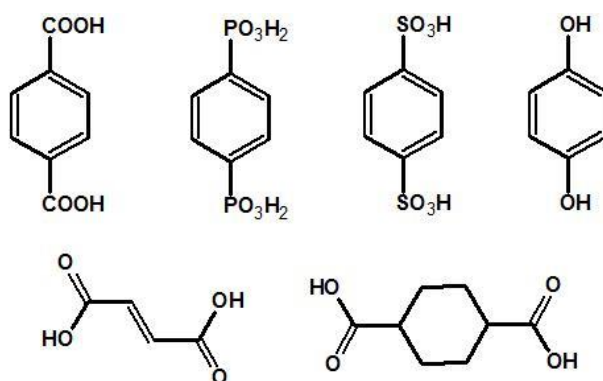


Abb. 2: Übersicht von Funktionalitäten der organischen Linkermoleküle, die für die MOF-Synthese eingesetzt werden können.

Weitere funktionelle Gruppen an den Linkermolekülen wie Halogene,<sup>38</sup> Methylgruppen<sup>9</sup> oder ähnliches sind ebenfalls vorstellbar. Diese Gruppen sind meist nicht aktiv an der Ausbildung des Gerüsts beteiligt. Es entstehen isoretikuläre Verbindungen, d.h. die gleiche Topologie und das gleiche Verknüpfungsmuster mit einem anderen Linker (auch mit anderem Metall möglich), aber mit Änderungen beispielsweise der Sorptionseigenschaften.<sup>39</sup> Da das Gebiet der MOFs noch relativ jung ist, gibt es bisher kaum MOFs in einer Anwendung zu finden, aber sie haben ein schier endloses Anwendungspotential z.B. in der Gasspeicherung<sup>40</sup> oder -trennung,<sup>41</sup> Wärmeadsorption,<sup>42</sup> Katalyse<sup>43</sup> oder auch in medizinischen Anwendungen.<sup>44,45</sup>

## 2. Präparative Methoden: Hochdurchsatzmethoden

Im Gegensatz zu organischen Synthesen, die oft planbar sind (Retrosynthese), sind die Reaktionsprodukte in der anorganischen Festkörperchemie nur selten vorhersagbar. Die Syntheseplanung neuer Verbindungen ist nicht trivial und eine optimierte Synthese meist nur durch zahlreiche Versuche erreichbar.<sup>46</sup> Durch Automatisierung, Miniaturisierung und Parallelisierung lässt sich der Prozess der Entdeckung und der Syntheseoptimierung effizient gestalten. Ein Verfahren, das diese drei Kriterien erfüllt, ist die Hochdurchsatzmethode.<sup>46</sup> Im Arbeitskreis von Prof. Stock wurde ein spezieller HD-Reaktor (Abb. 3) entwickelt, mit dem es möglich ist solvothermale Reaktionen, Synthesen bei denen die Reaktionstemperatur oberhalb des Siedepunktes des eingesetzten Lösungsmittels ist, durchzuführen.<sup>47</sup> Durch das Verkleinern der Autoklaven von einem Füllvolumen von 20 auf 2 ml wird der Einsatz der Edukte um ein Vielfaches verringert. Der Aufbau dieser speziellen Autoklaven ermöglicht die parallele Synthese von bis zu 48 Produkten, unter dem gleichen Temperatur- und Zeitprogramm, wobei das systematische Untersuchen des Einflusses von pH-Wert, Eduktverhältnisse oder der Einsatz von Additiven auf die Produktbildung ermöglicht wird. Eine anschließende automatische Filtration und pulverdiffraktometrische Untersuchung ermöglicht eine schnelle Charakterisierung aller Proben ohne großen Zeitverlust.<sup>46-48</sup> Mit dieser Methode konnten zahlreiche neue MOFs im Arbeitskreis von Prof. Stock entdeckt und deren Synthesebedingungen optimiert werden.<sup>17,38,49</sup> Allerdings hat dieser Aufbau einen großen Nachteil bezüglich der Optimierung von Reaktionszeiten und –temperaturen, da zunächst der Stahlautoklav durch konventionelles Heizen und erst dann die Reaktionsmischungen indirekt aufgeheizt werden. Dadurch ist es nicht möglich exakte Reaktionstemperaturen durch mögliche Abweichungen im Aufbau und exakte Reaktionszeiten durch die Verweildauer des indirekten Aufheizens zu bestimmen. Zusätzlich können die Reaktionen schwer gequenchet werden um mögliche Reaktionstrends in Abhängigkeit von kurzen Reaktionszeiten beobachten zu können. Allerdings ist es im Hinblick auf eine mögliche Aufskalierung nicht ausreichend eine Synthese nur auf das „optimale Produkt“ hin zu optimieren, denn bezogen auf die Raum-Zeit-Ausbeute ist insbesondere die Reaktionszeit ausschlaggebend. Durch den bisher genutzten Autoklaven wurden Reaktionszeiten von oftmals 24 h als optimal angesehen und anschließend nicht weiter untersucht/ optimiert, was allerdings nicht das wirkliche Optimum darstellen kann/muss. Aus diesem Grund kann nach dem alle Syntheseparameter abzüglich der Reaktionszeit und –temperatur optimiert wurden mit genau diesen Parametern in Glasreaktoren weitere Optimierungsschritte durchgeführt werden.<sup>50</sup>

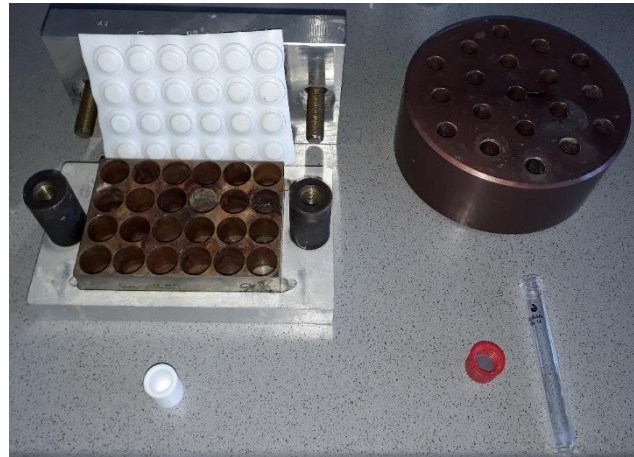


Abb. 3: Bestandteile eines HD-Blocks, wie er im Arbeitskreis von Prof. Stock zur Reaktionsoptimierung genutzt wird (links) und ein Reaktionsröhrchen sowie ein Aluminiumblock die zur Zeit- und Temperatur-Optimierung eingesetzt werden (rechts).

Die Gefäße werden in einem aufgeheizten Aluminiumblock gestellt und durch diesen erhitzt. Nun ist es möglich die Reaktion nach jedem beliebigen Zeitpunkt abubrechen und die Produkte in den Glasreaktoren durch das Abkühlen mit kaltem Wasser zu quenchen. Derselbe Versuch wird bei verschiedenen Temperaturen wiederholt, um am Ende eine Synthesevorschrift vorweisen zu können die auf alle Parameter optimiert ist und besonders für mögliche Aufskalierungsversuche die besten Raum-Zeit-Ausbeuten aufweist (Abb. 4).

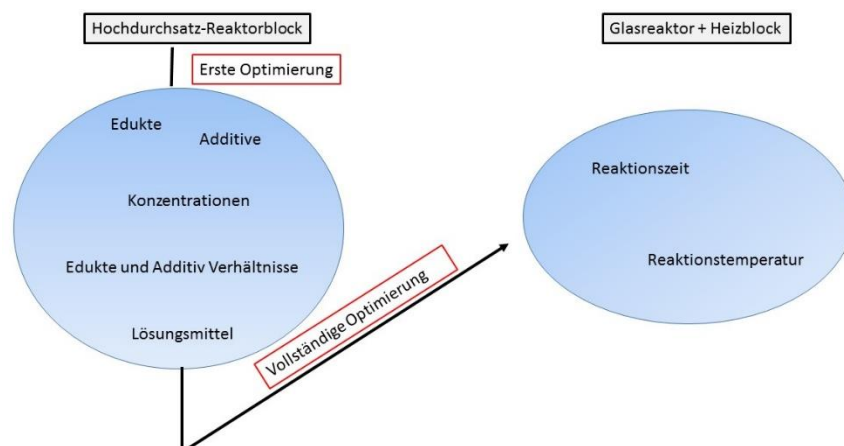


Abb. 4: Schematische Darstellung der zwei Syntheseoptimierungsschritte und den möglichen Optimierungsparametern. Im ersten Schritt sind nur die Standardparameter aufgeführt, selbstverständlich wären weitere Optimierungsparameter möglich.

### 3. Charakterisierungsmethoden: Gassorption

Alle Proben werden zunächst pulverdiffraktometrisch untersucht um festzustellen ob das gewünschte Reaktionsprodukt oder eine neue/andere Verbindung entstanden ist. Allerdings lässt sich aus diesen Untersuchungen wenig über die Eigenschaften des hergestellten Produkts ableiten. Aus diesem Grund ist es wichtig weitere Charakterisierungsmethoden anzuwenden. Bei porösen Materialien bietet sich besonders die Gassorption an um die Porosität zu bestimmen.<sup>51</sup> Stickstoff hat sich dabei als Standardgas für die ersten Messungen etabliert. Dies liegt unter anderem an der sehr hohen und günstigen Verfügbarkeit, der Inertheit und der einfachen Möglichkeit bei der Kondensationstemperatur des Gases zu arbeiten. Die erhaltenen Ergebnisse können in Form einer Ad- bzw. Desorptionsisotherme aufgetragen werden. Diese können wiederum mit verschiedenen mathematischen Verfahren wie der Langmuir-,<sup>52</sup> BET-Theorie,<sup>53</sup> dem t-plot<sup>54</sup> oder dem BJH-Modell<sup>55</sup> ausgewertet werden um verschiedene Aussagen zum Beispiel über die scheinbare-spezifische Oberfläche, das Mikroporenvolumen oder die Porenradienverteilungen zu erhalten.

Auf Grund des besonderen Aufbaus von MOFs sind die verschiedenen Modelle eigentlich nicht streng anwendbar. So wird bei der BET-Theorie von einer homogenen Oberfläche und von einer Mehrschichtadsorption ausgegangen, die aufgrund der Beschaffenheit und der Porengröße von < 2 nm in MOFs eigentlich auszuschließen ist.<sup>56</sup> Allerdings wurde sich auf dieses Verfahren geeinigt, wodurch die Ergebnisse, die an sich wahrscheinlich nur einen Trend angeben, unter einander wieder vergleichbar sind. Dies ist insbesondere wichtig, wenn neue Synthesemethoden (wie die hier beschriebenen Flussreaktorsynthesen) mit bekannten Verbindungen durchgeführt werden, denn so kann sehr schnell ermittelt werden ob sich die erhaltenen Eigenschaften in einem gleichen Rahmen bewegen. So ist es nicht ungewöhnlich, dass beispielsweise durch andere Heizmethoden die zu anderen Reaktionszeiten führen Produkte erhalten werden, die röntgendiffraktometrisch sehr ähnlich sind aber stark voneinander abweichende Sorptionseigenschaften aufweisen.

Neben Stickstoff ist es auch möglich Sorptionsmessungen mit anderen Gasen wie CO<sub>2</sub>, H<sub>2</sub>O, Methan, MeOH, H<sub>2</sub> oder Ähnlichen durchzuführen. Hier ist zu beachten, dass nicht all diese Gase inert sind und die gemessenen Proben während der Sorption zerstört werden könnten. Aus diesem Grund ist eine anschließende pulverdiffraktometrische Untersuchung unerlässlich. Messungen mit diesen Gasen sind insbesondere aus drei Gründen wichtig. Zum einen um das Verhalten der MOFs für bestimmte Anwendungen wie die Gesamtaufnahmekapazität für die Gasspeicherung, beispielsweise bei H<sub>2</sub><sup>40</sup> zu bestimmen, um die Affinität der Poren zu bestimmten Gasen (CO<sub>2</sub>) für eine Gastrennung zu ermitteln<sup>41</sup> oder aber um die Stabilität des MOFs über viele zyklische Sorptionsmessungen (z.B.: für die adsorptionsbasierte Wärmetransformation mit H<sub>2</sub>O) zu ermitteln.<sup>57</sup> Insbesondere bei der isoretikulären Chemie sind solche Messungen wichtig, da in den erhaltenen Pulverdiffraktogrammen



entweder geringe Unterschiede (zum Beispiel durch den Austausch von H<sub>2</sub>BDC durch H<sub>2</sub>PDC)<sup>50</sup> oder nur eine größere Verschiebung der Reflexe (zum Beispiel durch den Austausch von H<sub>2</sub>BDC durch H<sub>2</sub>BPDC)<sup>6</sup> zu messen sind. Die Sorptionseigenschaften hingegen sollten sich in diesen zwei Beispielen immens unterscheiden. Durch den Einbau eines stickstoffhaltigen Linkers wie H<sub>2</sub>PDC würde die Affinität der Poren zu Wasser im Vergleich zu einem normalen Benzolderivat immens steigen. Durch den Einsatz eines längeren Linkers wiederum sollte die Gesamtkapazität steigen.

Selbstverständlich sollte aber neben PXRD- und Gassorptionsmessungen auch noch weitere Charakterisierungsmethoden durchgeführt werden, denn die thermische Stabilität kann erst über thermogravimetrische Messungen oder über Temperatur-abhängige PXRD bestimmt werden. Zur genauen Ermittlung der eingebauten organischen Moleküle müssen Infrarot- und <sup>1</sup>H-NMR-Spektroskopie durchgeführt werden. Aber auch hochspezialisierte Methoden, die nur an Synchrotronquellen durchgeführt werden können, wie EXAFS- oder XANES- Messungen können essentiell sein, um bei sehr komplizierten Strukturen die genaue Koordinationsumgebung oder auch einfach um die Oxidationszahl der Metalle zu bestimmen.

Oft macht es den Anschein, dass eine der hier genannten Methoden die Wichtigste für die Charakterisierung von MOFs ist, aber erst die Summe der einzelnen Methoden macht eine Charakterisierung aussagekräftig und vollständig. Denn eine Struktur ohne bestimmte Sorptionseigenschaften, genauen Zusammensetzung oder Stabilität ist eben nur eine Struktur, genauso wie die Eigenschaften ohne Struktur eben nur Eigenschaften sind.

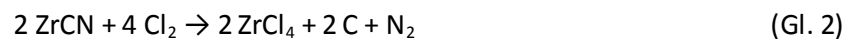
## **II Kumulativer Teil**

## 4.1 Kumulativer Teil Zr-MOFs

### 4.1.1 Einleitung

#### 4.1.1.1 Zirkonium: Synthese und Eigenschaften

Zirkonium kommt in der Natur nicht gediegen, sondern nur gebunden, in der Regel als Silicat  $ZrSiO_4$ , auch Zirkon genannt, oder als Zirkoniumdioxid  $ZrO_2$  (Zirkonerde oder Baddeleyit) vor und ist immer mit einem gewissen Anteil Hafnium (1 - 5 Gew.-%) verunreinigt.<sup>58</sup> Die großtechnische Synthese von reinem Zirkonium erfolgt zunächst in zwei Schritten. Als erstes muss Zirkoniumchlorid  $ZrCl_4$  hergestellt werden. Dies kann entweder durch Carbochlorierung von  $ZrO_2$  (Gl. 1) oder durch Chlorierung von Zirkoniumcarbonitrid  $ZrCN$  hergestellt werden (Gl.2).<sup>58</sup>



Anschließend wird das  $ZrCl_4$  im Kroll-Prozess bei hohen Temperaturen unter He-Atmosphäre mit Magnesium zu Zirkonium reduziert (Gl.3).<sup>58</sup>



Das nun erhaltene Produkt enthält weiterhin Hafniumverunreinigungen. Um ebenfalls das Hafnium abzutrennen sind drei Verfahren möglich: das Extraktionsverfahren, über Ionenaustauscher (Citronensäurelösung in Salpetersäure) oder die fraktionierende Destillation (als  $POCl_3$ -Komplexe). Für das Extraktionsverfahren werden die reinen Verbindungen zunächst in Thiocyanatsalze umgewandelt und dann mit organischen Lösungsmitteln versetzt. Die Löslichkeit von  $Hf(SCN)_4$  ist höher als die von  $Zr(SCN)_4$ , wodurch die beiden Verbindungen voneinander getrennt werden können.<sup>58</sup>

Zirkonium befindet sich in der fünften Periode und der vierten Gruppe (Titangruppe), wodurch es zu den Nebengruppenelementen und zu den Metallen gehört. Es leitet Wärme besser als Strom, ist weich, biegsam, silbrig glänzend und kristallisiert in zwei verschiedenen Modifikationen ( $\alpha$ -Zr und  $\beta$ -Zr).

In  $\alpha$ -Zr, das unter Normalbedingungen entsteht, liegt eine hexagonal-dichteste Kugelpackung (Mg-Typ)

vor. Bei einer Temperatur  $> 876\text{ °C}$  geht  $\alpha$ -Zr in  $\beta$ -Zr über, in der die Atome eine kubisch-raumzentrierte Kugelpackung (W-Typ) einnehmen (Abb. 5).<sup>58</sup>

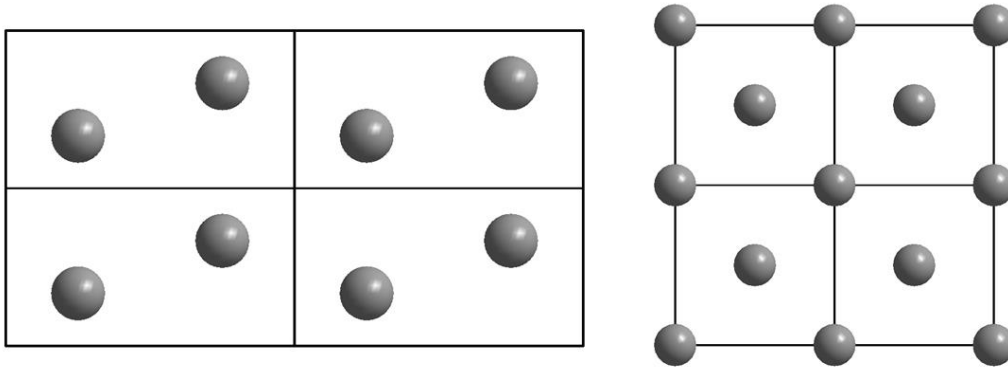


Abb. 5: Kristallstruktur von  $\alpha$ -Zr (links) und  $\beta$ -Zr (rechts).<sup>59</sup>

Die bevorzugte Oxidationsstufe von Zirkonium in seinen Verbindungen ist +IV (z.B.:  $\text{ZrCl}_4$  oder  $\text{ZrO}_2$ ) aber auch +III (z.B.:  $\text{ZrCl}_3$ ), +II (z.B.:  $\text{ZrO}$ ), +I (z.B.:  $\text{ZrCl}$ ) oder  $< 0$  (z.B.:  $[\text{Zr}(\text{CO})_6]^{2-}$ ) sind möglich. Als Koordinationszahlen für Zr(IV) sind von vier bis acht alle denkbar, wobei insbesondere die Koordinationszahl sechs mit einer oktaedrischen Anordnung (z.B.:  $\text{ZrCl}_4$ ) sehr häufig ist.<sup>58</sup>

Reines Zirkonium wird in der chemischen Verfahrenstechnik zur Herstellung von verschiedensten Bauteilen wie Pumpen, Düsen oder Rohren auf Grund der hohen Korrosionsbeständigkeit eingesetzt. Da Zirkonium einen sehr geringen Einfangquerschnitt zur Neutronenadsorption aufweist, wird es für Brennelementumhüllungen in Kernreaktoren eingesetzt. Für diese Anwendung muss es Hafnium frei sein, da der Einfangquerschnitt von Hafnium ca. 600-mal größer ist als der von Zirkonium. Auf Grund der hohen Affinität zu Sauerstoff ist Zirkonium zudem bedeutend als Fangstoff (Getter) in Hochvakuumpumpen oder in der Metallurgie zur Beseitigung von Sauerstoff.<sup>58</sup>

#### 4.1.1.2 Molekulare Zr-O-cluster

Auf Grund der möglichen, großen Koordinationszahlen von Zirkonium und der hohen Affinität zu Sauerstoff<sup>60</sup> ist es nicht verwunderlich das verschiedenste molekulare Zr-O-Cluster bekannt sind. Fast alle Zr-O-Cluster die im Folgenden vorgestellt werden, wurden aus Zirkoniumpropoxid ( $\text{Zr}(\text{O}_n\text{Pr})_4$ ) als Metallquelle und verschiedenen organischen Liganden in Propanol hergestellt. Der Ligand wurde immer im Überschuss eingesetzt, die genaue Menge weicht je nach Verbindung von einander ab. Alle molekularen Zr-O-Cluster konnten als Einkristalle erhalten werden, wodurch die Strukturbestimmung durch Einkristallröntgenbeugung möglich war. Die hier aufgeführte Aufzählung nimmt für sich nicht in Anspruch vollzählig zu sein, es soll eher als Hinführung auf die später beschriebenen Anorganischen

Baueinheiten in Zr-MOFs zu sehen sein. So gibt es einige Gemeinsamkeiten aber auch viele Unterschiede zwischen den molekularen Zr-O-Clustern und den anorganischen Baueinheiten in Zr-MOFs.

Im Jahr 1999 konnte der erste molekulare Zr-O-Cluster, mit einem  $Zr_6$ -Kern beschrieben werden. Als Ligand wurde Methacrylsäure (HOMc) im vierfachen Überschuss eingesetzt und die Reaktionszeit betrug einen Tag.<sup>61</sup> Die Summenformel des hexanuclearen Clusters lautet  $[Zr_6(O)_4(OH)_4(OMc)_{12}]$ . Zunächst ist jedes Zr-Atom quadratisch-antiprismatisch von acht Sauerstoffatomen umgeben, wobei eine Fläche des Quadrates von jeweils zwei  $\mu_3$ -OH und zwei  $\mu_3$ -O und die andere Fläche von Methacrylsäure-Sauerstoffatomen aufgespannt wird.<sup>61</sup> Die daraus entstehenden  $ZrO_8$ -Antiprismen teilen sich nun jeweils eine Kante mit vier weiteren  $ZrO_8$ -Antiprismen, wodurch sich der hexanucleare Cluster bildet (Abb. 6, links). Es sollte bereits hier darauf hingewiesen werden, dass die vier Hydroxid- bzw. Oxidgruppen nicht eindeutig lokalisiert werden konnten, aber auf Grund des Ladungsausgleiches von der vorher beschriebenen Summenformel ausgegangen wird. Dieser hexanucleare Cluster ist Grundlage für die Strukturen von vielen anderen Zr-O-Clustern wie auch für viele IBUs von Zr-MOFs. Allerdings sind auch andere Verknüpfungen bei einem  $Zr_6$ -Kern möglich, z.B. entsteht durch den Einsatz von 1-hydroxy- $\beta$ -naphtoesäure (HNT-OH) im zehnfachen Überschuss ein anderer hexanuclearer Zr-O-Cluster ( $[Zr_6(O)_2(OPr)_{16}(NT-O)_2(PrOH)_2]$ ). Die Struktur des Clusters setzt sich aus vier sechsfach koordinierten und zwei siebenfach koordinierten Zr-Atome zusammen. Die entstehenden  $ZrO_6$ - und  $ZrO_7$ -Polyeder sind kanten- und eckenverknüpft und bilden so eine andere, seltenere Struktur (Abb.6, rechts).<sup>62</sup>

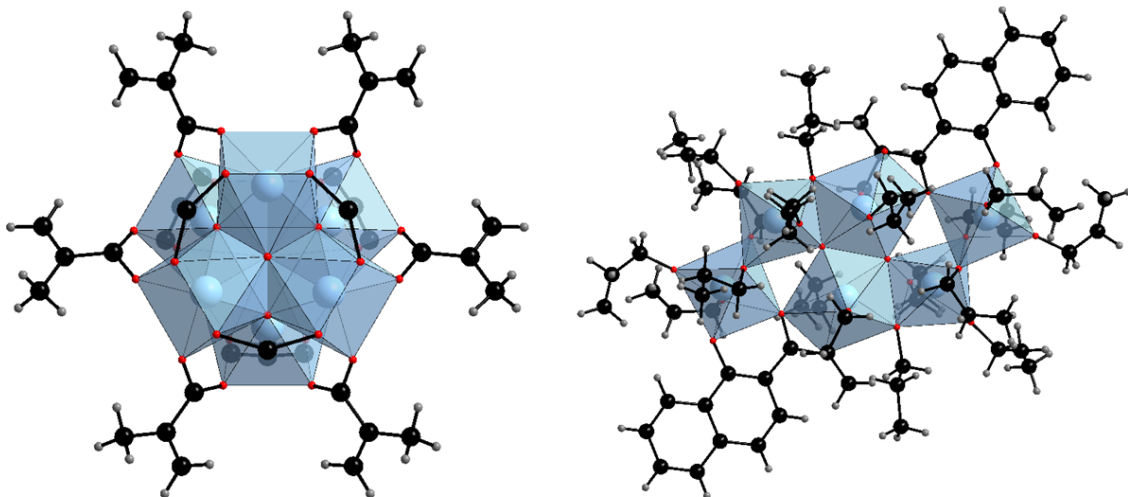


Abb. 6: Die Struktur von  $[Zr_6(O)_4(OH)_4(OMc)_{12}]$  aufgebaut aus sechs quadratisch-antiprismatisch umgebenen  $ZrO_8$ -Polyeder (links)<sup>61</sup> und die Struktur von  $[Zr_6(O)_2(OPr)_{16}(NT-O)_2(PrOH)_2]$  aufgebaut aus ecken und kantenverknüpften  $ZrO_6$ - und  $ZrO_7$ -Polyedern.<sup>62</sup>

Mit dem ersten beschriebenen hexanuklearen Cluster (Abb. 6, links) verwandt, sind die Cluster mit einem  $Zr_5$ -,  $Zr_{10}$ - und  $Zr_{12}$  Kern. Wird anstelle von Methacrylsäure, 2-Brom-isobutansäure (HOIB-Br) in vierfachem Überschuss verwendet, kann ein pentanuklearer Cluster mit der Summenformel  $[Zr_5(O)_4(OIB-Br)_{10}(OPr)_2(PrOH)_4]$  synthetisiert werden.<sup>63</sup> Der  $Zr_5$ -Kern kann durch den  $Zr_6$ -Kern beschrieben werden, indem ein  $ZrO_8$ -Polyeder von der Struktur entfernt wird. Allerdings sind in diesem Beispiel nicht alle Zr-Atome äquivalent. So besitzen drei Zr-Atome die Koordinationszahl acht und zwei die Koordinationszahl sieben (Abb. 7, links).<sup>63</sup> Durch den Einsatz von Salicylsäure (HSC-OH) in zehnfachem Überschuss entsteht ein  $Zr_{10}$ -Kern mit der Summenformel  $[Zr_{10}(O)_6(OH)_4(SC-OH)_8(SC-O)_8]$ . Der hexanukleare Cluster wird in diesem Fall durch zwei  $[Zr_2(O)(SC-OH)_2]$ -Baueinheiten ergänzt (Abb. 7, rechts).<sup>62</sup>

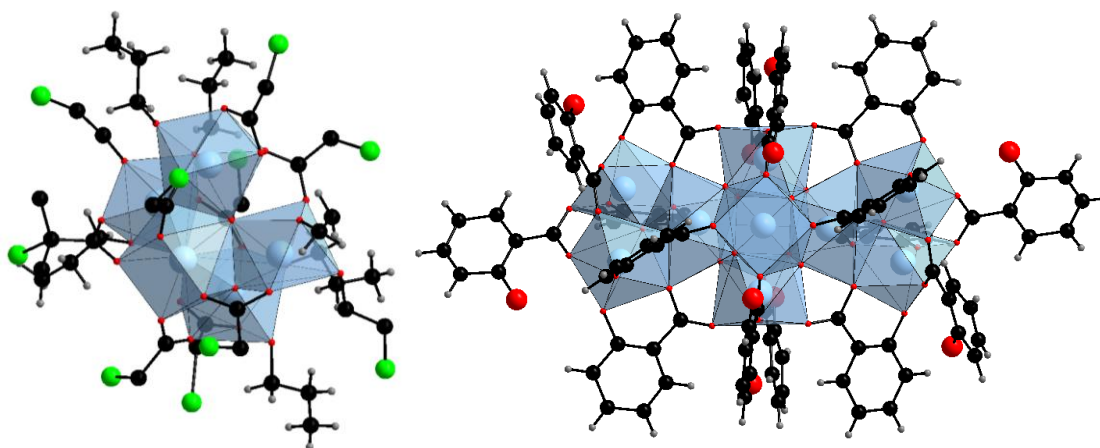


Abb. 7: Die Struktur von  $[Zr_5(O)_4(OIB-Br)_{10}(OPr)_2(PrOH)_4]$  (links)<sup>63</sup> und die Struktur von  $[Zr_{10}(O)_6(OH)_4(SC-OH)_8(SC-O)_8]$  (rechts).<sup>62</sup>

Für  $Zr_{12}$ -kernige Zr-O-Cluster sind bisher zwei verschiedene Motive beschrieben worden, wobei der erste beschriebene auch als eine weitere Variante des hexanuklearen Clusters angesehen werden könnte. Wird Methacrylsäure im vierfachen Überschuss in Butanol und einer organischen Säure wie Essigsäure versetzt entstehen zwei hexanukleare Cluster die über sechs Acetatanionen mit einander verbrückt werden ( $[Zr_6(O)_4(OH)_4(Ac)_3(OMc)_9]_2$ ; Abb. 8, rechts).<sup>64</sup> Wenn nun der Metallquelle die doppelte molare Menge 3,3-Dimethylbutansäure (HMBS) unter Argon-atmosphäre hinzugegeben wird, werden nach einem Tag Zr-O-Cluster aus zwei kondensierten hexanuklearen Clustern erhalten, wodurch ein „echter“  $Zr_{12}$ -Kern mit der Summenformel  $[Zr_6(\mu_3-O)_4(\mu_3-OH)_4(\mu-OH)_3(MBS)_9]_2$  erhalten wird.<sup>65</sup> Die beiden hexanuklearen Cluster werden durch sechs  $\mu$ -OH-Gruppen miteinander verbrückt (Fig 8, rechts).

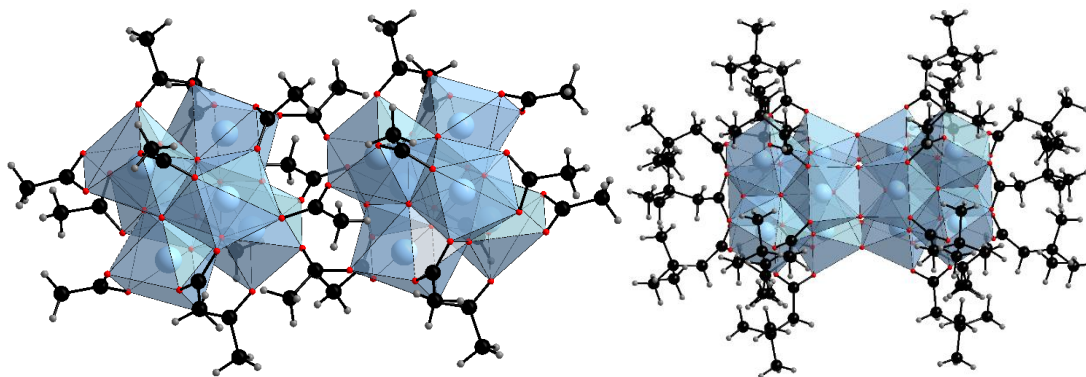


Abb. 8: Die Struktur von  $[\text{Zr}_6(\text{O})_4(\text{OH})_4(\text{Ac})_3(\text{OMc})_9]_2$  (links)<sup>64</sup> und die Struktur von  $[\text{Zr}_6(\mu_3\text{-O})_4(\mu_3\text{-OH})_4(\mu\text{-OH})_3(\text{MBS})_9]_2$  (rechts).<sup>65</sup>

Bisher konnten alle Zr-O-Cluster von dem hexanuklearen  $\{\text{Zr}_6(\text{O})_4(\text{OH})_4\}$ -Cluster abgeleitet werden, allerdings sind auch nicht mit diesem verwandte Cluster bekannt, insbesondere wenn weniger als sechs Zr-Atome zu dem Cluster gehören. So entsteht ein  $\text{Zr}_2$ -Kern wenn zwei  $\text{ZrO}_6$ -Oktaeder kantenverknüpft mit Isobutansäure die Verbindung  $[\text{Zr}_2(\mu\text{-IB})_2(\mu\text{-OPr})_2(\text{OPr})_4]_2$  bilden (Abb. 9, links).<sup>66</sup> Durch mehrere Kantenverknüpfungen von  $\text{ZrO}_7$ -Polyedern entsteht wiederum ein  $\text{Zr}_3$ -Kern mit der Summenformel  $[\text{Zr}_3(\text{O})(\text{OAc})_3(\text{OAc})_2(\text{OPri})_2(\text{OPri})_3]$  (Abb. 9, mitte).<sup>66</sup> Ein  $\text{Zr}_4$ -Kern kann beispielweise durch einen 15-fachen Überschuss an Methacrylsäure nach sieben Tagen synthetisiert werden. In der Verbindung mit der Summenformel  $[\text{Zr}_4(\text{O})_2(\text{OMc})_{12}]$  haben nicht alle Zr-Atom die gleiche Koordinationsumgebung. Drei Zr-Atome sind quadratisch-antiprismatisch umgeben. Das vierte Zr-Atom weist nur noch eine Koordinationszahl von sieben auf, was zu einem verzerrten, überkappten Oktaeder führt.<sup>61</sup> Die entstehenden  $\text{ZrO}_8$  bzw.  $\text{ZrO}_7$  Polyeder werden über Kanten und Ecken zu dem vierkernigen Cluster verbrückt (Abb. 9, rechts). Das Besondere an dieser Verbindung ist, dass die Liganden drei unterschiedliche Koordinationen eingehen. So bilden zwei eine Chelatbindung zum Zirkonium, neun binden symmetrisch zwischen zwei Zirkoniumatomen und einer bildet eine seltene  $\eta^2, \mu$ -Koordinationsart aus.<sup>61</sup> Diese Form wird auch als die asymmetrische Form bezeichnet, die in eine symmetrische Form überführt werden kann, in der das antisymmetrische Methacrylat nur noch als  $\mu$ -verbrückender Ligand fungiert.<sup>67</sup>

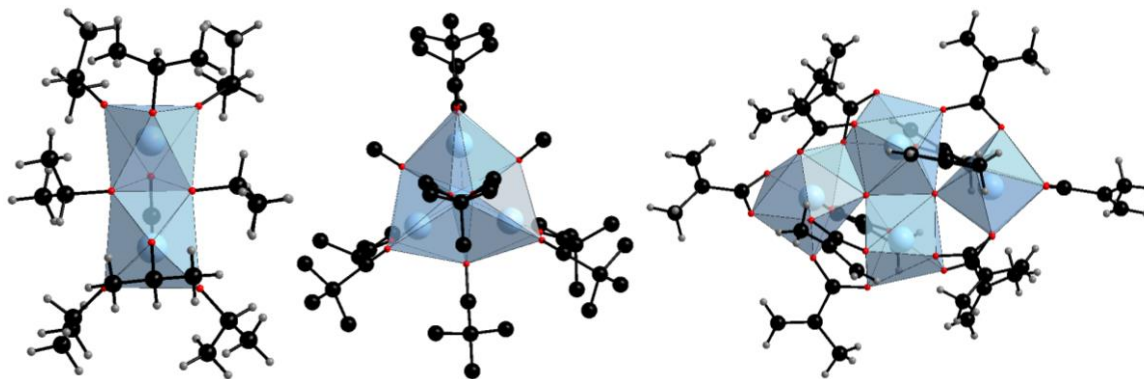


Abb. 9: Die Strukturen von  $[\text{Zr}_2(\mu\text{-IB})_2(\mu\text{-OPr})_2(\text{OPr})_4]_2$  (links)<sup>66</sup>,  $[\text{Zr}_3(\text{O})(\text{OAc})_3(\text{OAc})_2(\text{OPri})_2(\text{OPri})_3]$  (mitte)<sup>66</sup> und von  $[\text{Zr}_4(\text{O})_2(\text{OMc})_{12}]$  (rechts).<sup>61</sup>

Aber auch Zr-O-Cluster mit mehr als sechs Zr-Atomen im Kern sind bekannt. Verschiedene  $\text{ZrO}_8$ -Polyeder bilden bei der Reaktion mit Pentynsäure (HPS) in Butanol beispielsweise durch kanten- und Eckenverknüpfung den  $[\text{Zr}_9(\text{O})_6(\text{OBu})_{18}(\text{PS})_6]$ -cluster (Abb. 10, links).<sup>68</sup> Der bisher größte, publizierte Zr-O-Cluster besteht aus dem Kern  $\{\text{Zr}_{18}(\text{O})_{21}(\text{OH})\}$ , der aus  $\text{ZrO}_6$ -  $\text{ZrO}_7$ -,  $\text{ZrO}_8$ -Polyedern und insgesamt 28 Benzoatresten ( $\text{BA}^-$ ) besteht und in der Verbindung  $[\text{Zr}_{18}(\text{O})_{21}(\text{OH})_2(\text{BA})_{28}]$  kristallisiert (Abb. 10, rechts).<sup>69</sup>

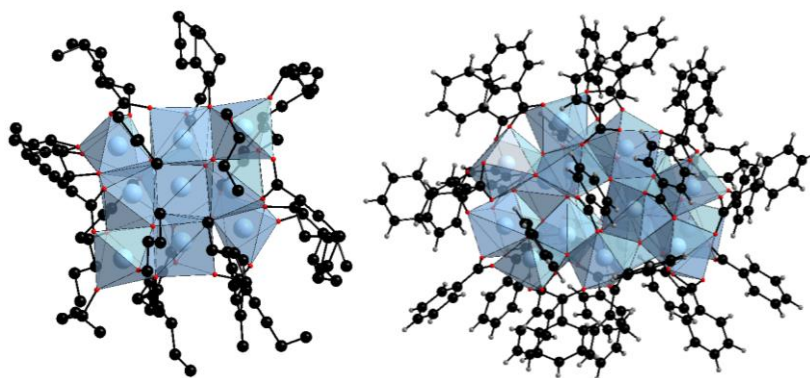


Abb.10: Die Strukturen von  $[\text{Zr}_9(\text{O})_6(\text{OBu})_{18}(\text{PS})_6]$  (links)<sup>68</sup> und  $[\text{Zr}_{18}(\text{O})_{21}(\text{OH})_2(\text{BA})_{28}]$  (rechts).<sup>69</sup>

Neben diesen reinen Zr-O-Clustern, sind auch Misch-Metallcluster bekannt. Insbesondere die Kombination von Zirkonium und Titan ist hierbei reizvoll. Durch den Einsatz verschiedener molarer Verhältnisse von Zirkonium zu Titan und Methacrylsäure als Liganden konnten vier verschiedene Zr-Ti-O-Cluster hergestellt werden, die sich insbesondere durch eine unterschiedliche Verknüpfung der einzelnen Polyeder unterscheiden. Es wurden jeweils zwei Verbindungen mit der allgemeinen Summenformel  $\text{M}_6\text{O}_4\text{L}_{16}$ <sup>70</sup> bzw.  $\text{M}_8\text{O}_6\text{L}_{20}$ <sup>70</sup> synthetisiert. In den Verbindungen mit der Zusammensetzung  $\text{M}_6\text{O}_4\text{L}_{16}$  bilden die M-O-Cluster  $\text{ZrO}_8$ - und  $\text{TiO}_6$ -Polyeder über eine Kantenverknüpfung eine Zickzack-Kette. Die beiden Verbindungen unterscheiden sich nur durch die



Anordnung der einzelnen Cluster. So ist in  $[\text{Ti}_2\text{Zr}_4(\text{O})_4(\text{OBu})_2(\text{OMc})_{14}]$  jeweils ein weiterer  $\text{ZrO}_8$ -polyeder an die Kette koordiniert (Abb. 11, oben links) und bei  $[\text{Ti}_4\text{Zr}_2(\text{O})_4(\text{OBu})_6(\text{OMc})_{10}]$  jeweils ein weiterer  $\text{TiO}_6$ -Polyeder (Abb. 11 oben rechts).<sup>70</sup> Die Struktur der Verbindungen mit der Zusammensetzung  $\text{M}_8\text{O}_6\text{L}_{20}$  ist auch aus einer Zigzag-Kette aus  $\text{ZrO}_8$ - und  $\text{TiO}_6$ -Polyedern aufgebaut, die hier um zwei  $\text{ZrO}_8$ -Polyeder erweitert ist (Abb. 11, unten).<sup>70</sup>

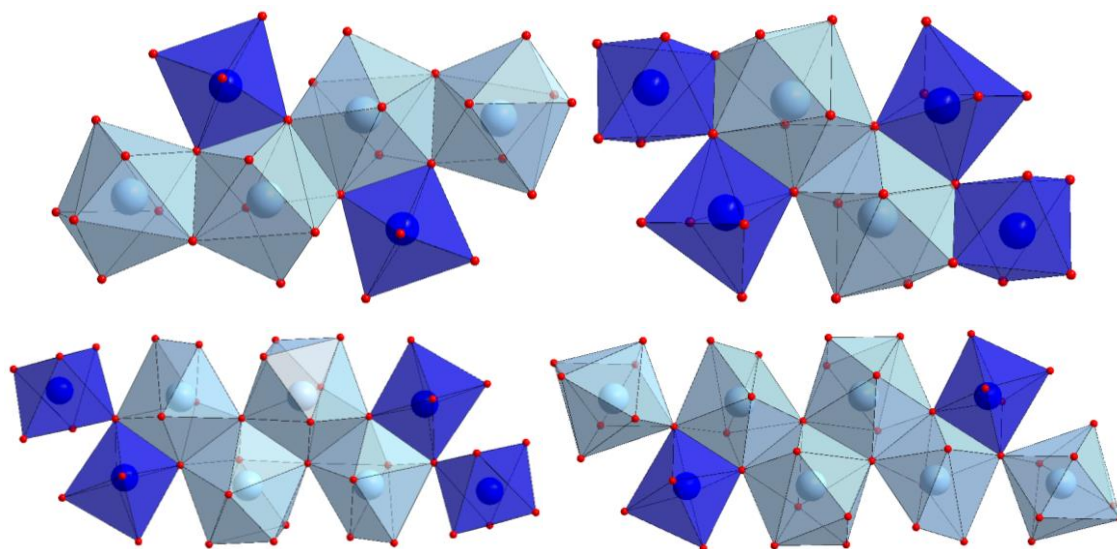


Abb. 11: Die M-O-Cluster in  $[\text{Ti}_2\text{Zr}_4(\text{O})_4(\text{OBu})_2(\text{OMc})_{14}]$  (oben links),  $[\text{Ti}_4\text{Zr}_2(\text{O})_4(\text{OBu})_6(\text{OMc})_{10}]$  (oben rechts),  $[\text{Ti}_4\text{Zr}_4(\text{O})_6(\text{OBu})_4(\text{OMc})_{16}]$  (unten links) und  $[\text{Ti}_2\text{Zr}_6(\text{O})_6(\text{OMc})_{20}]$  (unten rechts), für eine bessere Übersicht wurden die organischen Liganden nicht dargestellt.<sup>70</sup>

Zusammenfassend kann gesagt werden, dass es zwar einige molekulare Zr-O-Cluster gibt, aber viele auf das Motiv des hexanuklearen Zr-O-Cluster zurück zu führen sind oder aber bisher sehr selten wenn nicht sogar nur einmal synthetisiert werden konnten. Ein ähnliches Verhalten wird auch bei den IBUs von Zr-MOFs festgestellt.

#### 4.1.1.3 Zr-MOFs: IBU's, Strukturen und Synthesen

Wenn in der Literatur die Forschung an Zr-MOFs begründet wird, geschieht dies meistens mit der hohen thermischen wie chemischen Stabilität,<sup>71</sup> dem Ansatz der isoretikulären Chemie<sup>72</sup> oder den vielseitigen Anwendungsmöglichkeiten,<sup>71</sup> die unter echten Bedingungen allerdings erst noch nachgewiesen werden müssen. Da mittlerweile so viele verschiedene Zr-MOF beschrieben wurden, können diese Eigenschaften aber nicht für alle verallgemeinert werden, weswegen dieses Kapitel sich

mit den anorganischen Baueinheiten und einigen dazugehörigen exemplarischen Strukturen von Zr-MOFs und mögliche Syntheseansätzen befasst.

### Anorganische Baueinheiten und Strukturen von Zr-MOFs

Insgesamt sind bis heute zehn verschieden IBUs für Zr-MOFs bekannt. Von den molekularen Zr-O-Clustern, insbesondere von dem hexanuclearen Zr-O-Cluster, lassen sich bereits sechs IBUs ableiten, wobei drei dieser IBUs zu Beginn dieser Arbeit nicht bekannt waren.

2008 wurde der erste Zr-MOF, UiO-66 ( $[\text{Zr}_6(\text{O})_4(\text{OH})_4(\text{BDC})_6]$ , UiO = Universität in Oslo), mit Terephthalanionen als Linker und dem bereits beschriebenen hexanuclearen Cluster  $\{\text{Zr}_6(\text{O})_4(\text{OH})_4\}^{12+}$  als IBU publiziert.<sup>6</sup> Die freien Koordinationsstellen des Zr-Atoms werden durch zwölf Carboxylationen abgesättigt, gleichzeitig werden die Cluster dadurch mit einander verbrückt und eine dreidimensionale Gerüststruktur entsteht (Abb. 12 oben mitte). Das Gerüst weist eine **fcu**-Topologie mit zwei unterschiedlich großen Poren auf. Bereits in dieser sehr frühen Arbeit konnte zudem gezeigt werden, dass das Konzept der isoretikulären Chemie auch bei der Synthese von Zr-MOFs angewendet werden kann. So wurde UiO-67 mit 4,4'-Biphenyldicarbonsäure und UiO-68 mit Terphenyldicarbonsäure anstatt der vorher eingesetzten Terephthalsäure als Linker hergestellt. Die Strukturen beider Verbindungen weisen die gleiche Topologie von Zr-O-Clustern und Linker auf, nur dass sich die Porengröße in Abhängigkeit von den größeren Linkern verändert hat.<sup>6</sup> Dieses Konzept wurde in den folgenden Jahren immer wieder angewendet um neue Verbindungen mit UiO-66-Struktur herzustellen. So führte der Einsatz von funktionalisierten Terephthalsäuren,<sup>73,74</sup> aliphatischen Linkern wie Fumarsäure,<sup>36</sup> cyclischen Linkern wie *trans*-1,4-Cyclohexandicarbonsäure,<sup>37</sup> Azolinkern<sup>75</sup> oder Linkern bestehend aus stickstoffhaltigen Heterozyklen wie 2,5-Pyridindicarbonsäure<sup>50,76</sup> immer zu Verbindungen mit UiO-66-Struktur. Wenn der hexanucleare Zr-O-Cluster eine geringere Konnektivität aufweist, führt dies zu anderen Strukturen und Topologien. Beispielsweise konnte durch den Einsatz von 2,5-Thiophendicarbonsäure ( $\text{H}_2\text{TDC}$ ), je nach Synthesebedingung, DUT-69 ( $[\text{Zr}_6(\text{O})_4(\text{OH})_4(\text{TDC})_5(\text{Ac})_2]$ , DUT = Technische Universität Dresden) mit **bct**-Topologie (Abb. 12 oben rechts)<sup>77</sup> oder DUT-67 ( $[\text{Zr}_6(\text{O})_6(\text{OH})_2(\text{TDC})_4(\text{Ac})_2]$ ) mit **reo**-Topologie (Abb. 12 unten links)<sup>77</sup> synthetisiert werden. In diesen Verbindungen sind die Zr-O-Cluster zehn- bzw. achtfach verknüpft. Der notwendige Ladungsausgleich bei beiden MOFs wird durch an den Cluster gebundene Acetationen (Ac) ermöglicht. In DUT-84 ( $[\text{Zr}_6(\text{O})_8(\text{NDC})_3(\text{Ac})_2]$ ) verknüpft der Linker  $\text{NDC}^{2-}$  die Zr-O-Cluster nur sechsfach (Abb. 12 unten mitte).<sup>78</sup> Erneut dienen Acetatanionen zum Ladungsausgleich. Aber auch eine sehr geringe Zr-O-Cluster-verknüpfung von vier (**sqc**-Topologie) ist möglich, wenn Adipinsäure ( $\text{H}_2\text{AP}$ ) und Zirkoniumsulfat bei den richtigen Synthesebedingungen zur

Reaktion gebracht werden. Es entsteht Zr-AP-2 ( $[\text{Zr}_6(\text{OH})_{12}(\text{SO}_4)_4(\text{AP})_2(\text{H}_2\text{O})_4]$ ) in dem zum Ladungsausgleich weitere Hydroxidionen und Sulfationen an den Cluster gebunden sind (Abb. 12 unten rechts). Um die Koordinationssphäre ab zu sättigen, wird die Summenformel von Zr-AP-2 um vier Wassermoleküle ergänzt.<sup>79</sup>

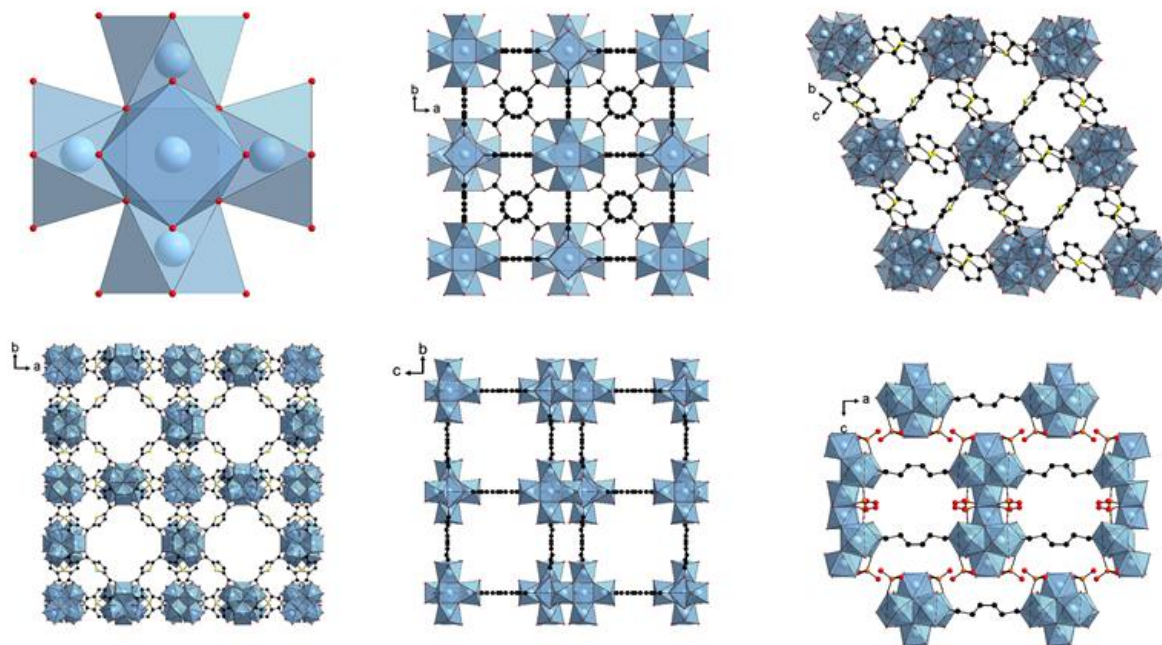


Abb. 12: Strukturen von unterschiedlich verknüpften hexanuklearen Zr-O-Clustern (oben links). UiO-66 ( $[\text{Zr}_6(\text{O})_4(\text{OH})_4(\text{BDC})_6]$ , 12fach, oben mitte),<sup>6</sup> DUT-69 ( $[\text{Zr}_6(\text{O})_4(\text{OH})_4(\text{TDC})_5(\text{Ac})_2]$ , 10fach, oben rechts),<sup>77</sup> DUT-67 ( $[\text{Zr}_6(\text{O})_6(\text{OH})_2(\text{TDC})_4(\text{Ac})_2]$ , 8fach, unten links),<sup>77</sup> DUT-84 ( $[\text{Zr}_6(\text{O})_8(\text{NDC})_3(\text{Ac})_2]$ , 6fach, unten mitte)<sup>78</sup> und Zr-AP-2 ( $[\text{Zr}_6(\text{OH})_{12}(\text{SO}_4)_4(\text{AP})_2(\text{H}_2\text{O})_4]$ , 4fach, unten rechts).<sup>79</sup>

Neben dem hexanuklearen Zr-O-Cluster, sind auch die beiden dodecanuklearen Zr-O-Cluster als IBU in Zr-MOFs bekannt. Die Synthese des über Acetationen verbrückten molekularen hexanuklearen Zr-O-Clusters wurde zunächst optimiert und dann direkt als Startmaterial für die Synthese des neuen MOFs eingesetzt. Bei dem Einsatz von  $\text{H}_2\text{BPDC}$  als Linker, konnte die Verknüpfung der Zr-O-Cluster nicht beibehalten werden und es entstand UiO-67. Wenn aber tris-(4-Carboxyphenyl)-phosphin ( $\text{H}_3\text{TPP}$ ) als Linker eingesetzt wird, bleibt die Verknüpfung erhalten und es entsteht der MOF Zr-TPP ( $[\text{Zr}_{12}\text{O}_8(\text{OH})_8(\text{Ac})_{18}(\text{TPP})_2]$ , Abb. 13 oben rechts).<sup>80</sup> Durch die Verknüpfung der einzelnen Zr-O-Cluster mit dem Linker entsteht eine selten beobachtete zwei-dimensionale Netzwerkstruktur mit **kgd**-Topologie.

Der kondensierte dodecanukleare Cluster wurde nicht vorab synthetisiert, sondern entstand beispielsweise während der Umsetzung von  $\text{ZrCl}_4$  mit Triphenyldicarbonsäure ( $\text{H}_2\text{TPDC}$ ) zu Zr-TPDC ( $[\text{Zr}_{12}(\text{O})_8(\mu_3\text{-OH})_8(\mu_2\text{-OH})_6(\text{TPDC})_9]$ ), in der eine drei-dimensionale Gerüststruktur

vorliegt (Abb. 13 unten links).<sup>81</sup> Die gleiche Gruppe veröffentlichte im gleichen Jahr noch drei isoretikuläre Verbindungen zu Zr-TPDC.<sup>82</sup> Zusätzlich konnten wir in diesem Jahr eine neue Verbindung (CAU-39) mit dem kondensierten dodecanuklearen Cluster und Azopyridindicarbonsäure ( $H_2APDC$ ) synthetisieren, in der die Cluster nur noch in zwei Dimensionen verbrückt sind, und für die folgende Summenformel abgeleitet wurde:  $[Zr_{12}(O)_8(\mu_3-OH)_8(\mu_2-OH)_6(OH)_6(H_2O)_6(APDC)_6]$  (Abb. 13 unten rechts).<sup>83</sup>

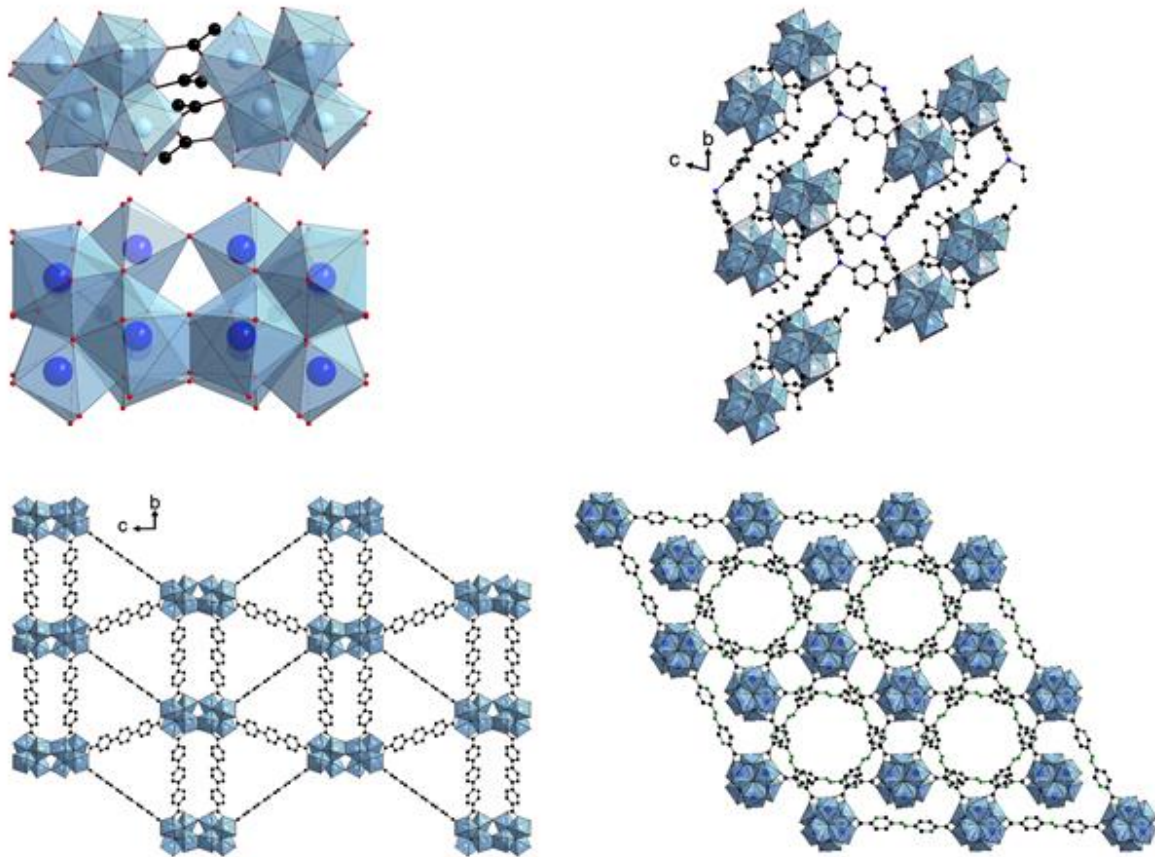


Abb. 13: Strukturen mit den verschiedenen dodecanuklearen Zr-O-Clustern (oben links) von Zr-TPP ( $[Zr_{12}O_8(OH)_8(Ac)_{18}(TPP)_2]$ , oben rechts),<sup>80</sup> Zr-TPDC ( $[Zr_{12}(O)_8(OH)_{14}(TPDC)_9]$ , unten links)<sup>81</sup> und CAU-39 ( $[Zr_{12}(O)_8(OH)_{20}(H_2O)_6(APDC)_6]$ , unten rechts).<sup>83</sup>

Neben den bisher beschriebenen IBUs sind zwei weitere bekannt, die von dem hexanuklearen Cluster abzuleiten sind, allerdings nicht als molekulare Zr-O-Cluster bekannt sind. Dies liegt wahrscheinlich daran, dass es sich im Gegensatz zu den vorher genannten nicht um null-dimensionale sondern um ein-dimensionale IBUs, d.h. Ketten, handelt. Zunächst kondensieren in CAU-22 die hexanuklearen Cluster über zwei Kanten, jeweils zwei Hydroxidionen, zu einer Kette von Zr-O-Clustern (Abb. 14 oben links). Diese Ketten werden über sechs Pyrazindicarboxylationen zu einer

drei-dimensionalen Struktur verknüpft. Die Verbindung weist die Summenformel  $[\text{Zr}_6(\mu_3\text{-O})_4(\mu_3\text{-OH})_4(\mu\text{-OH})_2(\text{OH})_2(\text{H}_2\text{O})_2(\text{HCO}_2)_2(\text{PzDC})_3]$  auf. Der Ladungsausgleich erfolgt durch Formiat- und Hydroxidionen und die Absättigung der Koordinationssphäre der Zr-Atome durch Wassermoleküle (Abb. 14 oben rechts).<sup>84</sup> Eine noch stärker kondensierte Kette von hexanuklearen Clustern werden in CAU-27 ( $[\text{Zr}_5\text{O}_4(\text{OH})_4(\text{OAc})_4(\text{BDC})_2]$ ) beobachtet (Abb. 14 unten).<sup>85</sup>

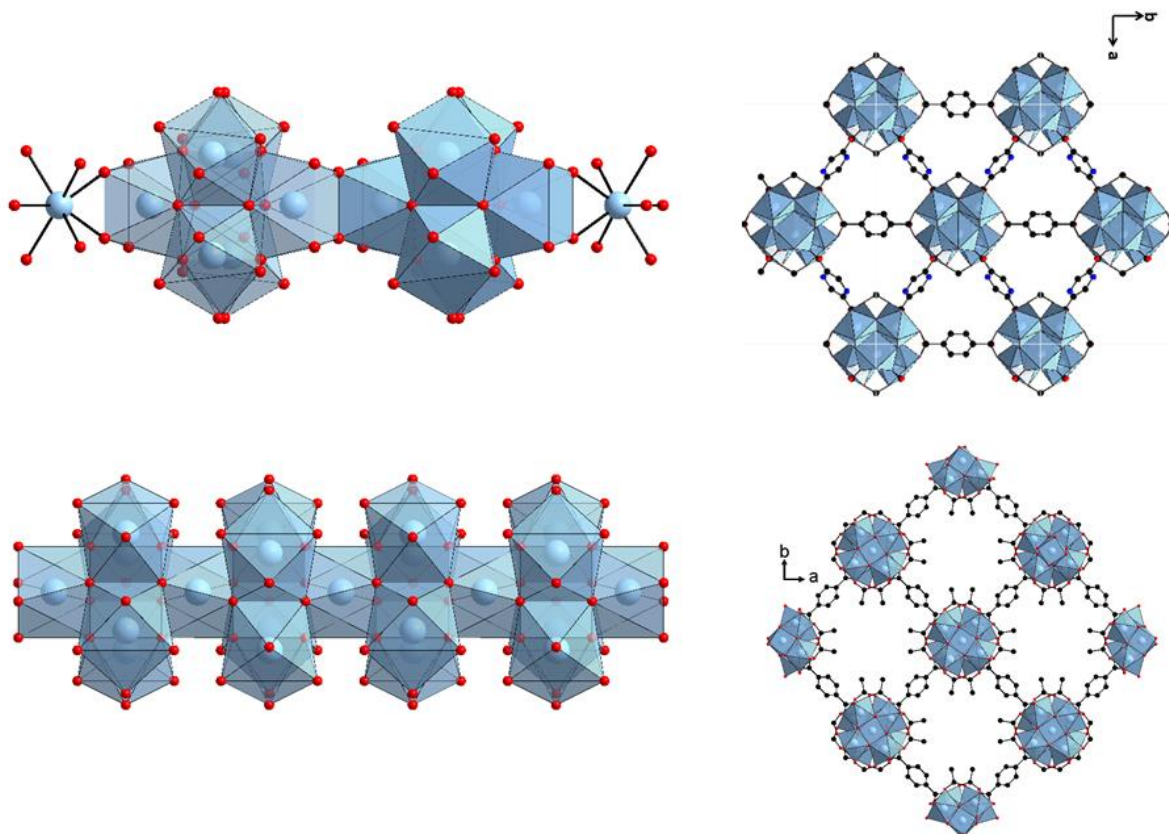


Abb. 14: IBUs und Strukturen von CAU-22 ( $[\text{Zr}_6(\text{O})_4(\text{OH})_8(\text{H}_2\text{O})_2(\text{HCO}_2)_2(\text{PzDC})_3]$ , oben)<sup>84</sup> bzw. CAU-27 ( $[\text{Zr}_5\text{O}_4(\text{OH})_4(\text{OAc})_4(\text{BDC})_2]$ , unten).<sup>85</sup>

Eine weitere ein-dimensionale IBU ist verwandt mit den zigzag-Ketten der molekularen Ti/Zr-O-Cluster. Sie besteht aus  $\text{ZrO}_7$ -Polyedern die miteinander kantenverknüpft sind (Abb. 15 links oben). Durch den Linker wird eine drei-dimensionale Struktur, das MIL-140 mit der Summenformel  $[\text{ZrOL}]$  gebildet. L bedeutet das mehrere isoretikuläre MOFs mit verschiedenen Dicarboxylationen als Linkermolekülen hergestellt werden können (Abb. 15 links unten).<sup>86</sup> Eine weitere eindimensionale IBU ist in MIL-163 mit 5,5'-(1,2,4,5-tetrazine-3,6-diyl)bis(benzene-1,2,3-triol) ( $\text{H}_6\text{TzGal}$ ) als Linker vorzufinden ( $[\text{Zr}(\text{H}_2\text{-TzGal})]$ ).<sup>35</sup> Allerdings besteht diese Kette aus kantenverknüpften  $\text{ZrO}_8$ -Polyedern und große quadratische Poren entstehen in dem Gerüst. Zwar sind weitere Phenolat-basierte Verbindungen mit dieser Baueinheit bekannt,<sup>87</sup> da diese aber nicht porös sind, werden sie hier nicht berücksichtigt.

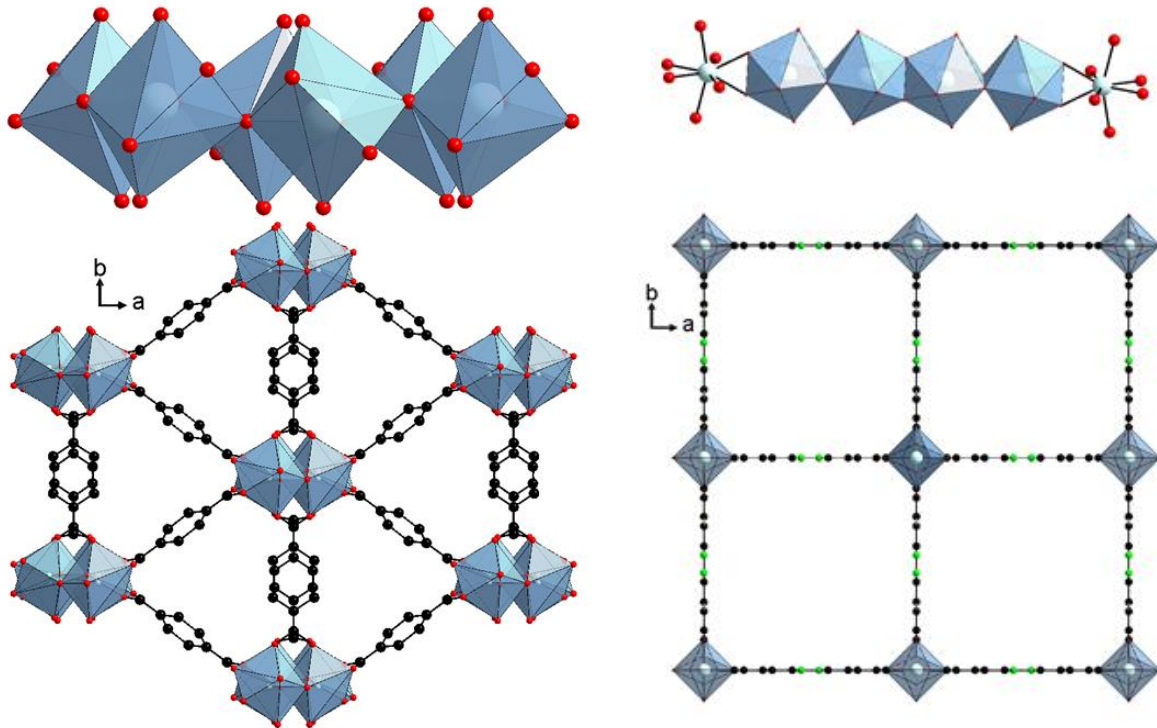


Abb. 15 IBUs und Strukturen von MIL-140 ([ZrO(BDC)], links)<sup>86</sup> und von MIL-163 ([Zr(H<sub>2</sub>-TzGal], rechts).<sup>35</sup>

Für Phosphonat-basierte Zr-MOFs wurden bisher zwei IBUs beschrieben, die sich aber sehr stark ähneln. Zunächst werden ZrO<sub>6</sub>-Polyeder mit PO<sub>3</sub>C-Tetradern über Ecken zu einer Kette verknüpft. In UPG-1 ([Zr(H<sub>4</sub>TTBMP)<sub>2</sub>], Abb. 16 oben) koordinieren diese Ketten weiter mit 2,4,6-tris(4-(phosphonomethyl)phenyl)-1,3,5-Triazine (H<sub>4</sub>TTBMP<sup>2-</sup>) und bilden eine drei-dimensionale Gerüststruktur. Allerdings koordinieren nur zwei der drei Hydrogenphosphonationen, die anderen zeigen in eine Pore, wodurch diese blockiert wird.<sup>31</sup> In CAU-30 ([Zr<sub>2</sub>(Ni-H<sub>2</sub>TPPP)(OH/F)<sub>2</sub>], Abb. 16 unten) sind die ZrO<sub>6</sub>-Polyeder zusätzlich noch eckenverknüpft. Außerdem bilden sich in dieser Verbindung durch den Einsatz eines Porphyrinlinkers quadratische Poren im Gegensatz zu runden Poren in UPG-1.<sup>32</sup>

## Kumulativer Teil Zr-MOFs: Einleitung

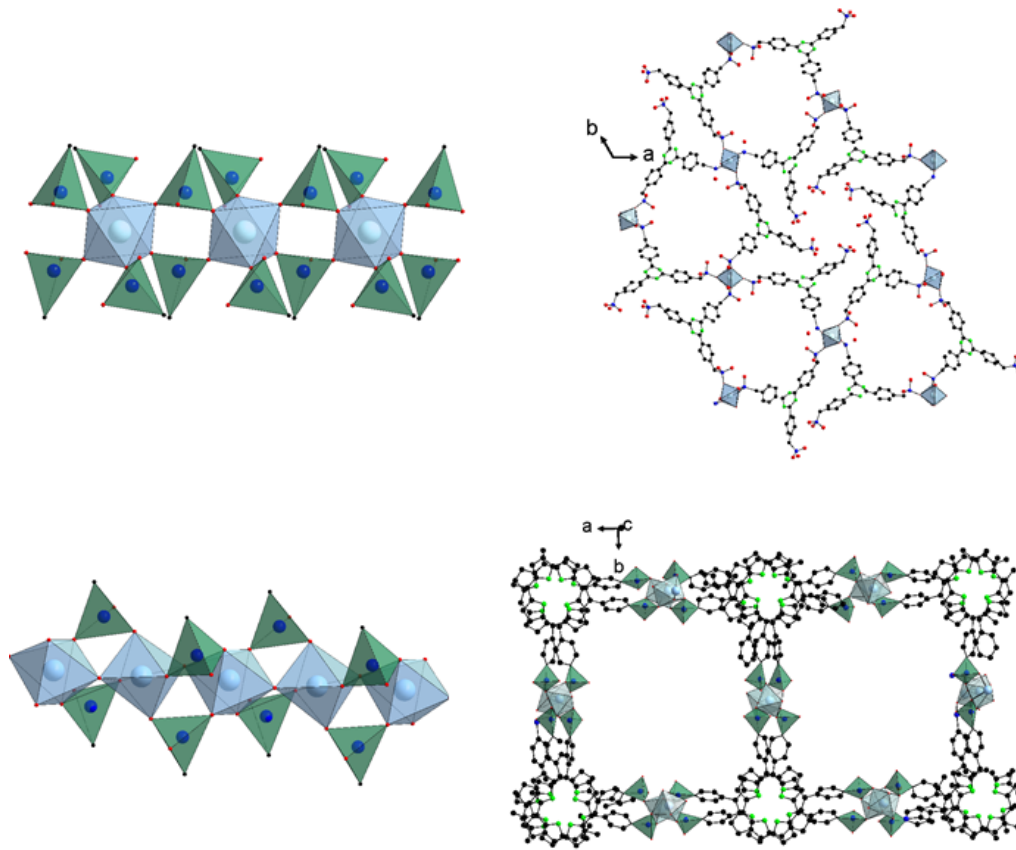


Abb. 16 IBUs und Strukturen von UPG-1 ( $[\text{Zr}(\text{H}_2\text{-TzGal})_2]_2$ , oben)<sup>31</sup> und CAU-30 ( $[\text{Zr}_2(\text{Ni-H}_2\text{TPPP})(\text{OH}/\text{F})_2]$ , unten).<sup>32</sup>

Der Vollständigkeit halber muss an dieser Stelle auch die IBU von PCN-221 ( $[\text{Zr}_8\text{O}_6(\text{TCPP})_3]$ ) vorgestellt werden. Auf Grund sehr schlechter Analytik, besteht der begründete Verdacht, dass diese IBU nicht wirklich so existiert. Es soll sich um einen  $\text{Zr}_8\text{O}_6$ -Polyeder handeln der über Porphyrinlinker verknüpft wird (Abb. 17). Wahrscheinlicher ist allerdings das es sich in Wahrheit um den bekannten hexanuklearen Zr-O-Cluster handelt.<sup>88</sup>

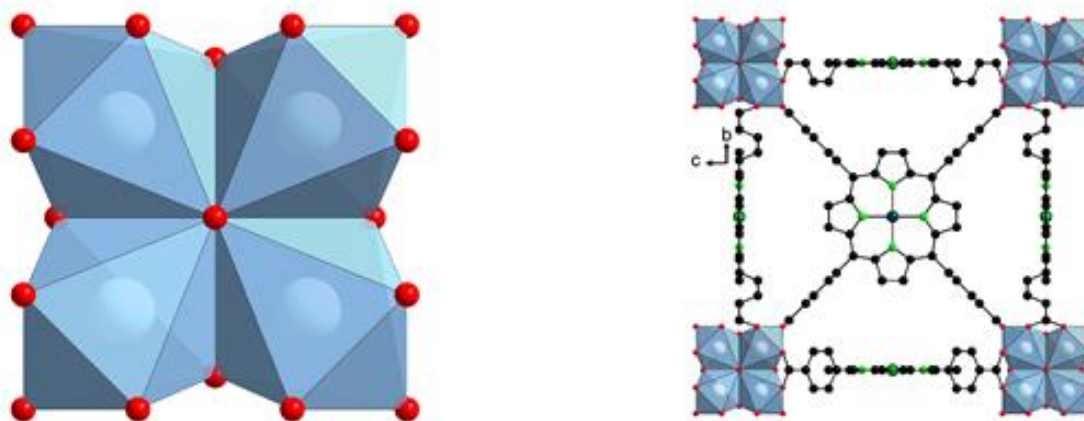


Abb. 17: IBU (links) und Struktur von PCN-221 ( $[\text{Zr}_8\text{O}_6(\text{TCPP})_3]$ , rechts).<sup>88</sup>

Mittlerweile sind zwar einige IBUs von Zr-MOFs bekannt aber wie in Tab. 1 zu sehen, sind die meisten davon erst in den letzten drei Jahren publiziert worden und es gibt abgesehen von dem hexanuklearen Zr-O-Cluster nur sehr wenige Verbindungen oder Strukturen pro IBU. Wenn nun die Ergebnisse der molekularen Zr-O-Cluster und der der IBUs in Zr-MOFs miteinander verglichen werden, ist eine große Ähnlichkeit bei den am meisten auftretenden Typen ersichtlich. Es zeigt aber auch, dass insbesondere bei den MOFs noch weiterer Forschungsbedarf besteht. So könnte es möglich sein, durch den gezielten Einsatz der in der MOF-Chemie unbekannteren molekularen Zr-O-Cluster neue IBUs und damit ganz neue MOFs zu erhalten.



## Kumulativer Teil Zr-MOFs: Einleitung

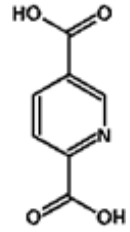
Tab. 1: Zusammenfassung der IBUs von Zr-MOFs mit jeweils einem Beispiel, Anzahl an publizierten Verbindungen mit dieser IBU, Jahr der Erstveröffentlichung und den dazugehörigen Literaturquellen.

Bsp.	IBU	Summenformel	Lösgm.	∑MOFs	Erstveröffentlichung	Quelle
UiO-66	${}^0\{\text{Zr}_6(\text{O})_4(\text{OH})_4\}$	$[\text{Zr}_6(\text{O})_4(\text{OH})_4(\text{BDC})_6]$	H <sub>2</sub> O	< 250	2008	6
Zr-TPP	${}^0\{\text{Zr}_6(\text{O})_4(\text{OH})_4(\text{Ac})_3\}_2$	$[\text{Zr}_{12}\text{O}_8(\text{OH})_8(\text{Ac})_{18}(\text{TPP})_2]$	DMF	1	2018	80
Zr-TPDC	${}^0\{\text{Zr}_6(\text{O})_4(\text{OH})_4(\text{OH})_3\}_2$	$[\text{Zr}_{12}(\text{O})_8(\mu_3\text{-OH})_8(\mu_2\text{-OH})_6(\text{TPDC})_9]$	DMF, H <sub>2</sub> O	4	2017	81-83
CAU-22	${}^1\{\text{Zr}_6\text{O}_4(\text{OH})_4(\mu\text{-OH})_2\}$	$[\text{Zr}_6(\mu_3\text{-O})_4(\mu_3\text{-OH})_4(\mu\text{-OH})_2(\text{OH})_2(\text{H}_2\text{O})_2(\text{HCO}_2)_2(\text{PzDC})_3]$	H <sub>2</sub> O	1	2016	84
CAU-27	${}^1\{\text{Zr}_5\text{O}_4(\text{OH})_4\}$	$[\text{Zr}_5\text{O}_4(\text{OH})_4(\text{OAc})_4(\text{BDC})_2]$	AA	3	---	85
MIL-140	${}^1\{\text{Zr}(\mu_3\text{-O})_3\text{O}_4\}$	$[\text{ZrO}(\text{BDC})]$	DMF	4	2012	86
MIL-163	${}^1\{\text{ZrO}_8\}$	$[\text{Zr}(\text{H}_2\text{-TzGal})]$	DMF, H <sub>2</sub> O	1	2015	35
UPG-1	${}^1\{\text{ZrO}_6\}$	$[\text{Zr}(\text{H}_4\text{TTBMP})_2]$	H <sub>2</sub> O	1	2014	31
CAU-30	${}^1\{\text{ZrO}_6\}$	$[\text{Zr}_2(\text{Ni-H}_2\text{TPPP})(\text{OH}/\text{F})_2]$	DMF	1	2018	32
PCN-221	${}^0\{\text{Zr}_8\text{O}_6\}$	$[\text{Zr}_8\text{O}_6(\text{Tcpp})_3]$	DMF	1	2013	88

### Synthesemethoden für Zr-MOFs

UiO-66 ist neben MIL-53,<sup>89</sup> HKUST-1<sup>90</sup> und ZIF-8<sup>91</sup> wohl der Prototyp-MOF und der am intensivsten, bezüglich möglicher Anwendungen und Synthesemethoden, untersuchte MOF.<sup>71</sup> Die Synthese von Zr-MOFs wird typischerweise bei 120 °C oder höher für eine Dauer von 24 h oder länger, in DMF als Lösungsmittel und in geschlossenen Reaktoren durchgeführt. Mit der reinen Zielsetzung neue Verbindungen herzustellen, ist diese Methode meistens ausreichend. Mit Blick auf die mögliche Überführung der Verbindungen von der akademischen Forschung in die industrielle Nutzung, muss aber etwas von dieser Route abgewichen werden. So wären möglichst niedrige Reaktionstemperaturen und -reaktionszeiten aus Kostengründen wünschenswert. Ebenso wäre der Austausch des toxischen Lösungsmittels DMF durch andere Lösungsmittel, im Idealfall Wasser, hervorragend. Allerdings gibt es abgesehen von (funktionalisierten) UiO-66-Verbindungen kein sehr großes Bestreben wasserbasierte Synthesen zu entwickeln. Dies liegt möglicherweise daran, dass solange dies nicht explizit gefordert wird, niemand diese nicht triviale Aufgabe auf sich nimmt. Da auf verschiedenen Synthesemethoden noch im Kapitel Flussreaktoren eingegangen wird und auch immer UiO-66 mit diesen hergestellt wird, soll hier nur herausgestellt werden, dass zwar viele funktionalisierte UiO-66 Verbindungen aus Wasser hergestellt wurden aber Bezug nehmend auf die bisher beschriebenen IBUs nur sehr wenige in Wasser beobachtet werden konnten. In den vorliegenden Ergebnissen wurde immer besonders darauf geachtet, DMF als Lösungsmittel zu vermeiden. Alle hier präsentierten Ergebnisse zu Zr-MOFs konnten unter wässrigen Bedingungen gewonnen werden. Wasser scheint also nicht nur das Lösungsmittel der Wahl zu sein, wenn es darum geht ein nicht giftiges Lösungsmittel zu verwenden, sondern auch um neue anorganische Baueinheiten in Zr-MOFs zu erhalten.

**4.1.2.1 Synthesis of M-UiO-66 (M = Zr, Ce or Hf) employing 2,5-pyridinedicarboxylic acid as linker: defect chemistry, framework hydrophilisation and sorption properties**



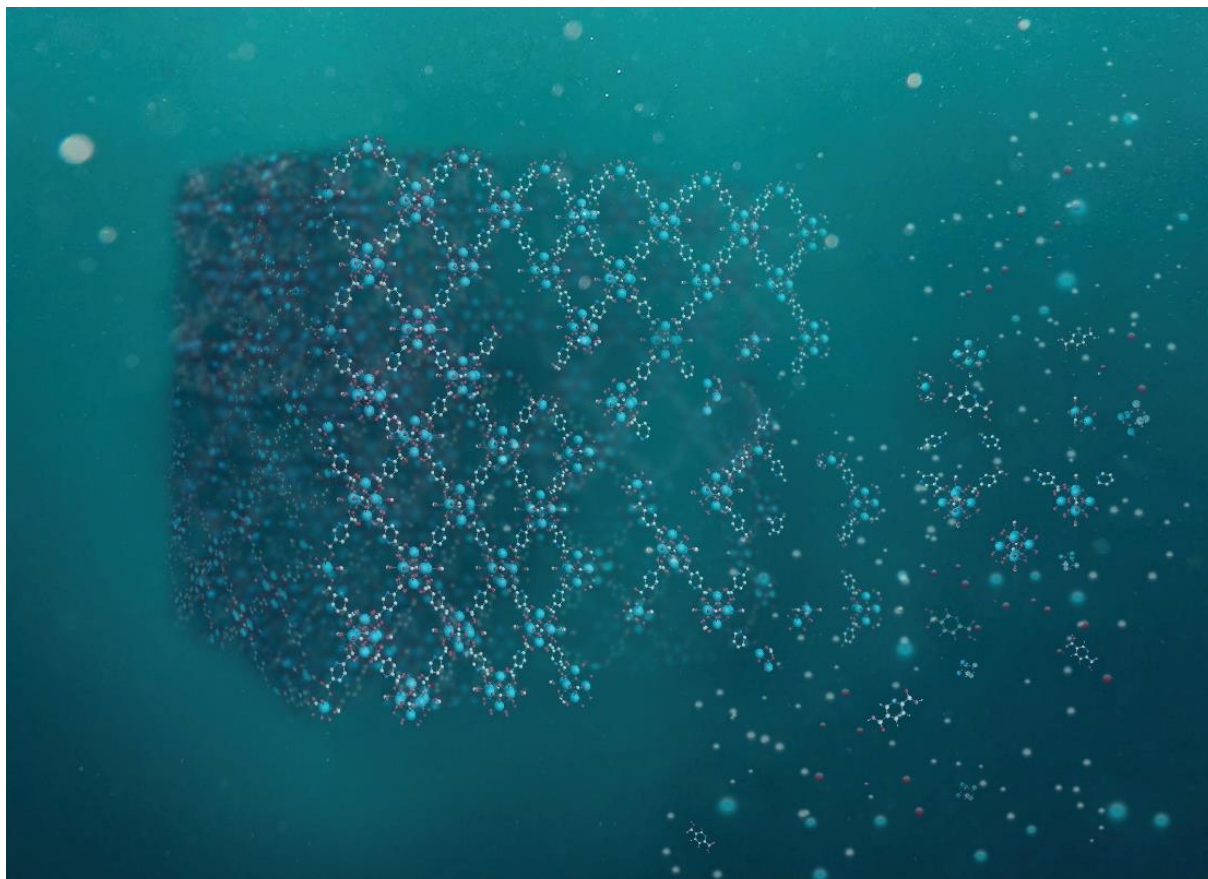
Der folgende Artikel wurde im Jahr 2018 in der Fachzeitschrift *Dalton Transactions, RSC* veröffentlicht. Die Wiedergabe erfolgt mit freundlicher Genehmigung der RSC. Reprinted with permission from S. Waitschat, D. Fröhlich, H. Reinsch, H. Terraschke, K. A. Lomachenko, C. Lamberti, H. Kummer, T. Helling, M. Baumgartner, S. Henninger and N. Stock, *Dalton Trans.*, **2018**, 47, 1062 – 1070, DOI: 10.1039/C7DT03641H. Copyright 2018 the Royal Society of Chemistry.

<http://pubs.rsc.org/en/Content/ArticleLanding/2018/DT/C7DT03641H#!divAbstract>

Die Wassersorptionseigenschaften von UiO-66-BDC sind für die Anwendung in Adsorptions-basierten Wärmepumpen nicht ideal. Aus diesem Grund wurde anstatt der Terephthalsäure (H<sub>2</sub>BDC) der hydrophilere Linker 2,5-Pyridindicarbonsäure (H<sub>2</sub>PDC) für die Synthese verwendet um die zu UiO-66-BDC isostrukturellen Verbindungen M-UiO-66-PDC mit M = Zr, Hf und Ce herzustellen. Kurz vor dieser Veröffentlichung konnte Zr-UiO-66-PDC bereits durch einen postsynthetischen Linkeraustausch,<sup>92</sup> in DMF<sup>76</sup> und in einem Wasser/Essigsäure-Gemisch<sup>93</sup> hergestellt werden. Allerdings wurde in diesen Arbeiten keine vollständige Strukturbestimmung durchgeführt. Zunächst wurden verschiedene Syntheseparameter wie Edukte, Lösungsmittel, Additive und verschiedene Verhältnisse von diesen Parametern unter Einsatz der Hochdurchsatzmethodik untersucht. Alle drei Verbindungen M-UiO-66-PDC mit M = Zr, Hf, Ce konnten in Wasser mit jeweils verschiedenen Additiven bei einer Reaktionstemperatur von 120 °C und einer Reaktionszeit von 24 h hergestellt werden. Mit diesen optimierten Parametern wurde die Synthese bezüglich der Raum-Zeit-Ausbeute mit Hilfe von Glasreaktoren und einem Aluminiumblock auf die Reaktionszeit und -temperatur optimiert. Die vollständige, optimierte Synthese konnte abschließend in 50 ml Rundkolben unter Rückfluss durchgeführt werden, was zu Ausbeuten von 1.56, 1.48 bzw. 3.25 g für M-UiO-66-PDC mit M = Zr, Hf bzw. Ce führte. Die UiO-66-Struktur konnte für alle drei synthetisierten Verbindungen durch Rietveld-Verfeinerungen und EXAFS-Messungen bestätigt werden. Die genauen Zusammensetzungen wurden durch EDX-Untersuchungen, thermogravimetrische Analysen und <sup>1</sup>H-NMR-Spektroskopie ermittelt. Es konnte folgende, allgemeine Summenformel angenommen werden [M<sub>6</sub>O<sub>4</sub>(OH)<sub>4</sub>(PDC)<sub>6-x</sub>(Cl)<sub>2x</sub>(H<sub>2</sub>O)<sub>4x</sub>] mit M = Zr, Hf und Ce und 0 ≤ x ≤ 2.

Alle Proben wurden bezüglich ihrer Lumineszenz- und Sorptionseigenschaften untersucht. Zr- und Hf-UiO-66-PDC zeigen die zu erwartenden Lumineszenzeigenschaften des Linkers, verschoben zu kleineren Wellenzahlen. Ce-UiO-66-PDC hingegen zeigt keine Emission.

Alle drei Verbindungen sind gegenüber  $N_2$  bzw.  $CO_2$ ,  $H_2O$  und MeOH bei  $-196$  bzw.  $25$  °C porös. Die Gesamtaufnahme unterscheidet sich dabei je nach eingebautem Metall und der genauen Zusammensetzung, ist aber vergleichbar mit den Werten, die in UiO-66-BDC beobachtet wurden. Allerdings ist der Onset der Wassersorption von  $p/p_0 = 0.3$  zu  $< 0.2$  verschoben. Dies ist auf Grund der höheren Hydrophilie von  $PDC^{2-}$  gegenüber  $BDC^{2-}$  zunächst zu erwarten gewesen. Für eine mögliche Anwendung muss die Verbindung zusätzlich über viele Adsorptions-Desorptions-Zyklen stabil sein. Aus diesem Grund wurden zyklische, thermogravimetrische Wasser-Adsorptions-Desorptions-Messungen durchgeführt. Zr-UiO-66-PDC verliert direkt nach dem ersten Zyklus ca. 30 % seiner Kapazität, was durch eine Abnahme in der Fernordnung der Kristalle der Verbindung erklärt werden kann, stabilisiert sich dann aber bei  $0.26 \text{ g}\cdot\text{g}^{-1}$ . Aus diesem Grund wurden die gleichen Untersuchungen ebenfalls mit MeOH als Adsorptiv durchgeführt. Die Kapazität von  $0.41 \text{ g}\cdot\text{g}^{-1}$  ist vergleichbar mit der MeOH-Kapazität von UiO-66-BDC. Allerdings nimmt die Aufnahme über mehrere Zyklen erneut ab, bis sie bei  $0.21 \text{ g}\cdot\text{g}^{-1}$  in ein Plateau läuft. Diese Abnahme ist durch einen post-synthetischen Austausch der Hydroxidgruppen durch Methoxygruppen zu erklären. Dieser Austausch wurde durch DRIFT-Messungen bestätigt. Durch eine erneute Behandlung mit Wasser und anschließender DRIFT-Untersuchungen konnte zudem fest gestellt werden, dass dieser Vorgang nicht reversibel ist.



Showcasing research from the joint collaboration of Christian-Albrechts-University, Fraunhofer Institute for Solar Energy Systems, ESRF, Southern Federal University and the University of Turin.

Synthesis of M-UiO-66 (M = Zr, Ce or Hf) employing 2,5-pyridinedicarboxylic acid as a linker: defect chemistry, framework hydrophilisation and sorption properties

Incorporation of N-heterocyclic linker molecules in UiO-66 type materials results in the hydrophilisation of the framework which in turn leads to changes in the gas and vapor sorption and luminescence properties. A shift of the water sorption isotherm to lower  $p/p_0$  values is observed and thermogravimetric ad-/desorption cycling experiments demonstrate the stable uptake after 20 cycles.

As featured in:



See N. Stock et al., *Dalton Trans.*, 2018, 47, 1062.



[rsc.li/dalton](https://rsc.li/dalton)

Registered charity number: 207890

Cite this: *Dalton Trans.*, 2018, **47**, 1062

## Synthesis of M-UiO-66 (M = Zr, Ce or Hf) employing 2,5-pyridinedicarboxylic acid as a linker: defect chemistry, framework hydrophilisation and sorption properties†

S. Waitschat,<sup>a</sup> D. Fröhlich,<sup>b</sup> H. Reinsch,<sup>c</sup> H. Terraschke,<sup>d</sup> K. A. Lomachenko,<sup>c,d</sup> C. Lamberti,<sup>d,e</sup> H. Kummer,<sup>b</sup> M. Baumgartner,<sup>b</sup> S. Henninger<sup>b</sup> and N. Stock<sup>a</sup>

Metal-organic frameworks of general composition  $[M_6(OH)_4(O)_4(PDC)_{6-x}(Cl)_{2x}(H_2O)_{2x}]$  with M = Zr, Ce, Hf; PDC<sup>2-</sup> = 2,5-pyridinedicarboxylate and  $0 \leq x \leq 2$  were obtained under reflux using formic, nitric or acetic acid as an additive. Rietveld refinements carried out using a fixed occupancy of the linker molecules according to the results of thermogravimetric measurements confirmed that the MOFs crystallize in the UiO-66 type structure and demonstrate that the structural models describe the data well. Further characterization was carried out by NMR spectroscopy, thermogravimetric analysis, Zr K-edge EXAFS- and Ce L<sub>3</sub>-edge XANES measurements. To highlight the influence of the additional nitrogen atom of the pyridine ring, luminescence and vapour sorption measurements were carried out. The hydrophilisation of the MOFs was shown by the adsorption of water at lower  $p/p_0$  (<0.2) values compared to the corresponding BDC-MOFs (0.3). For water and methanol stability cycling adsorption experiments were carried out to evaluate the MOFs as potential adsorbents in heat transformation applications.

Received 27th September 2017,  
Accepted 28th November 2017

DOI: 10.1039/c7dt03641h

rsc.li/dalton

### 1. Introduction

The increasing demand for heating and cooling in the world necessitates the development of new materials and technologies.<sup>1,2</sup> The use of low temperature waste energy in adsorptive heat transformation applications is one promising technology to improve energy efficiency.<sup>3</sup> Water as a working fluid of choice has numerous advantages, not the least in reducing the amount of world-wide used chlorofluorocarbons (CFCs) by the year 2047 as decided in the Montreal protocol of the UN.<sup>4</sup> Thus, adsorptive cooling and heating could replace conven-

tional heat pumps or air conditioning systems, which employ CFCs. As another advantage, lowering of CO<sub>2</sub> emission is feasible since low temperature waste energy is employed in this process.<sup>5</sup>

The industrially most relevant method for adsorptive heat transformation is a two-cycle process. Water is preferably employed due to its high enthalpy of evaporation (2500 kJ kg<sup>-1</sup>), abundance and non-toxicity.<sup>5</sup> Furthermore, methanol and ethanol are good candidates as working fluids, especially when the sorption material is not water stable or when low temperatures must be achieved.<sup>6</sup> In the working cycle the dry adsorbent adsorbs a working fluid and the heat of adsorption is released to the environment ( $Q_{ads}$ ).<sup>5</sup> When the sorption material is saturated with a working fluid, the second cycle, the regeneration cycle, starts. To desorb the working fluid, energy is necessary, which ideally would be waste heat from a different process ( $Q_{des}$ ). Thus, in this step, energy is consumed from the environment and cold is produced. Due to the condensation of the working fluid in a spatially separated reservoir, heat is produced again ( $Q_{con}$ ).<sup>3</sup> Hence the machine can work as an adsorption heat pump when intermediate temperatures ( $Q_{ads}$  and  $Q_{con}$ ) are used, or as a adsorption chiller when a lower temperature of  $Q_{evap}$  is used.<sup>3</sup>

For a good performance, the sorption material should have several properties. It must be stable during thousands of ad-

<sup>a</sup>Institut für Anorganische Chemie, Christian-Albrechts-Universität, Max-Eyth-Straße 2, D 24118 Kiel, Germany. E-mail: stock@ac.uni-kiel.de

<sup>b</sup>Fraunhofer-Institute for Solar Energy Systems ISE, Heidenhofstrasse 2, 79110 Freiburg, Germany

<sup>c</sup>European Synchrotron Radiation Facility, 71 Avenue des Martyrs, CS 40220, 38043 Grenoble Cedex 9, France

<sup>d</sup>IRC "Smart Materials", Southern Federal University, Zorge str. 5, 344090 Rostov-on-Don, Russia

<sup>e</sup>Department of Chemistry, CrisDi Centre and INSTM Reference Center, University of Turin, Via Giuria 7, 10125 Turin, Italy

† Electronic supplementary information (ESI) available: Details of high-throughput-syntheses and structure determination, variable temperature PXRD data, TG analysis, IR and NMR spectra. CCDC 1564158–1564160 contains the supplementary crystallographic data for M-UiO-66-PDC. See DOI: 10.1039/c7dt03641h

desorption cycles and should exhibit a high uptake (sorption capacity). Additionally, the isotherm should exhibit no hysteresis and have a sigmoidal shape in a  $p/p_0$ -range from 0.05 to 0.3.<sup>7</sup> While different adsorbents like silica gel, zeolites or SAPOs have already been employed in commercial cooling systems compounds known as MOFs (metal-organic frameworks) have recently emerged as alternative adsorbents showing superior performance.<sup>3,8,9</sup>

MOFs are composed of inorganic building units, usually metal ions or metal-oxygen clusters, which are interconnected by organic linker molecules.<sup>10</sup> They exhibit a remarkable structural diversity due to their modular composition.<sup>11,12</sup> The adsorbent with the highest water capacity is Cr-MIL-101 ( $[\text{Cr}_3\text{F}(\text{H}_2\text{O})_2\text{O}(1,4\text{-BDC})_3]$ ,  $1,4\text{-BDC}^{2-} = 1,4\text{-benzenedicarboxylate}$ , MIL = Material Institute Lavoisier), however, the uptake is in the range of  $0.3 \leq p/p_0 \leq 0.6$ .<sup>13,14</sup> Several thousand cycles of water vapour ad-/desorption without any loss of capacity was demonstrated for MIL-53-Fum ( $[\text{Al}(\text{OH})(\text{Fum})]$ ,  $\text{Fum}^{2-} = \text{fumarate}$ )<sup>15</sup> and CAU-10 ( $[\text{Al}(\text{OH})(1,3\text{-BDC})]$ ,  $1,3\text{-BDC}^{2-} = 1,3\text{-benzenedicarboxylate}$ , CAU = Christian-Albrechts-Universität).<sup>16,17</sup> These compounds exhibit high capacities and sigmoidal isotherms below  $p/p_0 < 0.3$ .<sup>17</sup>

There exist several ways to fully exploit the modular structure of MOFs in order to tailor the water sorption behaviour. In particular, the influence of hydrophilic groups on the sorption properties was investigated. Thus, formally replacing a  $-\text{CH}-$  group in 2-methylimidazole (HMIM) by  $-\text{N}-$  leads to the formation of a linker HMTZ (3-methyl-1,2,4-triazole). The resulting compounds  $[\text{Zn}(\text{MIM})_2]$  and  $[\text{Zn}(\text{MTZ})_2]$  exhibit very different water sorption properties. While the first compound is not porous, the latter is porous towards water.<sup>18</sup> A similar approach has been reported for the modification of CAU-10. 1,3-Benzenedicarboxylic acid was replaced by 3,5-pyridinedicarboxylic acid or 2,5-furandicarboxylic acid as linker molecules. The incorporation of more hydrophilic linker molecules leads to a higher uptake of water and a shift to lower  $p/p_0$  values compared to the parent compound.<sup>19</sup> In addition, the influence of additional amine groups was investigated for UiO-66 ( $[\text{Zr}_6(\text{O})_4(\text{OH})_4(\text{BDC}\text{-NH}_2)_6]$ , UiO = University of Oslo).<sup>20–22</sup> UiO-66-NH<sub>2</sub> not only shows a shift of the water uptake to lower  $p/p_0$  ranges but also a lower total uptake due to the steric demand of the NH<sub>2</sub>-group (Fig. 1).

Based on these results one could anticipate that the incorporation of N-heterocyclic linker molecules into the UiO-66 structure could lead to an increase in the sorption capacity and a shift to lower relative humidity values. Very recently the partial incorporation of 2,5-pyridinedicarboxylate (PDC<sup>2-</sup>) by solvent-assisted-linker-exchange (SALE) has been reported,<sup>23</sup> while the synthesis in DMF<sup>24</sup> or in a water/acetic acid mixture<sup>25</sup> leads to Zr-UiO-66-PDC, although no structure determination and water sorption behaviour were carried out in these studies.

Here, we describe the synthesis and detailed characterisation of three UiO-66-type compounds containing Zr, Ce or Hf in the IBU and 2,5-pyridinedicarboxylate instead of 1,4-benzenedicarboxylate ions, *i.e.* Zr-, Ce- and Hf-UiO-66-PDC. In addition, water and methanol sorption properties are reported.

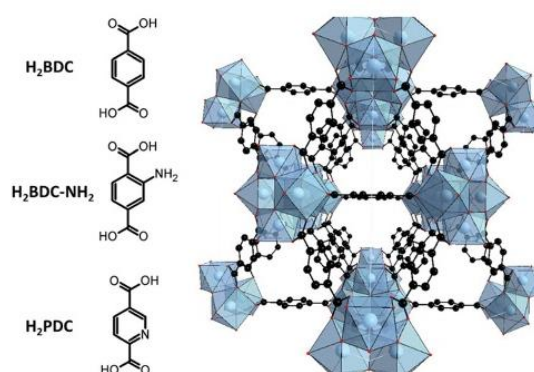


Fig. 1 Three linker molecules (left) that have been used for the synthesis of UiO-66 (right).

## 2. Experimental

### 2.1. Materials and methods

All chemicals were used as received. High throughput powder X-ray diffraction (PXRD) investigations were carried out using a Stoe Stadi P X-ray diffractometer equipped with a  $xy$ -stage in transmission geometry ( $\text{MoK}_{\alpha 1}$  radiation, Mythen detector). PXRD patterns for structure determination were recorded with a Stoe Stadi P X-ray diffractometer in transmission geometry using  $\text{CuK}_{\alpha 1}$  radiation and data were collected by a Mythen detector. Infrared (IR) spectra were recorded on a Bruker ALPHA-P A220/D-01 Fourier transform infrared (FTIR) spectrometer equipped with an attenuated total reflection (ATR) unit. NMR spectroscopy was carried out using a Bruker DRX 500 spectrometer. Thermogravimetric (TG) analysis was performed using a NETZSCH STA 429 CD analyser with a heating rate of  $4 \text{ K min}^{-1}$  under flowing air (flow rate:  $75 \text{ ml min}^{-1}$ ). Elemental analysis was performed using a EuroVector Euro EA elemental analyser. Nitrogen and  $\text{CO}_2$  sorption isotherms were measured at  $-196 \text{ }^\circ\text{C}$  and  $25 \text{ }^\circ\text{C}$ , respectively, using a BELSORP-Max apparatus. MeOH sorption isotherms were obtained with a Quantachrome Autosorb and  $\text{H}_2\text{O}$  adsorption was measured with a Quantachrome Hydrosorb at  $25 \text{ }^\circ\text{C}$ . Water cycling stabilities were examined on a Setaram<sup>TM</sup> TGA-DSC-111 on powdered samples. A humidified argon gas flow ( $40 \text{ }^\circ\text{C}$ , 76.3% relative humidity) was generated by using a Setaram WetSys humidity controller and passed through the sample chamber, while the temperature of the sample was varied and the mass of the adsorbent was monitored. For the multi-cycle ad-/desorption experiments, the temperature of the sample was varied between  $40 \text{ }^\circ\text{C}$  and  $140 \text{ }^\circ\text{C}$  with a cycle time of 5 h. Methanol cycling stability was examined using a Surface Measurement Systems Ltd DVS Vacuum. Before and after cycling, the sample was degassed at  $90 \text{ }^\circ\text{C}$  in a vacuum and equilibrium points were taken at  $25 \text{ }^\circ\text{C}$  by increasing the pressure of the gas flow at  $5 \text{ ml min}^{-1}$  and held constant at 115 hPa while varying the temperature of the sample between 25 and  $100 \text{ }^\circ\text{C}$ , which corresponds to a rela-

tive pressure  $p/p_0$  of 0.671 and 0.033, with cycle times of 1 h while cooling and 1 h on heating. *In situ* diffuse reflectance infrared Fourier transform spectroscopy (DRIFTS) measurement on Zr-UiO-66-PDC was carried out with a PerkinElmer Frontier spectrometer, equipped with a Diffuse Reflectance Accessory. A heat chamber with a ZnSe window was utilized for the *in situ* experiments. The spectra are averaged from 20 scans and recorded between 4000 and 700  $\text{cm}^{-1}$  with a resolution of 4  $\text{cm}^{-1}$ . Prior to the measurement the MOF was outgassed at 120 °C and reduced pressure. The experiment was conducted at 25 °C under a  $\text{N}_2$  gas atmosphere with a flow rate of 100  $\text{ml min}^{-1}$  controlled by using a Bronkhorst MassView. To investigate the influence of MeOH on the structure of the MOF, it was subjected 5 times to a MeOH dosed  $\text{N}_2$  stream for 30 seconds. The  $\text{N}_2$  stream was passed through a MeOH bath (298 K) with a bubble diffusor. After each treatment, the sample was treated with dry  $\text{N}_2$  until equilibrium and the spectrum was recorded. Luminescence measurements of the solid samples were carried out in Suprasil A quartz ampoules at room temperature. For this purpose, a FL-22 Fluorolog3 spectrometer (Horiba Jobin Yvon GmbH), equipped with a 450 W xenon lamp, a R928P photomultiplier and an iHR-320-FA triple grating imaging spectrograph was applied. Reflection spectra were also recorded at room temperature from the powdered samples with a Cary 5000 spectrometer (Varian Techtron Pty.) applying  $\text{BaSO}_4$  as a reference and diluting material. A Ce  $L_{3\text{-edge}}$  X-ray absorption near edge structure (XANES) spectrum of Ce-UiO-66-PDC was collected at the Southern Federal University (Russia) using a Rigaku R-XAS spectrometer. An experimental Zr K-edge (17 998 eV) extended X-ray absorption fine structure (EXAFS) spectrum of Zr-UiO-66-PDC was collected at BM23 beamline<sup>26</sup> of the European Synchrotron Radiation Facility (ESRF). All the XAS measurements were conducted in transmission mode at room temperature. Experimental details of XAS data collection are provided in the ESI.† The ring was operated in a 16-bunch regime with a maximum current of 90 mA. Experiments were conducted in transmission mode using Ar/He-filled ionization chambers as detectors. Gas pressure in the chambers was 0.4 bar Ar, +1.6 bar He for  $I_0$  and 2 bar of Ar for  $I_1$  resulting in roughly 20% and 70% absorption respectively. A Si (111) double-crystal monochromator was used for energy scanning, while Rh-coated mirrors positioned at an incidence angle of 3 mrad were employed for harmonic rejection. The sample was prepared in the form of self-supporting pellets (80 mg of powder in a 13 mm diameter disk, pressed with a force <500 kgf) resulting in the edge jump of 1.5. Measurements were conducted at room temperature. Excellent performance of the beamline allowed the data collection up to  $k = 23 \text{ \AA}^{-1}$  with a high signal-to-noise ratio.

## 2.2. Synthesis

The high-throughput investigations for the synthesis of the new compounds were carried out in a steel multiclave equipped with 24 Teflon reactors with a volume of 2 ml each.<sup>27</sup> Different metal salts, solvent combinations as well as modu-

lators were tested. The optimization of reaction time and temperature was performed in Pyrex glass tubes with a volume of 5 ml, which were heated and stirred in an aluminium block by using a laboratory heating plate. Details of the synthesis optimisation are listed in the ESI (SI2, SI3, and SI4†). The optimized reaction conditions for the scale-up to 50 ml reactors under reflux are described below.

**2.2.1. Synthesis of Zr-UiO-66-PDC.** 0.733 g (4.4 mmol)  $\text{H}_2\text{PDC}$  and 1.434 g (4.4 mmol)  $\text{ZrOCl}_2 \cdot 8\text{H}_2\text{O}$  were mixed in 45 ml formic acid and 5 ml water in a round bottom flask placed in an oil bath. The mixture was heated at 120 °C under reflux for 3 h. The reaction was quenched by placing the round bottom flask under cold water. The suspension was separated by centrifugation and subsequently washed twice with water and one time with ethanol (6000 rpm, 30 min, each). The product was dried under ambient conditions (yield: 1.56 g).

**2.2.2. Synthesis of Ce-UiO-66-PDC.** 1.670 g (10 mmol)  $\text{H}_2\text{PDC}$  and 5.480 g (10 mmol)  $(\text{NH}_4)_2[\text{Ce}(\text{NO}_3)_6]$  were mixed in 5 ml conc.  $\text{HNO}_3$  and 45 ml water in a round bottom flask. The mixture was heated at 90 °C under reflux for 30 minutes. The reaction was quenched by placing the round bottom flask under cold water. The suspension was separated by centrifugation and subsequently washed twice with water and one time with ethanol (6000 rpm, 30 min, each). The product was dried under ambient conditions (yield: 3.25 g).

**2.2.3. Synthesis of Hf-UiO-66-PDC.** 0.835 g (5 mmol)  $\text{H}_2\text{PDC}$  and 1.6 g (5 mmol)  $\text{HfCl}_4$  were mixed in 25 ml acetic acid and 25 ml water in a round bottom flask. The mixture was heated at 120 °C under reflux for 3 h. The reaction was quenched by placing the round bottom flask under cold water. The suspension was separated by centrifugation and subsequently washed twice with water and one time with ethanol (6000 rpm, 30 min, each). The product was dried under ambient conditions (yield: 1.48 g).

## 3. Results and discussion

Using high-throughput methods, we have been able to establish the water-based synthesis of three UiO-66-PDC compounds containing  $\text{Zr}^{4+}$ ,  $\text{Ce}^{4+}$  or  $\text{Hf}^{4+}$  ions on a g-scale using reflux conditions. Products of high crystallinity were obtained using different modulators.

### 3.1. Crystallography and defect chemistry

The structures of the three compounds M-UiO-66-PDC (M = Zr, Ce, and Hf) were refined from PXRD data (Fig. 2) using the Rietveld method by fixing the occupancy of the linker according to the results of the TG measurements (section S5.1, Table S5.1 and Fig. S5.1, S5.4, S5.7†).<sup>28</sup> In order to further confirm the presence of defects in the zirconium and hafnium based MOFs, the Rietveld refinement was also carried out by fixing the occupancy of the linker molecules to 1, hence assuming an ideal framework composition. While the Rietveld plots hardly change, the figures of merit are evidently inferior to the values obtained by refinement of the defective frame-



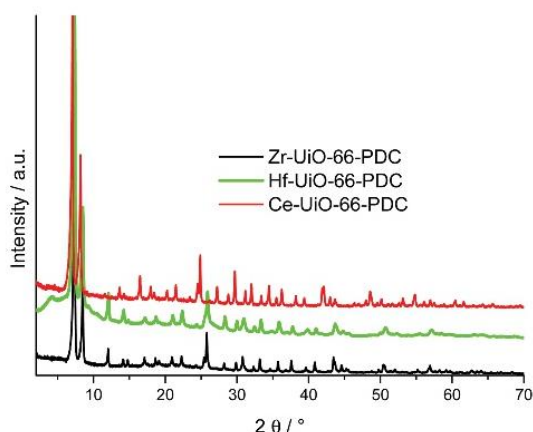


Fig. 2 PXRD patterns of the M-UiO-66-PDC compounds (M = Zr<sup>4+</sup>, Ce<sup>4+</sup> and Hf<sup>4+</sup>).

works (Table S5.2†). Hence our results show that our structural models describe the data well. All three structures are related to the ideal UiO-66 type framework and contain the hexanuclear clusters  $[M_6(O_4)(OH)_4]^{12-}$  with M = Zr<sup>4+</sup>, Ce<sup>4+</sup> and Hf<sup>4+</sup> respectively. In the ideal structure each cluster is connected by twelve terephthalate ions,<sup>29</sup> however compounds with linker and cluster defects are known.<sup>30–33</sup>

According to the results of the TG measurements, all three MOFs show different types of defect chemistry. The PXRD patterns of Zr- and Ce-UiO-66-PDC exhibit exclusively peaks that are consistent with the **fcu** topology (Fig. 2). The Rietveld refinements of the PXRD data support the absence of linker defects in the Ce-MOF. Thus, the compound has the ideal composition  $[Ce_6(O_4)(OH)_4(PDC)_6]$ . The oxidation state of cerium in the compound was verified by XANES measurements, which confirmed that only Ce<sup>4+</sup> is present in Ce-UiO-66-PDC (Fig. S5.11†). In contrast, the structure of the Zr-MOF was successfully refined with one statistically missing linker molecule per formula unit by fixing the site occupancy of the linker during the calculations. The composition of the product and the presence of Cl<sup>−</sup> ions for charge balance were confirmed by TG analysis (Fig. S9.4†), NMR spectroscopy (Fig. S6.1†) and EDX measurements (ratio Zr:Cl = 3:1). Although the localisation of H atoms is not possible and O, OH and H<sub>2</sub>O cannot be distinguished, the analytical data confirm the formula of Zr-UiO-66-PDC as  $[Zr_6(O_4)(OH)_4(Cl)_2(H_2O)_4(PDC)_5]$ .

To complement the results of the PXRD data, Zr K-edge EXAFS analysis of Zr-UiO-66-PDC was performed using a Zr-UiO-66-PDC sample washed with ethanol (for details see Fig. S5.10†). A fitting model included the nearest shells of one of the six equivalent Zr atoms in a UiO-66 cornerstone (Fig. 3a). Compared to the classical model proposed by Valenzano *et al.*,<sup>34</sup> several modifications were made based on the input of complementary techniques. First, the presence of missing linker defects was modelled by setting the degeneracy of the Zr–C path to 3.3 instead of 4, mimicking the C-site occu-

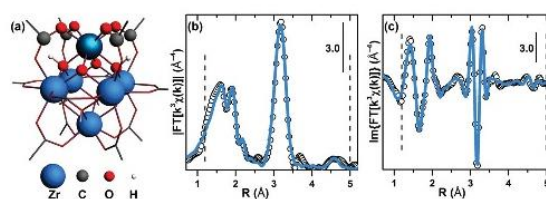


Fig. 3 (a) Structural model of the UiO-66 cornerstone. Absorbing Zr atom is highlighted, atoms included in the EXAFS fitting model (except for H) are shown as spheres. (b) Modulus and (c) imaginary part of the experimental (scattered circles)  $k^3$ -weighted phase-uncorrected Zr K-edge EXAFS FT for Zr-UiO-66-PDC together with the fit (blue line) made using the model from panel a. Fitting range (1.2–5.0 Å) is shown by the vertical dotted lines.

pancy of 0.83 as supported by PXRD and TG measurements. Then, since a Cl-containing salt was used in the synthesis and chloride was detected in the material by EDX analysis, the presence of the chloride ion at the position of missing linkers was assumed, following the thorough study of Shearer *et al.*<sup>35</sup> Accordingly, the degeneracy of the introduced Zr–Cl path was set to  $4 - 3.3 = 0.7$ . With reference to the O-coordination, two  $\mu_3$ -OH oxygens were parameterized together with the four carboxyl oxygen atoms (O1) in the same way as reported in the work of Valenzano *et al.*<sup>34</sup> due to the similarity of the lengths of these scattering paths.<sup>36</sup> Conversely, two  $\mu_3$ -O atoms were parameterized as a separate shell. Then, two zirconium shells were considered: four Zr neighbors in the plane of the octahedron (Zr1) and one Zr atom at the opposite vertex (Zr2). In contrast to all the abovementioned single-scattering shells, the Debye–Waller factor and bond elongation parameter for the Zr–Zr2 path were not independent, but derived from the corresponding parameters of the Zr–Zr1 path in order to decrease the number of free parameters in the fit using the assumption that the octahedron may only be isotropically distorted.

Overall, the fit demonstrated good agreement with the experimental data yielding physically meaningful parameters (Fig. 3b, c and Table 1). Interestingly, although the splitting of the first EXAFS maximum indeed appears due to the presence of the two distinct oxygen shells ( $4 O1 + 2 \mu_3$ -OH and  $2 \mu_3$ -O), the two peaks cannot be attributed to each of them separately. Conversely, such splitting in the modulus of the Fourier-transformed (FT) EXAFS data is justified by the partial cancellation of the signals from these two shells in the 1.75–1.8 Å range (phase-uncorrected) due to the significantly different bond lengths (2.07 Å for  $\mu_3$ -O vs. 2.22 Å for O1).

The PXRD pattern of Hf-UiO-66-PDC shows a broad peak at low 2 theta values compared to the **fcu** structure of the parent framework (Fig. 2). These peaks are due to the correlated nanoscale disorder in the crystal structure and are well known for Hf-UiO-66-BDC.<sup>37,38</sup> In these regions missing linkers and missing clusters result in a structure with the **reo** topology. Detailed characterisation by TG analysis (Fig. S9.6†), NMR spectroscopy (ESI Fig. S6.3†) and EDX analysis (ratio Hf:Cl = 3:2) excludes the presence of acetate ions and demonstrates the presence of Cl<sup>−</sup> ions. The deduced formula is  $[Hf_6(O_4)(OH)_4(Cl)_4(H_2O)_8(PDC)_4]$

**Table 1** Fit details and best-fit parameters for Zr K-edge EXAFS of Zr-UiO-66-PDC, presented in Fig. 3. Coordination numbers (left column) and atomic distances (right column) are given in parentheses

	Zr-UiO-66-PDC
R-Factor	0.017
Fitting range in $k$ , $\text{\AA}^{-1}$	3.7–20.6
Fitting range in $R$ , $\text{\AA}$	1.2–5.0
Number of independent points	40
Number of fitting parameters	12
$S_0^2$	1.00 ± 0.06
$\Delta E$ , eV	−1.3 ± 0.8
$R_{\text{H}_2\text{O}}^2$ , $\text{\AA}$ ( $N = 2$ )	2.07 ± 0.005 (2.13)
$\sigma_{\text{H}_2\text{O}}^2$ , $\text{\AA}^2$	0.003 ± 0.0004
$R_{\text{O}1}^2$ , $\text{\AA}$ ( $N = 6$ )	2.22 ± 0.005 (2.26)
$\sigma_{\text{O}1}^2$ , $\text{\AA}^2$	0.006 ± 0.0005
$R_{\text{Cl}}^2$ , $\text{\AA}$ ( $N = 0.7^a$ )	2.49 ± 0.01
$\sigma_{\text{Cl}}^2$ , $\text{\AA}^2$	0.006 ± 0.001
$R_{\text{C}}^2$ , $\text{\AA}$ ( $N = 3.3^a$ )	3.17 ± 0.02 (3.13)
$\sigma_{\text{C}}^2$ , $\text{\AA}^2$	0.006 ± 0.002
$R_{\text{Zr}1}^2$ , $\text{\AA}$ ( $N = 4$ )	3.52 ± 0.003 (3.50)
$\sigma_{\text{Zr}1}^2$ , $\text{\AA}^2$	0.005 ± 0.0002
$R_{\text{Zr}2}^2$ , $\text{\AA}$ ( $N = 1$ )	4.98 <sup>b</sup> (4.94)
$\sigma_{\text{Zr}2}^2$ , $\text{\AA}^2$	0.006 <sup>b</sup>
Highest correlations	$\Delta R_{\text{Zr}1}/\Delta E = 0.87$ $\sigma_{\text{Zr}1}^2/S_0^2 = 0.86$  Others  < 0.8

<sup>a</sup> $N_{\text{C}}$  and  $N_{\text{Cl}}$  were set to 3.3 and 0.7 respectively to simulate the missing linker defects detected by PXRD, TG, NMR, and EDX measurements. <sup>b</sup> $R_{\text{Zr}2}$  and  $\sigma_{\text{Zr}2}^2$  were derived from the values of  $R_{\text{Zr}1}$  and  $\sigma_{\text{Zr}1}^2$  respectively.

and a Rietveld refinement, neglecting the additional peaks originating from the **reo** defect topology, and fixing the occupancy of the linker to the value obtained from the TG measurement supports the composition. The structural model obtained indicates that statistically missing linker defects in the **fcu** framework of Hf-UiO-66-PDC lead to an identical composition as also present in the defect **reo** domains.

### 3.2. Thermal and chemical stabilities

Thermogravimetric analyses and temperature dependent PXRD experiments were carried out for all three MOFs to verify the deduced formulas and monitor the thermal stability. According to the PXRD data Zr-UiO-66-PDC is stable up to a temperature of 220 °C (Fig. S9.1†). The first weight loss up to 260 °C in the TG curve could be explained by the dehydration and loss of the HCl. Framework decomposition starts at approximately 300 °C (Fig. S9.4†). These observations indicate that the structure collapses at lower temperatures while thermal combustion is delayed up to higher temperatures. The weight loss corresponds to five linker molecules per cluster. Thus, the postulated sum formula of Zr-UiO-66-PDC is confirmed as  $[\text{Zr}_6(\text{O})_4(\text{OH})_4(\text{Cl})_2(\text{H}_2\text{O})_4(\text{PDC})_5]$ . A similar behaviour of the thermal stability is observed for Ce- and Hf-UiO-66-PDC. Ce-UiO-66-PDC is stable up to 150 °C but combustion starts at 250 °C (Fig. S9.2 & S9.5†). The TG analysis indicates an ideal composition of six linker molecules per cluster. Thus, the deduced formula for Ce-UiO-66-PDC is confirmed as  $[\text{Ce}_6(\text{O})_4(\text{OH})_4(\text{PDC})_6]$ . Hf-UiO-66-PDC is stable up to 150 °C based on the PXRD data

(Fig. S9.3†) but combustion is delayed up to 200 °C (Fig. S9.6†). The TG analysis proves the presence of defects in the structure and is in agreement with four linker molecules and four chloride ions per cluster. Thus, the postulated sum formula of Hf-UiO-66-PDC is confirmed as  $[\text{Hf}_6(\text{O})_4(\text{OH})_4(\text{Cl})_4(\text{H}_2\text{O})_6(\text{PDC})_4]$ .

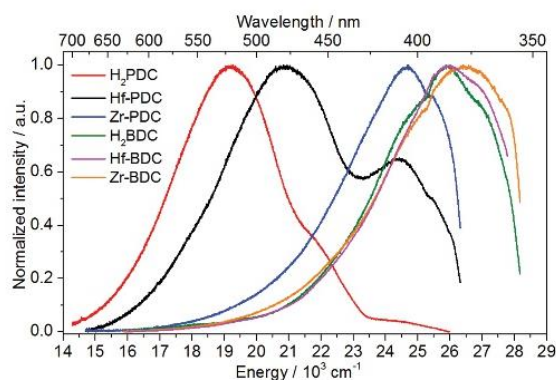
The chemical stability of the title compounds was studied by stirring 20 mg of each sample in 1 ml different organic solvents and different concentrations of aqueous HCl and NaOH for 24 hours at room temperature. All three MOFs are stable in a pH-range from 1 to 12 and in more basic solutions the MOFs are destroyed. None of the MOFs is stable in a 0.1 M phosphate buffer ( $\text{Na}_2\text{HPO}_4/\text{NaH}_2\text{PO}_4$ ). All three MOFs are stable in the tested organic solvents (Fig. S9.7–S9.12†).

### 3.3. Luminescence properties

To study the influence of the N-atom in the aromatic ring on the luminescence properties, the emission spectra of the title compounds and linker molecules  $\text{H}_2\text{PDC}$  and  $\text{H}_2\text{BDC}$  were recorded applying the excitation energies listed in Table 2 (Fig. 4, Fig. S10.1–S10.5†). Since radiative electronic transitions in the UV-Vis region are not possible in  $\text{Zr}^{4+}$  and  $\text{Hf}^{4+}$ , the optical properties of these MOFs are caused exclusively by the aromatic units of the organic linker, as often reported for other transition metal MOFs.<sup>39–41</sup> The emission spectrum of

**Table 2** Emission maximum, excitation energy and FWHM of emission spectra of  $\text{H}_2\text{PDC}$ , Hf-UiO-66-PDC, Zr-UiO-66-PDC,  $\text{H}_2\text{BDC}$ , Zr-UiO-66-BDC and Hf-UiO-66-BDC

Compound	Emission maximum	Excitation energy	FWHM
$\text{H}_2\text{PDC}$	19 197 $\text{cm}^{-1}$	27 777 $\text{cm}^{-1}$	3828 $\text{cm}^{-1}$
Hf-UiO-66-PDC	20 903 $\text{cm}^{-1}$	27 777 $\text{cm}^{-1}$	6885 $\text{cm}^{-1}$
Zr-UiO-66-PDC	24 752 $\text{cm}^{-1}$	27 777 $\text{cm}^{-1}$	3836 $\text{cm}^{-1}$
$\text{H}_2\text{BDC}$	25 900 $\text{cm}^{-1}$	30 769 $\text{cm}^{-1}$	4357 $\text{cm}^{-1}$
Zr-UiO-66-BDC	26 532 $\text{cm}^{-1}$	30 769 $\text{cm}^{-1}$	4498 $\text{cm}^{-1}$
Hf-UiO-66-BDC	26 022 $\text{cm}^{-1}$	30 769 $\text{cm}^{-1}$	4704 $\text{cm}^{-1}$

**Fig. 4** Emission spectra of  $\text{H}_2\text{PDC}$  (red curve), Hf-UiO-66-PDC (black curve) and Zr-UiO-66-PDC (blue curve) as well as  $\text{H}_2\text{BDC}$  (green curve), Hf-UiO-66-BDC (pink curve) and Zr-UiO-66-BDC (orange curve), applying excitation energies listed in Table 2.

Zr-UiO-66-PDC (Fig. 4, blue curve) consists of a broad band in the UV-blue spectral range with full width at half maximum (FWHM) of  $3836\text{ cm}^{-1}$  and maximum at  $24\,752\text{ cm}^{-1}$  (Table 2 and Fig. S10.1†). This band is blue-shifted in comparison with the emission spectrum of the H<sub>2</sub>PDC linker, which has an emission maximum located in the green spectral range at  $19\,197\text{ cm}^{-1}$  with a similar FWHM of  $3828\text{ cm}^{-1}$  (Fig. 4, red curve). Similar values were reported by Sun *et al.* for other MOFs containing PDC<sup>2-</sup> ions.<sup>42</sup> The blue shift after the incorporation of the organic linker into the MOF structure is explained in the literature by the enhancement of the  $\pi \rightarrow \pi^*$  energy due to the weakening effect of the skeleton vibration within the rigid framework.<sup>43</sup> This shift to higher energy is also observed in the emission spectrum of Hf-UiO-66-PDC (Fig. 4, black curve), broadly distributed between approximately  $15\,000\text{ cm}^{-1}$  and  $26\,000\text{ cm}^{-1}$  with a maximum at  $20\,903\text{ cm}^{-1}$ . In addition, the luminescence spectrum of Hf-UiO-66-PDC shows a second emission band of lower intensity with a maximum at  $24\,420\text{ cm}^{-1}$ . As observed in the recorded excitation spectra (Fig. S10.3†), the energy assigned to this band is self-absorbed by Hf-UiO-66-PDC, decaying radiatively through the emission at *ca.*  $20\,000\text{ cm}^{-1}$ . In contrast, Ce-UiO-66-PDC is not luminescent. Most probably, the blue shift of the emission band in comparison with H<sub>2</sub>PDC causes the overlap between the linker-based emission band and the absorbed spectral region of the Ce-UiO-66-PDC, shown by the diffuse reflectance spectra in Fig. S10.7† as previously observed for Ce-CAU-24.<sup>41</sup>

The emission spectrum of Zr-UiO-66-BDC (Fig. 4, orange curve) is located mostly in the UV spectral range with a maximum at  $26\,532\text{ cm}^{-1}$  (FWHM =  $4498\text{ cm}^{-1}$ ). In comparison with the H<sub>2</sub>BDC linker (Fig. 4, green curve) it is also blue-shifted. The same shift in emission maxima was reported for Zn terephthalates.<sup>43</sup> Similarly for the MOFs containing the H<sub>2</sub>PDC linker, the emission band measured for Hf-UiO-66-BDC (Fig. 4, pink curve) is also slightly blue-shifted in comparison with the emission band of the H<sub>2</sub>BDC linker, with a maximum at  $26\,022\text{ cm}^{-1}$  and FWHM of  $4704\text{ cm}^{-1}$ . The red shift between the emission spectra of PDC<sup>2-</sup> and BDC<sup>2-</sup> based structures has been previously observed for Zn-containing coordination polymers<sup>42</sup> and similar shifts between Zr-UiO-66 and Hf-UiO-66 as well as shifts caused by the functionalization of the H<sub>2</sub>BDC ligand with NH<sub>2</sub> groups have been reported by Yasin *et al.*<sup>44</sup> However, the cause for these effects still remains an open question and additional experiments are necessary for explaining these phenomena. In general, according to Yang *et al.* the additional lone pairs of the nitrogen atoms are advantageous for interacting with the  $\pi^*$  orbitals of the aromatic ring, enhancing the luminescence efficiency of the analogue H<sub>2</sub>PDC linker.<sup>45</sup> Moreover, the incorporation of N-heterocyclic linker molecules in MOFs has been reported to lead to an increase in the host-guest interactions with various guest species as well as enhanced luminescence properties, enabling the application of the modified UiO-66 compounds as sensor materials in the detection of Fe<sup>3+</sup>,<sup>46</sup> phosphates<sup>45</sup> and biological thiols.<sup>47</sup>

### 3.4. Gas sorption

To investigate the influence of the N-atom in the aromatic ring on the sorption properties, N<sub>2</sub>, CO<sub>2</sub>, H<sub>2</sub>O and MeOH isotherms were recorded at  $-196$  and  $25\text{ }^\circ\text{C}$  for N<sub>2</sub> and the other gases, respectively. Although Zr- and Ce-UiO-66-PDC were successfully activated at  $120\text{ }^\circ\text{C}$  for 16 hours under reduced pressure, the removal of guest molecules in Hf-UiO-66-PDC, even at ambient temperature and a pressure of  $0.1\text{ mbar}$ , led to the destruction of the structure (Fig. S11.2†). Zr- and Ce-UiO-66-PDC showed type I isotherms (Fig. 5) and evaluation by the BET method resulted in specific surface areas of  $S_{\text{BET}} = 1380$  and  $768\text{ m}^2\text{ g}^{-1}$ , respectively. The difference is due to the different number of linker defects and the higher molar masses of the Ce-MOF. Compared to the known Zr- and Ce-UiO-66-BDC structures, the uptake of the corresponding PDC-MOFs is higher for the Zr-MOF (lit.:  $S_{\text{BET}} = 1105\text{ m}^2\text{ g}^{-1}$ )<sup>35</sup> but lower for the Ce-MOF (lit.:  $S_{\text{BET}} = 1282\text{ m}^2\text{ g}^{-1}$ ).<sup>31</sup> These observations also confirm the linker defects observed in Zr-UiO-PDC and Ce-UiO-66-BDC. Both MOFs are also porous towards CO<sub>2</sub> (Fig. 5 and Table S11.1†).

The volumetric H<sub>2</sub>O and MeOH sorption isotherms of Zr-UiO-66-PDC and Ce-UiO-66-PDC show a type 1b shape (Fig. S11.4 and Fig. S11.5†). Due to the very strong hydrophilic adsorbent-adsorbate interactions uptake at  $p/p_0 < 0.01$  takes place. For water as the adsorptive, a linear uptake at  $p/p_0 > 0.3$  is observed. At this point ( $p/p_0 = 0.2$ ) Zr-UiO-66-PDC adsorbs  $0.34\text{ g g}^{-1}$  and Ce-UiO-66-PDC  $0.23\text{ g g}^{-1}$  water. In comparison with Zr-UiO-66-BDC and -BDC-NH<sub>2</sub> a shift of the main uptake from  $p/p_0 = 0.3$  in Zr-UiO-66-BDC to  $<0.2$  in Zr-UiO-66-PDC is observed, while the absolute amount of H<sub>2</sub>O vapour adsorbed is very similar ( $0.34\text{ g g}^{-1}$  and  $0.35\text{ g g}^{-1}$  for Zr-UiO-66-PDC and Zr-UiO-66-BDC respectively, Fig. 6).<sup>18</sup> Although small changes of the sorption properties could be due to different degrees of dehydroxylation of the hexanuclear Zr-O clusters, we anticipate that these shifts are much better explained by

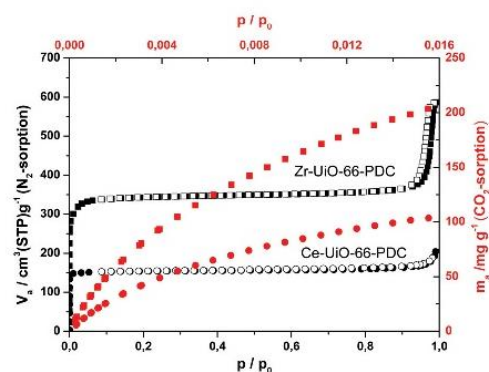


Fig. 5 Nitrogen (black curves, left and bottom axes) and CO<sub>2</sub> (red curves, right and top axes) isotherms of Zr-UiO-66-PDC (squares) and Ce-UiO-66-PDC (circles) measured at  $-196\text{ }^\circ\text{C}$  and  $25\text{ }^\circ\text{C}$  respectively. For the nitrogen isotherms, full and open symbols refer to adsorption and desorption respectively.

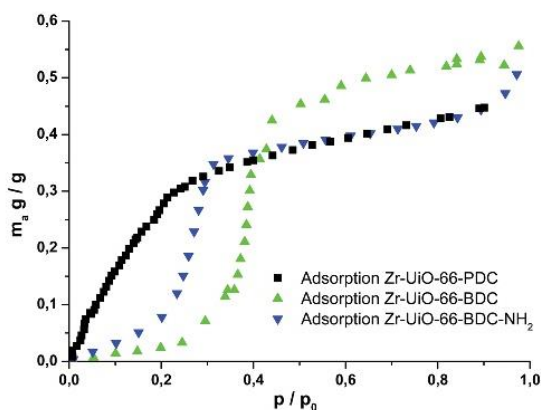


Fig. 6 Comparison of the  $\text{H}_2\text{O}$  isotherms of Zr-UiO-66-PDC (black), Zr-UiO-66-BDC-NH<sub>2</sub> (blue)<sup>20</sup> and Zr-UiO-66-BDC (green)<sup>20</sup> measured 25 °C.

the hydrophilicity of the different linker molecules in the UiO-66-type structures.

The affinity at low  $p/p_0$  values of the materials towards MeOH is comparable to the affinity towards water. The total capacity for both MOFs is similar with 0.31 and 0.30  $\text{g g}^{-1}$  for Zr- and Ce-UiO-66-PDC, respectively, which are relatively high numbers, compared to the values reported in the literature (Table S11.2†).<sup>3</sup>

Due to the water uptake of 0.34  $\text{g g}^{-1}$  in the region  $0.01 < p/p_0 < 0.3$ , the water stability of M-UiO-66-PDC (M = Zr and Ce) was tested by a multicycle ad-/desorption experiment in a thermogravimetric balance (Fig. 7). In this experiment a humidified argon gas flow of constant relative humidity is passed through the sample chamber and the temperature of the sample is varied (40 and 140 °C) and the mass of the

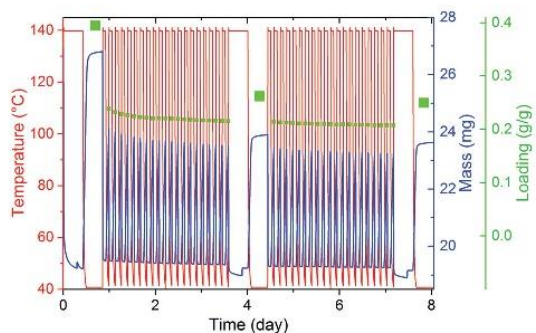


Fig. 7 Thermogravimetric water adsorption/desorption cycling experiments for 40 cycles of Zr-UiO-66-PDC. Long segments at the beginning and at the end of each experiment were conducted to determine the equilibrium loading of the sample (red: sample temperature, blue: mass, green: loading to the corresponding ad-/desorption pair). Adsorption temperature: 40 °C, desorption temperature: 140 °C, 76.3% RH at adsorption.

adsorbent is monitored. Under cycling conditions, Zr-UiO-66-PDC shows a very small dry mass degradation from 19.22 mg to 18.94 mg (2.5 wt%). During the cycle treatment a strong decrease in uptake capacity takes place after the first adsorption step, of about 30%, which remains relatively constant for the following adsorption steps. During the 20 ad-/desorption cycles a decrease in the water uptake capacity ( $(m_{\text{ads-H}_2\text{O}} - m_0)/m_0$ ) from 0.39 to 0.26  $\text{g g}^{-1}$  is observed (Fig. 7), which levels out to a constant value of 0.25  $\text{g g}^{-1}$  after an additional 20 cycles. This degradation is probably due to a structural change after the first ad-/desorption, which lowers the adsorption capacity, as the dry mass remains nearly constant but the uptake decrease is already stabilised after this first cycle. Compared to Zr-UiO-66-PDC and -BDC-NH<sub>2</sub> which show a substantial and continuous loss of water capacity in the cycling experiments, the Zr-UiO-66-BDC shows a higher stability.<sup>20</sup>

Ce-UiO-66-PDC shows a similar behaviour in the cycling experiments but due to its lower thermal stability the degradation is faster (Fig. S12.1†).

Additionally the methanol ad-/desorption cycling stability of Zr-UiO-66-PDC was examined in an *in situ* experiment using a Surface Measurement Systems Ltd DVS Vacuum in a temperature range between 25 and 100 °C. Parameters were chosen to mimic an adsorption chiller for cooling applications around 10 °C. The material treated for 100 cycles exhibited an increase in dry mass from 25.86 mg to 26.12 mg due to the exchange of the hydroxyl groups by methoxy groups (Fig. S13.1†). After a fast decline in the methanol uptake during the first cycles the decrease in capacity shows a small but continuous behaviour (Fig. 8). The total methanol capacity ( $(m_{\text{ads-MeOH}} - m_0)/m_0$ ) of about 0.41  $\text{g g}^{-1}$  drops constantly down to about 0.21  $\text{g g}^{-1}$  after 100 cycles. A plateau could not be reached due to instrumental limits of the set-up. The strong decrease at the beginning can be explained by a post-synthetic exchange of the

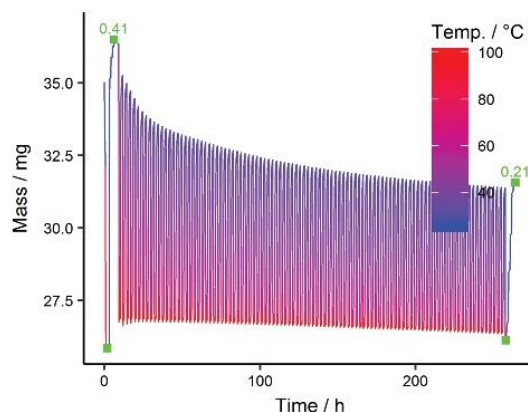


Fig. 8 Thermogravimetric methanol adsorption/desorption cycling experiments for 100 cycles of Zr-UiO-66-PDC (blue: mass). Adsorption from 25 °C (blue) to desorption 100 °C (red), 67.1% of the saturation pressure of MeOH at 25 °C. Green squares: loading of the first and last ad-/desorption pairs.

hydroxyl groups by methoxy groups, which has been reported previously<sup>48</sup> and is confirmed by diffuse reflectance infrared Fourier transform spectroscopy (DRIFTS) (Fig. S13.1†). Upon treatment with methanol new bands at 2928 and 2824  $\text{cm}^{-1}$  evolve which are assigned to the C–H stretchings of the methoxy groups. The intensity of the band at 2742  $\text{cm}^{-1}$ , assigned to the hydrogen-bonded OH/OH<sub>2</sub> groups in the hexanuclear cluster node, decreases simultaneously.<sup>48</sup> Zr-UiO-66-PDC exhibits a lower stability compared to other MOFs such as HKUST-1 or MIL-101(Cr)<sup>49</sup> under methanol ad-/desorption conditions.

## 4. Conclusions

In conclusion, we synthesised three new MOFs with 2,5-pyridinedicarboxylic acid as a linker and Zr<sup>4+</sup>, Hf<sup>4+</sup> and Ce<sup>4+</sup> respectively. All compounds could be fully characterized by combining the results of various characterization techniques, like TG analysis, NMR- and IR spectroscopy and Rietveld refinement using fixed occupancies of the linker molecules. The latter results show that the structural models describe the PXRD data well. The Zr- and Ce-MOFs are porous towards N<sub>2</sub>, CO<sub>2</sub>, H<sub>2</sub>O and MeOH. The influence of the additional nitrogen atom in the ring, compared to UiO-66-BDC was investigated by luminescence spectroscopy and sorption measurements. The water sorption measurements show similar capacity of water compared to UiO-66-BDC but a steeper adsorption at lower  $p/p_0$  values. The possibility for the use in heat transformation application was tested with cyclic vapour sorption measurement with water and methanol. The water sorption measurements show that the stability of the MOFs is not perfect and the MeOH measurements show a decrease in the total uptake which correspond to an exchange of the OH- groups to the methoxy groups.

## Conflicts of interest

There are no conflicts to declare.

## Acknowledgements

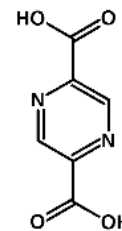
KAL acknowledges the Grant of the Southern Federal University (VnGr-07/2017-08). The authors acknowledge, in addition, the German Research Foundation (project TE 1147/1-1) for financial support and thank C. S. Cunha for the help with the luminescence measurements.

## Notes and references

- M. Isaac and D. P. van Vuuren, *Energy Policy*, 2009, **37**, 507–521.
- M. Sivak, *Energy Policy*, 2009, **37**, 1382–1384.
- M. F. de Lange, K. J. F. M. Verouden, T. J. H. Vlugt, J. Gascon and F. Kapteijn, *Chem. Rev.*, 2015, **115**, 12205–12250.
- U. N. E. P. O. Secretariat, *Handbook for the Montreal protocol on substances that deplete the ozone layer*, UNEP/Earthprint, 2006.
- F. Jeremias, D. Fröhlich, C. Janiak and S. K. Henninger, *New J. Chem.*, 2014, **38**, 1846.
- M. F. de Lange, B. L. van Velzen, C. P. Ottevanger, K. J. F. M. Verouden, L.-C. Lin, T. J. H. Vlugt, J. Gascon and F. Kapteijn, *Langmuir*, 2015, **31**, 12783–12796.
- J. Canivet, A. Fateeva, Y. Guo, B. Coasne and D. Farrusseng, *Chem. Soc. Rev.*, 2014, **43**, 5594–5617.
- S. K. Henninger, F. P. Schmidt and H.-M. Henning, *Appl. Therm. Eng.*, 2010, **30**, 1692–1702.
- L. W. Wang, R. Z. Wang and R. G. Oliveira, *Renewable Sustainable Energy Rev.*, 2009, **13**, 518–534.
- S. R. Batten, N. R. Champness, X.-M. Chen, J. Garcia-Martinez, S. Kitagawa, L. Öhrström, M. O’Keeffe, M. Paik Suh and J. Reedijk, *Pure Appl. Chem.*, 2013, **85**, 1715–1724.
- W. Lu, Z. Wei, Z.-Y. Gu, T.-F. Liu, J. Park, J. Park, J. Tian, M. Zhang, Q. Zhang, T. Gentle III, M. Bosch and H.-C. Zhou, *Chem. Soc. Rev.*, 2014, **43**, 5561–5593.
- N. Stock and S. Biswas, *Chem. Rev.*, 2012, **112**, 933–969.
- J. Ehrenmann, S. K. Henninger and C. Janiak, *Eur. J. Inorg. Chem.*, 2011, **2011**, 471–474.
- B. B. Saha, I. I. El-Sharkawy, T. Miyazaki, S. Koyama, S. K. Henninger, A. Herbst and C. Janiak, *Energy*, 2015, **79**, 363–370.
- F. Jeremias, D. Fröhlich, C. Janiak and S. K. Henninger, *RSC Adv.*, 2014, **4**, 24073.
- D. Fröhlich, S. K. Henninger and C. Janiak, *Dalton Trans.*, 2014, **43**, 15300–15304.
- D. Fröhlich, E. Pantatosaki, P. D. Kolokathis, K. Markey, H. Reinsch, M. Baumgartner, M. A. van der Veen, D. E. De Vos, N. Stock, G. K. Papadopoulos, S. K. Henninger and C. Janiak, *J. Mater. Chem. A*, 2016, **4**, 11859–11869.
- J.-P. Zhang, A.-X. Zhu, R.-B. Lin, X.-L. Qi and X.-M. Chen, *Adv. Mater.*, 2011, **23**, 1268–1271.
- A. Cadiau, J. S. Lee, D. Damasceno Borges, P. Fabry, T. Devic, M. T. Wharmby, C. Martineau, D. Foucher, F. Taulelle, C.-H. Jun, Y. K. Hwang, N. Stock, M. F. De Lange, F. Kapteijn, J. Gascon, G. Maurin, J.-S. Chang and C. Serre, *Adv. Mater.*, 2015, **27**, 4775–4780.
- F. Jeremias, V. Lozan, S. K. Henninger and C. Janiak, *Dalton Trans.*, 2013, **42**, 15967.
- M. Kandiah, M. H. Nilsen, S. Usseglio, S. Jakobsen, U. Olsbye, M. Tilset, C. Larabi, E. A. Quadrelli, F. Bonino and K. P. Lillerud, *Chem. Mater.*, 2010, **22**, 6632–6640.
- M. Kandiah, S. Usseglio, S. Svelle, U. Olsbye, K. P. Lillerud and M. Tilset, *J. Mater. Chem.*, 2010, **20**, 9848.
- L. Chen, J. Ou, H. Wang, Z. Liu, M. Ye and H. Zou, *ACS Appl. Mater. Interfaces*, 2016, **8**, 20292–20300.
- A. A. Barkhordarian and C. J. Kepert, *J. Mater. Chem. A*, 2017, **5**, 5612–5618.

- 25 Z. Wang, Y. Huang, J. Yang, Y. Li, Q. Zhuang and J. Gu, *Dalton Trans.*, 2017, **46**, 7412–7420.
- 26 O. Mathon, A. Beteva, J. Borrel, D. Bugnazet, S. Gatla, R. Hino, I. Kantor, T. Mairs, M. Munoz, S. Pasternak, F. Perrin and S. Pascarelli, *J. Synchrotron Radiat.*, 2015, **22**, 1548–1554.
- 27 N. Stock, *Microporous Mesoporous Mater.*, 2010, **129**, 287–295.
- 28 A. Coelho, *Topas-Academic v5*, Brisbane, Australia, 2012.
- 29 J. H. Cavka, S. Jakobsen, U. Olsbye, N. Guillou, C. Lamberti, S. Bordiga and K. P. Lillerud, *J. Am. Chem. Soc.*, 2008, **130**, 13850–13851.
- 30 G. C. Shearer, J. G. Vitillo, S. Bordiga, S. Svelle, U. Olsbye and K. P. Lillerud, *Chem. Mater.*, 2016, **28**, 7190–7193.
- 31 M. Lammert, M. T. Wharmby, S. Smolders, B. Bueken, A. Lieb, K. A. Lomachenko, D. D. Vos and N. Stock, *Chem. Commun.*, 2015, **51**, 12578–12581.
- 32 W. Liang, C. J. Coghlan, F. Ragon, M. Rubio-Martinez, D. M. D'Alessandro and R. Babarao, *Dalton Trans.*, 2016, **45**, 4496–4500.
- 33 C. Atzori, G. C. Shearer, L. Maschio, B. Civalleri, F. Bonino, C. Lamberti, S. Svelle, K. P. Lillerud and S. Bordiga, *J. Phys. Chem. C*, 2017, **121**, 9312–9324.
- 34 L. Valenzano, B. Civalleri, S. Chavan, S. Bordiga, M. H. Nilsen, S. Jakobsen, K. P. Lillerud and C. Lamberti, *Chem. Mater.*, 2011, **23**, 1700–1718.
- 35 G. C. Shearer, S. Chavan, J. Ethiraj, J. G. Vitillo, S. Svelle, U. Olsbye, C. Lamberti, S. Bordiga and K. P. Lillerud, *Chem. Mater.*, 2014, **26**, 4068–4071.
- 36 S. Øien, D. Wragg, H. Reinsch, S. Svelle, S. Bordiga, C. Lamberti and K. P. Lillerud, *Cryst. Growth Des.*, 2014, **14**, 5370–5372.
- 37 M. J. Cliffe, W. Wan, X. Zou, P. A. Chater, A. K. Kleppe, M. G. Tucker, H. Wilhelm, N. P. Funnell, F.-X. Coudert and A. L. Goodwin, *Nat. Commun.*, 2014, **5**, Art. n. 4176.
- 38 S. Jakobsen, D. Gianolio, D. S. Wragg, M. H. Nilsen, H. Emerich, S. Bordiga, C. Lamberti, U. Olsbye, M. Tilset and K. P. Lillerud, *Phys. Rev. B*, 2012, **86**, Art. n. 125429.
- 39 W. W. Lestari, P. Lönnecke, H. C. Streit, M. Handke, C. Wickleder and E. Hey-Hawkins, *Eur. J. Inorg. Chem.*, 2014, **2014**, 1775–1782.
- 40 W. W. Lestari, P. Lönnecke, H. C. Streit, F. Schleife, C. Wickleder and E. Hey-Hawkins, *Inorg. Chim. Acta*, 2014, **421**, 392–398.
- 41 M. Lammert, H. Reinsch, C. A. Murray, M. T. Wharmby, H. Terraschke and N. Stock, *Dalton Trans.*, 2016, **45**, 18822–18826.
- 42 J. Sun, D. Zhang, L. Wang, R. Zhang, J. Wang, Y. Zeng, J. Zhan, J. Xu and Y. Fan, *J. Solid State Chem.*, 2013, **206**, 286–292.
- 43 T. Lee, Y. H. Chang and H. L. Lee, *CrystEngComm*, 2017, **19**, 426–441.
- 44 A. S. Yasin, J. Li, N. Wu and T. Musho, *Phys. Chem. Chem. Phys.*, 2016, **18**, 12748–12754.
- 45 J. Yang, Y. Dai, X. Zhu, Z. Wang, Y. Li, Q. Zhuang, J. Shi and J. Gu, *J. Mater. Chem. A*, 2015, **3**, 7445–7452.
- 46 Y. Dong, H. Zhang, F. Lei, M. Liang, X. Qian, P. Shen, H. Xu, Z. Chen, J. Gao and J. Yao, *J. Solid State Chem.*, 2017, **245**, 160–163.
- 47 Y.-A. Li, C.-W. Zhao, N.-X. Zhu, Q.-K. Liu, G.-J. Chen, J.-B. Liu, X.-D. Zhao, J.-P. Ma, S. Zhang and Y.-B. Dong, *Chem. Commun.*, 2015, **51**, 17672–17675.
- 48 D. Yang, V. Bernales, T. Islamoglu, O. K. Farha, J. T. Hupp, C. J. Cramer, L. Gagliardi and B. C. Gates, *J. Am. Chem. Soc.*, 2016, **138**, 15189–15196.
- 49 H. Kummer, M. Baumgartner, P. Hügenell, D. Fröhlich, S. K. Henninger and R. Gläser, *Appl. Therm. Eng.*, 2017, **117**, 689–697.

#### 4.1.2.2. Water-based synthesis and characterization of a new Zr-MOF with a unique inorganic building unit



Der folgende Artikel wurde im Jahr 2016 in der Fachzeitschrift *Chemical Communications*, RSC veröffentlicht. Die Wiedergabe erfolgt mit freundlicher Genehmigung der RSC. Reprinted with permission from S. Waitschat, H. Reinsch and N. Stock, *Chem. Commun.*, **2016**, 52, 12698 – 12701, DOI: 10.1039/C6CC06287C. Copyright 2016 The Royal Society of Chemistry.

<http://pubs.rsc.org/en/Content/ArticleLanding/2016/CC/C6CC06287C#!divAbstract>

Von den zahlreichen Zr-MOFs, enthalten die meisten dieser Verbindungen den  $\{Zr_6O_4(OH)_4\}$ -Cluster als anorganische Baueinheit. Durch den Einsatz von 2,5-Pyrazindicarbonsäure ( $H_2PzDC$ ) als Linker konnte unter Einsatz der Hochdurchsatzmethodik die neue Verbindung CAU-22 ( $[Zr_6(O)_4(OH)_8(H_2O)_2(HCO_2)_2(PzDC)_3]$ ) mit einer, für Zr-Verbindungen gänzlich neuen IBU synthetisiert werden. Zunächst wurde die Synthese bezüglich des Metallsalzes und des Wasser zu Ameisensäure (FA) Verhältnisses optimiert. Das Produkt mit der höchsten Kristallinität konnte mit  $ZrOCl_2 \cdot 8 H_2O$  als Metallquelle, einem  $H_2O : FA$  Verhältniss von 50 : 50, einer Reaktionszeit von 24 h und einer Reaktionstemperatur von 120 °C hergestellt werden.

Die Struktur wurde durch Rietveld-Verfeinerung bestimmt. CAU-22 kristallisiert in der Raumgruppe  $C2/m$  mit den Gitterparametern  $a = 21.260(2)$ ,  $b = 14.516(2)$ ,  $c = 8.105(2)$  Å und  $\beta = 84.25(2)^\circ$ . Die anorganische Baueinheit von CAU-22 besteht aus den bekannten hexanuklearen Zr-O-Clustern die durch vier Hydroxidgruppen kantenverknüpft zu einer  $\{Zr_6(\mu_3-O)_4(\mu_3-OH)_4(\mu-OH)_2\}$ -Kette kondensieren. Jede Kette ist durch Linkermoleküle mit sechs weiteren Ketten verknüpft, wodurch 3 Å große, trigonale Poren entstehen. Zwei Formiatreste, wie zwei Wassermoleküle und zwei weitere Hydroxidgruppen befinden sich zum Ladungsausgleich und zur Absättigung der Zr-Koordinationssphäre in der Verbindung. Dadurch ergibt sich die Summenformel von CAU-22 wie folgt:  $[Zr_6(\mu_3-O)_4(\mu_3-OH)_4(\mu-OH)_2(OH)_2(H_2O)_2(HCO_2)_2(PzDC)_3]$ . Die Zusammensetzung wurde durch EDX-Untersuchungen (Abwesenheit von Chloridionen), thermogravimetrische- und Elementaranalysen sowie  $^1H$ -NMR-Spektroskopie (Anzahl an Formiationen) bestätigt.

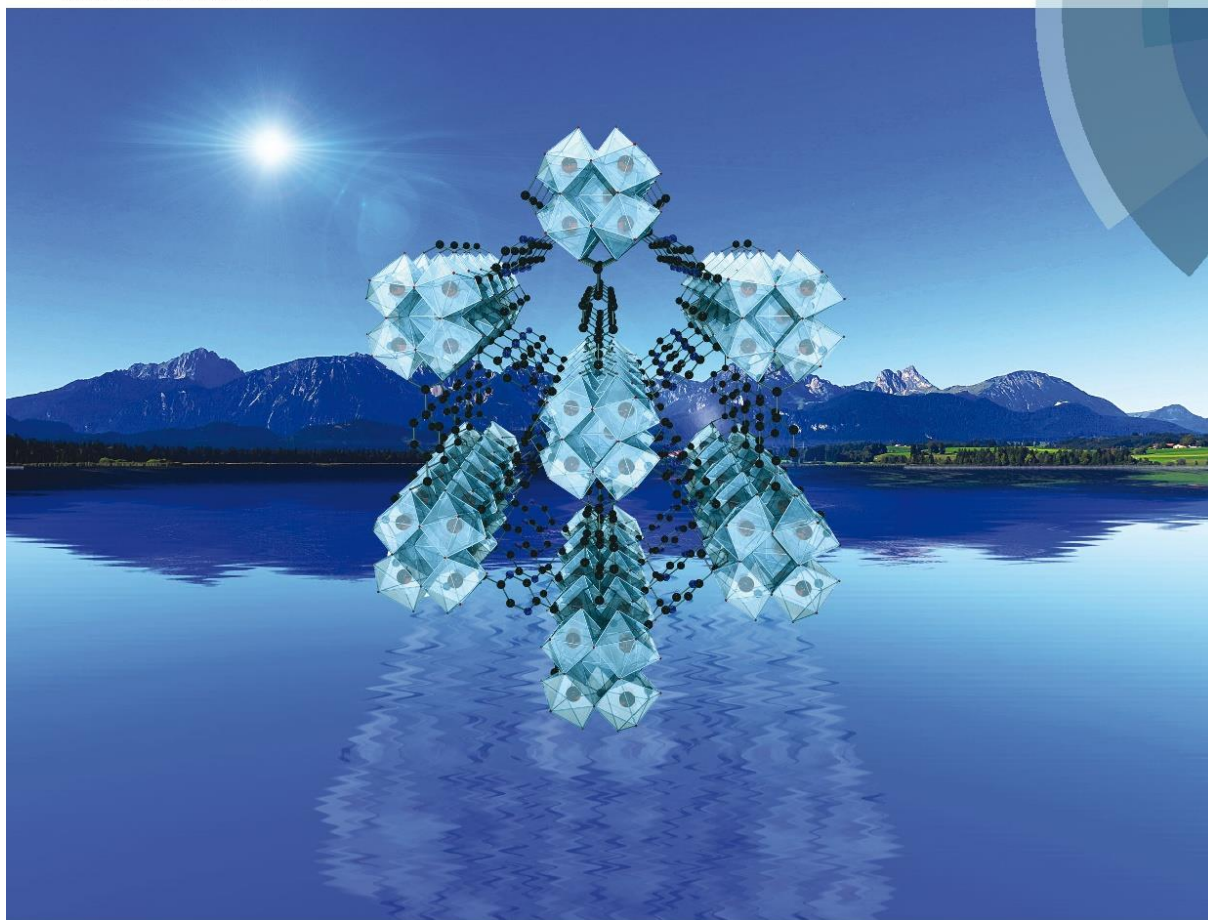
CAU-22 ist gegenüber  $N_2$  bzw.  $H_2O$  bei -196 bzw. 25 °C permanent porös und weist eine scheinbare, spezifische Oberfläche von 276  $m^2 \cdot g^{-1}$ , ein Mikroporenvolumen von 0.12  $cm^3 \cdot g^{-1}$  und eine

Wasseraufnahmekapazität von  $0.16 \text{ g} \cdot \text{g}^{-1}$  auf. Nach den Sorptionsmessungen wurden die Proben pulverdiffraktometrisch untersucht und es konnte keine Abnahme in der Kristallinität verzeichnet werden.



# ChemComm

Chemical Communications  
www.rsc.org/chemcomm



ISSN 1359-7345



COMMUNICATION

N. Stock *et al.*

Water-based synthesis and characterisation of a new Zr-MOF with a unique inorganic building unit

**175**  
YEARS



Cite this: *Chem. Commun.*, 2016, 52, 12698

Received 29th July 2016,  
Accepted 1st September 2016

DOI: 10.1039/c6cc06287c

www.rsc.org/chemcomm

## Water-based synthesis and characterisation of a new Zr-MOF with a unique inorganic building unit†

S. Waitschat, H. Reinsch and N. Stock\*

A new, microporous Zr-MOF was obtained using 2,5-pyrazinedi-carboxylic acid ( $H_2PzDC$ ). The linker leads to the formation of a new 1D inorganic building unit composed of  $\mu$ -OH bridged  $\{Zr_6O_4(OH)_4\}$  clusters which are arranged in a hexagonal array and connected by the  $PzDC^{2-}$  ions. The structure was determined from powder X-ray diffraction data.

Metal organic frameworks (MOFs) have been intensively investigated for various applications like gas storage,<sup>1</sup> gas separation,<sup>2</sup> catalysis,<sup>3</sup> heat transformation<sup>4</sup> or drug delivery<sup>5</sup> due to their high specific surface areas and the diversity of their structures.<sup>6</sup>

In particular Zr-MOFs are studied for possible applications, due to their thermal and chemical stability.<sup>7,8</sup> An outstanding structural feature in carboxylate-based Zr-MOFs is the presence of hexanuclear clusters of composition  $\{Zr_6O_4(OH)_4\}$  which are also well known from molecular Zr(IV) complexes (Fig. 1, bottom, left).<sup>9</sup> The clusters are readily formed under various reactions conditions and dominate the structural chemistry of Zr-MOFs. The first example that contains this inorganic building unit (IBU) is UiO-66 ( $\{Zr_6O_4(OH)_4(BDC)_6\}$ ,  $BDC^{2-}$  = benzenedicarboxylate, UiO = University of Oslo), which was reported in 2008. In the ideal structure the IBUs are twelvefold connected and form a fcu network topology.<sup>10</sup> Isorecticular structures have been reported as well with linkers of different sizes, e.g., DUT-52 (DUT = Dresden University of Technology)<sup>11</sup> or UiO-67,<sup>10</sup> Zr-Fum,<sup>12</sup> ZrSQ<sup>13</sup> or for example with functionalized terephthalic acids.<sup>14,15</sup> Other topologies have been observed as well, when the hexanuclear IBU is ten (DUT-69<sup>16</sup>), eight (DUT-67,<sup>16</sup> DUT-51,<sup>17</sup> MOF-841,<sup>18</sup> MOF-545<sup>19</sup> or PCN-521, PCN = porous coordination network<sup>20</sup>) or six connected (MOF-808<sup>18</sup>). Exceptions where other IBUs are observed are found in the structures of MIL-140 (MIL = Material Institute Lavoisier)<sup>21</sup>

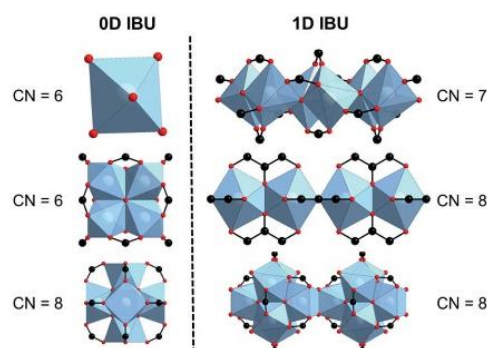


Fig. 1 Inorganic building units as observed in various Zr-MOFs.<sup>10,21–24</sup>

and PCN-221<sup>22</sup> where  $\{Zr(\mu_3-O)_3O_4\}$  chains (Fig. 1, top, right) and  $\{Zr_8O_6\}$  clusters (Fig. 1, middle, left) are incorporated. The  $\{Zr_8O_6\}$  cluster has been reported once and the structure refinement lead only to rather high  $R_1/wR_2$  values (0.1924/0.4359 for Zr-PCN-221(Cu)). In the phosphonate- and phenolate-based MOFs UPG-1<sup>23</sup> (UPG = University of Perugia) and MIL-163,<sup>24</sup>  $ZrO_6$ -polyhedra (Fig. 1, top, left) and edge-sharing  $ZrO_8$ -polyhedra IBUs (Fig. 1, middle, right) have been observed, respectively (Table S1.3, ESI†).

Zr-MOFs have been mainly synthesized under autogenous pressure using DMF as the solvent,<sup>8,10,16,18</sup> however, recently green synthesis routes and reaction upscaling have been reported.<sup>25–30</sup> For green syntheses the choice of the metal source and the solvent employed are crucial, and reactions in water, ethanol, acetic or formic acids are usually preferred.

Herein we report the water-based synthesis and detailed characterization of a new Zr-MOF, denoted as CAU-22 (CAU = Christian-Albrechts-Universität) which contains 2,5-pyrazinedi-carboxylate ions ( $PzDC^{2-}$ ) and a unique 1D IBU of edge-sharing hexanuclear  $\{Zr_6O_4(OH)_4\}$  clusters.

The linker  $H_2PzDC$  was synthesized as previously reported<sup>31</sup> (see S2, ESI†) and to the best of our knowledge it has only been

Institut für Anorganische Chemie, Christian-Albrechts-Universität, Max-Eyth-Straße 2, D 24118 Kiel, Germany. E-mail: stock@ac.uni-kiel.de

† Electronic supplementary information (ESI) available: Details of high-throughput-syntheses and structure determination, variable temperature PXRD data, TG analysis, IR- and NMR spectra, SEM micrographs. CCDC 1496183 contains the supplementary crystallographic data for CAU-22. See DOI: 10.1039/c6cc06287c

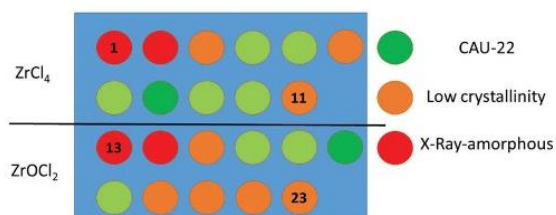


Fig. 2 Results of the synthesis optimization by systematically varying the ratio formic acid to H<sub>2</sub>O from 0% (1, 13) to 100% (11, 23) formic acid.

successfully used in the synthesis of a series of lanthanide-MOFs.<sup>32,33</sup>

The discovery and synthesis optimization of the title compound was carried out in 2 ml Teflon reactors using high-throughput methods as established in our group,<sup>34</sup> and setting the reaction time and temperature to 24 h and 120 °C. Initially the influence of the Zr salt on the product formation was evaluated. Using Zr(SO<sub>4</sub>)<sub>2</sub>·4H<sub>2</sub>O and ZrO(NO<sub>3</sub>)<sub>2</sub>·xH<sub>2</sub>O in a solvent mixture of water and formic acid yielded exclusively X-ray amorphous products, while the use of ZrCl<sub>4</sub> and ZrOCl<sub>2</sub>·8H<sub>2</sub>O resulted in crystalline products. Systematic optimization of the solvent composition (formic acid to H<sub>2</sub>O ratio) led to a highly crystalline product (Fig. 2). Synthesis details and PXRD patterns are given in the supporting information (Table S3.1 and Fig. S3.1–3.3, ESI†).

For both metal sources, ZrCl<sub>4</sub> and ZrOCl<sub>2</sub>·8H<sub>2</sub>O, an equimolar metal to linker ratio and similar formic acid:H<sub>2</sub>O ratios of 70:30 for and 50:50, respectively, results in the formation of the most crystalline reaction product. For full characterization of CAU-22, the synthesis was scaled up in a 30 ml Teflon reactor keeping the optimized reaction conditions constant and using ZrOCl<sub>2</sub>·8H<sub>2</sub>O as the metal source, which is much cheaper compared to ZrCl<sub>4</sub>.

CAU-22 was only obtained as a microcrystalline product and hence the structure had to be determined from PXRD data. Indexing was carried out with Topas<sup>35</sup> and the structure was solved by direct methods using the program suite Expo.<sup>36</sup> The initial structure model was completed using Material Studio<sup>37</sup> and could be successfully refined by Rietveld methods (Fig. 3, see S4, ESI† for details).

CAU-22 (Fig. 4) crystallizes in the monoclinic space group *C2/m* with the unit cell parameters  $a = 21.260(2)$ ,  $b = 14.516(2)$ ,  $c = 8.105(2)$  Å and  $\beta = 84.25(2)^\circ$ . The IBU is based on the very well-known hexanuclear cluster {Zr<sub>6</sub>O<sub>4</sub>(OH)<sub>4</sub>}.<sup>10</sup> In this cluster a square antiprismatic coordination of each Zr<sup>4+</sup> ion by eight oxygen atoms from O<sup>2-</sup>, OH<sup>-</sup> and -CO<sub>2</sub><sup>-</sup> groups is observed. In contrast to all other known Zr-MOFs, in CAU-22 these clusters are condensed into {[Zr<sub>6</sub>O<sub>4</sub>(OH)<sub>4</sub>(μ-OH)<sub>2</sub>]} chains by edge-bridging OH<sup>-</sup> ions (Fig. 4, see also ESI†). Each resulting 1D IBUs is connected to six others by PzDC<sup>2-</sup> linker molecules (Fig. 4) and 1D triangular pores with a diameter of *ca.* 3 Å are formed, taking the van der Waals radii of the atoms lining the pores into account. These pores are occupied by water molecules. Every hexanuclear subunit is coordinated by six PzDC<sup>2-</sup> linker molecules and furthermore two formate as well as H<sub>2</sub>O/OH<sup>-</sup> molecules capping residual coordination sites (Fig. S4.1–S4.10, ESI†).

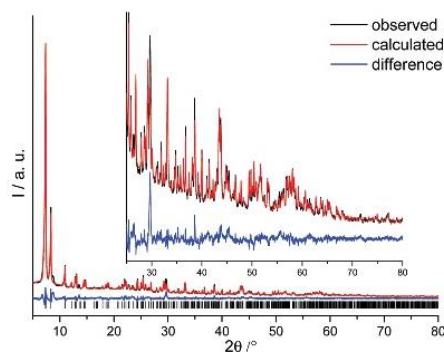


Fig. 3 Results of the Rietveld refinement for CAU-22. Black line gives the experimental data, red line gives the calculated curve, and the blue line the difference. Vertical bars mark the allowed Bragg positions.

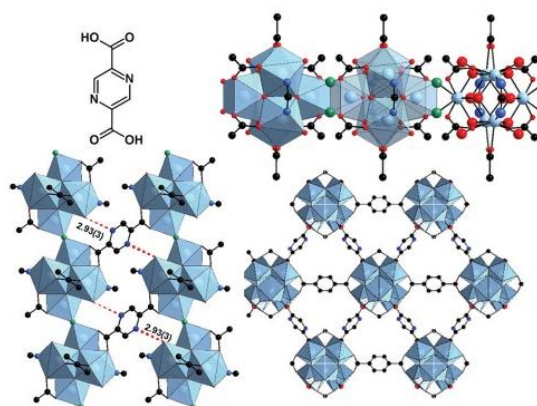


Fig. 4 Structure of CAU-22. Top left: 2,5-Pyrazine-dicarboxylic acid (H<sub>2</sub>PzDC), top right: 1D IBU in CAU-22 of composition {[Zr<sub>6</sub>O<sub>4</sub>(OH)<sub>4</sub>(μ-OH)<sub>2</sub>]} formed by edge-sharing of hexanuclear clusters (Zr<sub>6</sub>O<sub>4</sub>(OH)<sub>4</sub>) via μ-OH groups along the *c*-axis, bridging μ-OH groups shown in green, O atoms of formate groups in blue, while the rest of the O atoms (μ<sub>3</sub>-O, μ<sub>3</sub>-OH, H<sub>2</sub>O, OH<sup>-</sup> and -CO<sub>2</sub><sup>-</sup> groups) are shown in red; bottom left: proposed hydrogen bonding (red dotted line) between the bridging PzDC<sup>2-</sup> ions and H<sub>2</sub>O/OH<sup>-</sup> molecules coordinating to the Zr<sup>4+</sup> ions (view along [010]); bottom right: connection of the 1D IBUs by the PzDC<sup>2-</sup> ions (view along [001]) which leads to the formation of 1D pores with a diameter of *ca.* 3 Å.

The latter has been proposed for many other Zr-MOFs where a connectivity <12 of the clusters is observed.<sup>7</sup> Although H<sub>2</sub>O, OH<sup>-</sup> and O<sup>2-</sup> groups cannot be distinguished from the PXRD data, based on the available data and the structure of the hexanuclear clusters, we propose the following sum formula [Zr<sub>6</sub>(μ<sub>3</sub>-O)<sub>4</sub>(μ<sub>3</sub>-OH)<sub>4</sub>(μ-OH)<sub>2</sub>(OH)<sub>2</sub>(H<sub>2</sub>O)<sub>2</sub>(HCO<sub>2</sub>)<sub>2</sub>(PzDC)<sub>3</sub>] for CAU-22, which is also corroborated by additional characterization data.

In addition to the crystal structure analysis, CAU-22 was thoroughly characterised by various methods to confirm the composition and to evaluate the thermal and chemical stabilities as well as the porosity. Temperature dependent powder X-ray diffraction shows a thermal stability for CAU-22 up to approximately 270 °C (Fig. S5.1, ESI†). The thermogravimetric

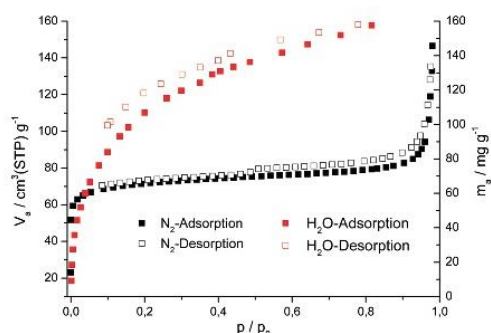


Fig. 5 Nitrogen (black) and water (red) sorption isotherms of CAU-22 measured at  $-196\text{ }^{\circ}\text{C}$  and  $25\text{ }^{\circ}\text{C}$  respectively.

and the elemental analysis (Fig. S5.3 and Table S5.2, ESI† respectively) are in good agreement with the postulated sum formula of the framework  $[\text{Zr}_6(\mu_3\text{-O})_4(\mu_3\text{-OH})_4(\mu_2\text{-OH})_2(\text{OH})_2(\text{H}_2\text{O})_2(\text{HCO}_2)_2(\text{PzDC})_3]$ , but the determined amount of adsorbed water molecules differs due to the hydrophilic properties of CAU-22. The presence of water molecules in the pores of CAU-22 is confirmed by IR-spectroscopy where a strong band centred at  $3267\text{ cm}^{-1}$  is observed (Fig. S6.1, ESI†). The  $^1\text{H}$  NMR spectrum of the dissolved MOF verifies the molar ratio  $\text{PzDC}^{2-}$  to formate ions of three to two (Fig. S7.1, ESI†). SEM micrographs of CAU-22 show that the particles consist of small platelets of approximately  $0.25\text{ }\mu\text{m}$  in diameter, which are assembled to larger aggregates of octahedral morphology (Fig. S8.1, ESI†).

To determine the porosity of CAU-22 a sample was activated at  $120\text{ }^{\circ}\text{C}$  for 16 h under reduced pressure. The nitrogen sorption measurement was carried out at  $-196\text{ }^{\circ}\text{C}$ . The isotherm shows a Type I behaviour, typical for microporous compounds (Fig. 5), with a small hysteresis (H4-type). The latter is typical for microporous aggregated samples (Fig. S3.6, ESI†).<sup>38</sup> The specific surface area is  $276\text{ m}^2\text{ g}^{-1}$  and the micropore volume is  $0.12\text{ cm}^3\text{ g}^{-1}$  (determined at  $p/p_0 = 0.5$ ). It is slightly smaller than the theoretical micropore volume of  $0.17\text{ cm}^3\text{ g}^{-1}$  calculated with the program Platon.<sup>39</sup> CAU-22 is highly hydrophilic, as demonstrated by water vapour sorption measurements carried out at  $25\text{ }^{\circ}\text{C}$  (Fig. 5).

The water isotherm shows a steep increase at low relative humidity values and an absolute uptake of about  $0.16\text{ g g}^{-1}$  CAU-22, which is in good agreement with the anticipated pore volume. Compared to UiO-66 ( $0.30\text{ g g}^{-1}$ ) the absolute water uptake is decreased but the steep rise in the isotherm starts at much lower  $p/p_0$  values, which can be associated with the more hydrophilic properties of the linker compared to terephthalate ions in UiO-66. After the sorption measurements, the high crystallinity of the samples was demonstrated by powder X-ray diffraction (Fig. S9.2, ESI†).

In conclusion, we synthesised a new Zr-MOF denoted CAU-22 by a water-based synthesis route employing a solvent mixture of water and formic acid. The structure of CAU-22 contains a unique 1D IBU which is formed by edge-sharing of the well-known hexanuclear  $\{[\text{Zr}_6(\mu_3\text{-O})_4(\mu_3\text{-OH})_4]\}$  clusters. It is permanently porous towards nitrogen and water and in contrast to UiO-66

CAU-22 is very hydrophilic which is due to the incorporation of pyrazinedicarboxylate ions as the linker. We anticipate that other linker molecules with similar functionalities will lead to the same IBU.

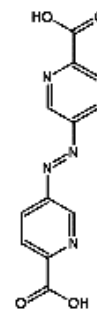
We thank Daria Smazna from the technical faculty of the CAU Kiel for taking the SEM micrographs.

## Notes and references

- J. A. Mason, M. Veenstra and J. R. Long, *Chem. Sci.*, 2014, 5, 32–51.
- J.-R. Li, R. J. Kuppler and H.-C. Zhou, *Chem. Soc. Rev.*, 2009, 38, 1477–1504.
- P. Valvekens, F. Vermoortele and D. De Vos, *Catal. Sci. Technol.*, 2013, 3, 1435–1445.
- F. Jermias, D. Frohlich, C. Janiak and S. K. Henninger, *New J. Chem.*, 2014, 38, 1846–1852.
- F. Ke, Y.-P. Yuan, L.-G. Qiu, Y.-H. Shen, A.-J. Xie, J.-F. Zhu, X.-Y. Tian and L.-D. Zhang, *J. Mater. Chem.*, 2011, 21, 3843–3848.
- H. Furukawa, K. E. Cordova, M. O’Keeffe and O. M. Yaghi, *Science*, 2013, 341, 974–986.
- Y. Bai, Y. Dou, L.-H. Xie, W. Rutledge, J.-R. Li and H.-C. Zhou, *Chem. Soc. Rev.*, 2016, 45, 2327–2367.
- T. Devic and C. Serre, *Chem. Soc. Rev.*, 2014, 43, 6097–6115.
- M. Puchberger, F. R. Kogler, M. Jupa, S. Gross, H. Fric, G. Kickelbick and U. Schubert, *Eur. J. Inorg. Chem.*, 2006, 3283–3293.
- J. H. Cavka, S. R. Jakobsen, U. Olsbye, N. Guillou, C. Lamberti, S. Bordiga and K. P. Lillerud, *J. Am. Chem. Soc.*, 2008, 130, 13850–13851.
- V. Bon, I. Senkowska, M. S. Weiss and S. Kaskel, *CrystEngComm*, 2013, 15, 9572–9577.
- G. Wißmann, A. Schaate, S. Lilienthal, I. Bremer, A. M. Schneider and P. Behrens, *Microporous Mesoporous Mater.*, 2012, 152, 64–70.
- B. Bueken, H. Reinsch, N. Reimer, I. Stassen, F. Vermoortele, R. Ameloot, N. Stock, C. E. A. Kirschhock and D. De Vos, *Chem. Commun.*, 2014, 50, 10055–10058.
- S. Biswas, J. Zhang, Z. Li, Y.-Y. Liu, M. Grzywa, L. Sun, D. Volkmer and P. Van Der Voort, *Dalton Trans.*, 2013, 42, 4730–4737.
- M. Kandiah, M. H. Nilsen, S. Usseglio, S. Jakobsen, U. Olsbye, M. Tilset, C. Larabi, E. A. Quadrelli, F. Bonino and K. P. Lillerud, *Chem. Mater.*, 2010, 22, 6632–6640.
- V. Bon, I. Senkowska, I. A. Baburin and S. Kaskel, *Cryst. Growth Des.*, 2013, 13, 1231–1237.
- V. Bon, V. Senkovskyy, I. Senkowska and S. Kaskel, *Chem. Commun.*, 2012, 48, 8407–8409.
- H. Furukawa, F. Gándara, Y.-B. Zhang, J. Jiang, W. L. Queen, M. R. Hudson and O. M. Yaghi, *J. Am. Chem. Soc.*, 2014, 136, 4369–4381.
- W. Morris, B. Voloskiy, S. Demir, F. Gándara, P. L. McGrier, H. Furukawa, D. Cascio, J. F. Stoddart and O. M. Yaghi, *Inorg. Chem.*, 2012, 51, 6443–6445.
- M. Zhang, Y.-P. Chen, M. Bosch, T. Gentle, K. Wang, D. Feng, Z. U. Wang and H.-C. Zhou, *Angew. Chem., Int. Ed.*, 2014, 53, 815–818.
- V. Guillerm, F. Ragon, M. Dan-Hardi, T. Devic, M. Vishnuvarthan, B. Campo, A. Vimont, G. Clet, Q. Yang, G. Maurin, G. Férey, A. Vittadini, S. Gross and C. Serre, *Angew. Chem., Int. Ed.*, 2012, 51, 9267–9271.
- D. Feng, H.-L. Jiang, Y.-P. Chen, Z.-Y. Gu, Z. Wei and H.-C. Zhou, *Inorg. Chem.*, 2013, 52, 12661–12667.
- M. Taddei, F. Costantino, F. Marmottini, A. Comotti, P. Sozzani and R. Vivani, *Chem. Commun.*, 2014, 50, 14831–14834.
- G. Mouchaham, L. Cooper, N. Guillou, C. Martineau, E. Elkaïm, S. Bourrelly, P. L. Llewellyn, C. Allain, G. Clavier, C. Serre and T. Devic, *Angew. Chem., Int. Ed.*, 2015, 54, 13297–13301.
- Z. Hu, Y. Peng, Z. Kang, Y. Qian and D. Zhao, *Inorg. Chem.*, 2015, 54, 4862–4868.
- H. Reinsch, S. Waitschat, S. M. Chavan, K. P. Lillerud and N. Stock, *Eur. J. Inorg. Chem.*, 2016, DOI: 10.1002/ejic.201600295.
- F. Ragon, B. Campo, Q. Yang, C. Martineau, A. D. Wiersum, A. Lago, V. Guillerm, C. Hemsley, J. F. Eubank, M. Vishnuvarthan, F. Taulelle, P. Horcajada, A. Vimont, P. L. Llewellyn, M. Daturi, S. Devautour-Vinot, G. Maurin, C. Serre, T. Devic and G. Clet, *J. Mater. Chem. A*, 2015, 3, 3294–3309.
- Q. Yang, S. Vaesen, F. Ragon, A. D. Wiersum, D. Wu, A. Lago, T. Devic, C. Martineau, F. Taulelle, P. L. Llewellyn, H. Jobic, C. Zhong, C. Serre,

- G. De Weireld and G. Maurin, *Angew. Chem., Int. Ed.*, 2013, **52**, 10316–10320.
- 29 H. Reinsch, B. Bueken, F. Vermoortele, I. Stassen, A. Lieb, K.-P. Lillerud and D. De Vos, *CrystEngComm*, 2015, **17**, 4070–4074.
- 30 H. Reinsch, *Eur. J. Inorg. Chem.*, 2016, DOI: 10.1002/ejic.201600286.
- 31 W. J. Schut, H. I. X. Mager and W. Berends, *Recl. Trav. Chim. Pays-Bas*, 1961, **80**, 391–398.
- 32 R. Plessius, R. Kromhout, A. L. D. Ramos, M. Ferbinteanu, M. C. Mittelmeijer-Hazeleger, R. Krishna, G. Rothenberg and S. Tanase, *Chem. – Eur. J.*, 2014, **20**, 7922–7925.
- 33 B. Cai, P. Yang, J.-W. Dai and J.-Z. Wu, *CrystEngComm*, 2011, **13**, 985–991.
- 34 N. Stock and S. Biswas, *Chem. Rev.*, 2012, **112**, 933–969.
- 35 A. *Topas Academics 4.2*, Coelho Software, Brisbane, 2007.
- 36 A. Altomare, M. Camalli, C. Cuocci, C. Giacovazzo, A. Moliterni and R. Rizzi, *J. Appl. Crystallogr.*, 2009, **42**, 1197–1202.
- 37 *C. Materials Studio Version 5.0*, Accelrys Inc., San Diego, 2009.
- 38 M. Thommes, K. Kaneko, V. Neimark Alexander, P. Olivier James, F. Rodriguez-Reinoso, J. Rouquerol and S. W. Sing Kenneth, *Pure Appl. Chem.*, 2015, **87**, 1051.
- 39 A. Spek, *Acta Crystallogr.*, 2009, **65**, 148–155.

#### 4.1.2.3. Direct water-based synthesis and characterization of new Zr/Hf-MOFs with dodecanuclear clusters as IBU



Der folgende Artikel wurde im Jahr 2018 in der Fachzeitschrift *CrystEngComm*, RSC veröffentlicht. Die Wiedergabe erfolgt mit freundlicher Genehmigung der RSC. Reprinted with permission from S. Waitschat, H. Reinsch, M. Arpacioğlu and N. Stock, *CrystEngComm*, **2018**, DOI: 10.1039/C8CE00949J. Copyright 2018 The Royal Society of Chemistry.

<http://pubs.rsc.org/en/content/articlelanding/2018/ce/c8ce00949j#!divAbstract>

Um eine zu CAU-22 isoretikuläre Verbindung mit einem größeren Porendurchmesser herzustellen, wurde ein Linker mit dem gleichen Stickstoff-Substitutions Motiv wie das von H<sub>2</sub>PzDC, der allerdings einen größeren Abstand zwischen den beiden Carbonsäuren aufweisen kann, gesucht und in Azopyridinedicarbonsäure (H<sub>2</sub>APDC) gefunden. Nach unserem Wissen ist dies die erste Beschreibung dieses Linkers für die Herstellung eines MOFs. Die Synthese orientierte sich an derjenigen von CAU-22, so wurde ZrOCl<sub>2</sub>·8H<sub>2</sub>O und HfCl<sub>4</sub> als Metallquellen eingesetzt. Während der Syntheseoptimierung wurde insbesondere das molare Verhältnis Modulator zu Wasser und die Reaktionszeit variiert. Für beide Verbindungen ist die optimierte Reaktionszeit 40 min und auch das Modulator zu Wasser Verhältnis ist gleich, nur wird für Zr-CAU-39 ([Zr<sub>12</sub>(O)<sub>8</sub>(OH)<sub>20</sub>(H<sub>2</sub>O)<sub>6</sub>(APDC)<sub>6</sub>]) Ameisensäure und für Hf-CAU-39 ([Hf<sub>12</sub>(O)<sub>8</sub>(OH)<sub>20</sub>(H<sub>2</sub>O)<sub>6</sub>(APDC)<sub>6</sub>]) Essigsäure als Modulator verwendet.

Die Struktur von M-CAU-39 mit M = Zr, Hf ist nicht isostrukturell zu CAU-22 allerdings zu der kürzlich veröffentlichten Struktur von Hf-*hcp*-UiO-67 mit BPDC<sup>2-</sup> als Linker.<sup>94</sup> Durch den Austausch von BPDC<sup>2-</sup> durch APDC<sup>2-</sup> und der damit verbundenen Vergrößerung des Linkers, ist es gelungen den Porenradius von 3 bei *hcp*-UiO-67 auf 6 Å bei CAU-39 zu erhöhen. Die IBU von CAU-39 ist der bisher selten beobachtete dodecanucleare Zr-O-Cluster {[Zr<sub>6</sub>(μ<sub>3</sub>-O)<sub>4</sub>(μ<sub>3</sub>-OH)<sub>4</sub>(μ-OH)<sub>3</sub>]<sub>2</sub>}. Er besteht aus zwei über sechs Hydroxidionen verbrückten hexanuklearen Zr-O-Clustern. Insgesamt sechs Linkeranionen verbrücken die Zr-O-Cluster zu einem zweidimensionalen Netzwerk. In CAU-39 wird eine AB-Stapelung der Schichten beobachtet. Zum Ladungsausgleich werden sechs weitere Hydroxidionen und zur Absättigung Koordinationssphäre der Metallionen sechs Wassermoleküle benötigt. Die daraus resultierende Summenformel ist [Zr<sub>12</sub>(μ<sub>3</sub>-O)<sub>8</sub>(μ<sub>3</sub>-OH)<sub>8</sub>(μ-OH)<sub>6</sub>](OH)<sub>6</sub>(H<sub>2</sub>O)<sub>6</sub>(APDC)<sub>6</sub>. Durch thermogravimetrische Untersuchungen wurde die Summenformel bestätigt und die thermische

Stabilität von ca. 350 °C bestimmt. Diese ist vergleichbar mit dem Wert der durch VT-PXRD Messungen erhalten wurde.

Zur Untersuchung der Sorptionseigenschaften wurden N<sub>2</sub>-Sorptionsuntersuchungen mit den hergestellten MOFs durchgeführt. Beide Verbindungen sind gegenüber Stickstoff bei -196 °C porös und haben eine scheinbare, spezifische Oberfläche von 430 bzw. 200 m<sup>2</sup>·g<sup>-1</sup> und ein Mikroporenvolumen von 0.21 bzw. 0.11 cm<sup>3</sup>·g<sup>-1</sup> für Zr-CAU-39 bzw. für Hf-CAU-39.



Cite this: DOI: 10.1039/c8ce00949j

Received 8th June 2018,  
Accepted 21st June 2018

DOI: 10.1039/c8ce00949j

rsc.li/crystengcomm

## Direct water-based synthesis and characterization of new Zr/Hf-MOFs with dodecanuclear clusters as IBUs†

Steve Waitschat, Helge Reinsch, Merve Arpacioğlu and Norbert Stock \*

Two new metal-organic framework compounds of composition  $[M_{12}(\mu_3-O)_8(\mu_3-OH)_8(\mu-OH)_6(OH)_6(H_2O)_6(APDC)_6]$ , with  $M = Zr$  and Hf, denoted as M-CAU-39, containing the azopyridinedicarboxylate ion ( $APDC^{2-}$ ) as a new linker, were obtained by a water-based synthesis. The crystal structure was determined from powder X-ray diffraction data. The inorganic building unit (IBU) is the dodecanuclear cluster  $\{M_{12}O_8(OH)_{14}\}$  and its connection results in a porous two-dimensional network.

Metal organic frameworks (MOFs) are an intensively investigated class of compounds in solid state research today, especially due to the diversity of their structures<sup>1</sup> and their various potential applications in areas such as gas storage,<sup>2</sup> gas separation,<sup>2</sup> catalysis,<sup>3</sup> heat transformation<sup>4</sup> or drug delivery.<sup>5</sup>

In particular, Zr-MOFs obtained from reactions with polycarboxylic acids are of interest, due to their high chemical and thermal stability.<sup>6,7</sup> In 2008, the first Zr-MOF, UiO-66 ( $[Zr_6O_4(OH)_4(BDC)_6]$ ,  $BDC^{2-} = 1,4$ -benzenedicarboxylate, UiO = University of Oslo) with the hexanuclear cluster  $^0_6\{Zr_6O_4(OH)_4\}$  as the IBU was reported (Fig. 1).<sup>8</sup> Several Zr-MOFs isorecticular to UiO-66 (ref. 9 and 10) and a manifold of new Zr-MOFs with a different framework topology and connectivity of the hexanuclear cluster were synthesized in the following years.<sup>11–15</sup> In 2012, a new IBU  $^1_{12}\{Zr(\mu_3-O)_3O_4\}$  was added to the Zr-MOF chemistry. It is composed of chains of edge-sharing  $ZrO_7$ -polyhedra and was exclusively observed in MIL-140 compounds ( $[ZrO(O_2C-R-CO_2)]_n$ , R = organic moiety, MIL = Material Institute Lavoisier).<sup>16</sup>

Recently, Zr-MOFs with new IBUs related to the archetypal hexanuclear cluster were also described. Thus, in 2016, CAU-

22 was reported (CAU = Christian-Albrechts-University), incorporating a condensed form of the hexanuclear cluster, resulting in  $^1_{12}\{Zr_6O_4(OH)_4(\mu-OH)_2\}$  chains as IBUs (Fig. 1)<sup>17</sup> and, in 2017, the first dodecanuclear cluster in a Zr-MOF was reported. In this IBU, two hexanuclear clusters are bridged by six edge-sharing hydroxide groups resulting in the formula  $^0_{12}\{Zr_{12}O_8(OH)_{14}\}$  (Fig. 1).<sup>18</sup> In 2018, the structure of a slightly differently connected cluster with the formula  $^0_{12}\{Zr_6O_4(OH)_4\}_2(CH_3COO)_4$  was published, which is formed by the bridging of two hexanuclear clusters by four formate anions (Fig. 1).<sup>19</sup> These results show that the diversity of hundreds of different Zr-MOF structures is based on only five IBUs.

Water is the most preferable solvent for the synthesis of materials.<sup>20</sup> Also, the water-based synthesis of Zr-MOFs has been studied by various groups.<sup>21–24</sup> All reported structures contain the hexanuclear cluster, with the exception of CAU-22, which has been recently reported by some of us.<sup>17</sup>

Herein we report the water-based synthesis and characterization of two new isorecticular MOFs, Zr- and Hf-MOFs, with the composition  $[M_{12}(\mu_3-O)_8(\mu_3-OH)_8(\mu-OH)_6(OH)_6(H_2O)_6(APDC)_6]$ , denoted as M-CAU-39 ( $M = Hf, Zr$ ), which contain

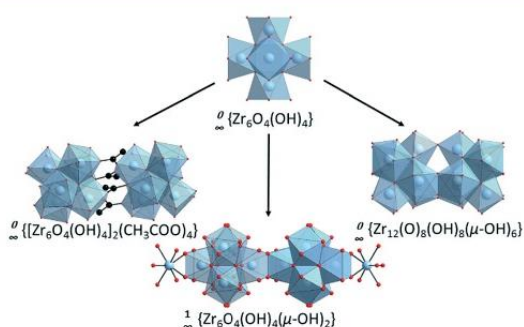


Fig. 1 IBUs in Zr-MOFs that are formally derived from the hexanuclear cluster  $(Zr_6O_4(OH)_4)$ . Structural data are taken from ref. 8 and 17–19. For clarity, the dimensionality of the building units  $^0_{12}$  and  $^1_{12}$  is added to the cluster formula.

Institute für Anorganische Chemie, Christian-Albrechts-Universität, Max-Eyth-Straße 2, D 24118 Kiel, Germany. E-mail: stock@ac.uni-kiel.de

† Electronic supplementary information (ESI) available: Details of synthesis optimization and structure determination, VT-PXRD data, TG analysis, and IR- and NMR spectra. CCDC 1843298 contains the supplementary crystallographic data for Hf-CAU-39. For ESI and crystallographic data in CIF or other electronic format see DOI: 10.1039/c8ce00949j



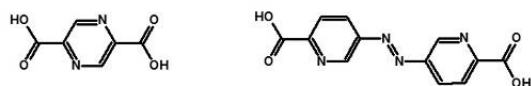


Fig. 2 Structure of the two linkers, H<sub>2</sub>PzDC (left) and H<sub>2</sub>APDC (right).

4,4'-azopyridine-dicarboxylate ions (APDC<sup>2-</sup>) and the dodecanuclear cluster  ${}^{\infty}\{M_{12}O_8(OH)_{14}\}$  with M = Zr or Hf.

The synthesis of M-CAU-39 was inspired by the synthesis conditions of CAU-22,<sup>17</sup> which contains pyrazinedicarboxylate (PzDC<sup>2-</sup>) as the linker (Fig. 2). The linker H<sub>2</sub>APDC was chosen since it has a very similar arrangement of pyridine N-atoms and -COOH groups (Fig. 2). Thus, we anticipated the formation of a new Zr-MOF, isorecticular to CAU-22. In addition, this linker has, to the best of our knowledge, not been reported for the synthesis of MOFs although it can be easily synthesized starting from 5-nitropicolinic acid and glucose.<sup>25</sup> Details are given in the ESI.†

The MOFs Zr/Hf-CAU-39 were synthesized under solvothermal reaction conditions using ZrOCl<sub>2</sub>·8H<sub>2</sub>O and HfCl<sub>4</sub> as the metal source, respectively. Optimisation of the synthesis conditions, by variation of the modulator, reaction time and temperature, was carried out under stirring in Pyrex tubes in an aluminium heating block (for a detailed description, see section S3). The optimised synthesis conditions of M-CAU-39 with M = Zr and Hf are very similar and only differ in the modulator. Formic acid was used for Zr-CAU-39 and

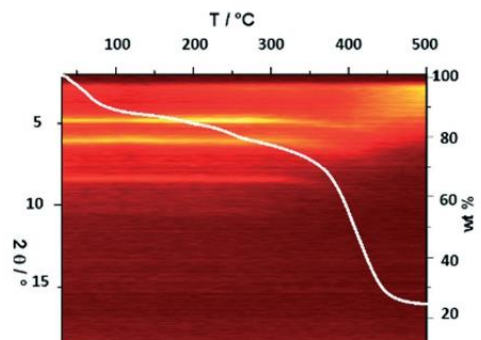


Fig. 4 The white line shows the thermogravimetric curve from Zr-CAU-39 and the results of the VT-PXRD measurements are shown behind.

acetic acid for Hf-CAU-39, which is in line with the different acidities of the used metal sources. The title compounds form in water at 140 °C within 40 minutes starting from a molar ratio of M<sup>4+</sup>:H<sub>2</sub>APDC = 1:1, which is lower than that observed in CAU-39 (M<sup>4+</sup>:H<sub>2</sub>APDC = 2:1).

The structures of the microcrystalline products were determined from powder X-ray diffraction (PXRD) data. Indexing of the PXRD pattern resulted in a hexagonal unit cell. Cliffe *et al.* recently reported the crystal structure of *hxl*-Hf-UiO-

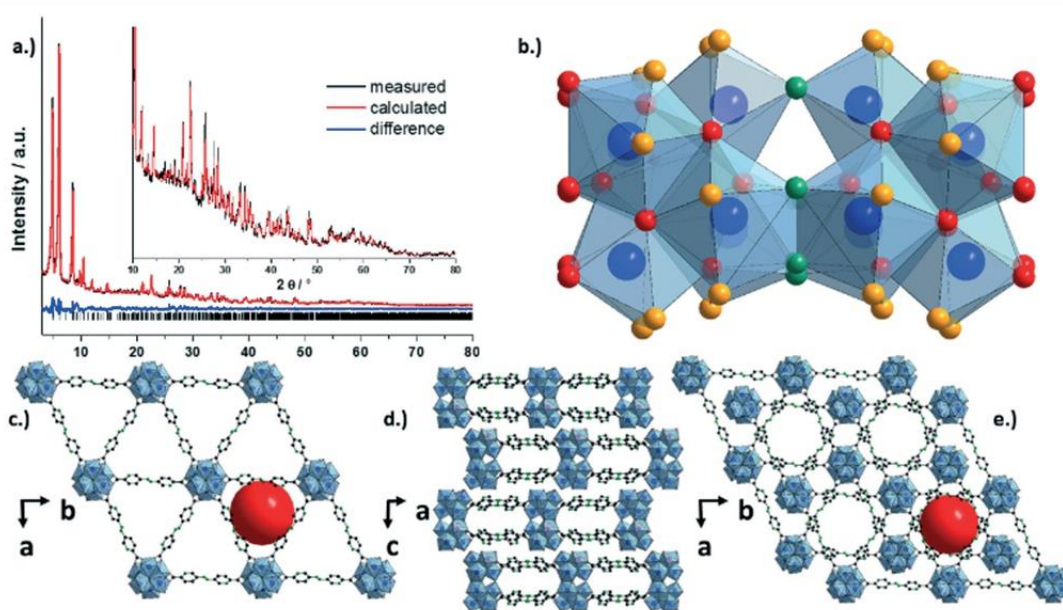


Fig. 3 a.) Results of the Rietveld refinement of Hf-CAU-39. Crystal structure of M-CAU-39,  $[M_{12}(\mu_3-O)_8(\mu_3-OH)_8(\mu-OH)_6(OH)_6(H_2O)_6(APDC)_6]$ . b.) IBU in M-CAU-39 of composition  ${}^{\infty}\{[Zr_{12}(\mu_3-O)_8(\mu_3-OH)_8(\mu-OH)_6]\}$  formed by two edge-sharing hexanuclear  $\{Zr_6O_4(OH)_4\}$  clusters via six  $\mu$ -OH groups. O atoms of the  $\mu$ -OH groups are shown in green, and O atoms of the  $-CO_2^-$  groups are presented in yellow while the rest of the O atoms ( $\mu_3-O$ ,  $\mu_3-OH$ ,  $H_2O$  and  $OH^-$  groups) are shown in red. c.) Connection of the dodecanuclear clusters in the *a,b*-plane. d.) ABAB-stacking of the layers along the *c*-axis. e.) View of d.) perpendicular to the layers. The red sphere describes the diameter of the trigonal windows (6 Å).

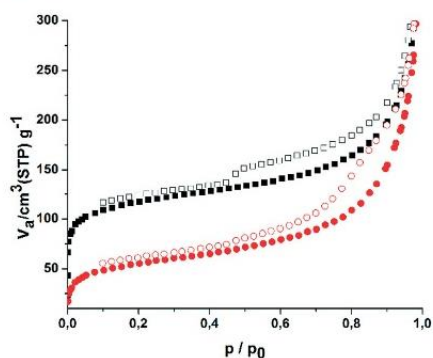


Fig. 5  $N_2$ -Adsorption and desorption of M-CAU-39 with M = Zr (black) and Hf (red) measured at  $-196\text{ }^\circ\text{C}$ .

67.<sup>26</sup> Based on this information – topology and composition – a starting model was developed using the linker replacement strategy.<sup>27</sup> Thus, biphenyl-4,4'-dicarboxylate ions were replaced by 4,4'-azopyridine-dicarboxylate ions, which leads to a change in space group symmetry from  $P6_3/mmc$  to  $P6_3/m$ . This structural model was energetically optimized by force-field calculations using the Forcite routine implemented in Materials Studio.<sup>28</sup> The subsequent Rietveld refinement (Fig. 3a) was successfully carried out for Hf-CAU-39 and confirmed the presence of the dodecanuclear clusters in the new MOF (Fig. 3b). For Zr-CAU-39, a meaningful Rietveld refinement could not be accomplished which is likely due to stacking disorder of the layered compound. Nevertheless, a LeBail fit of the PXRD data confirms the purity and the isoreticularity (Fig. S4.2†). Details of the structure determination and the results of the Rietveld refinement are presented in the ESI.†

M-CAU-39 crystallizes in the hexagonal space group  $P6_3/m$ . It has to be kept in mind that the position of protons cannot be reliably located from the PXRD data. Nevertheless, based on the information on Zr-MOFs,<sup>23,26</sup> the following structural description can be derived. The IBU is composed of two  $\{M_6O_4(OH)_4\}$  clusters which are interconnected by six edge-sharing hydroxide groups. Thus the dodecanuclear cluster  ${}^0\{M_{12}(\mu_3-O)_8(\mu_3-OH)_8(\mu-OH)_6\}$  is formed (Fig. 3b). Each cluster is connected to six others by twelve APDC<sup>2-</sup> ions, and the other metal coordination sites are occupied by  $OH^-$  and  $H_2O$  molecules, which results in the composition  $[M_{12}(\mu_3-O)_8(\mu_3-OH)_8(\mu-OH)_6(OH)_6(H_2O)_6(APDC)_6]$ . Thus 3<sup>o</sup> layers (*hxl* topology) are formed with trigonal windows of 6 Å in diameter, taking the van der Waals radii into account (Fig. 3c). These layers are arranged in an ABAB stacking order along the *c*-axis (Fig. 3d) and sinusoidal pores with a diameter of 6 Å (Fig. 3e) are formed. The extension of the linker in *hxl*-Hf-UiO-67 through the formal insertion of a  $-N=N-$  moiety leads to an increase in pore diameter from 3 Å in *hxl*-Hf-UiO-67 to 6 Å in M-CAU-39.

Only a few Zr/Hf-MOFs that crystallize in a layered structure have been reported to date, such as DUT-84,<sup>11</sup> Zr-FA<sup>29</sup>

and *hxl*-Hf-UiO-67, which is isoreticular to the title compounds. This MOF was only obtained from a metastable intermediate over a period of days under ambient conditions.<sup>26</sup> In contrast, CAU-39 can be easily prepared directly from water within 40 min.

The absence of chloride ions in M-CAU-39 was proven by EDX and TG measurements which confirmed their composition (Fig. 4 and Fig. S.5.2†). After the removal of non-coordinating water molecules up to ca. 170 °C, the dehydration of the clusters takes place (170–320 °C). The whole structure starts to decompose at approximately 320 °C for M-CAU-39. Further details are given in the ESI.†

Variable-temperature (VT) PXRD measurements were also carried out to determine the thermal stability (Fig. 4 and Fig. S.5.4†). In comparison with the TG measurements, a slightly higher thermal stability of 350 and 375 °C for Zr-CAU-39 and Hf-CAU-39, respectively, is observed, which can be explained by the different measurement set-ups. While VT-PXRD was performed in open capillaries, the TGA was carried out in a flow of air in an open crucible.

Both compounds are porous towards  $N_2$  at  $-196\text{ }^\circ\text{C}$ . For the  $N_2$ -sorption experiments, the samples were activated at 120 °C for 16 h. Both samples show a type-I isotherm typical for microporous compounds and a H4-type hysteresis typical for aggregated, microcrystalline samples (Fig. 5).<sup>30</sup> Evaluation by the BET method following the procedure reported by Rouquerol *et al.*<sup>31</sup> resulted in specific surface areas of 430 and 200  $m^2\text{ g}^{-1}$  (theoretical values: 650 and 494  $m^2\text{ g}^{-1}$ ) and micropore volumes of 0.21 and 0.11  $cm^3\text{ g}^{-1}$  (theoretical values: 0.47 and 0.36  $cm^3\text{ g}^{-1}$ ) for Zr-CAU-39 and Hf-CAU-39, respectively. The measured values are lower than the theoretical ones, calculated with Materials Studio<sup>28</sup> using  $N_2$  as the probe molecule, probably due to stacking faults in the layered structures.

In conclusion, we synthesised two new MOFs, Zr- and Hf-MOFs, of composition  $[M_{12}(\mu_3-O)_8(\mu_3-OH)_8(\mu-OH)_6(OH)_6(H_2O)_6(APDC)_6]$  (M-CAU-39) by a direct, water-based synthesis route employing a solvent mixture of water and the modulators acetic or formic acid for Zr-CAU-39 and Hf-CAU-39, respectively. In contrast to the synthesis of the isoreticular MOF *hxl*-Hf-UiO-67, the rapid formation of the dodecanuclear clusters  ${}^0\{M_{12}(\mu_3-O)_8(\mu_3-OH)_8(\mu-OH)_6\}$  and their incorporation in the layered structure is observed in M-CAU-39. The compounds are stable at temperatures  $>300\text{ }^\circ\text{C}$  and slightly porous towards  $N_2$  at  $-196\text{ }^\circ\text{C}$ .

## Conflicts of interest

There are no conflicts to declare.

## Notes and references

- N. Stock and S. Biswas, *Chem. Rev.*, 2012, **112**, 933–969.
- J.-R. Li, R. J. Kuppler and H.-C. Zhou, *Chem. Soc. Rev.*, 2009, **38**, 1477.

- 3 M. Lammert, M. T. Wharmby, S. Smolders, B. Bueken, A. Lieb, K. A. Lomachenko, D. D. Vos and N. Stock, *Chem. Commun.*, 2015, 51, 12578–12581.
- 4 D. Lenzen, P. Bendix, H. Reinsch, D. Fröhlich, H. Kummer, M. Möllers, P. P. C. Hügenell, R. Gläser, S. Henninger and N. Stock, *Adv. Mater.*, 2017, 1705869.
- 5 J. Zhuang, C.-H. Kuo, L.-Y. Chou, D.-Y. Liu, E. Weerapana and C.-K. Tsung, *ACS Nano*, 2014, 8, 2812–2819.
- 6 Y. Bai, Y. Dou, L.-H. Xie, W. Rutledge, J.-R. Li and H.-C. Zhou, *Chem. Soc. Rev.*, 2016, 45, 2327–2367.
- 7 M. Rimoldi, A. J. Howarth, M. R. DeStefano, L. Lin, S. Goswami, P. Li, J. T. Hupp and O. K. Farha, *ACS Catal.*, 2017, 7, 997–1014.
- 8 J. H. Cavka, S. Jakobsen, U. Olsbye, N. Guillou, C. Lamberti, S. Bordiga and K. P. Lillerud, *J. Am. Chem. Soc.*, 2008, 130, 13850–13851.
- 9 G. Wifmann, A. Schaate, S. Lilienthal, I. Bremer, A. M. Schneider and P. Behrens, *Microporous Mesoporous Mater.*, 2012, 152, 64–70.
- 10 S. Biswas, J. Zhang, Z. Li, Y.-Y. Liu, M. Grzywa, L. Sun, D. Volkmer and P. Van Der Voort, *Dalton Trans.*, 2013, 42, 4730.
- 11 V. Bon, I. Senkowska, M. S. Weiss and S. Kaskel, *CrystEngComm*, 2013, 15, 9572.
- 12 V. Bon, I. Senkowska, I. A. Baburin and S. Kaskel, *Cryst. Growth Des.*, 2013, 13, 1231–1237.
- 13 H. Furukawa, F. Gándara, Y.-B. Zhang, J. Jiang, W. L. Queen, M. R. Hudson and O. M. Yaghi, *J. Am. Chem. Soc.*, 2014, 136, 4369–4381.
- 14 A. C. Dreischarf, M. Lammert, N. Stock and H. Reinsch, *Inorg. Chem.*, 2017, 56, 2270–2277.
- 15 L. Feng, S. Yuan, L.-L. Zhang, K. Tan, J.-L. Li, A. Kirchon, L.-M. Liu, P. Zhang, Y. Han, Y. J. Chabal and H.-C. Zhou, *J. Am. Chem. Soc.*, 2018, 140, 2363–2372.
- 16 V. Guillermin, F. Ragon, M. Dan-Hardi, T. Devic, M. Vishnuvarthan, B. Campo, A. Vimont, G. Clet, Q. Yang, G. Maurin, G. Férey, A. Vittadini, S. Gross and C. Serre, *Angew. Chem., Int. Ed.*, 2012, 51, 9267–9271.
- 17 S. Waitschat, H. Reinsch and N. Stock, *Chem. Commun.*, 2016, 52, 12698–12701.
- 18 P. Ji, K. Manna, Z. Lin, X. Feng, A. Urban, Y. Song and W. Lin, *J. Am. Chem. Soc.*, 2017, 139, 7004–7011.
- 19 A. A. Bezrukov, K. W. Törnroos, E. Le Roux and P. D. C. Dietzel, *Chem. Commun.*, 2018, 54, 2735–2738.
- 20 H. Reinsch, *Eur. J. Inorg. Chem.*, 2016, 2016, 4290–4299.
- 21 H. Reinsch, S. Waitschat, S. M. Chavan, K. P. Lillerud and N. Stock, *Eur. J. Inorg. Chem.*, 2016, 2016, 4490–4498.
- 22 H. Reinsch, B. Bueken, F. Vermoortele, I. Stassen, A. Lieb, K.-P. Lillerud and D. De Vos, *CrystEngComm*, 2015, 17, 4070–4074.
- 23 S. Waitschat, D. Fröhlich, H. Reinsch, H. Terraschke, K. A. Lomachenko, C. Lamberti, H. Kummer, T. Helling, M. Baumgartner, S. Henninger and N. Stock, *Dalton Trans.*, 2018, 47, 1062–1070.
- 24 Z. Hu, Y. Peng, Z. Kang, Y. Qian and D. Zhao, *Inorg. Chem.*, 2015, 54, 4862–4868.
- 25 S. Ameerunisha and P. S. Zacharias, *J. Chem. Soc., Perkin Trans. 2*, 1995, 1679–1682.
- 26 M. J. Cliffe, E. Castillo-Martinez, Y. Wu, J. Lee, A. C. Forse, F. C. N. Firth, P. Z. Moghadam, D. Fairen-Jimenez, M. W. Gaultois, J. A. Hill, O. V. Magdysyuk, B. Slater, A. L. Goodwin and C. P. Grey, *J. Am. Chem. Soc.*, 2017, 139, 5397–5404.
- 27 I. Senkowska, F. Hoffmann, M. Fröba, J. Getzschmann, W. Böhlmann and S. Kaskel, *Microporous Mesoporous Mater.*, 2009, 122, 93–98.
- 28 Accelrys Inc., *Materials Studio Version 5.0*, San Diego, 2009.
- 29 W. Liang, R. Babarao, M. J. Murphy and D. M. D'Alessandro, *Dalton Trans.*, 2015, 44, 1516–1519.
- 30 M. Thommes, K. Kaneko, A. V. Neimark, J. P. Olivier, F. Rodriguez-Reinoso, J. Rouquerol and K. S. W. Sing, *Pure Appl. Chem.*, 2015, 87, 1051–1069.
- 31 P. L. Llewellyn, F. Rodriguez-Reinoso, J. Rouquerol and N. Seaton, *Stud. Surf. Sci. Catal.*, 2007, 160, 49.

## **4.2 Kumulativer Teil Flussreaktorsynthesen**

### **4.2.1 Einleitung**

#### **4.2.1.1 Aufskalierung von MOFs?**

MOFs werden gewöhnlich durch solvothermale Reaktionen in Batchreaktoren (Stahlautoklaven mit Tefloneinsätzen oder in druckbeständigen Glasampullen) synthetisiert. Der Energieeintrag kann durch konventionelles Heizen in Umluftöfen, durch Mikrowellenstrahlung oder auch durch Ultraschallwellen erzeugt werden.<sup>95</sup> Zur Entdeckung neuer Verbindungen ist diese Synthesemethode erprobt und sehr erfolgreich einsetzbar. Allerdings sind die produzierten Mengen meistens sehr klein und ein Aufskalieren ist nicht immer trivial. Dies kann z.B. an veränderten Drücken in den größeren Reaktionsgefäßen, einer schlechteren bzw. anderen Durchmischung oder unterschiedlicher Erwärmung der Reaktionsmischungen liegen. Selbstverständlich werden in der Industrie Batch-Reaktionen auch im sehr großen Maßstab durchgeführt, für MOF-Synthesen in Batchreaktoren mit einer Ausbeute > 100 g gibt es aber nur wenige Beispiele. Zu nennen sind hier die „Produktionen“ von Basolite A250 (Al-MIL-53-Fum) von der BASF,<sup>96</sup> eine wässrige Synthese bei Raumtemperatur von verschiedenen CPO-27-MOFs,<sup>97</sup> die Synthese von Cr-MIL-101<sup>98</sup> oder die Synthese von Fe-MIL-127.<sup>99</sup> Zusätzlich sind auch wenige Beispiele von aufskalierten Synthesen unter Reflux wie von CPO-27<sup>100</sup> oder CAU-10 publiziert.<sup>101</sup>

Aus diesem Grund wurden über die Jahre weitere Synthesemethoden zur Herstellung von MOFs getestet, wobei das Hauptaugenmerk auf eine konstante, kontinuierliche Produktion gelegt wurde. So konnte gezeigt werden, dass durch Sprühtrocknung HKUST-1 und ZIF-8<sup>102</sup> oder auch MOFs wie UiO-66, NOTT-100, MIL-88 oder MOF-14 hergestellt werden können.<sup>103</sup> Eine weitere Methode ist die mechanische, lösungsmittelfreie Synthese von ZIF-8 und Al-MIL-53-Fum in einem Extruder. Allerdings sollte hier angemerkt werden, dass die Synthese zwar lösungsmittelfrei ist, die Produkte anschließend aber mit teilweise enormen Mengen an Lösungsmittel gewaschen werden müssen um die Porosität der Proben zu erzeugen.<sup>104</sup>

#### **4.2.1.2 Flussreaktoren: Grundlagen**

Im Folgenden wird zunächst auf die Grundlagen zu Flussreaktorsynthesen eingegangen, sowie Vor- und Nachteile, Probleme und die verschiedenen Arten von Flussreaktoren beschrieben.

In der Regel besteht ein Flussreaktor in der einfachsten Ausführung, aus einer oder mehrerer Fördereinrichtungen (Pumpen), die eine Eduktlösung oder auch Eduktsuspension durch Schläuche pumpen, wobei am Ende des Schlauches das Produkt aufgefangen werden kann. Als Schlauchmaterial

wird in der Regel PTFE verwendet, da dieses chemisch inert ist. Dadurch dass nicht zuerst ein Stahlautoklav (wie bei einer Batchsynthese) erhitzt werden muss, sondern die Lösung/Suspension nahezu direkt erwärmt wird ist ein effizienter Energieeintrag gewährleistet.<sup>105</sup> Der größte Vorteil von Flussreaktorsynthesen gegenüber den Batchsynthesen ist allerdings der kontinuierliche Betrieb. Selbstverständlich muss immer wieder Edukt zugeführt und das Produkt aufgearbeitet werden, aber es gibt keine Leerlaufzeiten. Ein großer Nachteil von Flussreaktoren ist deren teilweise sehr hohe Spezifikation. Oftmals muss ein Flussreaktor explizit auf die Erfordernisse einer bestimmten Synthese angepasst und kann dadurch nicht einfach für andere Synthesen genutzt werden, anders als bei herkömmlichen Batchreaktoren. Zudem sind Flussreaktoren nicht billig, insbesondere vollständig vorgefertigte Flussreaktoren von Firmen wie Syrris. Die Reaktionsbedingungen können je nach Aufbau sehr ähnlich zu der von Batchsynthesen gewählt werden, so sind Synthesen bei mehreren hundert bar nicht ungewöhnlich und durch den Einbau von Rückdruckregulatoren möglich.<sup>106</sup>

Selbstverständlich ist das Arbeiten in Flussreaktoren mit einigen Herausforderungen verbunden. Das wahrscheinlich größte Problem ist das mögliche Verstopfen des Reaktors, das durch zu geringe Fließgeschwindigkeiten oder zu hohe Edukt/Produktkonzentrationen zu Stande kommen kann. Desweiteren ist eine Durchmischung der Edukte im gesamten Reaktor nicht immer oder nur sehr schwer zu gewährleisten.<sup>105,106</sup>

Flussreaktoren werden in der Regel in fünf verschiedene Klassen eingeteilt, den kontinuierlichen, den Tröpfchen-basierten und drei verschiedenen Microfluidic-Ansätzen auf die im Folgenden nicht weiter eingegangen wird.<sup>106</sup> In der kontinuierlichen Flussreaktorsynthese werden ein oder mehrere Ströme über ein Verbindungsstück vereint, in einen Reaktor gepumpt, aus diesem gespült und das Produkt kann abschließend aufgearbeitet werden. Bei dieser Methode ist es besonders wichtig darauf zu achten, dass sich die beiden Eduktströme mischen und nicht ein laminarer Fluss entsteht, bei dem beide Ströme einfach nebeneinander durch den Reaktor geführt werden.<sup>106</sup> Ein Ansatz der dieses direkt verhindert, ist die Tröpfchen-basierte Methode. So wird ein nicht mit den Eduktlösungen mischbares Lösungsmittel zu der Synthese hinzugeben. Dadurch entstehen in dem Füllmedium kleine Tröpfchen in den beide Eduktlösungen vereint sind und eine Mischung dieser beiden ist automatisch gewährleistet.<sup>106</sup> Allerdings entsteht hier das Problem, das anschließend an die Synthese beide Phasen wieder voneinander getrennt werden müssen, was insbesondere bei porösen Materialien nicht unbedingt trivial ist.<sup>107</sup>

### **4.2.1.3 Flussreaktoren: Einsatz in der MOF-Synthese**

Der Einsatz mit Flussreaktoren zur Synthese von Verbindungen wurde in der organischen<sup>108</sup> wie auch der anorganischen Chemie<sup>109,110</sup> bereits vielfach durchgeführt. In 2012 wurde jedoch erstmal ein MOF (HKUST-1) in einem Flussreaktor hergestellt.<sup>111</sup> Seitdem folgten weitere zahlreiche Veröffentlichungen

und Weiterentwicklungen.<sup>112-115</sup> Viele Veröffentlichungen gleichen sich dabei sehr stark. Der Aufbau der Flussreaktoren unterscheidet sich nur marginal, in den meisten Fällen wird mit HPLC-Pumpen unter hohen Drücken und Temperaturen gearbeitet.<sup>116,117</sup> Aus diesem Grund wird eine vollständige Übersicht der Arbeiten zu MOF-Synthesen in Flussreaktoren nur in Tabelle 2 gegeben.

Verbindungen mit MIL-88-Struktur konnten im Jahr 2013 über eine Tröpfchen basierte Flussreaktorsynthese erhalten werden.<sup>118</sup> Dies stellt gleichzeitig auch den ersten Flussreaktor dar der mit Spritzenpumpen betrieben wurde. Zusätzlich herausgestellt werden sollte die Veröffentlichung von Taddei et.al. aus dem Jahr 2016, in der zum ersten mal die Darstellung drei verschiedener MOFs mit einem Mikrowellen-gestützten Flussreaktor beschrieben wurde.<sup>119</sup> Außerdem ist die Arbeit von Rubio-Martinez et. al. bemerkenswert, in der nicht nur die Darstellung eines MOFs und die theoretische Raum-Zeit-Ausbeute bestimmt wurde, sondern real ca. 5 kg Al-MIL-53-Fum in einer Stunde hergestellt wurde.<sup>120</sup> Dies ist bis heute ein unerreichter Wert für die Flussreaktorsynthese von MOFs.

Ich möchte außerdem darauf hinweisen, dass die Anzahl an Veröffentlichungen zu diesem Thema in den letzten zwei Jahren stark rückläufig ist. Dies liegt zum einen wahrscheinlich daran, das viele Gruppen mit verschiedenen Flussreaktoren, verschiedenste MOFs herstellen konnten, das einfache „Proof of Concept“ Untersuchungen also nicht mehr relevant sind. Zum anderen konnte auch gezeigt werden, dass MOFs in sehr großem Maßstab von mehreren 100 g bis mehreren kilo pro Stunde hergestellt werden konnten. Es wurde also gezeigt, das MOF in „größeren“ Mengen durch Flussreaktoren hergestellt werden können. Aber ohne dass solche Mengen von der Industrie oder anderen Arbeitsgruppen nachgefragt werden, lohnt sich die Arbeit und der Aufwand nicht mehr.

Kumulativer Teil Flussreaktor: Einleitung

Tab.2: Zusammenfassung aller bisher hergestellten MOFs in Flussreaktoren mit den dazugehörigen Lösungsmitteln, Reaktionszeiten und -temperaturen, der Raum-Zeit-Ausbeute, der echten Ausbeute sowie Besonderheiten.

MOF	Lösungsmittel	T / °C	t / min	p / bar	STY / kg·m <sup>-3</sup> ·d <sup>-1</sup>	Yield / g·h	Besonderheiten
Cu-HKUST-1 <sup>121</sup>	H <sub>2</sub> O / Octanol	---	---	---	---	---	hohle MOF Kapseln
Cu-HKUST-1 <sup>111</sup>	DMF, EtOH	100 - 400	0.0167	250	---	132	Morphologie
Ni-CPO-27 <sup>111</sup>	DMF	100 - 400	0.0167	250	---	---	Morphologie
Cu-HKUST-1 <sup>117</sup>	H <sub>2</sub> O or EtOH	60 - 160	5	100	---	2,04	---
Fe-MIL-88B <sup>118</sup>	H <sub>2</sub> O, DMF	55 - 95	< 0.1	1	---	---	Tröpfchensynthese
Fe-MIL-88B <sup>118</sup>	H <sub>2</sub> O, DMF	95	4	1	---	---	Tröpfchensynthese
Fe-MIL-88B <sup>118</sup>	H <sub>2</sub> O, DMF	95	6	1	---	---	Tröpfchensynthese
[Ce <sub>5</sub> (BDC) <sub>7,5</sub> (DMF) <sub>4</sub> ] <sup>122</sup>	DMF	230	0,5	100	---	---	---
Cu-HKUST-1 <sup>123</sup>	DMF/EtOH/H <sub>2</sub> O	90	1 - 12	1	5,8	0,004	Kern-Schale-Partikel
Zn-MOF-5 <sup>123</sup>	DMF	120	3	1	---	---	Kern-Schale-Partikel
Zr-UiO-66 <sup>123</sup>	DMF/HCl	140	15	1	---	---	Kern-Schale-Partikel
Zn-IRMOF-3 <sup>123</sup>	DMF	120	3	1	---	---	Kern-Schale-Partikel
Al-MIL-53 <sup>124</sup>	H <sub>2</sub> O	250 & 300	20.0	230	1300	125	Aufskalierung 500 g
Cu-HKUST-1 <sup>124</sup>	EtOH	200 & 300	5,10	75	730	2,1	---
Cu-HKUST-1 <sup>116</sup>	EtOH	140	1,2	---	4533	61.2	---
Zr-UiO-66 <sup>116</sup>	DMF	130	10	1	672	1,68	---
NOTT-400 <sup>116</sup>	DMF/THF/H <sub>2</sub> O	85	15	1	741	2,78	---
Zr-UiO-66 <sup>107</sup>	DMF	120	45	1	428	---	---
Al-CAU-13 <sup>107</sup>	DMF/AcOH	130	20	1	3049	---	---

Kumulativer Teil Flussreaktor: Einleitung

Cd-STA-12 <sup>107</sup>	H <sub>2</sub> O/KOH	70	15	1	1269	---	---
Ni-MOF-74 <sup>125</sup>	H <sub>2</sub> O, DMF	70 -150	8	2,5	---	80 - 90	MW-unterstützt
Zn-ZIF-8 <sup>126</sup>	MeOH	90 - 180	---	1	---	---	Solvo-Jet
Zn-ZIF-8 <sup>127</sup>	H <sub>2</sub> O/ NH <sub>4</sub> OH	100	5	1	3874	810	direkte Aktivierung
Fe-MIL-88A <sup>128</sup>	H <sub>2</sub> O,C <sub>8</sub> H <sub>18</sub> O,TBA	40	20	1	---	---	hohle MOF Kapseln
Zr-UiO-66-Fum <sup>129</sup>	H <sub>2</sub> O/ AA	85	22	1	2733	205	Kontinuierlicher Prozess gezeigt
Zr-UiO-66-NH2 <sup>129</sup>	H <sub>2</sub> O / AA	85	20	1	4346	325	Kontinuierlicher Prozess gezeigt
Ga-PMOF <sup>130</sup>	DMF/H <sub>2</sub> O	100	60	1	796	---	Partikelgröße
In-PMOF <sup>130</sup>	DMF/H <sub>2</sub> O	100	60	1	---	---	Partikelgröße
Al-MIL-53-Fum <sup>120</sup>	H <sub>2</sub> O /NaOH	65	1	1	97159	5643	Große Aufskalierung
Zr-UiO-66 <sup>131</sup>	DMF	120	0,4 - 2,2	1	---	---	Nanopartikel
Zr-UiO-66-NH2 <sup>131</sup>	DMF	120	1,1	1	---	---	Nanopartikel
Zr-UiO-66 <sup>119</sup>	DMF, H <sub>2</sub> O, AA	---	7	2	7204	14,4	MW- unterstützt
Al-MIL-53 <sup>119</sup>	DMF	---	4	4	3618	7,1	MW- unterstützt
Cu-HKUST-1 <sup>119</sup>	DMF	---	1	5	64800	79,4	MW- unterstützt
Zn-ZIF-8 <sup>132</sup>	H <sub>2</sub> O/MeOH/NH <sub>3</sub>	25	0,25- 1,5	1	210000	---	Microreaktor
Zn-MOF-5 <sup>133</sup>	DMF bzw. DEF	140	60 - 420	1	504	2,1	---
Zr-UiO-66-NH2 <sup>134</sup>	DMF	???	???	1	0,5 - 1	---	Nanoreaktor
Zr-UiO-66 <sup>135</sup>	DMF, H <sub>2</sub> O	115, 180	---	---	19,6	---	Flussreaktor+Sprühtrocknung
Fe-MIL-100 <sup>135</sup>	DMF	135, 180	---	---	---	---	Flussreaktor+Sprühtrocknung



#### 4.2.1.4 Beschreibungen der während dieser Arbeit entwickelten Flussreaktoren

Während dieser Arbeit konnten zwei Flussreaktoren gebaut werden, die im Folgenden als **Reaktor 1** (Abb. 18) bzw. **Reaktor 2** (Abb. 19) bezeichnet werden. **Reaktor 1** besteht aus einem gewickelten Teflonschlauch und wird in einem Ölbad auf die Reaktionstemperatur aufgeheizt.



Abb.18: **Reaktor 1** bestehend aus Spritzenpumpen, einem Reaktor aus gewickeltem Teflonschlauch und einem Ölbad als Heizquelle.

Der Innendurchmesser des Schlauches kann 1 mm oder auch 4 mm betragen. Allerdings wurde während verschiedener Testversuche festgestellt, dass bei dem Einsatz des Schlauches mit einem Innendurchmesser von 4 mm die Durchmischung der Eduktlösungen auf Grund des laminaren Stroms stark erschwert wird. Dies liegt daran, dass mit Spritzenpumpen gearbeitet wird, wobei die eingesetzten Spritzen nur den Einsatz eines Schlauches mit 1 mm Innendurchmesser erlauben. Werden diese nun über ein Verbindungsstück mit einem größeren Schlauch vereint, laufen die einzelnen Ströme einfach übereinander. Aus diesem Grund wurde in allen weiteren Versuchen nur noch mit dem Schlauch mit 1 mm Innendurchmesser gearbeitet, was insgesamt zu kleineren Reaktorvolumina führt. Dadurch konnten nur Reaktionen mit Reaktionszeiten  $\leq 120$  min durchgeführt werden. Der Einsatz von Spritzenpumpen ermöglicht nur den Einsatz von klaren Lösungen zur Synthese, da sich der Feststoff sonst absetzen würde und keine definierte Konzentration eingespritzt werden könnte. Allerdings sollte erwähnt werden, dass es beheizbare Spritzen gibt, wodurch die Löslichkeit der Edukte gesteigert werden könnte. Der besondere Vorteil, der hier eingesetzten Spritzenpumpen ist die exakte Steuerung der Reaktionszeit. Zunächst wird das Reaktorvolumen ermittelt, in dem eine Methylblaulösung eingespritzt wird. Das geförderte Volumen wird direkt an der Spritze angezeigt, dafür muss nur der

Spritzeninnendurchmesser an der Pumpe eingegeben werden. Mit dem Reaktorvolumen  $V$  und der gewünschten Reaktionszeit  $t$  kann durch folgende Gleichung:

$$a = \frac{V}{t}$$

die Gesamtfließgeschwindigkeit  $a$  bestimmt werden. Wenn die Eduktlösungen mit identischer Konzentration hergestellt werden, kann das Verhältnis der Edukte zueinander direkt über die Fließgeschwindigkeit gesteuert werden. Es ist zu beachten, dass die Pumpen theoretisch sehr, sehr kleine Mengen reproduzierbar befördern können (bis  $0.001 \text{ ml} \cdot \text{min}^{-1}$ ). Diese Angaben gelten allerdings nur für klare Lösungen. Dadurch, dass bei den MOF-Synthesen nach einer bestimmten Zeit Feststoff in den Schläuchen entsteht, muss die Fließgeschwindigkeit so gewählt werden, dass der Strom auch nachdem Entstehen des Feststoffes weiter durch den Schlauch fließt. Aus diesem Grund muss bei sehr langen Reaktionszeiten immer abgewogen werden, ob dieser Reaktoraufbau noch sinnvoll ist oder ob Überdruckventile eingebaut werden sollten. Durch diese ist es möglich unter Druck zu arbeiten, wodurch es möglich wird die Reaktionstemperatur zu erhöhen was wiederum mit einer Verringerung der Reaktionszeit einhergeht.

**Reaktor 2** (Abb. 19) besteht ebenfalls aus einem gewickelten Teflonschlauch, allerdings mit einem größeren Innendurchmesser (zwischen vier und sechs mm). Der Schlauch wird um ein Gestell aus Aluminiumlochblech gewickelt, dort fixiert und in einem Umluftofen platziert. Um das Reaktorvolumen zu bestimmen, wurde aus einem definierten Volumen das Wasser gepumpt um bei Austritt aus dem Schlauch aus der Differenz das Volumen des Reaktors zu ermitteln. So wurde für die Reaktoren mit einem Schlauchinnendurchmesser von 4 bzw. 6 mm ein Volumen von ca. 1850 bzw. 3350 ml ermittelt.



Abb.19: **Reaktor 2** bestehend aus einer Magnetmembranpumpe, einem Reaktor aus gewickeltem Teflonschlauch und einem Umluftofen als Heizquelle.

Auf Grund der erhöhten Fördermengen wird nun eine Magnetmembranpumpe eingesetzt. Dies hat den Vorteil, dass nun auch Eduktsuspensionen gepumpt werden können, allerdings auch einige Nachteile. So kann bei diesen Pumpen nicht direkt eine Fließgeschwindigkeit eingestellt werden, sondern nur eine Pumpfrequenz in Hübem pro Minute und eine Pumprate, die die prozentuale Auslastung eines Hubes angibt. Vom Hersteller werden zwar Tabellen bereitgestellt, denen man zu verschiedenen Einstellungen eine dazugehörige Fließgeschwindigkeit entnehmen kann. Allerdings beziehen sich diese Werte alle auf Wasser, ohne weitere Bestandteile, bei Raumtemperatur und Normaldruck. Dies bedeutet, dass die Werte nicht übernommen werden können und nur durch mehrfaches wiederholen der Versuche und Variation der Pumpeinstellungen die gewünschte Reaktionszeit eingestellt werden kann. Da sich die Fließgeschwindigkeit jeder Lösung je nach eingesetztem Metall, Linker, Additiv und Konzentration unterscheidet, ist es auch nicht möglich die Einstellungen für andere MOF-Synthesen zu übernehmen, sondern die Parameter müssen für jede Reaktion individuell ermittelt werden. Zunächst wurde in dieser Arbeit auf Grund von ökonomischen und ökologischen Gründen nur mit einer Menge von ca. 100 ml Eduktlösung gearbeitet. Anschließend wird das gesamte Edukt/Produkt mit dem eingesetzten Lösungsmittel (in der Regel Wasser) weiter durch den Reaktor gespült. Soll nun aber eine kontinuierliche Produktion durchgeführt werden, was impliziert, dass der Reaktor vollständig mit Edukt bzw. Produkt gefüllt ist, müssen die Parameter erneut optimiert werden. Dies liegt daran, dass nun vielmehr Feststoff im Reaktor vorhanden ist, als wenn nur 100 ml Suspension und der Rest mit Lösungsmittel gefüllt ist. Die gleichen Pumpeinstellungen sind nun zu „schwach“ und führen so entweder zu einem Verstopfen des Reaktors oder aber zu viel längeren Reaktionszeiten.

#### 4.2.2.1 Flow-synthesis of carboxylate and phosphonate based metal–organic frameworks under non-solvothetical reaction conditions

Der folgende Artikel wurde im Jahr 2015 in der Fachzeitschrift *Dalton Transactions, RSC* veröffentlicht. Die Wiedergabe erfolgt mit freundlicher Genehmigung der RSC. Reprinted with permission from S. Waitschat, M. T. Wharmby and N. Stock, *Dalton Trans.*, **2015**, 44, 11235 – 11240, DOI: 10.1039/C5DT01100K . Copyright 2015 the Royal Society of Chemistry.

<http://pubs.rsc.org/en/Content/ArticleLanding/2015/DT/C5DT01100K#!divAbstract>

Die Arbeit beschreibt die Entwicklung und den Einsatz eines Flussreaktors für die Synthese von MOFs. Als Fördermedium wurden Spritzenpumpen verwendet, in denen jeweils eine Metallsalz- bzw. eine Linkerlösung vorgelegt wurden. Diese werden in Teflonschläuche gepumpt, die über ein Verbindungsstück mit einander vereint wurden. Die nun vollständige Eduktlösung/suspension wird weiter in den eigentlichen Reaktor gepumpt. Dieser besteht ebenfalls aus einem Teflonschlauch, der in einem Ölbad erwärmt wird. Die maximale Reaktionstemperatur bei Synthesen in diesem Flussreaktor muss unterhalb des Siedepunktes des Lösungsmittels liegen, da dieses sonst zu sieden beginnt und eine genaue Reaktionszeit nicht mehr einstellbar ist. Wird dies berücksichtigt, kann die Reaktionszeit über das Reaktorvolumen und die gesamte Pumpgeschwindigkeit eingestellt werden.

Um die hohe Flexibilität dieses Flussreaktors zur Synthese von MOFs aufzuzeigen wurden insgesamt drei sehr unterschiedliche MOFs hergestellt und anschließend charakterisiert. Dabei wurde jeweils eine aromatische, eine cyclische Carbonsäure bzw. eine Phosphonsäure als Linkermolekül verwendet. Zunächst wurde UiO-66 [ $Zr_6(O)_4(OH)_4(BDC)_6$ ] erfolgreich synthetisiert. Da es während der Synthese zu einem Verstopfen des Reaktors kam, wurden zwei Möglichkeiten getestet, dieses zu verhindern. Erstens wurde eine zusätzliche Spritze mit Paraffinöl dazu geschaltet. Dadurch entstanden kleine Tropfen, in denen die Reaktion stattfand und ein Verstopfen des Reaktors konnte verhindert werden. Allerdings ergaben sich bei der Aufarbeitung dieser Proben Probleme, da das Paraffinöl nur unvollständig entfernt werden konnte. Aus diesem Grund wurde ein Ultraschallfinger in das Ölbad getaucht um eine Verstopfung im Reaktor durch die Ultraschallbehandlung zu verhindern. Zusätzlich wurde noch CAU-13 [ $Al(OH)(CDC)$ ] ( $CDC^{2-}$  = Cyclohexandicarboxylat) in einem DMF/Essigsäuregemisch und zum aller ersten mal Cd-STA-12 [ $Cd_2(H_2O)L$ ] ( $L^{4-}$  = N,N'-Piperidinbismethylphosphonat) aus wässrigen Lösungen hergestellt. Trotz der tatsächlichen, kleinen hergestellten Mengen (194 mg UiO-66, 615 mg CAU-13) ist die theoretische Raum-Zeit-Ausbeute mit 428 bzw. 3049  $kg \cdot m^{-3} \cdot d^{-1}$  für UiO-66 bzw. CAU-13 vergleichsweise hoch. Um diese Zahl zu erhalten, wird die eigentliche Ausbeute so

hochgerechnet, als ob die Synthese für 24 h in einem 1000 l Reaktor durchgeführt worden wäre. Aus diesem Grund ist die Zahl leider nicht als realistisch anzusehen, da eine Aufskalierung in diesem Maßstab nicht trivial ist. Aber bis heute ist das der Wert, an dem sich die Wissenschaftler in der Literatur messen.

Um zu überprüfen ob die Eigenschaften der erhaltenen Produkte mit denen aus herkömmlichen Batchsynthesen vergleichbar sind, wurden  $N_2$ -Sorptionmessungen durchgeführt um die scheinbaren, spezifischen Oberflächen zu bestimmen. Dabei wurde festgestellt, dass UiO-66 mit  $1263 \text{ m}^2 \cdot \text{g}^{-1}$  verglichen mit Literaturwerten eine höhere spezifische Oberfläche aufweist. Dies ist auf die Anwesenheit struktureller Linkerdefekte zurückzuführen. Durch thermogravimetrische Messungen wurde gezeigt, dass anstatt von 12 Linker pro Cluster nur sieben Linker pro Cluster vorhanden sind. Dies ist auf die vergleichsweise geringe Reaktionstemperatur und -zeit zurückzuführen. Die scheinbare, spezifische Oberfläche von CAU-13 ( $401 \text{ m}^2 \cdot \text{g}^{-1}$ ) ist vergleichbar mit den publizierten Werten und Cd-STA-12 weist eine geringe, aber im Rahmen der STA-12-Familie zu erwartende, spezifische Oberfläche auf ( $134 \text{ m}^2 \cdot \text{g}^{-1}$ ).



Cite this: *Dalton Trans.*, 2015, **44**, 11235

## Flow-synthesis of carboxylate and phosphonate based metal–organic frameworks under non-solvothermal reaction conditions†

Steve Waitschat,<sup>a</sup> Michael T. Wharmby<sup>\*a,b</sup> and Norbert Stock<sup>\*a</sup>

A continuous flow reactor was developed for the synthesis of porous metal–organic frameworks (MOFs) under mild reaction conditions. Commodity hardware was used to assemble the device, giving it a great degree of flexibility in its configuration. The use of paraffin to encapsulate reactions and also ultrasonic treatment were employed to prevent clogging of the reactor. Reactor design was optimised through studies of the synthesis of zirconium carboxylate framework UiO-66. Synthesis of the aluminium carboxylate CAU-13 was also performed, to demonstrate the versatility of the device. Finally the reactor was used to synthesise a new cadmium phosphonate framework, bearing the STA-12 network.

Received 19th March 2015,  
Accepted 14th May 2015

DOI: 10.1039/c5dt01100k

www.rsc.org/dalton

### Introduction

Metal–organic frameworks (MOFs) are composed of organic linkers which join metal ions or clusters, to form networks with potential porosity.<sup>1</sup> The wide diversity of attainable topologies and the possibility of tuning properties through the addition of functional groups to the linkers make permanently porous MOFs candidate materials for applications such as gas storage,<sup>2</sup> gas separation,<sup>3</sup> drug-delivery<sup>4</sup> or heat-transformation.<sup>5</sup> Such applications would however require the preparation of large quantities of material<sup>6</sup> and many MOF syntheses are only reported as small scale batch reactions. The upscaling of such batch reactions can be problematic, requiring much time to be expended on re-optimising the reaction conditions. One method to produce larger quantities would be to use a continuous flow reactor.<sup>7</sup> Flow reactors are frequently utilized within the field of organic synthesis,<sup>8</sup> especially for the synthesis of peptide & saccharide oligomers, but also for continuous production of high-value pharmaceuticals.<sup>9</sup> In inorganic chemistry they have been extensively used for the synthesis of metal chalcogenide and oxide nanoparticles,<sup>10,11</sup> and flow synthesis of MOFs has only been demonstrated for a select range of frameworks (Table S1.1†),<sup>7,12–17</sup> HKUST-1,

which readily forms under a wide range of parameters, has been synthesised in flow under both mild ( $p \sim$  ambient;  $T = 60$  °C)<sup>12</sup> and more severe ( $p = 250$  bar;  $T = 100$ – $400$  °C)<sup>13</sup> reaction conditions. Syntheses in flow of other widely studied frameworks, including CPO-27,<sup>13</sup> MIL-53(Al),<sup>7</sup> MIL-88B(Fe)<sup>17</sup> and UiO-66,<sup>15,16,18</sup> have been reported relatively recently. It should be noted that, with the exception of MIL-88B(Fe) and HKUST-1, all other flow synthesis studies were performed under solvothermal reactions conditions, *i.e.* at temperatures above the boiling point of the reaction solvent and thus under increased pressure. Furthermore, to date there has only been one report of a new MOF synthesised in a flow reactor, Ce<sub>3</sub>(BDC)<sub>7.5</sub>(DMF)<sub>4</sub>.<sup>19</sup>

Herein we describe the development of a flow reactor for the synthesis of MOFs under mild reaction conditions and its application to the synthesis of the known frameworks, UiO-66<sup>20</sup> ([Zr<sub>6</sub>O<sub>4</sub>(OH)<sub>4</sub>(BDC)<sub>6</sub>], BDC = 1,4-benzenedicarboxylate) and CAU-13<sup>21</sup> ([Al(OH)(CDC)-1.5H<sub>2</sub>O, CDC = *trans*-1,4-cyclohexane-dicarboxylate). In addition we were also able to prepare a new metal phosphonate, [Cd<sub>2</sub>(H<sub>2</sub>O)<sub>2</sub>L] $\cdot$ xH<sub>2</sub>O (H<sub>2</sub>L = *N,N'*-piperazinebis(methylenephosphonic acid), which is a new member of the STA-12 family of compounds.<sup>22</sup>

### Experimental

#### X-ray crystallography

Initial characterisation was performed using a Stoe Stadi P diffractometer fitted with an  $\chi$ -stage, in transmission geometry using Cu K $_{\alpha 1}$  radiation and with data collected by an image plate detector. Powder X-ray diffraction (PXRD) patterns for Pawley fitting and Rietveld refinement were measured with a Stoe Stadi P diffractometer in transmission geometry

<sup>a</sup>Institute für Anorganische Chemie, Christian-Albrechts-Universität, Max-Eyth-Straße 2, D 24118 Kiel, Germany.

E-mail: michael.wharmby@diamond.ac.uk, stock@ac.uni-kiel.de

<sup>b</sup>Diamond Light Source Ltd., Diamond House, Harwell Science and Innovation Campus, Didcot, Oxfordshire, OX11 0DE, UK

† Electronic supplementary information (ESI) available: Description of the flow reactor system, in depth description of the synthesis and characterisation of the title compounds, crystallographic data of STA-12(Cd), CCDC reference number 1051836. See DOI: 10.1039/c5dt01100k

using Cu K $\alpha_1$  radiation and with data collected using a Mythen detector.

Data analysis for all three compounds was performed using the TOPAS-Academic V5 suite.<sup>23</sup> The PXRD patterns of all three compounds were indexed and subsequently Pawley fits were performed to confirm the unit cell parameters as obtained from the indexing routine. For STA-12(Cd), the profile parameters, unit cell and space group were used as the starting point for a Rietveld refinement. STA-12(Mn)<sup>22</sup> was used as the initial model for the refinement, with Mn<sup>2+</sup> replaced by Cd<sup>2+</sup>. Restraints were applied to all coordinative bonds around the Cd<sup>2+</sup> ion and also to all bonding distances within the organic ligand. After several cycles of refinement of the framework, all pore water molecules were removed and new positions were determined from Fourier difference maps. Occupancies of these sites were then refined. In the final cycles of refinement, framework and water positions were refined together with isotropic displacement parameters.

### Physical measurements

Infrared spectra were recorded on a Bruker ALPHA-P A220/D-01 FTIR spectrometer fitted with an ATR unit, over the spectral range 4000–400 cm<sup>-1</sup>. Thermogravimetric analysis was carried out using a NETSCH STA 429 CD analyser with a heating rate of 4 K min<sup>-1</sup> and under flowing air (flow rate 75 ml min<sup>-1</sup>) or a TA Instruments TGA Q500 with a heating rate of 5 K min<sup>-1</sup> and under flowing air (60 ml min<sup>-1</sup>). Elemental analysis was performed using a EuroVector EuroEA elemental analyser. NMR spectroscopy was performed using a Bruker DRX 500 spectrometer. Scanning Electron Micrographs were collected using an FEI Quanta FEG 600 electron microscope, whilst N<sub>2</sub> sorption isotherms were recorded at 77 K with a BELSORP-max apparatus (BEL Japan Inc.).

## Results & discussion

### Design of the flow reactor

The flow reactor was designed to be easy to set up whilst having sufficient flexibility to allow a wide variety of reaction parameters to be investigated, including molar ratios and heating method (ESI S3†). The device is built up from two syringe pumps, which contain respectively the metal salt and the organic linker in solution (Fig. 1 and S3.1†). In cases where the amount of precipitate causes the reactor to block, a third pump can be added, to pump a transport medium (*e.g.* paraffin) to encapsulate the reaction as droplets in flow.<sup>24</sup> Additionally an ultrasonic probe can be used to both improve mixing and also to prevent clogging of the reactor.

Solutions are combined by pumping along PTFE tubing to mixers, which in the simplest form of the system are either three way Y-connectors or four way X-connectors. From these mixers, the solution flows into the reactor itself, a coil of PTFE tubing immersed in an oil bath for heating. The length and internal diameter of this tube, in combination with the total pumping rate, determine the reaction time, whilst the molar



Fig. 1 Schematic of the flow reactor in a two pump configuration, showing the hotplate and oil bath in which the coil of PTFE tube forming the reactor is immersed.

ratio of the reaction is determined by varying the pumping rate of each pump individually (ESI S3†).

### Zirconium terephthalate UiO-66

Zr-based UiO-66 ([Zr<sub>6</sub>O<sub>4</sub>(OH)<sub>4</sub>(BDC)<sub>6</sub>]) is one of the most intensively studied MOFs and thus was selected for the initial test of the reactor. Initial reaction conditions were chosen to mimic the reported batch syntheses (ZrCl<sub>4</sub>:H<sub>2</sub>BDC = 1 : 1, 120 °C, 24 h).<sup>25</sup> The first attempts utilised a two syringe pump set-up, with one pump loaded with ZrCl<sub>4</sub> in DMF and a second containing H<sub>2</sub>BDC in DMF (Table 1). However, this design led to precipitates forming in the tube and clogging of the reactor. The design was then modified to add a third syringe containing either DMF or paraffin as a transport medium to prevent clogging.<sup>24</sup> Amounts of solid obtained with the additional DMF were found to be too low, whilst with paraffin, although more solid was recovered, isolation of the UiO-66 product could only be achieved by repeated washing steps with dichloromethane or toluene, which resulted in significantly lower yields. BET surface area values were also found to be significantly lower than literature values (Table 2). The reactor configuration was therefore changed again, back to a two pump set-up, with an ultrasonic probe fitted which improves mixing of the reagents and most importantly prevents clogging of the reactor (Table 1). Following optimisation of the synthesis conditions, highly-crystalline, phase pure UiO-66 could be obtained using a molar ratio of 1 : 3 (Zr<sup>4+</sup> : H<sub>2</sub>BDC) at 120 °C in just 45 min.

### Characterisation

The phase purity of the UiO-66 material was confirmed by Pawley fitting of the laboratory powder X-ray diffraction (PXRD) data. A good fit to the data was obtained, however in addition to the expected UiO-66 reflections, two symmetry forbidden reflections were also observed (Fig. 2). These have been attributed to lower symmetry defect rich regions incorporated within the perfect UiO-66 structure.<sup>26,27</sup>

Given the low reaction temperature, the presence of defects in flow reactor prepared UiO-66 is unsurprising. Evidence for their presence is also found from TGA, EDX and adsorption experiments. TGA data (Fig. S4.3†) found a cluster : linker ratio of 1 : 3.5, significantly lower than the ideal 1 : 6 ratio of perfect UiO-66.<sup>27</sup> Defects have previously been linked to lower thermal stability of UiO-66, however TGA data (Fig. S4.3†) indicate our material is stable to in excess of 400 °C. Samples of the material were activated for adsorption measurements (220 °C,

**Table 1** Summary of the reaction conditions tested for the synthesis of UiO-66, using the two syringe (top), three syringe (middle) and two syringe with ultrasonic probe (bottom) reactor configurations

Reactor volume/ml	ZrCl <sub>4</sub> flowrate/ ml min <sup>-1</sup>	H <sub>2</sub> BDC flowrate/ ml min <sup>-1</sup>	Transport <sup>a</sup> flowrate/ ml min <sup>-1</sup>	Temp./°C	Time/min	Ultra sound	
						Cycle	Amplitude
16.87	0.094	0.281	—	120	45	—	—
16.80	0.070	0.210	—	120	60	—	—
14.45	0.040	0.120	0.161 (Para.)	120	45	—	—
16.83	0.047	0.140	0.187 (DMF)	130	45	—	—
16.87 <sup>b</sup>	0.094	0.281	—	120	45	0.25	100%
16.80	0.070	0.210	—	120	60	0.25	100%

<sup>a</sup> A transport medium in addition to the reaction solvent, used to prevent clogging of the reactor. <sup>b</sup> This reaction produced the most crystalline and phase pure UiO-66, which is further analysed in this work. This is equivalent to a reaction ratio of 1 : 3 (ZrCl<sub>4</sub> : H<sub>2</sub>BDC).

**Table 2** Comparison of the synthesis conditions and specific surface areas (*a*<sub>BET</sub>) of UiO-66 samples prepared in this work with reported syntheses in batch and flow reactions

Flow/ batch	Zr : BDC : HCl	Temp./ °C	Time/ min	<i>a</i> <sub>BET</sub> / m <sup>2</sup> g <sup>-1</sup>	Ref.
Batch	1 : 1 : 0	120	1440	1187	20
Batch	2 : 1 : 2	220	1200	1105 <sup>a</sup>	27
Flow	1 : 1 : 0	130	10 + 2 days	1186	15
Flow	1 : 1 : 1	140	15	1059	16
Flow	1 : 3 : 0	120	45	1263	This work

<sup>a</sup> This is the maximum *a*<sub>BET</sub> expected for the 'ideal' framework.

$p < 10^{-2}$  kPa, 12 h) and these were found by elemental analysis to still contain nitrogen, which may indicate that missing linker sites are partially occupied by DMF molecules.<sup>25</sup> Chloride ions occupying these sites have also been suggested, and EDX measurements indicate the presence of up to two chloride ions per zirconium in our sample.<sup>27</sup> The presence of defects in the structure influences the BET surface area (1263 m<sup>2</sup> g<sup>-1</sup>), which is significantly higher than the surface area of the defect-free compound (1125 m<sup>2</sup> g<sup>-1</sup>) (Fig. 3).<sup>27</sup>

We also provide a comparison of the surface areas of other flow reactor prepared UiO-66 materials (Table 2). The presence of defects is potentially beneficial for applications in catalysis.<sup>28</sup>

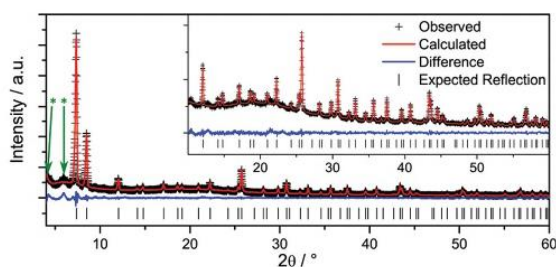


**Fig. 2** Pawley fit of UiO-66 obtained from a flow reactor in a two-syringe configuration. Cell refined to  $a = 20.7367(4)$  Å (space group:  $Fm\bar{3}m$ ;  $R_{wp} = 5.59\%$ ,  $\chi^2 = 3.644$ ), consistent with reported lattice parameters.<sup>20</sup> Green arrows indicate forbidden reflections.

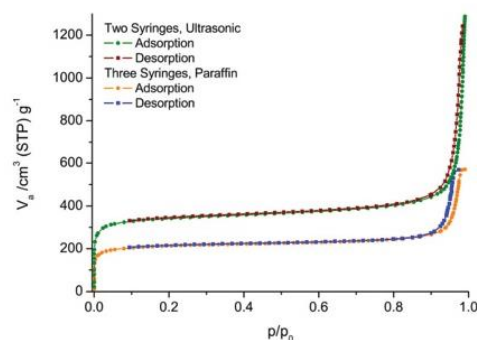


**Fig. 3** N<sub>2</sub> adsorption and desorption isotherms measured at 77 K on samples of UiO-66 produced in a two-pump (ultrasonic probe; green & red traces) and three-pump (paraffin transport; orange & blue traces) flow reactor.

### Aluminium cyclohexanedicarboxylate CAU-13

To demonstrate the versatility of the flow reactor set-up for the preparation of a variety of different MOFs, the synthesis of CAU-13 ([Al(OH)(CDC)]·1.5H<sub>2</sub>O) was investigated.<sup>21</sup> The reported batch synthesis of CAU-13 is performed using a 1 : 1 AlCl<sub>3</sub>·6H<sub>2</sub>O : H<sub>2</sub>CDC molar ratio, and a 4 : 1 (vol.) DMF : water mixture, which is heated at 130 °C for 12 hours. As these conditions would lead to a build-up of pressure, the synthesis was modified to use pure DMF as the solvent (Table S5.1†). A two syringe pump set-up was again chosen. One syringe was loaded with a 0.5 M AlCl<sub>3</sub>·6H<sub>2</sub>O in DMF solution and a second with a 0.5 M H<sub>2</sub>CDC and 4.5 M acetic acid in DMF solution. Acetic acid was added to act as a modulator, to favour the formation of the  $-(Al-O-Al-O)-$  chains. Using a temperature of 130 °C and a reaction time of 20 min, it was possible to prepare microcrystalline CAU-13.

### Characterisation

Phase purity was confirmed by Pawley fitting of the PXRD pattern (Fig. 4), with CAU-13 crystallizing in its open form. TGA and elemental analysis results were consistent with the reported CAU-13 composition and the BET surface area was



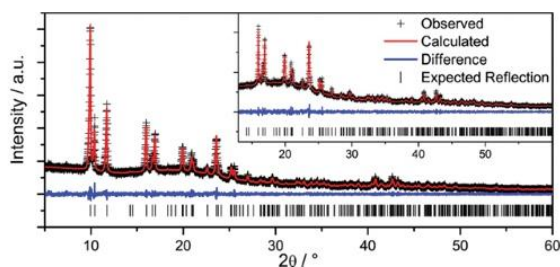


Fig. 4 Pawley fit of CAU-13 obtained from a flow reactor in a two-syringe configuration. Cell refined to  $a = 6.6111(4)$  Å,  $b = 9.4498(6)$  Å,  $c = 9.4652(5)$  Å,  $\alpha = 107.652(4)^\circ$ ,  $\beta = 107.690(6)^\circ$  and  $\gamma = 93.185(5)^\circ$  (space group:  $P\bar{1}$ ;  $R_{wp} = 4.71\%$ ,  $\chi^2 = 1.080$ ), consistent with reported lattice parameters.<sup>21</sup>

slightly higher than reported (measured:  $401 \text{ m}^2 \text{ g}^{-1}$ ; reported:  $378 \text{ m}^2 \text{ g}^{-1}$ ) (Fig. 5 and ESI S5.7†).

To determine whether this slight increase in BET surface area was due to the presence of defect sites, occupied by acetic acid modulator from the synthesis, a sample of CAU-13 was digested in base and analysed by solution state NMR. No additional resonances were observed in the spectra (Fig. 5) and thus no additional acetic acid molecules are thought to be incorporated, in agreement with the elemental analysis.

#### Synthesis scaling

Once the reaction is running, the space time yield for syntheses of UIO-66 and CAU-13 is  $428 \text{ kg m}^{-3} \text{ d}^{-1}$  (yield: 194 mg,

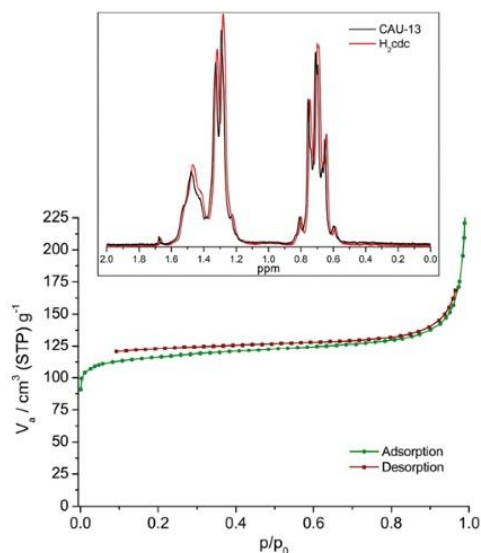


Fig. 5  $\text{N}_2$  adsorption isotherm measured for CAU-13 –  $a_{\text{BET}} = 401 \text{ m}^2 \text{ g}^{-1}$ . Inset shows the solution state  $^1\text{H}$  NMR spectrum of CAU-13; only resonances attributable to  $\text{H}_2\text{cdc}$  were identified and thus no acetic acid was incorporated.

87%) and  $3049 \text{ kg m}^{-3} \text{ d}^{-1}$  (yield: 615 mg, 53%), respectively. Although in this study only product amounts of 200–600 mg per synthesis were obtained, this set-up can be used, in principle, for obtaining larger amounts by running the flow synthesis in a steady state for a longer period of time.

#### Cadmium phosphonate STA-12(Cd)

Beyond optimization and scaled up synthesis, the flow reactor set-up is well suited for the discovery of new compounds. STA-12 is a porous metal phosphonate framework, obtained with a wide range of divalent metal cations (e.g. Mg, Mn, Fe, Co, Ni),<sup>22</sup> however it remains unknown with Cd. STA-12 is usually synthesized with a metal to ligand ratio of 2:1 and using reaction conditions of 160–220 °C for 18–72 h in water. Alternative reaction conditions were needed for the synthesis using the flow reactor, as under these hydrothermal conditions, high pressures would be developed. At lower temperature however, the linker,  $N,N'$ -piperazinebis(methylenephosphonic acid) ( $\text{H}_4\text{L}$ ), is insoluble in water. To overcome this problem,  $\text{H}_4\text{L}$  was neutralized with KOH to form its soluble sodium salt. A 0.1 M aqueous solution of this was loaded into one syringe of a two syringe pump set-up, whilst the other syringe was charged with a 0.1 M metal solution. Reaction conditions, determined from studies of the known compounds STA-12(Co) and STA-12(Ni), were carried out by screening the reaction temperature, time and metal to linker ratios (ESI S6, Table S6.1 and S6.2†).<sup>20,26</sup> The best conditions are a reaction temperature of 70 °C and a M:L ratio of 1:2 for STA-12(Co) and 1:1 for STA-12(Ni). For the synthesis of STA-12(Cd) the parameters of STA-12(Ni) were chosen and an aqueous solution of  $\text{Cd}(\text{AcO})_2 \cdot 2\text{H}_2\text{O}$  was used. The reaction time was varied between 5–20 min by controlling the total pumping rate (Table S6.3†). Crystallinity increases with greater residence time (up to 15 min – Fig. 6).

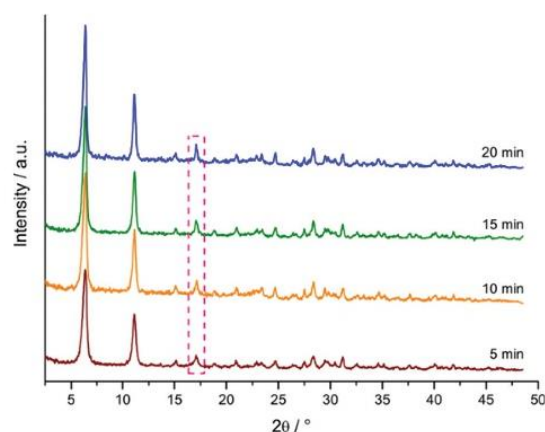


Fig. 6 Samples of STA-12(Cd) prepared in the flow reactor with reaction times increasing from 5 to 20 minutes. Dashed box indicates the (140) reflection, which narrows with increasing reaction time, indicating an increase in particle size.

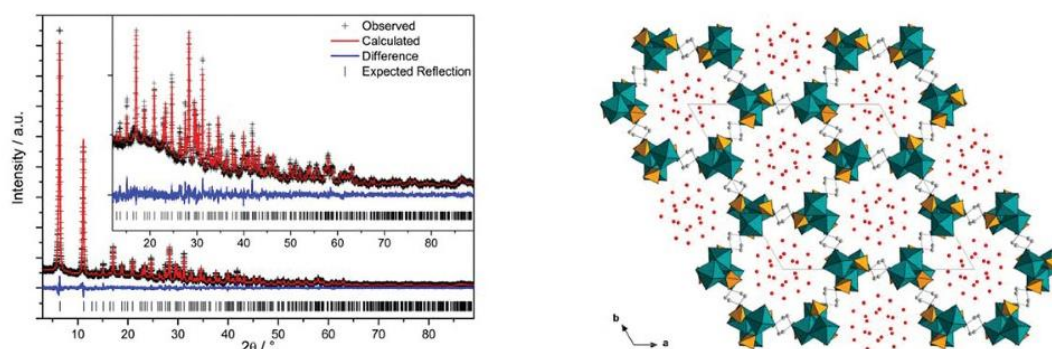


Fig. 7 Rietveld plot of STA-12(Cd) (left) obtained from flow reactor and the structure determined (right). The final cycle of refinement gave  $R_{wp} = 6.43\%$ ,  $R_{Bragg} = 1.56\%$  and  $\chi^2 = 1.141$ .

### Characterisation

The final product was analysed by PXRD and the structure was confirmed by Rietveld refinement (Fig. 7, left); the final refinement gave  $R_{wp} = 6.43\%$ ,  $R_{Bragg} = 1.56\%$  and  $\chi^2 = 1.141$  (Table S6.4†). STA-12(Cd) was refined in a trigonal unit cell in the space group  $R\bar{3}$  and unit cell parameters of  $a = b = 27.4100(8)$  Å  $c = 6.7279(2)$  Å. The structure consists of helical  $Cd^{2+}$  phosphonate chains, parallel to the  $c$ -axis, bridged by piperazinyllinker units, which coordinate the  $Cd^{2+}$  ions through the N atoms (Fig. 7, right). The structure differs slightly from previously reported STA-12 frameworks in that the piperazinyllinker ring plane is in the  $c$ -direction, whereas in other structures it is perpendicular.<sup>22</sup> STA-12(Cd) is porous to  $N_2$  (Fig. S6.8†), with a pore volume of  $0.08$  cm<sup>3</sup> g<sup>-1</sup> and a BET surface area of  $134$  m<sup>2</sup> g<sup>-1</sup>.  $N_2$  uptake is lower than the  $Co^{2+}$  and  $Ni^{2+}$  compounds, which is partly attributed to the greater mass of the framework forming cation.

### Conclusions

We have developed a highly flexible and easy to set up flow reactor system for the preparation of porous MOFs under mild (*i.e.* sub-solvothermal) conditions, using commodity hardware. Using this device we have demonstrated the synthesis of three MOFs: two reported metal carboxylate compounds (UiO-66 and CAU-13) and a new porous metal phosphonate (STA-12 (Cd)), the structure of which was confirmed by Rietveld refinement. All three compounds are porous to  $N_2$  gas, and UiO-66 shows a higher than expected BET surface area, attributed to defects, which may make it interesting for catalytic applications. The flow reactor design should allow simple and cheap scale-up of the syntheses of all three MOFs, making its development significant for industrial applications of this class of compounds.

### Acknowledgements

Dr G. Lampronti (University of Cambridge) is thanked for collection of SEM images; Achim Fölster (CAU, Kiel) is thanked for the preparation of Fig. 1.

### Notes and references

- 1 S. R. Batten, N. R. Champness, X.-M. Chen, J. Garcia-Martinez, S. Kitagawa, L. Öhrström, M. O'Keeffe, M. Paik Suh and J. Reedijk, *Pure Appl. Chem.*, 2013, **85**, 1715–1724.
- 2 U. Eberle, M. Felderhoff and F. Schüth, *Angew. Chem., Int. Ed.*, 2009, **48**, 6608–6630.
- 3 D. Britt, H. Furukawa, B. Wang, T. G. Glover and O. M. Yaghi, *Proc. Natl. Acad. Sci. U. S. A.*, 2009, **106**, 20637–20640.
- 4 P. Horcajada, R. Gref, T. Baati, P. K. Allan, G. Maurin, P. Couvreur, G. Férey, R. E. Morris and C. Serre, *Chem. Rev.*, 2011, **112**, 1232–1268.
- 5 S. K. Henninger, F. Jeremias, H. Kummer and C. Janiak, *Eur. J. Inorg. Chem.*, 2012, **2012**, 2625–2634.
- 6 A. U. Czaja, N. Trukhan and U. Müller, *Chem. Soc. Rev.*, 2009, **38**, 1284–1293.
- 7 P. A. Bayliss, I. A. Ibarra, E. Perez, S. Yang, C. C. Tang, M. Poliakoff and M. Schroder, *Green Chem.*, 2014, **16**, 3796–3802.
- 8 I. R. Baxendale, S. V. Ley, C. D. Smith and G. K. Tranmer, *Chem. Commun.*, 2006, 4835–4837.
- 9 F. Lévesque and P. H. Seeberger, *Angew. Chem., Int. Ed.*, 2012, **51**, 1706–1709.
- 10 J. B. Ediel, R. Fortt, J. C. deMello and A. J. deMello, *Chem. Commun.*, 2002, 1136–1137.
- 11 A. Abou-Hassan, O. Sandre and V. Cabuil, *Angew. Chem., Int. Ed.*, 2010, **49**, 6268–6286.
- 12 R. Ameloot, F. Vermoortele, W. Vanhove, M. B. J. Roeffaers, B. F. Sels and D. E. De Vos, *Nat. Chem.*, 2011, **3**, 382–387.

- 13 M. Gimeno-Fabra, A. S. Munn, L. A. Stevens, T. C. Drage, D. M. Grant, R. J. Kashtiban, J. Sloan, E. Lester and R. I. Walton, *Chem. Commun.*, 2012, **48**, 10642–10644.
- 14 K.-J. Kim, Y. J. Li, P. B. Kreider, C.-H. Chang, N. Wannemacher, P. K. Thallapally and H.-G. Ahn, *Chem. Commun.*, 2013, **49**, 11518–11520.
- 15 M. Rubio-Martinez, M. P. Batten, A. Polyzos, K.-C. Carey, J. I. Mardel, K.-S. Lim and M. R. Hill, *Sci. Rep.*, 2014, **4**.
- 16 M. Faustini, J. Kim, G.-Y. Jeong, J. Y. Kim, H. R. Moon, W.-S. Ahn and D.-P. Kim, *J. Am. Chem. Soc.*, 2013, **135**, 14619–14626.
- 17 L. Paseta, B. Seoane, D. Julve, V. Sebastián, C. Téllez and J. Coronas, *ACS Appl. Mater. Interfaces*, 2013, **5**, 9405–9410.
- 18 P. M. Schoenecker, G. A. Belancik, B. E. Grabicka and K. S. Walton, *AIChE J.*, 2013, **59**, 1255–1262.
- 19 L. D'Arras, C. Sassoie, L. Rozes, C. Sanchez, J. Marrot, S. Marre and C. Aymonier, *New J. Chem.*, 2014, **38**, 1477–1483.
- 20 J. H. Cavka, S. Jakobsen, U. Olsbye, N. Guillou, C. Lamberti, S. Bordiga and K. P. Lillerud, *J. Am. Chem. Soc.*, 2008, **130**, 13850–13851.
- 21 F. Niekel, M. Ackermann, P. Guerrier, A. Rothkirch and N. Stock, *Inorg. Chem.*, 2013, **52**, 8699–8705.
- 22 M. T. Wharmby, G. M. Pearce, J. P. S. Mowat, J. M. Griffin, S. E. Ashbrook, P. A. Wright, L.-H. Schilling, A. Lieb, N. Stock, S. Chavan, S. Bordiga, E. Garcia, G. D. Pirngruber, M. Vreeke and L. Gora, *Microporous Mesoporous Mater.*, 2012, **157**, 3–17.
- 23 A. Coelho, *TOPAS-Academic v5*, Coelho Software, Brisbane, Australia, 2012.
- 24 H. Song, J. D. Tice and R. F. Ismagilov, *Angew. Chem., Int. Ed.*, 2003, **42**, 768–772.
- 25 L. Valenzano, B. Civaleri, S. Chavan, S. Bordiga, M. H. Nilsen, S. Jakobsen, K. P. Lillerud and C. Lamberti, *Chem. Mater.*, 2011, **23**, 1700–1718.
- 26 M. J. Cliffe, W. Wan, X. Zou, P. A. Chater, A. K. Kleppe, M. G. Tucker, H. Wilhelm, N. P. Funnell, F.-X. Coudert and A. L. Goodwin, *Nat. Commun.*, 2014, **5**, 4176.
- 27 G. C. Shearer, S. Chavan, J. Ethiraj, J. G. Vitillo, S. Svelle, U. Olsbye, C. Lamberti, S. Bordiga and K. P. Lillerud, *Chem. Mater.*, 2014, **26**, 4068–4071.
- 28 F. Vermoortele, B. Bueken, G. Le Bars, B. Van de Voorde, M. Vandichel, K. Houthoofd, A. Vimont, M. Daturi, M. Waroquier, V. Van Speybroeck, C. Kirschhock and D. E. De Vos, *J. Am. Chem. Soc.*, 2013, **135**, 11465–11468.

#### 4.2.2.2 Nanoscale Synthesis of Two Porphyrin-Based MOFs with Gallium and Indium

Der folgende Artikel wurde im Jahr 2016 in der Fachzeitschrift *Inorg. Chem.*, ACS veröffentlicht. Die Wiedergabe erfolgt mit freundlicher Genehmigung der ACS. Reprinted with permission from T. Rhauderwiek, S. Waitschat, S. Wuttke, H. Reinsch, T. Bein and N. Stock, *Inorg. Chem.*, **2016**, 55 (11), 5312 – 5319, DOI: 10.1021/acs.inorgchem.6b00221. Copyright 2016 American Chemical Society.

<https://pubs.acs.org/doi/10.1021/acs.inorgchem.6b00221>

Durch den Einsatz von Hochdurchsatzmethoden konnten die zwei, zum Al-PMOF isoretikulären PMOFs mit der Summenformel  $[M_2(OH)_2(H_2TCPP)]$ , mit  $M = Ga$  und  $In$ , entdeckt und die Synthese optimiert werden. Die Struktur der beiden Verbindungen wurde durch Rietveld-Verfeinerung bestimmt und durch Gassorption, IR-Spektroskopie und Thermogravimetrie weiter charakterisiert. Anschließend wurde die Partikelgröße durch den Einsatz verschiedener Synthesemethoden variiert. Neben der Batchsynthese wurde dabei eine Flussreaktorsynthese bzw. eine Synthese unter Ultraschallbehandlung gewählt.

Für die Flussreaktorsynthese wurde der Spritzenreaktor (**Reaktor 1**) gewählt und es konnten beide Verbindungen erhalten werden. Während in den Pulverdiffraktogrammen des In-PMOFs die Bildung kristalliner Verunreinigungen beobachtet wurde, konnte der Ga-PMOF nach einer Stunde Reaktionszeit bei Reaktionstemperaturen von 100 und 120 °C phasenrein erhalten werden. Aus diesem Grund wurde auch nur der Ga-PMOF vollständig charakterisiert. Interessanterweise war es mit der Ultraschall-gestützten Synthese hingegen nicht möglich den Ga-PMOF sondern nur den In-PMOF zu synthetisieren. Alle phasenreinen Produkte sind gegenüber Stickstoff bei - 196 °C porös und weisen eine scheinbare spezifische Oberfläche von ca. 1200  $m^2 \cdot g^{-1}$  für die Produkte aus der Batch- und der Ultraschall-gestützten Synthese und ca. 1400  $m^2 \cdot g^{-1}$  für den Ga-PMOF aus der Flussreaktorsynthese auf. Letzteres Produkt zeigt die geringste Abweichung von dem theoretischen Wert von 1500  $m^2 \cdot g^{-1}$  für die spezifische Oberfläche.

Die Partikelgröße bzw. der hydrodynamische Durchmesser der Proben wurde zunächst durch dynamische Lichtstreuung bestimmt. Der Ga-PMOF, hergestellt mit dem Flussreaktor bei 120 °C, weist dabei die kleinste Partikelgröße mit  $65 \pm 18$  nm auf. Im Vergleich dazu ist der hydrodynamische Durchmesser des Ga-PMOFs hergestellt im Batchreaktor mit  $92 \pm 25$  nm ca. 50 % größer. Ähnliche Werte für die Partikelgrößen wurden durch Anwendung der Scherrer-Gleichung<sup>136</sup> durch Auswertung der Pulverdiffraktogramme erhalten (38 bzw. 64 nm). Der Polydispersitätsindex (PI) beider Proben

weist mit  $<0.2$  auf eine monodisperse Verteilung hin. Dahingegen ist der PI des Ga-PMOF synthetisiert im Flussreaktor bei einer Reaktionstemperatur von  $120\text{ °C}$  eher polydispers (PI = 0.3) und auch der hydrodynamische Durchmesser ist mit  $156 \pm 28\text{ nm}$  ca. 2.5-mal größer. Dies kann möglicherweise damit erklärt werden, dass auf Grund der höheren Reaktionstemperatur die Kristallbildung schneller beginnt, wodurch mehr Zeit zum Kristallwachstum vorhanden ist.

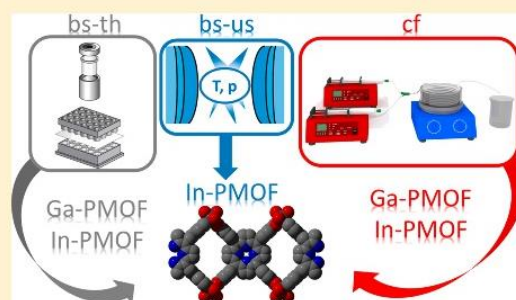
Zusätzlich wurden SEM-Aufnahmen von allen Proben aufgenommen, die die anderen Ergebnisse bestätigen. Von dem In-PMOF, synthetisiert im Batchreaktor, wurden zudem TEM-Aufnahmen gemacht, in denen sogar die Poren abgebildet werden konnten.

## Nanoscale Synthesis of Two Porphyrin-Based MOFs with Gallium and Indium

Timo Rhauderwiek,<sup>†</sup> Steve Waitschat,<sup>†</sup> Stefan Wuttke,<sup>‡</sup> Helge Reinsch,<sup>§</sup> Thomas Bein,<sup>‡</sup> and Norbert Stock<sup>\*,†</sup><sup>†</sup>Institute of Inorganic Chemistry, Christian-Albrechts-Universität, Max-Eyth Straße 2, D-24118 Kiel, Germany<sup>‡</sup>Department of Chemistry and Center for NanoScience (CeNS), University of Munich (LMU), Butenandtstraße 5-13, D-81377 Munich, Germany<sup>§</sup>Department of Chemistry, University of Oslo, N-0371 Oslo, Norway

## Supporting Information

**ABSTRACT:** Two porphyrin-based metal–organic frameworks (MOFs) containing gallium or indium,  $[\text{Ga}_2(\text{OH})_2(\text{H}_6\text{TCPP})] \cdot 3\text{DMF} \cdot 3\text{H}_2\text{O}$  (Ga-PMOF) and  $[\text{In}_2(\text{OH})_2(\text{H}_6\text{TCPP})] \cdot 3\text{DMF} \cdot 4\text{H}_2\text{O}$  (In-PMOF) ( $\text{H}_6\text{TCPP}$  = 4-tetracarboxyphenylporphyrin), were discovered using high-throughput methods. The structure was refined by the Rietveld-method starting from the structure model of Al-PMOF,  $[\text{Al}_2(\text{OH})_2(\text{H}_6\text{TCPP})]$ . The new PMOFs exhibit BET surface areas between 1150 and 1400  $\text{m}^2 \text{g}^{-1}$  and are also porous toward  $\text{CO}_2$  (Ga-PMOF, 15.2 wt %; In-PMOF, 12.9 wt %). They are thermally stable in air up to 330 °C, but show limited chemical stabilities toward acids and bases. In order to achieve size control, different synthesis routes were investigated, i.e., batch synthesis at different temperatures (yield: In-PMOF-bs-th 96%, Ga-PMOF-bs-th 87%), ultrasound-assisted synthesis (yield: In-PMOF-bs-us 85%), and continuous-flow synthesis (yield: Ga-PMOF-cf 71%). By using these different methods we could control the nucleation rate and the crystal size. The crystal sizes were found to vary about 60 to 160 nm and 70 to 130 nm for Ga- and In-PMOF, respectively, which was proven by dynamic light scattering (DLS), powder X-ray diffraction (PXRD), scanning electron microscopy (SEM), and transmission electron microscopy (TEM) measurements.



## INTRODUCTION

In the field of crystalline porous materials, metal–organic frameworks (MOFs) exhibit tunable pore sizes and surface chemistry, which in turn lead to a wide range of chemical and physical properties.<sup>1–3</sup> Hence MOFs are investigated in applications such as gas storage and separation, catalysis, and drug delivery.<sup>2,4–7</sup> An important challenge for the use of MOFs in drug delivery is to construct highly porous, nanoscaled, biocompatible materials consisting of nontoxic metals and linkers. Porphyrin-based linker molecules in combination with biocompatible metals like Ga and In, which have been shown to be toxic only in very high concentrations, could lead to MOFs suitable for applications in drug delivery.<sup>4,8–17</sup>

4-Tetracarboxyphenylporphyrin ( $\text{H}_6\text{TCPP}$ ) is the most intensively investigated linker for the synthesis of porphyrin-based MOFs, and nearly 30 compounds containing this linker are known.<sup>12</sup> In most cases, these MOFs are based on di- and tetravalent metal ions like  $\text{Zn}^{2+}$  and  $\text{Zr}^{4+}$ .<sup>12</sup> For zirconium the compounds PCN-221,<sup>18</sup> MOF-545,<sup>19</sup> MOF-525,<sup>19</sup> PCN-223,<sup>20</sup> PCN-224,<sup>21</sup> and PCN-225<sup>22</sup> have been reported. These porphyrin-based Zr-MOFs exhibit high specific surface areas and have been tested, for example, as heterogeneous catalysts

for the oxidation of cyclohexane (PCN-221),<sup>18</sup> or for the coupling reaction of  $\text{CO}_2$ /propylene oxide (PCN-224).<sup>21</sup> To date only a few compounds with trivalent metal ions such as iron (MIL-141,  $[\text{NaFe}(\text{Ni-TCCP})]^{23}$  and  $[\text{Fe}_2(\text{Fe-TCCP}) \cdot (\text{C}_4\text{H}_4\text{N}_2)(\text{OH}_2)]$  ( $\text{C}_4\text{H}_4\text{N}_2$  = pyrazine)<sup>24</sup>) and aluminum (Al-PMOF,  $[\text{Al}_2(\text{H}_6\text{TCPP})(\text{OH})_2] \cdot 3\text{DMF} \cdot 2\text{H}_2\text{O}$ )<sup>25</sup> have been described with the  $\text{H}_6\text{TCPP}$  linker.<sup>26</sup> Al-PMOF was investigated in the photocatalytic methyl viologen assisted  $\text{H}_2$ -generation on colloidal platinum.<sup>25</sup> With the homologues gallium and indium only In-MOFs containing porphyrin-based linkers have been reported (MMPF-7,  $[\text{In}_{1.29}\text{O}_{0.57}(\text{TCCP})]$ ,<sup>27</sup> MMPF-8  $[\text{In}(\text{In-TCBPP})] \cdot 12\text{DMF}$  ( $\text{H}_6\text{TCBPP}$  = tetrakis-4-carboxybiphenylporphyrin)<sup>27</sup> and UNLPF-10  $[\text{In}_3(\text{TBCPPP})]$  ( $\text{H}_{10}\text{TBCPPP}$  = tetrakis-3,5-bis[4-carboxyphenyl]phenyl porphyrin)<sup>28</sup>).

For the possible application of porphyrin-based MOFs, for example in catalysis or drug delivery, the control of particle size can be very important.<sup>3,10,29</sup> Various methods have been reported for the synthesis of nanoscale MOFs, such as batch

Received: February 3, 2016

Published: May 20, 2016

synthesis with thermal heating (bs-th),<sup>30–33</sup> ultrasound-assisted batch synthesis (bs-us),<sup>34</sup> and continuous-flow (cf) synthesis.<sup>35–37</sup> The latter has also been successfully employed for the synthesis of CdS nanoparticles.<sup>38</sup> In addition, this synthesis approach has been used for the continuous production of MOFs such as UiO-66,<sup>36</sup> Al-MIL-53,<sup>37</sup> or CAU-13<sup>35</sup> with high space–time yields of several hundred kilograms per cubic meter and day. Although synthetic strategies providing control of the particle size have been carried out for tetrapyrrolylporphyrin-based MOFs like Zn- and Cu-TpP,<sup>39–41</sup> such studies have not been reported so far for tetracarboxyphenylporphyrin-based MOFs.

Herein, we present the synthesis and detailed characterization of two porphyrin-based MOFs containing Ga and In (Ga-PMOF and In-PMOF). Three synthesis methods, batch synthesis with thermal heating (bs-th), ultrasound-assisted batch synthesis (bs-us), and continuous-flow (cf) synthesis, were employed to study their influence on the purity and particle size of the MOFs.

## EXPERIMENTAL SECTION

**Materials.** Ga(NO<sub>3</sub>)<sub>3</sub>·H<sub>2</sub>O (99.99%, ABCR), In(NO<sub>3</sub>)<sub>3</sub>·H<sub>2</sub>O (99.99%, ABCR), DMF (99%, Grüssing), acetone (99%, Walther), and EtOH (99%, Walther) were used without further purification. The metal salts were dissolved in distilled H<sub>2</sub>O to achieve different concentrations. The linker 4,4',4'',4'''-(5,10,15,20-porphyrin-tetrayl)-tetrabenzoic acid (H<sub>4</sub>TCPP) was synthesized according to literature procedures<sup>42–44</sup> starting with 4-formylbenzoic acid (98%, ABCR) and pyrrole (98%, ABCR) in propionic acid (99%, Grüssing). Details are given in the Supporting Information.

**Characterization.** For the optimization of synthesis conditions, our high-throughput (HT) methodology employing a 24-high-throughput reactor system was used.<sup>33,35,46</sup> The high-throughput PXRD measurements were carried out with a STOE HT diffractometer equipped with an *xy*-stage and an IPDS system (Cu K $\alpha$  radiation) in transmission geometry. High resolution PXRD patterns were measured on a STOE Stadi-P powder diffractometer equipped with a Mythen detector (Cu K $\alpha$  radiation). For the ultrasound-assisted syntheses the ultrasonication bath (Sonorex RK 100, 40 kHz, 80/160 W, Bandelin) and glass vials from Duran ( $V_{\max}$  = 7.0 mL, Pyrex) were used. IR spectra were recorded using a Bruker ALPHA-FT-IR A220/D-01 spectrometer equipped with an ATR unit. NMR data were measured on a Bruker DRX 500 spectrometer. For the quantitative analysis of occluded guest molecules, <sup>1</sup>H NMR spectroscopy was employed. The samples were dissolved in a mixture of 10% deuteriochloric acid (DCl) in D<sub>2</sub>O and deuterated dimethyl sulfoxide (*d*<sub>6</sub>-DMSO) (molar ratio = 1:7). Sorption experiments were performed with a BEL Japan Inc. BELSORP-max. Before sorption measurements all samples were activated at 140 °C under vacuum (10<sup>-2</sup> kPa) for 16 h. Thermogravimetric measurements were performed on a NETZSCH STA 409 CD analyzer under a flow of air (75 mL min<sup>-1</sup>) with a heating rate of 4 °C min<sup>-1</sup> over a temperature range between 25 and 700 °C in Al<sub>2</sub>O<sub>3</sub> crucibles. The data were corrected for buoyancy and current effects. Dynamic light scattering measurements were performed on a Delsa Nano C particle analyzer from Beckman Coulter with ethanol as solvent. Prior to the measurements, the samples which were stored in ethanol were redispersed. In the case of the reaction products Ga- and In-PMOF-bs-th as well as Ga-PMOF-cf the redispersion was accomplished by ultrasonication for 30 min. In-PMOF-bs-us formed a stable dispersion after washing with ethanol. For the measurement, 20  $\mu$ L of the respective dispersion were added to a cuvette containing 4 mL of ethanol and measured subsequently. The particle sizes of all obtained samples were also determined from PXRD data using the program suite TOPAS academics V4.1. A LaB<sub>6</sub> standard was used to determine the instrumental line broadening, and the particle size was calculated employing the Scherrer equation.<sup>47,48</sup> For SEM imaging a Zeiss

NVision40 microscope was used. Secondary electron images were acquired using the inlense detector and a low acceleration voltage of 2.5 keV for all samples except for sample Ga-PMOF-cf (120 °C), which was imaged at an acceleration voltage of 5 keV. TEM studies were carried out with the In-PMOF-bs-us nanoparticles using a Titan-Themis 60-300 TEM (FEI Company) operating at 300 kV with a high-angle annular dark field detector. A droplet of the diluted nanoparticle dispersion in absolute ethanol was dried on a carbon-coated copper grid.

**Preparation.** Three different synthesis methods, i.e., batch synthesis with thermal heating in HT Teflon inserts = bs-th, ultrasound-assisted batch synthesis = bs-us, and continuous-flow synthesis = cf, for the formation of Ga- and In-PMOF were investigated (Figure 1).

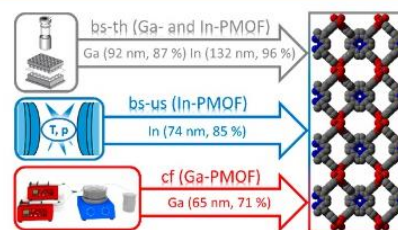


**Figure 1.** Schematic presentation of the different synthesis methods used in this study. The setups for the batch synthesis with thermal heating (bs-th), the ultrasound-assisted batch synthesis (bs-us), and the continuous-flow (cf) synthesis are shown in gray, blue, and red, respectively. Values in parentheses show the particle size measured by DLS and the yield of the individual reactions.

The synthesis of Ga- and In-PMOF-bs-th was studied using high-throughput methods ( $V_{\max}$  = 2.0 mL per Teflon insert, details see Figure S2). Different reaction temperatures between 80 and 160 °C in 20 °C steps, different molar ratios of reactants, additives like benzoic, formic, and acetic acid, and different volume ratios of H<sub>2</sub>O:DMF between 1:6 and 1:38 were tested. The results of the HT experiments leading to highly crystalline Ga- and In-PMOF-bs-th are shown in Figure S2, and the optimized synthesis conditions are described in the following paragraphs.

Optimized batch reactor synthesis of Ga-PMOF-bs-th: H<sub>4</sub>TCPP (15 mg,  $1.9 \times 10^{-2}$  mmol), DMF (724  $\mu$ L), and 1 M aqueous Ga(NO<sub>3</sub>)<sub>3</sub>·H<sub>2</sub>O solution (37.8  $\mu$ L,  $3.8 \times 10^{-2}$  mmol) were added to the 2.0 mL reactor. The reactor was heated for 48 h at 120 °C and cooled down to rt in 6 h. The resulting product was washed two times each with DMF and acetone. A yield of 220 mg, 87% (based on H<sub>4</sub>TCPP) was obtained for Ga-PMOF-bs-th, [Ga<sub>2</sub>(H<sub>2</sub>TCPP)(OH)<sub>2</sub>] $\cdot$ 3DMF $\cdot$ 3H<sub>2</sub>O.

Optimized batch reactor synthesis of In-PMOF-bs-th: H<sub>4</sub>TCPP (15 mg,  $1.9 \times 10^{-2}$  mmol), DMF (724  $\mu$ L), and 0.5 M aqueous In(NO<sub>3</sub>)<sub>3</sub>·H<sub>2</sub>O solution (75.6  $\mu$ L,  $3.8 \times 10^{-2}$  mmol) were added to the 2.0 mL reactor. The reactor was heated for 48 h at 120 °C and cooled down to rt in 6 h. The resulting product was washed two times each with DMF and acetone. A yield of 292 mg, 96% (based on H<sub>4</sub>TCPP) was obtained for In-PMOF-bs-th [In<sub>2</sub>(H<sub>2</sub>TCPP)(OH)<sub>2</sub>] $\cdot$ 3DMF $\cdot$ 4H<sub>2</sub>O. Both MOF syntheses can be scaled up in 30 mL Teflon reactors by using the 12-fold amount of all reactants, the same molar ratio of metal to linker (2:1), the same temperature–time program, and the same washing procedures.

Elemental analysis for Ga-PMOF-bs-th and In-PMOF-bs-th:



calcd (%) C 55.5, H 4.5, N 7.9; found (%) C 55.1, H 4.4, N 8.0



calcd (%) C 51.0, H 4.3, N 7.3; found (%) C 51.2, H 4.3, N 7.8

Ultrasound-assisted synthesis could only be achieved for the In-PMOF. In-PMOF-bs-us was synthesized in glass-vials ( $V_{\max} = 7.0$  mL) by mixing  $H_6$ TCPP (51 mg,  $6.5 \times 10^{-2}$  mmol), DMF (4 mL), and 0.5 M aqueous  $In(NO_3)_3 \cdot H_2O$  solution (257.0  $\mu$ L,  $12.9 \times 10^{-2}$  mmol). The glass vial was ultrasonicated in a water bath for 7 h. The final temperature of the water bath was 50 °C. The resulting product was centrifuged for 30 min at 20000 rpm and washed three times with ethanol by subsequent centrifugation, each time for 30 min at 20000 rpm. A yield of 68 mg, 85% (based on  $H_6$ TCPP) was obtained for In-PMOF-bs-us,  $[In_2(H_6TCPP)(OH)_2] \cdot 3DMF \cdot 4H_2O$ .

Continuous-flow synthesis of Ga-PMOF-cf and In-PMOF-cf was carried out using a two-syringe-pump flow reactor setup as previously described.<sup>35</sup> The MOFs were obtained using concentrations of 0.1 mol  $L^{-1}$  of  $Ga(NO_3)_3$  and  $H_6$ TCPP in a mixture of 94 vol % DMF and 6 vol % water. For the synthesis of In-PMOF-cf, corresponding solutions with a concentration of 0.05 mol  $L^{-1}$  were used. The solutions were injected into a flow reactor ( $V = 15$  mL) with flow rates of 0.167 mL  $min^{-1}$  for metal and 0.084 mL  $min^{-1}$  for the linker solution respectively, giving a total reaction time of 60 min. The different flow rates for metal and linker solution led to a molar metal-to-linker ratio of 2 to 1. During the reaction the flow reactor was kept at a temperature of 100 °C. In a second experiment a flow rate of 0.125 mL  $min^{-1}$  for both starting materials was used (molar ratio metal-to-linker 1:1) and the reaction temperature was raised to 120 °C. The products were collected and isolated by centrifugation for 15 min at 15000 rpm and washed three times with ethanol by subsequent centrifugation, each time for 15 min at 15000 rpm. The formation of Ga-PMOF-cf at 100 °C yielded 397 mg, 71% (based on  $H_6$ TCPP) with a space-time yield of 648 kg  $m^{-3} d^{-1}$ . The corresponding synthesis of In-PMOF-cf at 100 °C was also carried out, but the reaction product contains X-ray amorphous impurities. Hence a detailed characterization of this product was not carried out. To confirm that In-PMOF-cf was obtained a Pawley fit was performed (Figure S5).

## RESULTS AND DISCUSSION

**Synthesis.** Three different synthesis settings (batch synthesis with thermal heating = bs-th, ultrasound-assisted batch synthesis = bs-us, continuous-flow synthesis = cf) were used to synthesize the two new porphyrin-based MOFs Ga- and In-PMOF. The two MOFs were investigated by high-throughput methods, and the resulting high-throughput experiment that led to the highly crystalline Ga- and In-PMOF-bs-th is shown in Figure S2. The optimized synthesis time and temperature was 48 h at 120 °C to achieve highly crystalline products with different particle sizes (92 (25) for Ga-PMOF and 132 (25) nm for In-PMOF). Using ultrasound-assisted and continuous-flow synthesis, it was possible to vary the resulting particle size of both MOFs in the range of 100 nm. In case of the ultrasound-assisted batch synthesis (bs-us) only In-PMOF-bs-us could be obtained. The synthesis was established in an ultrasonication bath within 7 h, which led to an increase of the reaction temperature to 50 °C. This synthesis led to particles sized at the order of 60 nm. Continuous-flow synthesis (cf) led to both MOFs, but In-PMOF-cf was only obtained with X-ray amorphous impurities. For the synthesis of Ga-PMOF-cf two different temperatures, 120 and 100 °C, were employed, which led to products with different particle sizes of about 65 nm (120 °C) and 156 nm (100 °C), respectively. Details regarding the particle size are given in the corresponding section below.

**Crystal Structure.** All compounds were obtained as microcrystalline powders. Initial powder X-ray diffraction (PXRD) measurements confirmed that Ga- and In-PMOF are isostructural to Al-PMOF.<sup>25</sup> For the structure refinement high resolution PXRD patterns of the batch synthesis products were used. Pawley fits of the high resolution data of Ga- and In-PMOF-bs-th with the program TOPAS academic V4.1<sup>48</sup> are in

good agreement with the cell parameters of Al-PMOF, corresponding to the different metal ion.<sup>25</sup> Using the structure of Al-PMOF<sup>25</sup> with the respective metal ion gallium or indium as starting model, their crystal structures were successfully refined by Rietveld methods with TOPAS academic V4.1.<sup>48</sup> The crystallographic data and the results of the Rietveld refinement are shown in Table 1 and Figures 2 and 3. Pawley

**Table 1.** Crystallographic Data of Al-, Ga-, and In-PMOF

	Al-PMOF <sup>25</sup>	Ga-PMOF-bs-th	In-PMOF-bs-th
SG	<i>Cmmm</i>	<i>Cmmm</i>	<i>Cmmm</i>
<i>a</i> [Å]	31.978(3)	32.950(4)	33.432(2)
<i>b</i> [Å]	6.5812(4)	6.700(2)	7.152(1)
<i>c</i> [Å]	16.862(2)	16.556(2)	16.718(1)
GOF		2.4	1.6
$R_{wp}$	4.0	6.5	5.7
$R_{Bragg}$		0.75	0.76

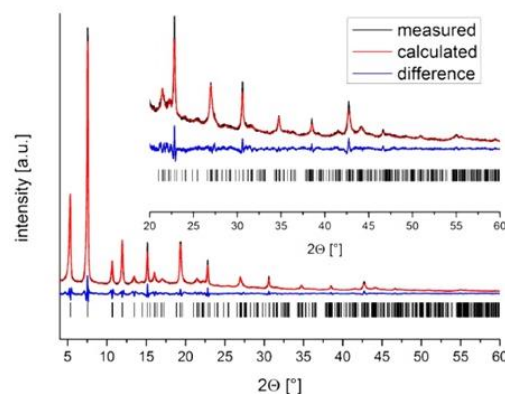


**Figure 2.** Result of the Rietveld refinement of Ga-PMOF-bs-th. Measured data are shown as a black line and calculated data as a red line, and the blue line gives the difference plot. Predicted peak positions are marked as vertical bars.

fits were also carried out for the products In-PMOF-bs-us, Ga-PMOF-cf, and In-PMOF-cf. The results of the Pawley fits and

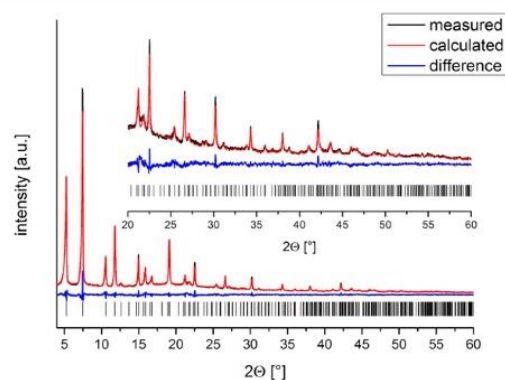


**Figure 3.** Result of the Rietveld-refinement of In-PMOF-bs-th. Measured data are shown as a black line, calculated data as a red line and the blue line gives the difference plot. Predicted peak positions are marked as vertical bars.



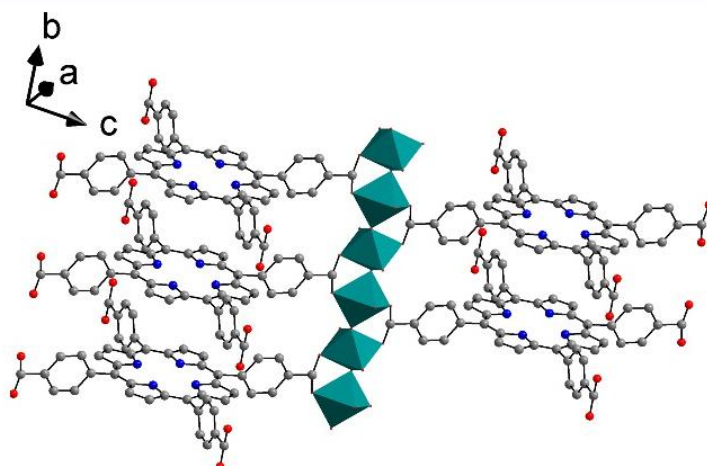


**Figure 4.** Chains of trans corner-sharing  $\text{GaO}_6$  and  $\text{InO}_6$  polyhedra in Ga- and In-PMOF with a few added linker molecules.

the refined cell parameters are shown in Figures S3, S4, and S5 and Table S1.<sup>48</sup>

The title compounds of framework composition  $[\text{Ga}_2(\text{H}_2\text{TCCP})(\text{OH})_2]$  and  $[\text{In}_2(\text{H}_2\text{TCCP})(\text{OH})_2]$  crystallize in the space group  $Cmmm$ . They are isostructural to the corresponding Al-PMOF<sup>25</sup> which contains the same linker, and therefore the structure is only briefly described.  $\text{GaO}_6$  and  $\text{InO}_6$  polyhedra are connected by  $\mu\text{-OH}$  groups and form chains of trans corner-sharing polyhedra (Figure 4). The other coordinating O atoms are from deprotonated carboxylate groups of the linker molecules. The chains are connected by  $\text{H}_2\text{TCCP}^{4-}$  molecules to form a three-dimensional framework. Two types of pores are formed each along  $[010]$  and  $[001]$ , with diameters of 5.0/11.8 Å and 3.4/11.8 Å respectively for Ga-PMOF (Figure 5) and 5.0/11.8 Å and 4.0/12.6 Å respectively for In-PMOF. The diameters were determined using DIAMOND V.3 taking the van der Waals radii of guest molecules into account.<sup>49,50</sup>

**Sorption Properties.** Sorption experiments using  $\text{N}_2$  and  $\text{CO}_2$  as adsorptives were performed. All samples were activated at 140 °C under vacuum ( $10^{-2}$  kPa) for 16 h.  $\text{N}_2$  sorption measurements at 77 K were measured for all the different reaction products obtained using the three synthesis methods (Table 2, Figure 6, and Figures S7 and S8). The micropore volumes  $V_m$  were determined by using the amount of adsorbed  $\text{N}_2$  at the relative pressure  $p/p_0 = 0.5$ .  $\text{CO}_2$  sorption measurements at 298 K were only performed for the samples obtained from the scale-up reaction using the batch synthesis, i.e., Ga- and In-PMOF-bs-th (Table 2, Figure S6). To verify the stability of all the investigated products, PXRD measurements were carried out after every sorption experiment. The data are shown in Figure S9 and confirm the stability of the compounds.

Depending on the synthesis method employed, the specific surface areas are in the range of 1150 to 1400  $\text{m}^2 \text{g}^{-1}$  and 1200 to 1250  $\text{m}^2 \text{g}^{-1}$  for the various Ga- and In-PMOFs, respectively. These values compare well with the reported one for Al-PMOF (1400  $\text{m}^2 \text{g}^{-1}$ ). Taking into account the different atomic masses of Al, Ga, and In, very similar specific surface areas in  $\text{m}^2 \text{mmol}^{-1}$  are found. The theoretical specific surface areas of Al-, Ga-, and In-PMOF were simulated using the program suite Materials Studio (v. 5.0)<sup>51</sup> and employing the strategy reported by Düren et al.<sup>52</sup> With this strategy the surface area is calculated

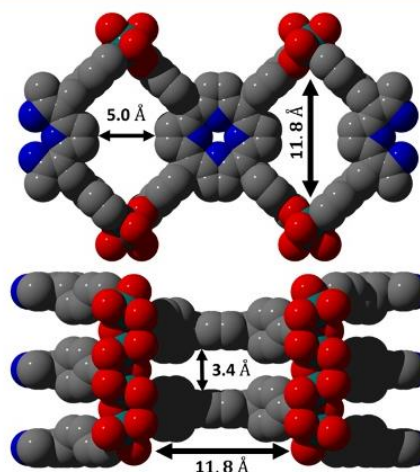


**Figure 5.** Space filling model of the crystal structure of Ga-PMOF; view along  $[010]$  (top) and along  $[001]$  (bottom). The pores along  $[010]$  have diameters of 5.0 and 11.8 Å, and along  $[001]$  pores with diameters of 3.4 and 11.8 Å are observed. Carbon is shown in gray, oxygen in red, nitrogen in blue, and gallium in turquoise. In the crystal structure of In-PMOF the pores along  $[010]$  have the same size as Ga-PMOF, and along  $[001]$  pores with diameters of 4.0 and 12.6 Å are observed.

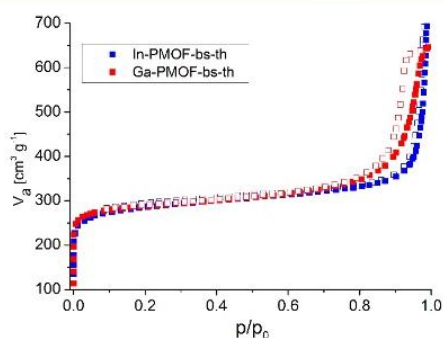
from the center of a sphere with a diameter of 3.60 Å that rolls across the pore surface. The observed surface area values are slightly smaller by about 100–200  $\text{m}^2 \text{g}^{-1}$  compared to the calculated ones. The  $\text{CO}_2$  sorption measurements, which were only performed for the scaled-up products of Ga- and In-PMOF-bs-th, show an uptake of 15.2 and 12.9 wt % at 1 bar and 298.15 K for Ga- and In-PMOF-bs-th, respectively.

**Thermal and Chemical Stability.** To remove nonreacted linker molecules as well as solvent molecules and to investigate the chemical stability of the PMOFs, the samples were treated in different solvents ( $\text{H}_2\text{O}$ , EtOH, MeOH, acetone) at rt for 24 h under stirring followed by thermal activation between 120 and 180 °C for 12 h under vacuum ( $10^{-2}$  kPa). The results of these experiments (Figure 7) show that the crystallinity of the Ga- and In-PMOF correlates strongly with the presence of

**Table 2.** Results of the Sorption Experiments ( $N_2$  at 77 K and  $CO_2$  at 298.15 K) of the Ga- and In-PMOFs Obtained Using Different Synthesis Methods: Ga-PMOF-bs-th (scaled up), In-PMOF-bs-th (scaled up), In-PMOF-bs-us, and Ga-PMOF-cf<sup>a</sup>

	Al-PMOF <sup>25</sup>	Ga-PMOF-bs-th	In-PMOF-bs-th	In-PMOF-bs-us	Ga-PMOF-cf
$N_2$ (as-syn.) [m <sup>2</sup> g <sup>-1</sup> ] [m <sup>2</sup> mmol <sup>-1</sup> ]	1400 1229	1150 1108	1200 1264	1250 1318	1400 1350
$N_2$ (access. surf.) [m <sup>2</sup> g <sup>-1</sup> ] <sup>b</sup>	1600	1550	1500	1500	1550
$N_2$ ( $V_a$ ) [cm <sup>3</sup> g <sup>-1</sup> ]	0.63	0.48	0.50	0.55	0.59
$CO_2$ (upt.) [mol mol <sup>-1</sup> ] [wt %]	-	3.8 15.2	3.2 12.9		

<sup>a</sup>These results are compared to the literature values of Al-PMOF.<sup>25</sup> The micropore volume was calculated at  $p/p_0 = 0.5$ . <sup>b</sup>The theoretically accessible surface areas were calculated using the strategy reported by Düren et al.<sup>52</sup>

**Figure 6.**  $N_2$ -sorption isotherms of Ga- and In-PMOF-bs-th measured at 77 K. Filled squares represent adsorption and empty squares desorption, respectively.

DMF molecules in the pores, which was determined by <sup>1</sup>H NMR spectroscopy. Washing with water, 2 M HCl, or 2 M NaOH leads to a decrease or loss of long-range order (Figure 7). Corresponding stability tests at pH = 7 using a  $Na_2HPO_4/NaH_2PO_4$  buffer system were also carried out and led to the formation of X-ray amorphous products. Due to these experiments, the best activation procedure was determined as

washing with EtOH, MeOH, or acetone and activation at 140 °C under vacuum ( $10^{-2}$  kPa) for 16 h.

Samples treated with  $H_2O$  and HCl could be easily regenerated within a few seconds by impregnation with DMF at room temperature. Thermal activation above 145 °C at  $10^{-2}$  kPa leads to the removal of all DMF molecules and a strong decrease in crystallinity (Figure 7). These samples could also be regenerated in all cases by impregnation with DMF at room temperature within a few seconds. This indicates that loss of the long-range order is a reversible process.

The thermal stability was also investigated with thermogravimetric measurements (TG). For Ga- and In-PMOF-bs-th, TG measurements were carried out for the as-synthesized and the activated form, to determine the amount of solvent molecules in the pores. For all other compounds the TG data of the as-synthesized products are shown. The results of the TG investigations are summarized in Table 3, and the TG curves are presented in Figure 8 and Figures S10–S14. In the as-synthesized samples three characteristic steps of weight loss are observed. The loss up to 100 °C is assigned to the release of physisorbed water molecules and the one between 100 and 300 °C to the evaporation of DMF. Above 330 °C the decomposition of the PMOFs take place and the final products are  $In_2O_3$  and  $Ga_2O_3$  as confirmed by PXRD measurements

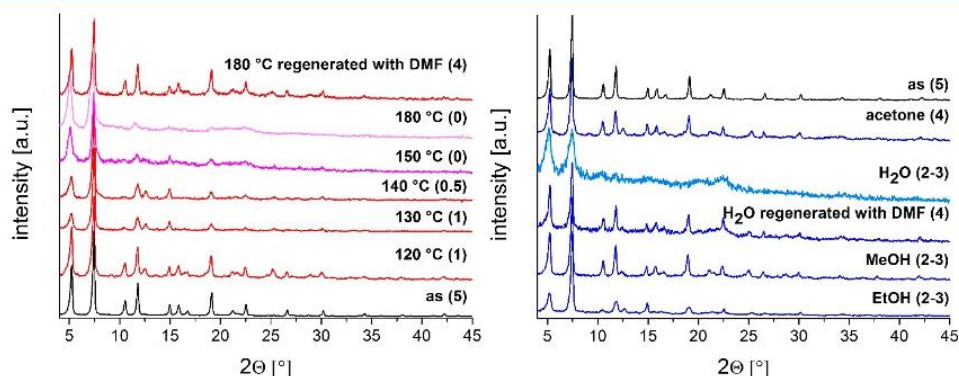
**Figure 7.** Thermal (left) and chemical stability (right) shown for In-PMOF-bs-th at activation temperatures between 120 and 180 °C and in different solvents (24 h, stirring at room temperature). The values in parentheses denote the number of DMF molecules per  $H_2TCPP^{4-}$  ion (as = as synthesized).

Table 3. Results of the Thermogravimetric Measurements of All Obtained Compounds<sup>a</sup>

	residual mass [%]	mass loss linker decompn [%]		mass loss physisorbed [%]	
		measd	calcd	H <sub>2</sub> O	DMF
Ga-PMOF-bs-th (as)	14.4	68.0 (1:1.8)	63.0 (1:2.0)	2.9 (1.9 H <sub>2</sub> O)	13.5 (2.2 DMF)
Ga-PMOF-bs-th (act)	19.1	76.4 (1:2.1)	80.6 (1:2.0)	4.6 (2.6 H <sub>2</sub> O)	
In-PMOF-bs-th (as)	19.4	53.8 (1:2.1)	57.3 (1:2.0)	3.0 (2.6 H <sub>2</sub> O)	24.9 (5.2 DMF)
In-PMOF-bs-th (act)	24.0	73.5 (1:1.9)	70.9 (1:2.0)	3.0 (1.9 H <sub>2</sub> O)	
In-PMOF-bs-us (as)	19.3	57.9 (1:2.0)	57.1 (1:2.0)	3.4 (2.6 H <sub>2</sub> O)	20.0 (3.9 DMF)
Ga-PMOF-cf (as)	14.2	59.9 (1:2.0)	62.2 (1:2.0)	5.5 (4.1 H <sub>2</sub> O)	10.3 (1.9 DMF)

<sup>a</sup>The number of solvent molecules per formula unit and resulting metal to linker ratios are shown in parentheses. The abbreviations “as” and “act” in parentheses denote as-synthesized and activated samples (solvent exchange and thermal activation at 140 °C and 10<sup>-2</sup> kPa for 16 h).

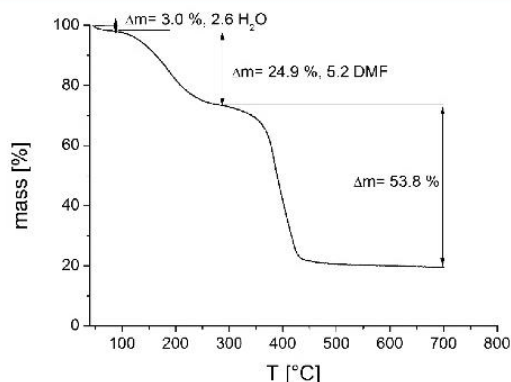


Figure 8. Thermogravimetric curve of an as-synthesized sample of In-PMOF-bs-th. Evaluation of the measurement reveals a molar ratio of linker:metal:H<sub>2</sub>O:DMF of 1:2.1:2.6:5.2 (Table 3).

(Figure S15). The results of the thermogravimetric analyses fit well with the elemental analyses given in the Experimental Section. Only the amounts of occluded solvent molecules differ slightly due to the storage conditions of the samples prior to the measurements. The TG curves of the activated samples of Ga- and In-PMOF-bs-th show a small mass loss of a few percent up to 100 °C, which is due to the release of 2 to 3 physisorbed H<sub>2</sub>O molecules per formula unit (Table 3).

**IR Spectroscopy.** IR spectra of as-synthesized samples of Ga- and In-PMOF-bs-th are shown in Figure S16, and the assignment of the bands is given in Table S2. Since the bands for the title compounds are observed at very similar wave numbers, only the IR spectrum of Ga-PMOF is briefly discussed. The stretching vibration of the N–H group is observed at 3320 cm<sup>-1</sup>. The asymmetric ( $\nu_{as}$ ) and symmetric ( $\nu_s$ ) stretching vibrations of the coordinating carboxylate groups are observed at 1590 and 1415 cm<sup>-1</sup>, respectively. The characteristic  $\nu(C=C)$  valence vibration of the phenyl rings is observed at 1545 cm<sup>-1</sup>. Further characteristic vibrations such as the  $\nu(C-N)$  valence vibration and  $\delta(C-H, N-H)$  and  $\gamma(C-H)$  deformation vibrations of the porphyrin moiety are found at 1362, 961, and 796 cm<sup>-1</sup>, respectively (Table S2). The vibration at 1710 cm<sup>-1</sup> is due to the presence of DMF molecules and can be assigned to the  $\nu(C=O)$  stretching vibration.<sup>53,54</sup>

**Particle Size.** The influence of the synthesis method on the particle sizes of the resulting PMOFs was studied using dynamic light scattering (DLS), SEM, and TEM measurements. While the first method leads to quantitative information on the bulk properties and yields the hydrodynamic radius, the latter is used to get information about the particle shape. In addition

crystallographic details such as lattice parameters can be obtained for the PMOFs.

**DLS.** The results of the DLS measurements are shown in Figures S17 and S18. The observed particle sizes are between about 60 and 160 nm for Ga-PMOF and 70 and 130 nm for In-PMOF (Table 4). The synthesis of Ga-PMOF in the

Table 4. Particle Sizes of Ga-PMOF-bs-th, In-PMOF-bs-th, In-PMOF-bs-us, and Ga-PMOF-cf as Obtained from DLS Measurements and the Evaluation of the PXRD Data Using the Scherrer Equation<sup>a</sup>

	$r_H^b$ [nm]	PI <sup>c</sup>	particle size (PXRD) [nm]
Ga-PMOF-cf (120 °C)	65 (18)	0.19	38 (11)
Ga-PMOF-bs-th	92 (25)	0.12	64 (22)
Ga-PMOF-cf (100 °C)	156 (28)	0.30	
In-PMOF-bs-us	74 (21)	0.23	92 (30)
In-PMOF-bs-th	132 (25)	0.20	105 (70)

<sup>a</sup>Values in parentheses are the standard deviations. <sup>b</sup> $r_H$  = hydrodynamic radius. <sup>c</sup>PI = polydispersity index.

continuous-flow reactor using synthesis temperatures of 100 and 120 °C and molar ratios of reactants of metal-to-linker of 2:1 and 1:1 leads to different particle sizes of 65 nm (120 °C) and 156 nm (100 °C), respectively.

**PXRD.** The particle sizes of all obtained samples were also determined from PXRD data. They are in most cases consistent with the DLS measurements taking into account that the hydrodynamic radius is larger than the particle size (Table 4).<sup>55</sup> In one case the particle size determined from PXRD and DLS data is in the same range, but in this case high standard deviations are found.

**SEM.** The samples were also characterized by SEM measurements (Figures S19–S23). The micrographs reveal plate-shaped morphologies for all samples, and the edges of the plates are not very well-defined. Therefore, and because of particle agglomeration, the determination of a particle size distribution of the samples was not possible.<sup>55</sup> From the micrographs one can deduce that thermal heating leads to larger particles than the ones obtained under ultrasonication and that in the flow reactor at 120 °C the smallest particles are obtained. This is in agreement with the other characterization measurements.

The particle size and morphology of In-PMOF-bs-us nanoparticles were also investigated by TEM measurements (Figure 9). This sample was chosen due to its high crystallinity and the smallest particle size of the synthesized In-PMOFs, as shown with DLS measurements (Figure S18).

Figure 9 shows a typical TEM image of the In-PMOF-bs-us sample, in which the morphology and size of the crystalline

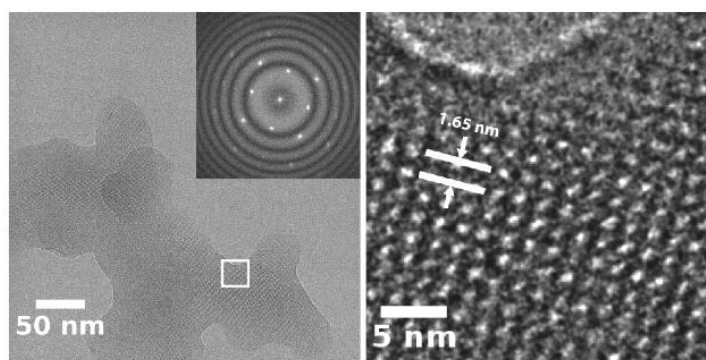


**Figure 9.** Left: TEM image of the as-synthesized In-PMOF-bs-us on a carbon support film. The inset shows the Fourier transform of the TEM image, in which the radial distance represents the lattice fringe distance. Right: Details of the TEM image shown on the left side with the lattice planes corresponding to the [001] reflection of In-PMOF-bs-us (1.65 nm).

particles are visible, in addition to individual sets of lattice planes. The particles exhibit different types of morphology and sizes and tend to agglomerate. Most of the particles appear almost circular in the projection, hinting at a spherical shape. Other particles are bounded by straight lines, indicating the formation of facets. The lateral size of the particles ranges from 25 to about 80 nm.

In order to determine the lattice parameters of the crystalline phase, the interplanar distances between the various sets of lattice planes were measured by means of digital image analysis. The inset in Figure 9 shows a Fourier transform (FT) of the TEM image. The radial distance of the apparent spots indicates the lattice distance in reciprocal space. A comparison with calculated values for the In-PMOF-bs-us sample shows very good agreement with the measured ones (Table 5).

**Table 5.** Measured Lattice Distances from TEM Micrographs Compared with the Calculated Ones from the Crystal Structure of In-PMOF<sup>a</sup>

measd lattice distance [nm]	calcd lattice distance from PXRD [nm]	corresponding lattice plane [hkl]
1.65	1.67	[001]
11.6	11.8	[201]
0.74	0.75	[202]

<sup>a</sup>The corresponding lattice planes are also shown.

## CONCLUSION

We demonstrated the successful synthesis and characterization of two new porphyrin based MOFs containing gallium and indium, i.e., Ga-PMOF [Ga<sub>2</sub>(H<sub>2</sub>TCP)(OH)<sub>2</sub>·3DMF·3H<sub>2</sub>O] and In-PMOF [In<sub>2</sub>(H<sub>2</sub>TCP)(OH)<sub>2</sub>·3DMF·4H<sub>2</sub>O], respectively. The synthesis of both MOFs was investigated by high-throughput methods,<sup>33</sup> and the structures were successfully refined by the Rietveld method. Three synthesis methods, i.e., batch synthesis, ultrasound-assisted, and continuous-flow synthesis were employed to vary the particle size of the resulting PMOFs. The resulting nanoparticles had diameters between about 60 and 160 nm for Ga-PMOF and 70 and 130 nm for In-PMOF as demonstrated by DLS, PXRD, SEM, and TEM measurements (for In-PMOF-bs-us). The TEM measurements show that In-PMOF-bs-us is obtained as nanoparticles of high crystallinity. The use of the continuous flow synthesis allows us to synthesize Ga-PMOF-cf at gram scale with a space–time

yield of 648 kg m<sup>-3</sup> d<sup>-1</sup>. Both MOFs show a high BET surface area between 1100 and 1400 m<sup>2</sup> g<sup>-1</sup> as determined from N<sub>2</sub> physisorption measurements at 77 K, and they are also porous toward CO<sub>2</sub> (uptake in Ga-PMOF is 15.2 and In-PMOF it is 12.9 wt % at 298.15 K and 1 bar).

Both MOFs show thermal stability up to about 145 °C and chemical stability in all tested organic solvents. The observed loss of long-range order after treatment with H<sub>2</sub>O or activation temperatures above 145 °C is reversible; impregnation with DMF at room temperature for a short time restores highly crystalline materials. The small particle size and the high crystallinity of the title compounds in combination with their porosity could make these porphyrin-based MOFs possible candidates in drug delivery applications or in catalysis.

## ASSOCIATED CONTENT

### Supporting Information

The Supporting Information is available free of charge on the ACS Publications website at DOI: 10.1021/acs.inorgchem.6b00221.

Synthesis and characterization of H<sub>6</sub>TCP and other experimental details (PDF)

Crystallographic data of Ga-PMOF-bs-th (CIF)

Crystallographic data of In-PMOF-bs-th (CIF)

CCDC 1438646 and 1438647 also contain crystallographic data for this paper. These data can be obtained free of charge from The Cambridge Crystallographic Data Centre via [www.ccdc.cam.ac.uk/getstructures](http://www.ccdc.cam.ac.uk/getstructures).

## AUTHOR INFORMATION

### Corresponding Author

\*E-mail: [stock@ac.uni-kiel.de](mailto:stock@ac.uni-kiel.de)

### Notes

The authors declare no competing financial interest.

## ACKNOWLEDGMENTS

We appreciate support from the Deutsche Forschungsgemeinschaft (SPP-1362; STO 643/5-2), and we thank Achim Fölster for help in designing Figure 1. The authors thank Dr. Steffen Schmidt for assistance with TEM data acquisition and Ramona Hoffmann for measuring the SEM images.

## ■ REFERENCES

- (1) Yaghi, O. M.; O'Keeffe, M.; Ockwig, N. W.; Chae, H. K.; Eddaoudi, M.; Kim, J. *Nature* **2003**, *423*, 705–714.
- (2) Furukawa, H.; Cordova, K. E.; O'Keeffe, M.; Yaghi, O. M. *Science* **2013**, *341*, 1230444.
- (3) Stock, N.; Reinsch, H.; Schilling, L.-H. Synthesis of MOFs. In *Metal Organic Frameworks as Heterogeneous Catalysts*; The Royal Society of Chemistry: 2013; Chapter 2, pp 9–30.
- (4) Sun, C.-Y.; Qin, C.; Wang, X.-L.; Su, Z.-M. *Expert Opin. Drug Delivery* **2013**, *10*, 89–101.
- (5) Janiak, C.; Vieth, J. K. *New J. Chem.* **2010**, *34*, 2366–2388.
- (6) Mueller, U.; Schubert, M.; Teich, F.; Puetter, H.; Schierle-Arndt, K.; Pastre, J. J. *Mater. Chem.* **2006**, *16*, 626–636.
- (7) Zhou, H.-C.; Long, J. R.; Yaghi, O. M. *Chem. Rev.* **2012**, *112*, 673–674.
- (8) Bernini, M. C.; Fairen-Jimenez, D.; Pasinetti, M.; Ramirez-Pastor, A. J.; Snurr, R. Q. *J. Mater. Chem. B* **2014**, *2*, 766–774.
- (9) Horcajada, P.; Chalati, T.; Serre, C.; Gillet, B.; Sebrie, C.; Baati, T.; Eubank, J. F.; Heurtaux, D.; Clayette, P.; Kreuz, C.; Chang, J.-S.; Hwang, Y. K.; Marsaud, V.; Bories, P.-N.; Cynober, L.; Gil, S.; Férey, G.; Couvreur, P.; Gref, R. *Nat. Mater.* **2010**, *9*, 172–178.
- (10) Horcajada, P.; Gref, R.; Baati, T.; Allan, P. K.; Maurin, G.; Couvreur, P.; Férey, G.; Morris, R. E.; Serre, C. *Chem. Rev.* **2012**, *112*, 1232–1268.
- (11) Horcajada, P.; Serre, C.; Vallet-Regí, M.; Sebban, M.; Taulelle, F.; Férey, G. *Angew. Chem.* **2006**, *118*, 6120–6124.
- (12) Gao, W.-Y.; Chrzanowski, M.; Ma, S. *Chem. Soc. Rev.* **2014**, *43*, 5841–5866.
- (13) Harvey, R. A.; Ferrier, D. R. *Biochemistry*; Wolters Kluwer Health: 2011.
- (14) Martel, B.; Cassidy, K. *Chemical Risk Analysis: A Practical Handbook*; Taylor & Francis: 2000.
- (15) Nakajima, M.; Takahashi, H.; Sasaki, M.; Kobayashi, Y.; Ohno, Y.; Usami, M. *Teratog., Carcinog., Mutagen.* **2000**, *20*, 219–227.
- (16) Ungvary, G. *J. Toxicol. Environ. Health, Part A* **2000**, *59*, 27–42.
- (17) Ivanoff, C. S.; Ivanoff, A. E.; Hottel, T. L. *Food Chem. Toxicol.* **2012**, *50*, 212–215.
- (18) Feng, D.; Jiang, H.-L.; Chen, Y.-P.; Gu, Z.-Y.; Wei, Z.; Zhou, H.-C. *Inorg. Chem.* **2013**, *52*, 12661–12667.
- (19) Morris, W.; Volosskiy, B.; Demir, S.; Gándara, F.; McGrier, P. L.; Furukawa, H.; Cascio, D.; Stoddart, J. F.; Yaghi, O. M. *Inorg. Chem.* **2012**, *51*, 6443–6445.
- (20) Feng, D.; Gu, Z.-Y.; Chen, Y.-P.; Park, J.; Wei, Z.; Sun, Y.; Bosch, M.; Yuan, S.; Zhou, H.-C. *J. Am. Chem. Soc.* **2014**, *136*, 17714–17717.
- (21) Feng, D.; Chung, W.-C.; Wei, Z.; Gu, Z.-Y.; Jiang, H.-L.; Chen, Y.-P.; Darenbourg, D. J.; Zhou, H.-C. *J. Am. Chem. Soc.* **2013**, *135*, 17105–17110.
- (22) Jiang, H.-L.; Feng, D.; Wang, K.; Gu, Z.-Y.; Wei, Z.; Chen, Y.-P.; Zhou, H.-C. *J. Am. Chem. Soc.* **2013**, *135*, 13934–13938.
- (23) Fateeva, A.; Devautour-Vinot, S.; Heymans, N.; Devic, T.; Grenèche, J.-M.; Wuttke, S.; Miller, S.; Lago, A.; Serre, C.; De Weireld, G.; Maurin, G.; Vimont, A.; Férey, G. *Chem. Mater.* **2011**, *23*, 4641–4651.
- (24) Fateeva, A.; Clarisse, J.; Pilet, G.; Grenèche, J.-M.; Nouar, F.; Abeykoon, B. K.; Guegan, F.; Goutaudier, C.; Luneau, D.; Warren, J. E.; Rosseinsky, M. J.; Devic, T. *Cryst. Growth Des.* **2015**, *15*, 1819–1826.
- (25) Fateeva, A.; Chater, P. A.; Ireland, C. P.; Tahir, A. A.; Khimyak, Y. Z.; Wiper, P. V.; Darwent, J. R.; Rosseinsky, M. J. *Angew. Chem.* **2012**, *124*, 7558–7562.
- (26) Huh, S.; Kim, S.-J.; Kim, Y. *CrystEngComm* **2016**, *18*, 345.
- (27) Gao, W.-Y.; Zhang, Z.; Cash, L.; Wojtas, L.; Chen, Y.-S.; Ma, S. *CrystEngComm* **2013**, *15*, 9320–9323.
- (28) Johnson, J. A.; Luo, J.; Zhang, X.; Chen, Y.-S.; Morton, M. D.; Echeverría, E.; Torres, F. E.; Zhang, J. *ACS Catal.* **2015**, *5*, 5283–5291.
- (29) He, C.; Liu, D.; Lin, W. *Chem. Rev.* **2015**, *115*, 11079–11108.
- (30) Rabenau, A. *Angew. Chem.* **1985**, *97*, 1017–1032.
- (31) Bauer, S.; Stock, N. *Chem. Unserer Zeit* **2007**, *41*, 390–398.
- (32) Sheldrick, W. S.; Wachhold, M. *Angew. Chem.* **1997**, *109*, 214–234.
- (33) Stock, N. *Microporous Mesoporous Mater.* **2010**, *129*, 287–295.
- (34) Safarifard, V.; Morsali, A. *Coord. Chem. Rev.* **2015**, *292*, 1–14.
- (35) Waitschat, S.; Wharmby, M. T.; Stock, N. *Dalton Trans.* **2015**, *44*, 11235.
- (36) Rubio-Martinez, M.; Batten, M. P.; Polyzos, A.; Carey, K.-C.; Mardel, J. I.; Lim, K.-S.; Hill, M. R. *Sci. Rep.* **2014**, DOI: 10.1038/srep05443.
- (37) Bayliss, P. A.; Ibarra, I. A.; Perez, E.; Yang, S.; Tang, C. C.; Poliakov, M.; Schroder, M. *Green Chem.* **2014**, *16*, 3796–3802.
- (38) Edel, J. B.; Fortt, R.; deMello, J. C.; deMello, A. J. *Chem. Commun.* **2002**, 1136–1137.
- (39) Shi, N.; Xie, L.; Sun, H.; Duan, J.; Yin, G.; Xu, Z.; Huang, W. *Chem. Commun.* **2011**, *47*, S055–S057.
- (40) Hu, J.-S.; Guo, Liang, H.-P.; Wan, L.-J.; Jiang, L. *J. Am. Chem. Soc.* **2005**, *127*, 17090–17095.
- (41) Shi, N.; Du, W.; Jin, X.; Zhang, Y.; Han, M.; Xu, Z.; Xie, L.; Huang, W. *Cryst. Growth Des.* **2014**, *14*, 1251–1257.
- (42) Jeong, E.-Y.; Ansari, M. B.; Mo, Y.-H.; Park, S.-E. *J. Hazard. Mater.* **2011**, *185*, 1311–1317.
- (43) Harada, A.; Yamaguchi, H.; Okamoto, K.; Fukushima, H.; Shiotsuki, K.; Kamachi, M. *Photochem. Photobiol.* **1999**, *70*, 298–302.
- (44) Garcia, G.; Sol, V.; Lamarche, F.; Granet, R.; Guilloton, M.; Champavier, Y.; Krausz, P. *Bioorg. Med. Chem. Lett.* **2006**, *16*, 3188–3192.
- (45) Forster, P. M.; Stock, N.; Cheetham, A. K. *Angew. Chem., Int. Ed.* **2005**, *44*, 7608–7611.
- (46) Stock, N. *Chem. Ing. Tech.* **2010**, *82*, 1039–1047.
- (47) Balzar, D.; Audebrand, N.; Daymond, M. R.; Fitch, A.; Hewat, A.; Langford, J. I.; Le Bail, A.; Louer, D.; Masson, O.; McCowan, C. N.; Popa, N. C.; Stephens, P. W.; Toby, B. H. *J. Appl. Crystallogr.* **2004**, *37*, 911–924.
- (48) Coelho, A., *TOPAS-Academic V4.1*; Coelho Software: 2007.
- (49) Brandenburg, K. *Diamond Version 3*; Crystal Impact GbR: Bonn, 2012.
- (50) Pennington, W. J. *Appl. Crystallogr.* **1999**, *32*, 1028–1029.
- (51) *Materials Studio Version 5.0*; Accelrys Inc.: San Diego, CA, 2009.
- (52) Düren, T.; Millange, F.; Férey, G.; Walton, K. S.; Snurr, R. Q. *J. Phys. Chem. C* **2007**, *111*, 15350–15356.
- (53) Socrates, G. *Infrared and Raman Characteristic Group Frequencies: Tables and Charts*; Wiley: 2004.
- (54) Hesse, M.; Meier, H.; Zeeh, B. *Spektroskopische Methoden in der organischen Chemie*; Thieme: 2005.
- (55) Hirschle, P.; Preiß, A.; Auras, F.; Pick, A.; Volkner, J.; Valdeperez, D.; Witte, G.; Parak, W. J.; Radler, J. O.; Wuttke, S. *CrystEngComm* **2016**, DOI: 10.1039/C6CE00198J.

#### 4.2.2.3 A Facile “Green” Route for Scalable Batch Production and Continuous Synthesis of Zirconium MOFs

Der folgende Artikel wurde im Jahr 2016 in der Fachzeitschrift *Eur. J. Inorg. Chem.*, Wiley-VCH Verlag GmbH & Co. KGaA veröffentlicht. Die Wiedergabe erfolgt mit freundlicher Genehmigung des Wiley-VCH Verlag GmbH & Co. KGaA. Reprinted with permission from H. Reinsch, S. Waitschat, S. M. Chavan, K.-P. Lillerud and N. Stock, *Eur. J. Inorg. Chem.*, **2016**, 27, 4490 – 4498, DOI: 10.1002/ejic.201600295. Copyright 2016 Wiley-VCH Verlag GmbH & Co. KGaA.

<https://onlinelibrary.wiley.com/doi/abs/10.1002/ejic.201600295>

In dieser Arbeit wird die grüne Synthese von verschiedenen Zr-MOFs (UiO-66, DUT-67 und MOF-808) in Batch- und Flussreaktoren und deren Aufskalierung beschrieben. Zunächst wurde durch die Hochdurchsatzmethodik das ideale Metallsalz zu Modulator zu Linker Verhältnis ermittelt. Die Reinheit der Proben wurde durch Rietveld-Verfeinerung und durch Gassorptionmessungen bestimmt.

Um zu zeigen, dass mit Flussreaktoren nicht nur theoretisch große Mengen (hochgerechnet auf 1000 l Reaktoren), sondern auch real „große“ Mengen produziert werden können, wurde ein neuer Flussreaktor (**Reaktor 2**) entwickelt. Zunächst wurde der Innendurchmesser des Teflonschlauches auf 4 mm erhöht. Um mehr Schlauch für den Reaktor verwenden zu können, wurde anstatt eines Ölbadens ein Umluftofen zum Beheizen des Reaktors verwendet. In diesem wurde ein Gerüst aus Aluminiumlochplatten befestigt um das wiederum der Schlauch gewickelt wurde, insgesamt ca. 150 m, was zu einem Reaktorvolumen von ca. 1850 ml führte. Statt mehrerer Spritzenpumpen wurde eine Magnetmenbranpumpe eingesetzt, die es ermöglicht auch Suspension zu pumpen. Diese wurde vorgelegt und kontinuierlich durchmischt. Für diesen Reaktor wurden nun die aus Batch-Synthesen optimierten Synthesebedingungen von UiO-66-Fum und UiO-66-NH<sub>2</sub> übertragen und jeweils eine Reaktion durchgeführt, so dass der Reaktor eine gewisse Zeit vollständig mit Edukt bzw. Produkt gefüllt war. Dies sollte theoretisch eine kontinuierliche Produktion simulieren, denn es wird für gewöhnlich behauptet, dass die Produkte einer kontinuierlichen Synthese identisch sind und die gleichen Eigenschaften aufweisen. Um dies zu testen, wurde alle fünf Minuten ein Teil des Produktes isoliert und getrennt aufgearbeitet. Anschließend wurden die Eigenschaften aller Produkte, die während des gesamten Prozesses erhalten wurden, ermittelt. Dazu wurde von allen Proben Pullverdiffraktogramme aufgenommen. Sowohl die Diffraktogramme von UiO-66-Fum als auch die von UiO-66-NH<sub>2</sub> zeigen, dass die jeweiligen Produkte entstanden sind. Die Diffraktogramme weisen untereinander kaum Unterschiede auf. Anschließend Stickstoffsorptionmessungen zeigten allerdings, dass nicht alle

## Kumulativer Teil Flussreaktor: Flussreaktoraufskalierung

UiO-66-Fum Verbindungen die gleichen Sorptionseigenschaften aufweisen. Die scheinbare spezifische Oberfläche variiert von 900 bis 1200  $\text{m}^2 \cdot \text{g}^{-1}$ . Dies wurde auf ein mögliches Problem beim Durchmischen der Edukte im Vorratsgefäß oder sogar während der Reaktion zurückgeführt. Dahingegen zeigen die Sorptionsdaten der UiO-66-NH<sub>2</sub> Proben über die ganze Zeit kaum Abweichungen untereinander und es wurden Werte für die spezifische Oberfläche von 1150  $\text{m}^2 \cdot \text{g}^{-1}$  ermittelt.

Die Raum-Zeit-Ausbeute ist mit 2733 bzw. 4346  $\text{kg} \cdot \text{m}^{-3} \cdot \text{d}^{-1}$  für UiO-66-Fum bzw. UiO-66-NH<sub>2</sub> wie für die meisten Flussreaktorsynthesen recht hoch. Die echten Ausbeuten von 205 und 325  $\text{g} \cdot \text{h}^{-1}$  sind mit die höchsten, die bisher für MOFs erzielt wurden.


**Continuous Synthesis**

## A Facile “Green” Route for Scalable Batch Production and Continuous Synthesis of Zirconium MOFs

Helge Reinsch,<sup>\*[a]</sup> Steve Waitschat,<sup>[a]</sup> Sachin M. Chavan,<sup>[b,c]</sup> Karl Petter Lillerud,<sup>[b,c]</sup> and Norbert Stock<sup>\*[a,c]</sup>

**Abstract:** Considering the requirements for the commercial production of metal–organic frameworks (MOFs), we investigated the aqueous synthesis of zirconium MOFs. A highly versatile route was identified employing  $\text{ZrOCl}_2 \cdot 8\text{H}_2\text{O}$ ,  $\text{H}_2\text{O}$ , acetic acid and the respective linker molecule as starting materials. These synthesis conditions are suitable to obtain zirconium MOFs with different topologies like  $\text{UiO-66-(OH)}_2$ , zirconium fumarate, zirconium mesaconate, DUT-67 or MOF-808 with synthesis times of 1 to 5 h under microwave irradiation. The scalability of the synthesis of zirconium fumarate was demonstrated

at multigram scale under reflux conditions using conventional dielectric heating. To ease the recovery of this MOF which bypasses filter paper as a pure product, we identified sodium polyacrylate as a suitable additive to induce aggregation of the particles. Moreover, a custom-made prototype flow reactor was developed which allows for the continuous synthesis of zirconium fumarate and  $\text{UiO-66-NH}_2$  starting from a slurry of the starting materials. The commonly employed toxic organic solvents needed for activation/purification of the MOFs could be successfully replaced by a basic aqueous solution.

### Introduction

Metal–organic frameworks (MOFs) have been comprehensively investigated for their potential use in a variety of applications. A large number of studies were dedicated to the storage of hydrogen<sup>[1]</sup> or methane<sup>[2]</sup> and to the catalytic properties of MOFs.<sup>[3,4]</sup> Their luminescence properties<sup>[5]</sup> and their water adsorption behaviour<sup>[6]</sup> for use in heat pumps or as desiccants have come into focus more recently. While the synthesis conditions for MOFs cover a wide range<sup>[7]</sup> the desirable conditions for the industrial scale-up were only sparsely investigated. According to the requirements given by industrial researchers,<sup>[8]</sup> the preparative route determines the industrial and commercial feasibility of MOF synthesis and therefore also their implementation into real-life applications. The main problem is constituted by the commonly employed solvent *N,N*-dimethylformamide (DMF) which is toxic, flammable and teratogenic. Moreover, it easily decomposes and can contain various impurities, which can affect the properties of a desired product.<sup>[9–12]</sup> A preferred synthetic route would also restrict the reactants to commercially available chemicals which can be purchased in reasonable amounts. Metal nitrates and chlorides should be ex-

cluded from the synthesis – if possible – since they pose the risks of explosion (nitrates) or corrosion (chlorides). To enable the facile scale-up in existing pilot plants and larger facilities, the synthesis should be carried out preferably with stirring and at ambient pressure. So far only few compounds have been reported to be easily obtained under such conditions, such as the canonical MOFs HKUST-1<sup>[13]</sup> and Ni-CPO-27<sup>[14]</sup> (HKUST: Hong-Kong University of Science and Technology; CPO: Coordination Polymer Oslo). Another example for such a “scalable” MOF is aluminium fumarate<sup>[8]</sup> which exhibits the framework topology of MIL-53<sup>[15]</sup> (MIL: Material Institute Lavoisier).

The synthesis of zirconium MOFs has recently been in focus due to their high thermal and chemical stability,<sup>[16,17]</sup> their remarkable catalytic activity,<sup>[18,19]</sup> and their structural tunability.<sup>[20,21]</sup> There have also been intense efforts to obtain MOFs with the archetypical **fcu** topology of the  $\text{UiO-66}$  framework (UiO: University of Oslo) using a “green” preparative synthesis route. It was for example revealed that zirconium fumarate, exhibiting the desired topology, can be easily prepared from aqueous mixtures under hydrothermal conditions after 24 h<sup>[22]</sup> while the original synthesis method utilized the organic solvent DMF.<sup>[23]</sup> Similarly, the functionalized MOF  $\text{UiO-66-(CO}_2\text{H)}_2$  could be obtained from aqueous mixtures<sup>[24]</sup> while first synthesis protocols were based on mixtures of DMF and formic acid.<sup>[25]</sup> However, the aqueous route is relatively time-consuming since an initially formed gel must be retreated and thus the reaction time sums up to 40 h. In a similar manner, employing only the respective linker molecule,  $\text{ZrCl}_4$  and water,  $\text{UiO-66-CO}_2\text{H}$  has been obtained.<sup>[26]</sup> Very recently the synthesis of  $\text{UiO-66-NO}_2$  was reported in water.<sup>[27]</sup> Using hydrochloric acid as additive greatly accelerated the reaction, however, no data on the porosity was given. This preparative route based on water, linker and

[a] *Institute of Inorganic Chemistry, Christian-Albrechts University Kiel, Max-Eyth-Straße 2, 24118 Kiel, Germany*  
E-mail: stock@ac.uni-kiel.de  
hreinsch@ac.uni-kiel.de  
<http://www.ac.uni-kiel.de/de/stock>

[b] *Department of Chemistry, University of Oslo, P. O. Box 1033 Blindern, 0315 Oslo, Norway*

[c] *ProfMOF AS, Kirkegårdsveien 45, 3616 Kongsberg, Norway*

Supporting information for this article is available on the WWW under <http://dx.doi.org/10.1002/ejic.201600295>.



ZrCl<sub>4</sub> and long reaction times can also be employed at the multigram scale.<sup>[24,26]</sup>

Employing mixtures of water and acetic acid allowed for the synthesis of several zirconium MOFs with UiO-66 structure starting from Zr(NO<sub>3</sub>)<sub>4</sub> as the metal source.<sup>[28]</sup> Again the reaction times are comparably long (24 h). In addition the purification of the raw product required methanol and dichloromethane and was also very time consuming (6 d). Nevertheless, several MOF can be obtained pure at the gram scale, for example UiO-66-NH<sub>2</sub> and UiO-66-F<sub>4</sub>.

The aforementioned reports all described procedures utilizing Zr<sup>IV</sup> chlorides or nitrates as the metal sources. Some of us also investigated if Zr(SO<sub>4</sub>)<sub>2</sub>·4H<sub>2</sub>O can be used for the synthesis of zirconium MOFs. Unfortunately, it was observed that strong interactions of the sulfate ion with the inorganic building units<sup>[29]</sup> lowered the framework connectivity in most cases, and thus resulted in decreased framework rigidity and porosity.<sup>[30]</sup> Thus, only UiO-66-F<sub>4</sub> could be obtained while other products based on aminoterephthalic acid or pyromellitic acid exhibited the eightfold connected **bcu** topology.

We herein report the results of our studies in the field of scalable synthesis of Zr-MOFs. Suitable conditions could be identified which allow for the synthesis of a variety of MOFs under microwave irradiation. The scalability was tested under reflux conditions and in a continuous process. Moreover, an activation method that excludes toxic organic solvents like DMF could be established. The obtained products were studied in detail using powder X-ray diffraction, EDX spectroscopy, thermogravimetric analysis and physisorption and their properties are compared to data reported in the literature.

## Results and Discussion

After several preliminary test reactions (see Supporting Information) we identified the chemical system ZrOCl<sub>2</sub>·8H<sub>2</sub>O/linker/H<sub>2</sub>O/acetic acid as suitable to obtain different zirconium MOFs under mild conditions (95 °C in a microwave oven whilst stirring) after comparably short reaction times (1–5 h). The concentration was set to 0.2 M for the respective linker and Zr<sup>4+</sup> since this resulted in a mixture that could be constantly agitated by magnetic stirring. The reaction scale of 20 mL in the microwave oven was sufficient to obtain yields between 0.5 and 1 g. Thus we could obtain MOFs with isorecticular frameworks using fumaric acid (zirconium fumarate), methylfumaric acid (i.e. mesaconic acid; zirconium mesaconate)<sup>[31]</sup> and dihydroxyterephthalic acid [UiO-66-(OH)<sub>2</sub>]<sup>[17]</sup> all exhibiting the **fcu** topology and with the idealized composition of [Zr<sub>6</sub>O<sub>4</sub>(OH)<sub>4</sub>(linker)<sub>6</sub>]. By adjusting the metal ion to linker ratio to the stoichiometry in the desired product we also obtained the well-known DUT-67<sup>[32]</sup> based on thiophenedicarboxylic acid {H<sub>2</sub>TDC; DUT = Dresden University of Technology; idealized composition [Zr<sub>6</sub>O<sub>4</sub>(OH)<sub>8</sub>(TDC)<sub>4</sub>(H<sub>2</sub>O)<sub>4</sub>] and MOF-808 based on trimesic acid {H<sub>3</sub>BTC; idealized composition [Zr<sub>6</sub>O<sub>4</sub>(OH)<sub>10</sub>(BTC)<sub>2</sub>(H<sub>2</sub>O)<sub>6</sub>].<sup>[33]</sup>

Varying amounts of chloride were occluded in the products after synthesis, thus we tried to develop a method for chloride removal without using toxic organic solvents. Employing aqueous sodium acetate solutions (0.1 M concentration) removed

virtually all chloride impurities. After additional washing with H<sub>2</sub>O the obtained products were further characterized. Only minor impurities were observed by EDX spectroscopy (Table S1).

The PXRD patterns show that all products are highly crystalline (Figure 1, Figure 2, Figures S3–S5). Starting with the unit cell parameters reported in the literature, the cell parameters for zirconium fumarate, UiO-66-(OH)<sub>2</sub> and MOF-808 were refined using the Pawley method. The fits indicate that no crystalline by-products are formed and the refined values are in very good agreement with the reported data (Figures S3–S5, Table 1).

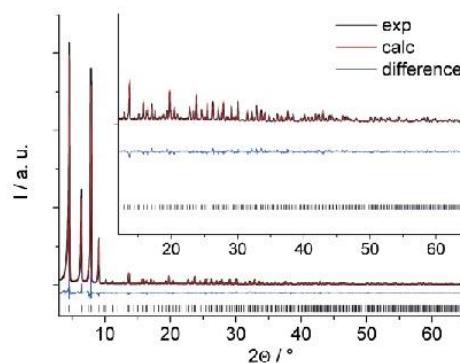


Figure 1. Rietveld plot for DUT-67 obtained from the synthesis in water. The black line represents the measured data, red line the calculated fit, while the blue line gives the difference curve. Vertical bars mark the allowed Bragg reflection position.

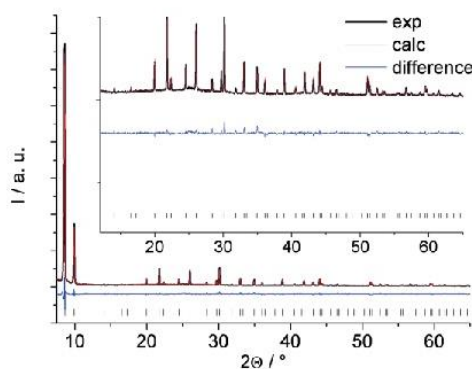


Figure 2. Rietveld plot for the obtained zirconium mesaconate. The black line represents the measured data, red line the calculated fit, while the blue line gives the difference curve. Vertical bars mark the allowed Bragg reflection position.

Table 1. The cell parameters, observed space groups and figures of merit for the respective compounds obtained by Pawley refinement.

MOF	Zr fumarate	UiO-66-(OH) <sub>2</sub>	MOF-808
Space group	<i>Pn</i> $\bar{3}$	<i>Fm</i> $\bar{3}m$	<i>Fd</i> $\bar{3}m$
<i>a</i> [Å]	17.834(2)	20.7849(2)	35.1448(4)
Exp. <i>a</i> [Å]	17.9309(4) <sup>[40]</sup>	20.7551(5) <sup>[16]</sup>	35.0764(10) <sup>[40]</sup>
<i>R</i> <sub>WP</sub> [%]	6.9	7.3	7.5

For DUT-67 we carried out a Rietveld refinement. The original crystal structure<sup>[34]</sup> indicated that noninterconnecting inorganic

building units are occluded inside the framework's cavities. However, according to the refinement by Rietveld methods (Figure 1, Table 2) no additional inorganic units are observed in the product obtained from the aqueous synthesis. Further experimental details can be found in the supporting information.

Table 2. Some relevant parameters for the Rietveld refinements of DUT-67 and zirconium mesaconate.

Compound	DUT-67	Zr mesaconate
$\lambda$ [Å]	1.5406 (Cu- $K_{\alpha 1}$ )	1.5406 (Cu- $K_{\alpha 1}$ )
Space group	$Fm\bar{3}m$	$Fm\bar{3}$
$a = b = c$ [Å]	38.8394(6)	17.7804(2)
$\alpha = \beta = \gamma$ [°]	90	90
$R_{wp}$ [%]	9.0	7.5
$R_{Bragg}$ [%]	3.6	2.4
GoF	1.85	1.45

The structure of zirconium mesaconate was also refined by Rietveld methods (Figure 2, Table 2) since to the best of our knowledge no such characterization had been reported. The refinement converged for a crystal structure in  $Fm\bar{3}$  space group symmetry with disordered  $\text{CH}_3$  side groups, details can be found in the supporting information. Some relevant parameters of the refinements are summarized in Table 2.

The crystal structures of all obtained compounds are based on the very same inorganic building unit. This is a hexanuclear cluster with a  $\text{Zr}_6\text{O}_4(\text{OH})_4^{12+}$  core which can be coordinated by up to 12 carboxylate groups.<sup>[34]</sup> In the frameworks of zirconium fumarate, zirconium mesaconate and UiO-66-(OH)<sub>2</sub> this leads to structures in which the clusters arrange in a face-centred cubic packing and are twelvefold connected (**fcu** topology, Figure 3).

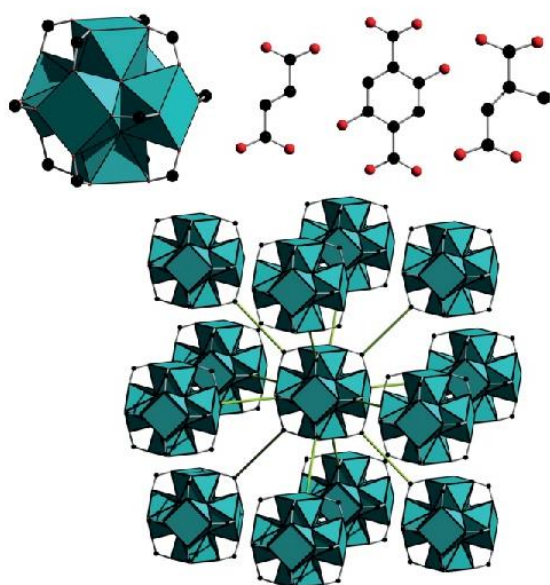


Figure 3. Top: The hexanuclear building unit in the **fcu** frameworks and the respective organic building units fumarate, dihydroxyterephthalate and mesaconate. Bottom: The twelvefold connectivity in the respective MOFs. ZrO polyhedra in cyan, oxygen atoms in red and carbon atoms in black.

The crystal structure of DUT-67 is based on eightfold connected inorganic building units forming a framework with **reo** topology (Figure 4). Thus, octahedral and cuboctahedral cavities are observed. The original crystal structure described the occlusion of additional inorganic building units inside the cuboctahedral cavities. However, during the refinement we only identified additional electron density inside the octahedral cages, which was attributed to guest molecules like water. This observation is also in good agreement with the thermogravimetric measurements (Table 3, Figure S10).

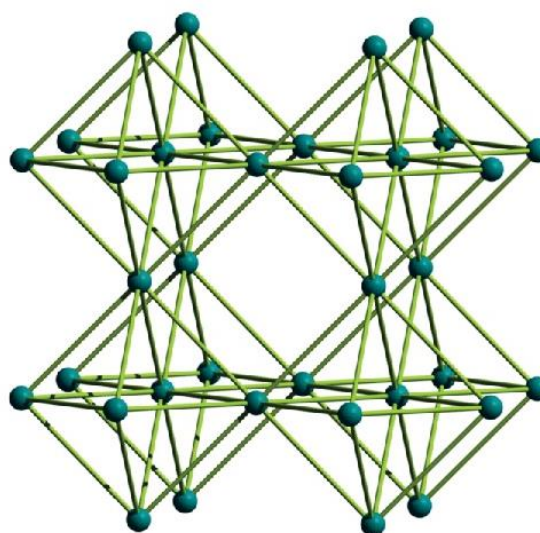
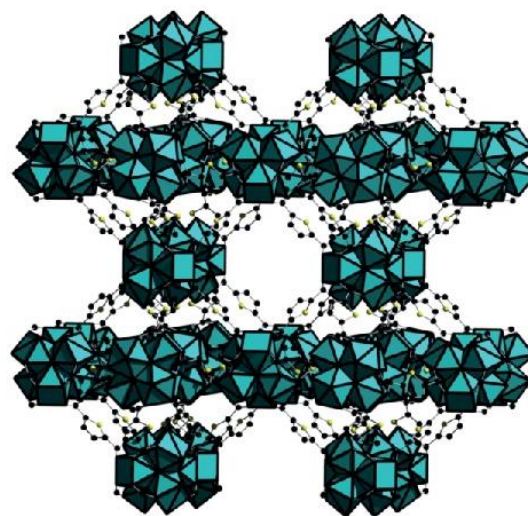


Figure 4. Top: The framework of DUT-67 exhibiting **reo** topology. Bottom: The underlying simplified network. ZrO polyhedra and nodes in cyan, sulfur atoms in yellow and carbon atoms in black.

The structure of MOF-808 is based on sixfold connected inorganic building units which are assembled into a framework with **spn** topology (Figure 5) exhibiting supertetrahedra formed from the clusters and the organic trimesate linker molecules.

Table 3. Expected and observed molar ratios Zr/linker as deduced from the thermogravimetric experiments.

MOF	Zr fum.	Zr mes.	UiO-66-(OH) <sub>2</sub>	MOF-808	DUT-67
Ideal ratio	6:6	6:6	6:6	6:2	6:4
Obs. ratio	6:5.2	6:5	6:5.3	6:2.04	6:3.9
Thermal stability [°C]	250	250	260	300	300

These supertetrahedra are assembled in a fashion that corresponds to a simple diamondoid framework structure.

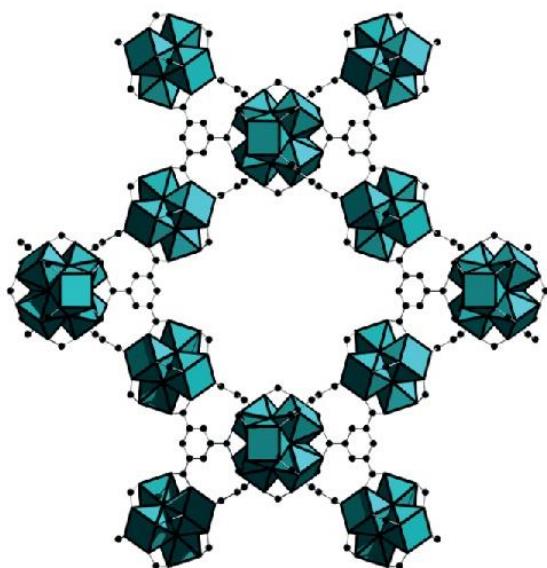


Figure 5. The framework of MOF-808 exhibiting **spn** topology as seen along [0 1 1]. ZrO polyhedra in cyan and carbon atoms in black.

MOFs that are based on Zr<sup>4+</sup> ions (or Hf<sup>4+</sup> ions) exhibit a well-investigated defect chemistry for the reported **fcu** frameworks. Both, inorganic and organic building units can be vacant<sup>[35]</sup> and thus the framework properties like catalytic activity or porosity can be altered.<sup>[36]</sup> The more common missing linker defects cannot be reliably estimated just based on PXRD data. However, they can be relatively easily deduced from thermogravimetric measurements by comparison to expected values of mass loss for an ideal framework. The results of these experiments are summarized in Table 3 and the corresponding TG curves can be found in the supporting information (Figures S6–S10).

For zirconium fumarate and mesaconate the observed values represent reasonable amounts which agree well with the number of missing linker defects reported in the literature.<sup>[37]</sup> For DUT-67, the number of linker molecules nearly matches the expected value. In MOF-808, the observed weight losses also correspond well with the ideal composition. However, the values deduced from these results should be in general considered as tentative. The nature of the nonconnecting sites in Zr-MOFs is not fully understood and might also change upon dehydration.<sup>[38]</sup> For the calculations in this paper we assumed that sites which are not coordinated by a carboxylate group are occupied by one OH<sup>-</sup> ion and one water molecule.

The porosity of the obtained products was evaluated by nitrogen physisorption experiments. Prior to the measurement all samples were activated for several hours under vacuum (0.1 mbar) at elevated temperatures (150 °C, except for zirconium mesaconate and MOF-808 which were activated at 120 °C). The sorption isotherms are shown in Figures 6 and 7.

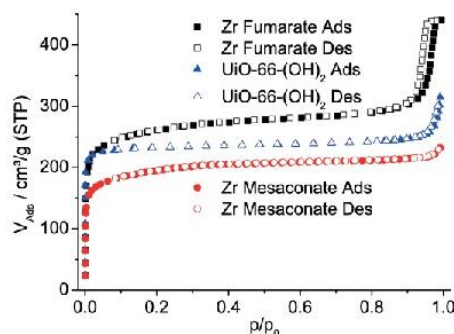


Figure 6. N<sub>2</sub> sorption isotherms for the reported MOFs with **fcu** topology.

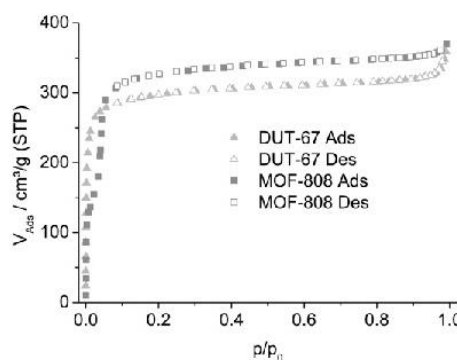


Figure 7. N<sub>2</sub> sorption isotherms for DUT-67 and MOF-808.

The MOFs with **fcu** topology all exhibit isotherms which clearly indicate the presence of micropores in the frameworks. However, the isotherm for zirconium fumarate also shows a hysteresis loop typical for mesoporous materials. Since the intrinsic structural pores have a maximum diameter of only 7.5 Å we attribute this to the presence of interparticle porosity.

The isotherm for DUT-67 also shows an isotherm characteristic for the presence of micropores (Figure 7), while the curve for MOF-808 exhibits an inflection point. The latter is typical for 3D frameworks with cavities in the mesopore range like MOF-808.<sup>[39]</sup>

The BET surface areas and the micropore volumes (the latter determined from the amount adsorbed at  $p/p_0 = 0.5$ ) are mostly in reasonable agreement with literature values (Table 4). The comparably high value for zirconium fumarate is in good agreement with the presence of defects in the material obtained in this study. The  $S_{\text{BET}}$  values for zirconium mesaconate and UiO-66-(OH)<sub>2</sub> are 60 m<sup>2</sup> and more than 300 m<sup>2</sup> higher than some numbers reported in the literature. This could again be caused by the presence of defects. In addition, the higher volatility of water in comparison with DMF, which was mostly used in previ-

ous studies, could also result in a more complete activation under vacuum than in previous studies.

Table 4. Apparent specific surface areas and micropore volumes.

MOF	Zr fum.	Zr mes.	UiO-66-(OH) <sub>2</sub>	MOF-808	DUT-67
$S_{\text{BET}}$ [m <sup>2</sup> /g]	990	725	940	1210	1150
$V_{\text{Mic}}$ [cm <sup>3</sup> /g]	0.43	0.32	0.37	0.53	0.48
Reported	856 <sup>[23]</sup>	662 <sup>[33]</sup>	617 <sup>[25]</sup>	2060 <sup>[42]</sup>	1064 <sup>[34]</sup>
$S_{\text{BET}}$ [m <sup>2</sup> /g]	990 <sup>[40]</sup>		1145 <sup>[42]</sup>		
Reported	0.45 <sup>[42]</sup>	–	0.22 <sup>[25]</sup>	0.84 <sup>[42]</sup>	0.44 <sup>[34]</sup>
$V_{\text{Mic}}$ [cm <sup>3</sup> /g]					

For DUT-67 the slightly increased values agree well with the absence of unbound inorganic building units inside the cuboctahedral cavities. However, the measured values are much lower than the theoretical maximum surface area (1767 m<sup>2</sup>/g<sup>[34]</sup>) which was also the case for the MOF obtained in DMF. We assume that some pores are partially blocked, even after activation under vacuum, and therefore not all cavities are accessible for guest molecules. The measured values for MOF-808 are much lower than the reported ones. However, in the original description of the material it was also observed that after one adsorption/desorption cycle employing water vapour as adsorptive, the pore volume decreased massively by about 50 %.<sup>[42]</sup> Since the compound synthesized in this contribution was synthesized in H<sub>2</sub>O and thus thermal activation represents water desorption, this could explain the comparably low porosity towards nitrogen and is in line with the reported properties.

The major drawback of the nevertheless versatile method described herein is the fact that most of the products have to be recovered by centrifugation since the synthesized particles are too small to be separated by filtration. The reason for this could be the comparably high nucleation rate for zirconium MOFs in the presence of water.<sup>[26,27]</sup> With the exception of UiO-66-(OH)<sub>2</sub>, all obtained MOFs bypassed the used filter paper and this is a substantial challenge for production of the MOFs at larger scale. However, upon addition of a 10 wt.-% aqueous solution of sodium polyacrylate (MW ≈ 5100 g/mol), the particles of zirconium fumarate prepared at multigram scale under reflux aggregated in a sufficient manner to filtrate the product. This solid was subsequently activated in a similar manner as the MOF obtained in the microwave oven. We assume that the polymer interconnects the particles by coordination to zirconium sites on the particle's surface and thus leads to the formation of larger agglomerates. However, this means as well that not a pure MOF is obtained but a MOF-polymer composite. This composite exhibits a lower porosity than the pure compound (Figure 8).

The specific surface area decreases from  $S_{\text{BET}} = 990$  m<sup>2</sup>/g for zirconium fumarate by ≈12 % to 874 m<sup>2</sup>/g for the composite. The same tendency is observed for the micropore volume which drops from 0.43 cm<sup>3</sup>/g to 0.38 cm<sup>3</sup>/g for the composite. Moreover, the hysteresis loop attributed to interparticle mesoporosity for the pure zirconium fumarate is absent in the isotherm of the composite. While this clearly facilitates the recovery, we have to mention that the obtained composite still

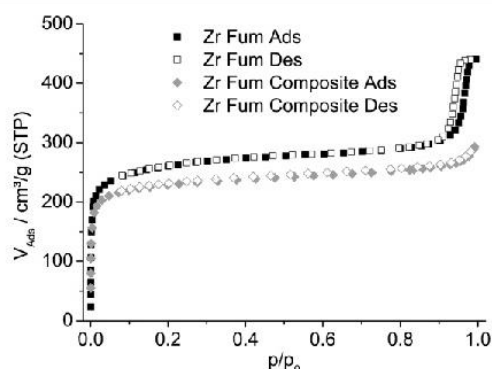


Figure 8. N<sub>2</sub> sorption isotherms for zirconium fumarate and the zirconium fumarate composite.

needs several hours to be filtered using a simple suction filter, still leaving challenges for the optimization of the procedure.

To arouse industrial interest in a certain material, not only the properties of the compound are important but also the facile production of large amounts with constant quality. Flow reactor synthesis can be employed for such purposes due to the continuous reaction performance resulting in steady product quality. Moreover, such a process can be automated relatively easily. Flow reactors are a very well-known synthesis tool, for example in organic chemistry<sup>[41]</sup> or for the synthesis of gold nanoparticles.<sup>[42]</sup> The first reported MOF obtained by this synthesis method was HKUST-1 in 2012.<sup>[43]</sup> Several studies followed which mostly focussed on reactions under solvothermal reaction conditions with temperatures up to 200 °C and pressures up to 300 bar.<sup>[44–46]</sup> As in the case of batch synthesis, these reaction conditions pose severe challenges for the reactor materials and safety precautions. Only two studies reported the synthesis of MOFs in flow reactors with reaction temperatures below the boiling point of the solvent, i.e. pressureless reaction conditions.<sup>[47,48]</sup> Such reactions are much easier to handle. UiO-66 was synthesized by both approaches with high space-time yields (STY) and high porosity.<sup>[47,50]</sup> However, while the reported STYs are usually very promising, the absolute amounts obtained are mostly at the one gram scale. In addition, to the best of our knowledge, all reported procedures for the continuous synthesis of MOFs utilize solutions of the reactants and focus mostly on very short reaction times of a few minutes. Thus, herein we report a flow reactor set-up that allows the synthesis of MOFs starting from a slurry and which is carried out at the multigram (or multilitre) scale, yielding amounts > 100 g.

In order to handle the slurries utilized for our green synthesis approach, we developed a new flow reactor assembled from commercially available parts. Approximately 150 m of Teflon tube were coiled around three interleaved cylinders made of aluminium plates, which results in a reactor volume of approximately 1850 mL. This unit was placed inside a conventional heating oven and a magnetic membrane pump was used to supply the feed to the tube (Figure S11, Table S3). To optimize the flow reactor synthesis the reaction time had to be determined. Preliminary batch test reactions for the synthesis of zir-

conium fumarate in small Pyrex tubes (8 mL volume) under synthesis conditions identical to the microwave-assisted syntheses were carried out for 10–60 min (Figure S12). The PXRD patterns indicated that the obtained zirconium fumarate exhibits high crystallinity already after 10 min. The yield does not improve any further after 20 min.

For the continuous reaction, we prepared five litres of a 0.2 M slurry using 1 mol  $\text{ZrOCl}_2 \cdot 8\text{H}_2\text{O}$  and 1 mol fumaric acid (322 g of zirconium salt and 116 g of fumaric acid) in a mixture of 2.5 L water and 2.5 L acetic acid. This feed slurry was transferred into a beaker placed on a magnetic stirrer to yield a homogeneous feed mixture. The pump was adjusted to 55 strokes per minute and the stroke length was set to 50%. The reaction temperature in the oven was set to 85 °C. These pumping parameters in combination with the reactor volume result in a total reaction time of 22 min. Prior to the reaction the reactor tubing was filled with water. Once this water was displaced by the reaction slurry we started collecting the product in five-minute batches. After the slurry was fully transferred to the reactor water was again used as feed. It is important to note that because of the initial and final water filling of the reactor the pump speed changes slightly at the beginning and at the end of the flow reaction. The reason for this is the different density and viscosity of the water and the reaction slurry. Thus, the reaction conditions remain identical only once the whole reactor is completely filled with the reaction slurry. From each five-minute fraction, 20 mL was centrifuged and washed with a 0.1 M  $\text{NaO}_2\text{CCH}_3$  solution and subsequently with ethanol. Each sample obtained in this way was characterized by powder X-ray diffraction and nitrogen sorption measurements. The powder patterns of all samples show high crystallinity and unambiguously identify the product as zirconium fumarate (Figure S13). In order to estimate the yield, we assumed that based on literature values<sup>[42]</sup> 30 wt.-% of the product consists of adsorbed water and the zirconium to linker ratio is approximately 6:5 as observed in the product of the microwave-assisted synthesis. The average yield of this reaction varies between 54 and 70%. Only the very first and the very last samples show a lower yield, most probably due to the mixing with water which was used as the

pressure-transmitting medium (Table ). The real-time yield of 205 g/h and the STY of 2733 kg/m<sup>3</sup>/d are remarkably high.

Prior to nitrogen sorption measurements every sample was activated under vacuum (0.1 mbar) at a temperature of 120 °C for 16 h. All isotherms exhibit the typical shape for microporous materials (Figure 9) and also show the hysteresis loop attributed to interparticle porosity. The values for the BET surface area are mostly in the range of  $1200 \pm 50 \text{ m}^2/\text{g}$  although in some fractions values between 900 and 1000  $\text{m}^2/\text{g}$  are observed. The values for the micropore volume also vary, mostly between 0.4 and 0.5  $\text{cm}^3/\text{g}$ .

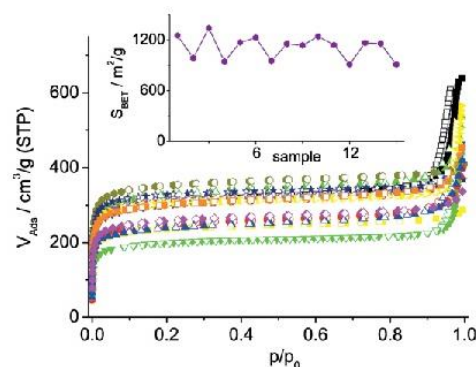


Figure 9.  $\text{N}_2$  sorption isotherms and BET surface areas for different fractions of zirconium fumarate synthesized in the flow reactor.

Compared to the reported surface areas and the values observed for zirconium fumarate prepared by microwave heating (Table 4) the porosity is for most fractions substantially higher. We assume that this is due to a higher number of framework defects, resulting from the comparably short reaction time and low temperature.

Inspired by these results, we also investigated the flow synthesis of another zirconium MOF, UiO-66- $\text{NH}_2$ , which is based on aminoterephthalic acid as linker molecules. Hence we used nearly identical reaction parameters and conditions as for the synthesis of zirconium fumarate. Initially we prepared four litres of 0.2 M starting slurry of  $\text{ZrOCl}_2 \cdot 8\text{H}_2\text{O}$  and aminoterephthalic acid [258.9 g (0.8 mol)  $\text{ZrOCl}_2 \cdot 8\text{H}_2\text{O}$  and 142.3 g (0.79 mol)  $\text{H}_2\text{BDC-NH}_2$  in a mixture of 2 L of water and 2 L of acetic acid] in a beaker placed on a magnetic stirrer to yield a homogeneous slurry feed. The pump was adjusted to 55 strokes per minute and the stroke length was set to 50%. The reaction temperature in the oven was set to 85 °C. Because of the different composition of the slurry this resulted in a reaction time of about 20 min. The product fractions were again collected in five-minute batches and 20 mL of each batch were further treated with sodium acetate solution and ethanol as described for zirconium fumarate. All products show the typical powder pattern for UiO-66 structures (Figure S14). In order to estimate the yield, we assumed that based on literature values<sup>[49]</sup> 30 wt.-% of the product consists of adsorbed water and the zirconium to linker ratio is approximately 6:5. The average yield of this reaction is approximately  $74 \pm 5\%$  which is slightly higher than for zirconium fumarate. In addition, only the very first sample shows a lower yield compared to the other samples, possibly

Table 5. The absolute yields (based on 20 mL fractions), relative yields, apparent specific surface areas and micropore volumes of all zirconium fumarate samples.

Time slot	Yield [mg]	Yield [%]	$S_{\text{BET}}$ [ $\text{m}^2/\text{g}$ ]	$V_{\text{MC}}$ [ $\text{cm}^3/\text{g}$ ]
1	675	51	1255	0.52
2	772	58	987	0.42
3	786	59	1342	0.57
4	805	61	946	0.42
5	806	61	1173	0.49
6	721	54	1229	0.50
7	894	67	954	0.41
8	892	67	1156	0.49
9	932	70	1138	0.49
10	910	69	1242	0.53
11	860	65	1142	0.49
12	812	61	913	0.39
13	781	59	1167	0.50
14	827	62	1160	0.49
15	532	40	911	0.38

due to mixing with pure water in the flow reactor (Table 6). The real-time yield of 325 g per hour and the STY of 4346 kg/m<sup>3</sup>/d are again remarkably high.

Table 6. The absolute yields (based on 20 mL fractions), relative yields, apparent specific surface areas and micropore volumes of all UiO-66-NH<sub>2</sub> samples.

Charge	Yield [g]	Yield [%]	S <sub>BET</sub> [m <sup>2</sup> /g]	V <sub>Mic</sub> [cm <sup>3</sup> /g]
1	1.06	65	1164	0.47
2	1.22	75	1194	0.50
3	1.30	79	1179	0.48
4	1.17	72	1149	0.47
5	1.32	81	1190	0.50
6	1.17	72	1150	0.48
7	1.17	72	1224	0.51
8	1.17	72	1110	0.46
9	1.15	70	1205	0.50
10	1.15	70	1100	0.45
11	1.22	75	1118	0.44

Prior to physisorption experiments the samples were activated at 120 °C under vacuum (0.1 mbar). The shape of the isotherms indicates microporosity and the evaluated specific surface areas and micropore volumes are in the range of 1150 ± 50 m<sup>2</sup>/g and about 0.5 cm<sup>3</sup>/g for all samples (Figure 10).

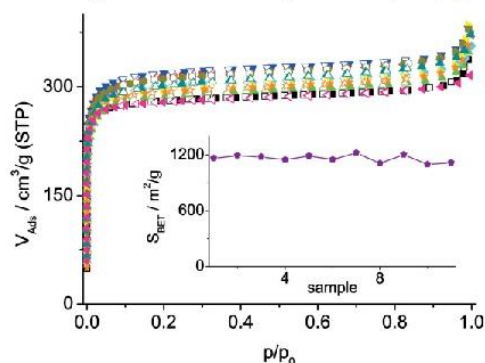


Figure 10. N<sub>2</sub> sorption isotherms and BET surface areas for different fractions of UiO-66-NH<sub>2</sub> synthesized in the flow reactor.

Thus, UiO-66-NH<sub>2</sub> is in general obtained with higher yields and improved homogeneity of the products, which show less fluctuations regarding porosity compared to zirconium fumarate. We assume that this can be attributed to the different solubility and reactivity of the linker molecules under the investigated green synthesis conditions.

## Conclusions

Summarizing our results we were able to develop a versatile green method for the synthesis and activation of diverse zirconium MOFs at gram to multigram scale. These conditions are suitable for batch and continuous synthesis and yield compounds with high porosity and crystallinity. This demonstrates a further step towards the synthesis of MOFs at an industrial scale. Nevertheless, there is still plenty of room for optimization. Thus, the particle size of the resulting products is not yet tunable and therefore impedes the separation at lab scale, although, as shown for zirconium fumarate, the addition of a

polymer can substantially facilitate this process. Moreover, suitable methods have to be investigated in order to purify the produced liquid waste or to recycle it. We are also currently investigating how the yields of the reactions could be further increased.

## Experimental Section

**Methods:** All chemicals were used as received. Powder X-ray diffraction data were measured with a STOE Stadi-P powder diffractometer in transmission geometry (Cu-K<sub>α1</sub> radiation) using a Mythen detector system. The thermogravimetric (TG) analyses were carried out under air with a Netzsch STA 449 F1 Jupiter. The samples were heated in Al<sub>2</sub>O<sub>3</sub> crucibles and the TG data were corrected for buoyancy and current effects. Gas sorption experiments were performed with BEL JAPAN INC. Belsorp<sub>max</sub> and Belsorp<sub>mini</sub> instruments. The software used for indexing and refinement of the powder data was TOPAS Academics.<sup>[50]</sup> Structural models (see Supporting Information) were set up using Materials Studio.<sup>[51]</sup> The synthesis at 20 mL scale was carried out using glass vials equipped with a magnetic stirrer in a Biotage Initiator microwave oven.

### Syntheses in the Microwave Oven

**Zirconium Fumarate:** A mixture of 464 mg (4 mmol) fumaric acid, 1.288 g (4 mmol) ZrOCl<sub>2</sub>·8H<sub>2</sub>O, water (10 mL) and acetic acid (10 mL) was heated at 95 °C for 1 h whilst stirring. The resulting mixture was centrifuged (19000 rpm, 30 min), redispersed in aqueous sodium acetate solution (15 mL, 0.1 M; twice) and water (15 mL; once) and finally dried at 95 °C in air overnight; yield 820 mg (ca. 88 %).

**Zirconium Mesaconate:** A mixture of 520 mg (4 mmol) mesaconic acid, 1.288 g (4 mmol) ZrOCl<sub>2</sub>·8H<sub>2</sub>O, water (10 mL) and acetic acid (10 mL) was heated at 95 °C for 5 h whilst stirring. The resulting mixture was centrifuged (19000 rpm, 30 min), redispersed in aqueous sodium acetate solution (15 mL, 0.1 M; twice) and water (15 mL; once) and finally dried at 95 °C in air overnight; yield 440 mg (ca. 40 %).

**UiO-66-(OH)<sub>2</sub>:** A mixture of 792 mg (4 mmol) 2,5-dihydroxyterephthalic acid, 1.288 g (4 mmol) ZrOCl<sub>2</sub>·8H<sub>2</sub>O, water (10 mL) and acetic acid (10 mL) was heated at 95 °C for 1 h whilst stirring. The resulting mixture was centrifuged (19000 rpm, 30 min), redispersed in aqueous sodium acetate solution (15 mL, 0.1 M; twice) and water (15 mL; once) and finally dried at 95 °C in air overnight; yield 1170 mg (ca. 90 %).

**DUT-67:** A mixture of 458 mg (2.66 mmol) 2,5-thiophenedicarboxylic acid, 1.288 g (4 mmol) ZrOCl<sub>2</sub>·8H<sub>2</sub>O, water (10 mL) and acetic acid (10 mL) was heated at 95 °C for 1 h whilst stirring. The resulting mixture was centrifuged (19000 rpm, 30 min), redispersed in aqueous sodium acetate solution (15 mL, 0.1 M; twice) and water (15 mL; once) and finally dried at 95 °C in air overnight; yield 785 mg (ca. 70 %).

**MOF-808:** A mixture of 280 mg (1.33 mmol) 1,3,5-benzenetricarboxylic acid, 1.288 g (4 mmol) ZrOCl<sub>2</sub>·8H<sub>2</sub>O, water (10 mL) and acetic acid (10 mL) was heated at 95 °C for 5 h whilst stirring. The resulting mixture was centrifuged (19000 rpm, 30 min), redispersed in aqueous sodium acetate solution (15 mL, 0.1 M; twice) and water (15 mL; once). Because of the observed instability upon desorption of H<sub>2</sub>O from the pores the product was redispersed one more time in acetone and dried under ambient conditions; yield 820 mg (ca. 81 %).

**Reflux Synthesis of Zirconium Fumarate Polymer Composite:** A mixture of fumaric acid (23.2 g, 0.2 mol),  $ZrOCl_2 \cdot 8H_2O$  (64.4 g, 0.2 mol), water (500 mL) and acetic acid (500 mL) in a 2.5 L flask equipped with a magnetic stirring bar was refluxed for 2 h whilst stirring. After switching off the heating mantle, an aqueous solution of sodium polyacrylate (10 wt.-%, 200 mL;  $MW = 5100$  g/mol) was added whilst stirring while the mixture was still hot. After 30 min stirring the product slurry was recovered by filtration. The raw product was redispersed whilst stirring for 2 h in aqueous sodium acetate solution (1000 mL, 0.1 M) at room temperature and filtered again. The thus-activated MOF was washed on the filter paper with water and acetone and dried for 2 h at 95 °C. It is worth mentioning that the filtration step is the most time-consuming part of the synthesis and can take several hours (2–3 h in our set-up).

#### Syntheses in the Flow Reactor

**Zirconium Fumarate:** A mixture of 116 g (1 mol) fumaric acid, 322 g (1 mol)  $ZrOCl_2 \cdot 8H_2O$ , water (2.5 L) and acetic acid (2.5 L) in a beaker equipped with a large stirring bar was placed on a magnetic stirrer. This stirred slurry was pumped into the flow reactor which had been filled with  $H_2O$  and heated to 85 °C prior to the synthesis. After the initial water filling of the reactor was completely replaced by the reaction mixture we started to collect fractions of the product slurry at intervals of five minutes. Once the reactant slurry was consumed, additional water was filled into the beaker and pumped into the reactor as the pressure-transmitting medium. A sample of 20 mL was taken from each product fraction and centrifuged (15000 rpm, 15 min), redispersed in aqueous sodium acetate solution (20 mL, 0.1 M; once) and ethanol (20 mL; once) and dried at 70 °C overnight.

**UiO-66-NH<sub>2</sub>:** A mixture of 2-aminoterephthalic acid (142.3 g, 0.79 mol),  $ZrOCl_2 \cdot 8H_2O$  (258.9 g, 0.8 mol), water (2 L) and acetic acid (2 L) in a beaker equipped with a large stirring bar was placed on a magnetic stirrer. This stirred slurry was pumped into the flow reactor which had been filled with  $H_2O$  and heated to 85 °C prior to the synthesis. After the initial water filling of the reactor was completely replaced by the reaction mixture we started to collect fractions of the product slurry at intervals of five minutes. Once the reactant slurry was consumed additional water was filled into the beaker and pumped into the reactor as the pressure-transmitting medium. A sample of 20 mL was taken from each fraction and centrifuged (15000 rpm, 20 min), redispersed in aqueous sodium acetate solution (20 mL, 0.1 M; once) and ethanol (20 mL; once) and dried at 70 °C overnight.

**Keywords:** Synthesis design · Flow reactor · Continuous synthesis · Green chemistry · Metal–organic frameworks · Zirconium

- [1] L. J. Murray, M. Dincă, J. R. Long, *Chem. Soc. Rev.* **2009**, 38, 1294–1314.  
 [2] Y. He, W. Zhou, G. Qian, B. Chen, *Chem. Soc. Rev.* **2014**, 43, 5657–5678.  
 [3] P. Valvекens, F. Vermoortele, D. De Vos, *Catal. Sci. Technol.* **2013**, 3, 1435–1445.  
 [4] T. Zhang, W. Lin, *Chem. Soc. Rev.* **2014**, 43, 5982–5993.  
 [5] J. Heine, K. Müller-Buschbaum, *Chem. Soc. Rev.* **2013**, 42, 9232–9242.  
 [6] J. Canivet, A. Fateeva, Y. Guo, B. Coasne, D. Farrusseng, *Chem. Soc. Rev.* **2014**, 43, 5594–5617.  
 [7] N. Stock, S. Biswas, *Chem. Rev.* **2012**, 112, 933–969.  
 [8] M. Gaab, N. Trukhan, S. Maurer, R. Gummaraju, U. Müller, *Microporous Mesoporous Mater.* **2012**, 157, 131–136.  
 [9] J. Juillard, *Pure Appl. Chem.* **1977**, 49, 885–892.  
 [10] E. Buncel, E. A. Symons, *J. Chem. Soc. D* **1970**, 164–165.  
 [11] C. L. Øpstad, T.-B. Melø, H.-R. Sliwka, V. Partali, *Tetrahedron* **2009**, 65, 7616–7619.

- [12] J. C. Trisler, B. F. Freasier, S.-M. Wu, *Tetrahedron Lett.* **1974**, 15, 687–690.  
 [13] G. Majano, J. Pérez-Ramírez, *Adv. Mater.* **2013**, 25, 1052–1057.  
 [14] S. Cadot, L. Veyre, D. Luneau, D. Farrusseng, E. A. Quadrelli, *J. Mater. Chem. A* **2014**, 2, 17757–17763.  
 [15] E. Alvarez, N. Guillou, C. Martineau, B. Bueken, B. Van de Voorde, C. Le Guillouzer, P. Fabry, F. Nouar, F. Taulelle, D. de Vos, J.-S. Chang, K. H. Cho, N. Ramsahye, T. Devic, M. Daturi, G. Maurin, C. Serre, *Angew. Chem. Int. Ed.* **2015**, 54, 3664–3668; *Angew. Chem.* **2015**, 127, 3735.  
 [16] J. H. Cavka, S. Jakobsen, U. Olsbye, N. Guillou, C. Lamberti, S. Bordiga, K. P. Lillerud, *J. Am. Chem. Soc.* **2008**, 130, 13850–13851.  
 [17] M. Kandiah, M. H. Nilsen, S. Usseglio, S. Jakobsen, U. Olsbye, M. Tilset, C. Larabi, E. A. Quadrelli, F. Bonino, K. P. Lillerud, *Chem. Mater.* **2010**, 22, 6632–6640.  
 [18] F. Vermoortele, B. Bueken, G. Le Bars, B. Van de Voorde, M. Vandichel, K. Houthoofd, A. Vimont, M. Daturi, M. Waroquier, U. Olsbye, C. Serre, C. Kirschhock, D. De Vos, *J. Am. Chem. Soc.* **2013**, 135, 11465–11468.  
 [19] C. Gomes Silva, I. Luz, F. X. Llabres i Xamena, A. Corma, H. Garcia, *Chem. Eur. J.* **2010**, 16, 11133–11138.  
 [20] A. Schaate, P. Roy, A. Godt, J. Lippke, F. Waltz, M. Wiebcke, P. Behrens, *Chem. Eur. J.* **2011**, 17, 6643–6651.  
 [21] B. Bueken, H. Reinsch, N. Reimer, I. Stassen, F. Vermoortele, R. Ameloot, N. Stock, C. E. A. Kirschhock, D. De Vos, *Chem. Commun.* **2014**, 50, 10055–10058.  
 [22] G. Zahn, H. A. Schulze, J. Lippke, S. König, U. Szazama, M. Fröba, P. Behrens, *Microporous Mesoporous Mater.* **2015**, 203, 186–194.  
 [23] G. Wißmann, A. Schaate, S. Lilienthal, I. Bremer, A. M. Schneider, P. Behrens, *Microporous Mesoporous Mater.* **2012**, 152, 64–70.  
 [24] Q. Yang, S. Vaesen, F. Ragon, A. D. Wiersum, D. Wu, A. Lago, T. Devic, C. Martineau, F. Taulelle, P. L. Llewellyn, H. Jobic, C. Zhong, C. Serre, G. De Weireld, G. Maurin, *Angew. Chem. Int. Ed.* **2013**, 52, 10316–10320; *Angew. Chem.* **2013**, 125, 10506.  
 [25] S. Biswas, P. Van Der Voort, *Eur. J. Inorg. Chem.* **2013**, 2154–2160.  
 [26] F. Ragon, B. Campo, Q. Yang, C. Martineau, A. D. Wiersum, A. Lago, V. Guillerme, C. Hemsley, J. F. Eubank, M. Vishnuvarthan, F. Taulelle, P. Horcajada, A. Vimont, P. L. Llewellyn, M. Daturi, S. Devautour-Vinot, G. Maurin, C. Serre, T. Devic, G. Clet, *J. Mater. Chem. A* **2015**, 3, 3294–3309.  
 [27] F. Ragon, H. Chevreau, T. Devic, C. Serre, P. Horcajada, *Chem. Eur. J.* **2015**, 21, 7135–7143.  
 [28] Z. Hu, Y. Peng, Z. Kang, Y. Qian, D. Zhao, *Inorg. Chem.* **2015**, 54, 4862–4868.  
 [29] H. Reinsch, I. Stassen, B. Bueken, A. Lieb, R. Ameloot, D. De Vos, *CrystEngComm* **2015**, 17, 331–337.  
 [30] H. Reinsch, B. Bueken, F. Vermoortele, I. Stassen, A. Lieb, K.-P. Lillerud, D. De Vos, *CrystEngComm* **2015**, 17, 4070–4074.  
 [31] M. Sk, S. Bhowal, S. Biswas, *Eur. J. Inorg. Chem.* **2015**, 20, 3317–3322.  
 [32] V. Bon, I. Senkovska, I. A. Baburin, S. Kaskel, *Cryst. Growth Des.* **2013**, 13, 1231–1237.  
 [33] J. Jiang, F. Gándara, Y.-B. Zhang, K. Na, O. M. Yaghi, W. G. Klempner, *J. Am. Chem. Soc.* **2014**, 136, 12844–12847.  
 [34] G. Kickelbick, U. Schubert, *Chem. Ber./Recueil* **1997**, 130, 473–477.  
 [35] M. J. Cliffe, W. Wan, X. Zou, P. A. Chater, A. K. Kleppe, M. G. Tucker, H. Wilhelm, N. P. Funnell, F.-X. Coudert, A. L. Goodwin, *Nat. Commun.* **2014**, 5, 4176.  
 [36] Z. Fang, B. Bueken, D. E. De Vos, R. Fischer, *Angew. Chem. Int. Ed.* **2015**, 54, 7324–7325; *Angew. Chem.* **2015**, 127, 7340–7362.  
 [37] F. Vermoortele, M. Vandichel, B. Van de Voorde, R. Ameloot, M. Waroquier, V. Van Speybroeck, D. De Vos, *Angew. Chem. Int. Ed.* **2012**, 51, 4887–4890; *Angew. Chem.* **2012**, 124, 4971.  
 [38] L. Valenzano, B. Civalieri, S. Chavan, S. Bordiga, M. H. Nilsen, S. Jakobsen, K. P. Lillerud, C. Lamberti, *Chem. Mater.* **2011**, 23, 1700–1718.  
 [39] A. Sonnauer, F. Hoffmann, M. Fröba, L. Kienle, V. Duppele, M. Thommes, C. Serre, G. Férey, N. Stock, *Angew. Chem. Int. Ed.* **2009**, 48, 3791–3794; *Angew. Chem.* **2009**, 121, 3849.  
 [40] H. Furukawa, F. Gandara, Y. Zhang, J. Jiang, W. L. Queen, M. R. Hudson, O. M. Yaghi, *J. Am. Chem. Soc.* **2014**, 136, 4369–4381.  
 [41] C. D. Smith, I. R. Baxendale, G. K. Tranmer, M. Baumann, S. C. Smith, R. A. Lewthwaite, S. V. Ley, *Org. Biomol. Chem.* **2007**, 5, 1562–1568.  
 [42] J. Wagner, J. M. Köhler, *Nano Lett.* **2005**, 5, 685–691.

- [43] M. Gimeno-Fabra, A. S. Munn, L. A. Stevens, T. C. Drage, D. M. Grant, R. J. Kashtiban, J. Sloan, E. Lester, R. I. Walton, *Chem. Commun.* **2012**, 48, 10642–10644.
- [44] K.-J. Kim, Y. J. Li, P. B. Kreider, C.-H. Chang, N. Wannenmacher, P. K. Thallapally, H.-G. Ahn, *Chem. Commun.* **2013**, 49, 11518–11520.
- [45] M. Rubio-Martinez, M. P. Batten, A. Polyzos, K.-C. Carey, J. I. Marde, K.-S. Lim, M. R. Hill, *Sci. Rep.* **2014**, 4, 5443.
- [46] M. Faustini, J. Kim, G.-Y. Jeong, J. Y. Kim, H. R. Moon, W.-S. Ahn, D.-P. Kim, *J. Am. Chem. Soc.* **2013**, 135, 14619–14626.
- [47] L. Paseta, B. Seoane, D. Julve, V. Sebastian, C. Tellez, J. Coronas, *ACS Appl. Mater. Interfaces* **2013**, 5, 9405–9410.
- [48] S. Waitschat, M. T. Wharmby, N. Stock, *Dalton Trans.* **2015**, 44, 11235–11240.
- [49] F. Jeremias, D. Fröhlich, C. Janiak, S. K. Henninger, *New J. Chem.* **2014**, 38, 1846–1852.
- [50] *Topas Academics 4.2*, Coelho Software, **2007**.
- [51] *Materials Studio*, version 5.0, Accelrys Inc., San Diego, CA, USA, **2009**.

---

Received: March 15, 2016

Published Online: June 16, 2016



## 5. Zusammenfassung

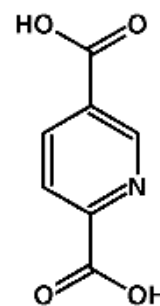
Die Ergebnisse lassen sich grob in zwei Kapitel unterteilen. Im ersten (5.1) sind die Ergebnisse zum Einsatz stickstoffhaltiger Linkermoleküle zur Darstellung von Zr- und Hf-MOFs beschrieben. In Kapitel 5.2 sind die Ergebnisse zusammengefasst, die sich mit der Entwicklung und dem Einsatz von Flussreaktoren zur Darstellung von MOFs beschäftigen.

### 5.1 Synthese von Zr-MOFs mit stickstoffhaltigen Heterozyklen

- Durch den Einsatz von linearen, stickstoffhaltigen Linkern ( $H_2PDC$ ,  $H_2PzDC$  und  $H_2APDC$ ) konnten insgesamt sechs neue MOFs unter wässrigen Synthesebedingungen hergestellt werden. Drei dieser Verbindungen sind isoretikular zu UiO-66-BDC mit den Metallen Zirkonium, Cer und Hafnium und 2,5-Pyridindicarbonsäure als Linkermolekül. M-CAU-39 mit  $M = \text{Zirkonium und Hafnium}$  und Azopyridindicarbonsäure als Linkermolekül ist isoretikular zu *hcp*-UiO-67, wobei der Linker  $H_2APDC$  zum ersten mal für die Synthese eines MOFs eingesetzt wurde. Zudem wurde der neue MOF CAU-22 mit Zirkonium und 2,5-Pyrazindicarbonsäure synthetisiert und charakterisiert. Die Ergebnisse dieser Arbeiten wurden in drei Publikationen veröffentlicht.

#### 5.1.1 Synthese und Charakterisierung von M-UiO-66-PDC

- Unter Einsatz von 2,5-Pyridindicarbonsäure ( $H_2PDC$ ) konnte eine wässrige Reflux Synthese für die Herstellung von M-UiO-66-PDC mit  $M = \text{Zr, Ce und Hf}$  etabliert werden. In Abhängigkeit von dem eingesetzten Metall weisen die Strukturen unterschiedliche Defektdichten und die allgemeine Zusammensetzung  $[M_6(O)_4(OH)_4(Cl)_{2x}(H_2O)_{2x}(PDC)_{6-x}]$  mit  $M = \text{Zr, Ce und Hf}$  auf.
- Die Struktur der Verbindungen wurde durch Rietveld-Verfeinerung bestimmt. Die Zusammensetzung wurde durch thermogravimetrische Analysen, EDX-Messungen, IR- und  $^1H$ -NMR-Spektroskopie bestimmt. Die thermische Stabilität von 220 bzw. 150 °C für Zr-UiO-66-PDC bzw. Ce- und Hf-UiO-66-PDC wurde durch Temperatur-abhängige Pulverdiffraktometrie und die chemische Stabilität durch chemische Stabilitätstest mit anschließender pulverdiffraktometrischer Untersuchung bestimmt. Zusätzlich wurde der



## Zusammenfassung

Zr-O-Cluster durch EXAFS- und die Oxidationsstufe des Ce<sup>4+</sup> durch XANES-Untersuchungen bestätigt.

- Die Verbindungen sind porös gegenüber N<sub>2</sub> und CO<sub>2</sub> bei -196 bzw. 25 °C, die genauen Ergebnisse sind in der folgenden Tabelle dargestellt:

MOF	a <sub>s,BET</sub> /m <sup>2</sup> g <sup>-1</sup>	a <sub>s,BET</sub> /m <sup>2</sup> mmol <sup>-1</sup>	V <sub>mic.</sub> /cm <sup>3</sup> g <sup>-1</sup>	Kap./mg g <sup>-1</sup>	Kap./mg mmol <sup>-1</sup>
Zr-UiO-66	1376	2267	0.54	200	330
Ce-UiO-66	768	1505	0.24	100	196
Hf-UiO-66	383	823	0.18	---	---

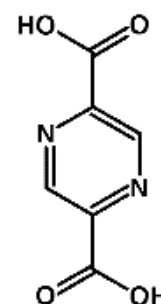
- Zr-UiO-66-PDC und Ce-UiO-66-PDC sind zudem porös gegenüber H<sub>2</sub>O und MeOH bei 25 °C, die genauen Ergebnisse sind in der folgenden Tabelle aufgeführt:

MOF	H <sub>2</sub> O			MeOH		
	Kap./g g <sup>-1</sup>	Kap./g mmol <sup>-1</sup>	α	Kap./g g <sup>-1</sup>	Kap./g mmol <sup>-1</sup>	α
Zr-UiO-66	0.34	0.56	0.01 - 0.2	0.31	0.51	0.2
Ce-UiO-66	0.23	0.45	0.1	0.30	0.59	0.2

- Durch den Einbau von 2,5-Pyridindicarboxylationen konnte die Hydrophilie des UiO-66 Gerüsts gegenüber UiO-66-BDC gesteigert werden.
- Es wurden zyklische Wassersorptionsmessungen mit Zr-UiO-66-PDC durchgeführt um die Stabilität zu testen. Auf Grund von einer Abnahme in der Fernordnung nimmt die Wasseraufnahmekapazität von 0.39 auf 0.26 g g<sup>-1</sup> um 33 % ab.
- Es wurden die weltweit ersten zyklische Methanolsorptionsmessungen mit Zr-UiO-66-PDC durchgeführt um die Stabilität zu messen. Dabei wurde eine Abnahme der Kapazität festgestellt (von 0.41 auf 0.21 g g<sup>-1</sup>), die auf einen Austausch der Hydroxidgruppen durch Methoxygruppen zurück zu führen ist. Dies wurde durch DRIFT-Messungen bestätigt.

### 5.1.2 Synthese und Charakterisierung von CAU-22

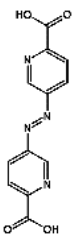
- Durch den Einsatz von 2,5-Pyrazindicarbonsäure in einer wässrigen Solvothermalsynthese konnte CAU-22 nach 24 h Reaktionszeit bei einer Reaktionstemperatur von 120 °C erhalten werden.



## Zusammenfassung

- Die IBU von CAU-22 ist eine eindimensionale Kette von Zr-O-Clustern, die durch kantenverknüpfte hexanukleare  $\{Zr_6(\mu_3-O_4)(\mu_3-OH)_4(\mu-OH)_2\}$ -cluster gebildet werden. Diese Baueinheit ist in der gesamten Zirkoniumchemie noch nie beschrieben worden. Die einzelnen Ketten werden durch insgesamt sechs Linker mit einander verbunden, wodurch ein dreidimensionales Gerüst entsteht. Die Summenformel von CAU-22 lautet:  $[Zr_6(\mu_3-O)_4(\mu_3-OH)_4(\mu-OH)_2(OH)_2(H_2O)_2(HCO_2)_2(PzDC)_3]$ .
- Die Kristallstruktur von CAU-22 wurde durch Rietveld-Verfeinerung ermittelt und die Zusammensetzung durch thermogravimetrische Analysen, EDX-Messungen, IR- und  $^1H$ -NMR-Spektroskopie bestimmt. Die thermische Stabilität von ca. 270 °C wurde durch Temperatur-abhängige Pulverdiffraktometrie erhalten.
- CAU-22 weist ca. 3 Å große, trigonale Poren auf und ist porös gegenüber  $N_2$  bei -196 °C mit einer scheinbaren, spezifischen Oberfläche von ca. 280  $m^2 \cdot g^{-1}$  und einem Mikroporenvolumen (gemessen bei  $p/p_0 = 0.5$ ) von 0.12  $cm^3 \cdot g^{-1}$ .
- Das Gerüst von CAU-22 weist eine hohe Hydrophilie und Wasseraufnahmekapazität von ca. 0.16  $g \cdot g^{-1}$  auf, was durch Wassersorptionsmessungen bei 25 °C ermittelt wurde.

### 5.1.3 Synthese und Charakterisierung von M-CAU-39

- Um eine zu CAU-22 isoretikuläre Verbindung mit einem größeren Porendurchmesser zu erhalten, wurde Azopyridindicarbonsäure in einer wässrigen Synthese als Linkermolekül eingesetzt. Dabei wurde die neue Verbindungen M-CAU-39 mit  $M = Zr$  und  $Hf$  nach 40 min bei 140 °C erhalten.
- 
- Die IBU von CAU-39 ist ein Dimer aus über sechs Hydroxidionen kantenverbrückter hexanuklearer Zr-O-Cluster, wodurch ein dodecanuklearer Zr-O-Cluster  $\{Zr_{12}(\mu_3-O_8)(\mu_3-OH)_8(\mu-OH)_6\}$  gebildet. Diese Baueinheit ist als molekularer Zr-O-Cluster bekannt, als IBU in Zr-MOFs aber erstmals 2017 beschrieben worden. Die einzelnen Zr-O-Cluster werden durch 12 Linkermoleküle miteinander verbunden und bilden ein zwei-dimensionales Gerüst mit einer AB-Stapelung aus. Die Summenformel von M-CAU-39 lautet:  
 $[M_{12}(\mu_3-O)_8(\mu_3-OH)_8(\mu-OH)_6(OH)_6(H_2O)_6(APDC)_6]$ .

## Zusammenfassung

- Die Kristallstruktur von M-CAU-39 wurde durch Rietveld-Verfeinerung ermittelt. Die Zusammensetzung wurde durch thermogravimetrische Analysen, EDX-Messungen und IR-Spektroskopie bestimmt. Die thermische Stabilität von ca. 350 °C wurde durch Temperaturabhängige Pulverdiffraktometrie erhalten.
- CAU-39 weist ca. 6 Å große, hexagonale Poren auf und ist porös gegenüber N<sub>2</sub> bei -196 °C mit einer scheinbaren, spezifischen Oberfläche von ca. 430 bzw. 200 m<sup>2</sup>·g<sup>-1</sup> für Zr-CAU-39 bzw. Hf-CAU-39.

### 5.2 Entwicklung und Anwendung von Flussreaktoren zur Synthese von MOFs

- Es wurden zwei unterschiedliche Flussreaktoren (**Reaktor 1** und **Reaktor 2**) entwickelt mit denen insgesamt sieben verschiedene MOFs hergestellt werden konnten. Es wurden immer große Raum-Zeit-Ausbeuten erhalten, aber auch reale Ausbeuten von bis zu 320 g·h<sup>-1</sup> wurden erreicht. Die Ergebnisse dieser Arbeiten konnten in insgesamt drei Publikationen veröffentlicht werden.

**Reaktor 1**



**Reaktor 2**



In der folgenden Tabelle sind alle in dieser Arbeit beschriebenen, in einem Flussreaktor hergestellten MOF mit dazugehörigen Ausbeuten zusammengefasst.

Reaktor	MOF	STY / kg m <sup>-3</sup> d <sup>-1</sup>	Ausbeute / mg	Ausbeute / g h <sup>-1</sup>
Reaktor 1	UiO-66	428	194	---
Reaktor 1	CAU-13	3049	615	---
Reaktor 1	Cd-STA-12	1269	192	---
Reaktor 1	Ga-TCPP	648	397	---
Reaktor 1	In-TCPP	---	---	---
Reaktor 2	Zr-UiO-66-Fum	2733	---	205
Reaktor 2	Zr-UiO-66-NH <sub>2</sub>	4346	---	325

### 5.2.1 Ergebnisse, die durch den Einsatz von Reaktor 1 erhalten wurden

- **Reaktor 1** besteht aus einem gewickelten Teflonschlauch mit einem Innendurchmesser von 1 mm und einem Reaktorvolumen von ca. 15 ml. Der Reaktor befindet sich in einem Ölbad, welches durch einen Heizrührer erwärmt wird. Die Eduktlösungen werden durch Spritzenpumpen durch den Reaktor befördert. In diesem Reaktor können keine solvothermalen Synthesen durchgeführt werden.
- Mit **Reaktor 1** konnten MOFs mit aromatischen und zyklischen Carbonsäure- und Phosphonsäure- sowie Porphyrin-basierten Linkern hergestellt werden. Neben UiO-66 konnten zudem CAU-13, In-TCPP und Ga-TCPP das erste mal in einem Flussreaktor hergestellt werden. Außerdem wurde Cd-STA-12 unter Verwendung dieses Reaktors entdeckt.

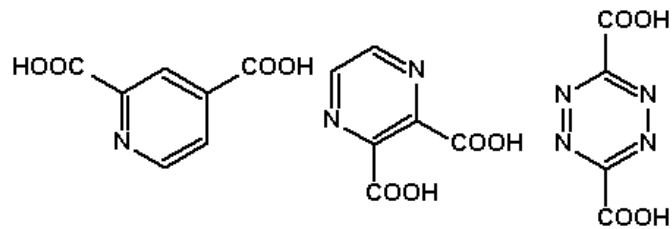
### 5.2.2 Ergebnisse, die durch den Einsatz von Reaktor 2 erhalten wurden

- **Reaktor 2** besteht aus ca. 150 m um ein Aluminiumblech gewickelten Teflonschlauch mit einem Innendurchmesser von 4 mm was zu einem Reaktorvolumen von ca. 1850 ml führt. Beheizt wird der Reaktor durch einen konventionellen Umluftofen und als Förderquelle wird eine Magnetmembranpumpe genutzt. Dadurch ist es möglich auch Suspensionen einzusetzen.
- Es wurden UiO-66-Fum und UiO-66-NH<sub>2</sub> in einer wasserbasierten Synthese hergestellt, wobei detailliert untersucht wurde, ob die Produkte zu jeder Zeit die gleichen Eigenschaften aufweisen. Dazu wurde alle fünf Minuten Proben entnommen und charakterisiert.
- Durch pulverdiffraktometrische Messungen konnte festgestellt werden, dass zu jeder Zeit UiO-66-Fum bzw. UiO-66-NH<sub>2</sub> entstanden ist. Anschließend N<sub>2</sub>-Sorptionsuntersuchungen für UiO-66-Fum bei -196 °C ergaben allerdings scheinbare spezifische Oberflächen mit bis zu 300 m<sup>2</sup>·g<sup>-1</sup> Unterschied. Im Gegensatz dazu zeigten die N<sub>2</sub>-Sorptionsuntersuchungen von UiO-66-NH<sub>2</sub> bei -196 °C eine nahezu identische scheinbare spezifische Oberfläche.
- Die Raum-Zeit Ausbeuten für UiO-66-Fum bzw. UiO-66-NH<sub>2</sub> sind mit 2733 bzw. 4346 kg m<sup>-3</sup> d<sup>-1</sup> relativ hoch, aber besonders hervorzuheben sind die „echten“ Ausbeuten von 205 bzw. 325 g·h<sup>-1</sup>.

## 6. Ausblick

### 6. 1 Synthesemöglichkeiten

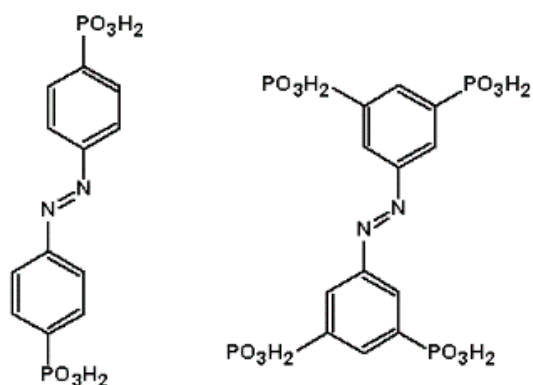
Es konnte eindeutig gezeigt werden, dass es möglich ist mit wasserbasierten Synthesen neue Zr-MOFs mit stickstoffhaltigen Heterozyklen als Linkermoleküle und ungewöhnlichen IBUs herzustellen. Aus diesem Grund könnten weitere Pyridin- oder Pyrazinderivate oder auch andere stickstoffhaltige Heterozyklen als Linker eingesetzt werden.



Zudem könnten die bisher genutzten Linker mit anderen Metallen wie beispielsweise Aluminium umgesetzt werden. Diese sind ebenfalls nicht toxische Metalle mit einer hohen Verfügbarkeit, was für potentielle Anwendungen relevant ist. Diese Metalle weisen eine andere Koordinationsumgebung als Zirkonium auf, wodurch möglicherweise weitere, neue IBUs und neue MOFs synthetisiert werden könnten.

Der Einsatz von CAU-39 als Precursor scheint auf Grund der vielen freien Koordinationsstellen am Zr-O-Cluster und dem Vorliegen einer Schichtverbindung eine vielversprechende Möglichkeit neue, komplexe Mixed-Linker MOFs herzustellen.

Die hier vorgestellte Azokupplung zur Darstellung neuer Linkermoleküle ist sehr einfach durchzuführen und eröffnet ein großes Spektrum an möglichen neuen Linkern wie beispielsweise Azo-Phosphonsäuren, die dann mit zahlreichen Metallsalzen umgesetzt werden könnten.



## 6.2. Flussreaktorsynthesen

Die Art des Energieeintrags hat in vielen Fällen einen Einfluss auf die Produktbildung. So können sowohl unterschiedliche Verbindungen als auch Reaktionsprodukte unterschiedlicher Morphologie erhalten werden. So wurde beispielsweise eine Mikrowellen-gestützte Flussreaktorsynthese für die Darstellung von MOFs beschrieben, der Aufbau könnte aber genutzt werden um weitere MOFs in unseren Reaktoren herzustellen, z.B. zum Starten der Nukleation mit anschließendem Wachstum in den bereits etablierten Flussreaktoren. Dadurch könnten möglicherweise die Partikelgrößen der Verbindungen gezielt gesteuert werden.

Desweiteren könnten mit einem Ultraschall-Flussreaktor auf Grund des hohen, schnellen Energieeintrags weitere MOFs in sehr kurzen Reaktionszeiten hergestellt werden.

Letztlich könnte man aus den individuellen Flussreaktorsystemen mit Ultraschall-, Mikrowellen- und konventionellen Energieeintrag einen komplexen Reaktoraufbau entwickeln, bei dem je nach Syntheseanforderungen die einzelnen Reaktoren in der passenden Reihenfolge über Verbindungsstücke kombiniert werden können.

**7.1 Supporting Information for: Synthesis of M-UiO-66 (M = Zr, Ce or Hf) employing 2,5-pyridinedicarboxylic acid as linker: defect chemistry, framework hydrophilisation and sorption properties**

Electronic Supplementary Material (ESI) for Dalton Transactions.  
This journal is © The Royal Society of Chemistry 2018

**Supporting Information**

**Synthesis of M-UiO-66 (M = Zr, Ce or Hf) employing 2,5-pyridinedicarboxylic acid as linker: defect chemistry, framework hydrophilisation and sorption properties**

*S. Waitschat<sup>a</sup>, D. Fröhlich<sup>b</sup>, H. Reinsch<sup>a</sup>, H. Terraschke<sup>a</sup>, K. A. Lomachenko<sup>c,d</sup>, C. Lamberti<sup>d,e</sup>,  
H. Kummer<sup>b</sup>, T. Helling<sup>b</sup>, M. Baumgartner<sup>b</sup>, S. Henninger<sup>b</sup> and N. Stock<sup>a\*</sup>*

<sup>a</sup> *Institut für Anorganische Chemie, Christian-Albrechts-Universität,  
Max-Eyth-Straße 2, D 24118 Kiel, Germany*

<sup>b</sup> *Fraunhofer-Institute for Solar Energy Systems ISE, Heidenhofstrasse 2, 79110  
Freiburg, Germany*

<sup>c</sup> *European Synchrotron Radiation Facility, 71 Avenue des Martyrs, CS 40220,  
38043 Grenoble Cedex 9, France*

<sup>d</sup> *IRC "Smart Materials", Southern Federal University, Zorge str. 5, 344090  
Rostov-on-Don, Russia*

<sup>e</sup> *Department of Chemistry, CrisDi Centre and INSTM Reference Center, University  
of Turin, Via Giuria 7, 10125 Turin, Italy*

Prof. Dr. Norbert Stock, Tel.: +49-431-880-1675, Fax: +49-431-880-1775,

Email: [stock@ac.uni-kiel.de](mailto:stock@ac.uni-kiel.de)



**Table of Contents**

<b>S1</b>	<b>Methods and Reagents</b> .....	<b>03</b>
<b>S2</b>	<b>Discovery, Optimization and Synthesis of Zr-UiO-66-PDC</b> .....	<b>06</b>
<b>S3</b>	<b>Discovery, Optimization and Synthesis of Hf-UiO-66-PDC</b> .....	<b>10</b>
<b>S4</b>	<b>Discovery, Optimization and Synthesis of Ce-UiO-66-PDC</b> .....	<b>15</b>
<b>S5</b>	<b>Structural Analysis of M-UiO-66-PDC (M = Zr<sup>4+</sup>, Ce<sup>4+</sup>, Hf<sup>4+</sup>):</b> .....	<b>16</b>
<b>S6</b>	<b>NMR Spectroscopy</b> .....	<b>25</b>
<b>S7</b>	<b>IR Spectroscopy</b> .....	<b>27</b>
<b>S9</b>	<b>Thermal &amp; chemical stability</b> .....	<b>28</b>
<b>S10</b>	<b>Luminescence Experiments</b> .....	<b>35</b>
<b>S11</b>	<b>N<sub>2</sub>, CO<sub>2</sub>, H<sub>2</sub>O and MeOH Sorption Experiments</b> .....	<b>38</b>
<b>S12</b>	<b>Ce-UiO-66-PDC Cycling water vapor sorption experiments</b> .....	<b>42</b>
<b>S13</b>	<b>In situ DRIFTS MeOH experiment</b> .....	<b>43</b>
<b>S14</b>	<b>References</b> .....	<b>45</b>

## S1 Methods and Reagents

Initial characterization was performed using a Stoe Stadi P X-ray diffractometer equipped with a  $\theta$ - $\theta$ -stage in transmission geometry using Mo  $K_{\alpha 1}$  radiation and with data collected by a Mythen detector. Powder X-Ray Diffraction (PXRD) patterns for structure determination were measured using a Stoe Stadi P diffractometer in transmission geometry using Cu  $K_{\alpha 1}$  radiation and with data collected using a Mythen detector. Infrared spectra were recorded on a Bruker ALPHA-P A220/D-01 FTIR spectrometer fitted with an ATR unit, over the spectral range of 4000-400  $\text{cm}^{-1}$ . Thermogravimetric analysis was carried out using a NETZSCH STA 429 CD analyzer with a heating rate of 4  $\text{K min}^{-1}$  and under flowing air (flow rate 75  $\text{ml min}^{-1}$ ). Elemental analysis was performed using a EuroVector EuroEA elemental analyzer. NMR spectroscopy was performed using a Bruker DRX 500 spectrometer. Scanning Electron Micrographs were recorded using an SEM, Zeiss Ultra Plus with FE-gun. Sorption isotherms were measured at -196  $^{\circ}\text{C}$  for  $\text{N}_2$  and 25  $^{\circ}\text{C}$  for  $\text{CO}_2$  with a BELSORP-max apparatus (BEL Japan Inc.). MeOH sorption isotherm were obtained with a Quantachrome Autosorb and  $\text{H}_2\text{O}$  sorption isotherms with a Quantachrome Hydrosorb at 25  $^{\circ}\text{C}$ . Powder cycle stabilities were examined in a Setaram<sup>TM</sup> TGA-DSC-111. A humidified argon gas flow (40  $^{\circ}\text{C}$ , 76.3% relative humidity) was generated by a Setaram<sup>TM</sup> WetSys humidity controller and passed through the sample chamber, while the temperature of the sample chamber itself was varied. For multi-cycle ad/desorption experiments, the temperature of the sample chamber was varied between 40  $^{\circ}\text{C}$  and 140  $^{\circ}\text{C}$  with a cycle time of 5 h. Methanol cycle stability was examined in a Surface Measurement Systems Ltd. DVS Vacuum. Before and after cycling, the sample was degassed at 90  $^{\circ}\text{C}$  in vacuum and equilibrium points were taken at 25  $^{\circ}\text{C}$  by increasing the pressure of the gas flow of 5  $\text{ml/min}$  was held constant at 115 hPa while varying the temperature of the sample between 25  $^{\circ}\text{C}$  and 100  $^{\circ}\text{C}$ , which corresponds to a relative pressure  $p/p_0$  of 0.671 and 0.033, with cycle times of 1 h while cooling an 1 h when heating. Luminescence measurements of the solid samples have been carried out in Suprasil A quartz ampoules, at room temperature. For this purpose, a FL-22 Fluorolog3 spectrometer (HORIBA Jobin Yvon GmbH), equipped with a 450 W xenon lamp, a R928P Photomultiplier and an iHR-320-FA triple grating imaging spectrograph was applied. Reflection spectra were also recorded at room temperature from the powdered sample with a Cary 5000 spectrometer (Varian Techtron Pty.) applying  $\text{BaSO}_4$  as reference and diluting material.

Ce  $L_3$ -edge XANES measurements of Ce-UiO-66-PDC and Ce(IV) oxide were performed in the Southern Federal University (Rostov-on-Don, Russia) using Rigaku R-XAS spectrometer. X-ray tube with fixed water-cooled tungsten anode was operating at 12 kV and 80 mA. Incident X-ray beam was monochromatized by a single Johansson-type Ge (220) crystal, ensuring energy resolution of around 1 eV at 5730 eV. Measurements were conducted in transmission mode using an Ar-filled ionization chamber and a scintillation counter to monitor the intensity of incident ( $I_0$ ) and transmitted ( $I_1$ ) radiation respectively. Helium-filled bag filled the space between the X-ray tube, the monochromator and  $I_0$  detector to reduce the X-rays absorption in air.

Ce(III) nitrate XANES spectrum was collected at the BM23 beamline [4] of the European Synchrotron Radiation Facility (Grenoble, France) in transmission mode using Si (111) double-crystal monochromator, Si mirrors for harmonics rejection and N<sub>2</sub>/He-filled ionization chambers for photon detection, yielding comparable resolution with laboratory measurements.

Experimental Zr K-edge (17998 eV) EXAFS spectrum of cubic Zr-UiO-66-PDC was collected at BM23 beamline [4] of the ESRF. The ring was operating in 16-bunch regime with 90 mA maximum current. Experiment was conducted in transmission mode using Ar/He-filled ionization chambers as detectors. Gas pressure in the chambers was 0.4 bar Ar and 1.6 bar He for I<sub>0</sub> and 2 bar of Ar for I<sub>1</sub> resulting in roughly 20% and 70% absorption respectively. Si (111) double-crystal monochromator was used for energy scanning, while Rh-coated mirrors positioned at 3 mrad incidence angle were employed for harmonic rejection. The sample was prepared in the form of self-supporting pellet (13 mm diameter, 80 mg of powder, pressure < 500 kg) resulting in the edge jump of 1.5. Measurements were conducted at room temperature. Sampling step was set to 5 eV for the pre-edge and 0.5 eV in the edge region. In the EXAFS region the spectra were collected with a constant k step of  $\Delta k = 0.035 \text{ \AA}^{-1}$ . Integration time was set to 1 s/point in all spectral region. A total of 6 spectra were collected and averaged before the normalization. Excellent performance of the beamline allowed the data collection up to  $k=23 \text{ \AA}^{-1}$  with high signal-to-noise ratio.

## Anhang

**Table S1.1.** List of reagents used in the synthesis and their suppliers.

Reagent	Supplier	Reagent	Supplier
Zr(SO <sub>4</sub> ) <sub>2</sub> ·4H <sub>2</sub> O	ABCR	Formic acid	BASF
ZrOCl <sub>2</sub> ·8H <sub>2</sub> O	ABCR	Acetic acid	VWR
ZrCl <sub>4</sub>	ABCR	HCl	Walter CMP
Zr(NO <sub>3</sub> ) <sub>2</sub> ·xH <sub>2</sub> O	ABCR	Benzoic acid	Merck
Zr(OH) <sub>2</sub> CO <sub>3</sub> ·ZrO <sub>2</sub>	Riedel-de Haen AG	NaOH	Grüssing
(NH <sub>4</sub> ) <sub>2</sub> [Ce(NO <sub>3</sub> ) <sub>6</sub> ]	Alfa Aesar	Ethanol	Walter CMP
HfCl <sub>4</sub>	ABCR	Dimethylformamide	Grüssing
Dichloromethane	Walter CMP	Acetonitrile	Sigma-Aldrich
Tetrahydrofuran	Walter CMP	Acetone	Walter CMP
n-Hexane	Walter CMP	Dimethylsulfoxide	Grüssing
Toluol	Walter CMP	Ethyl-acetate	Walter CMP

## S2 Discovery, Optimization and Synthesis of Zr-UiO-66-PDC

The systematic investigation of the chemical system  $Zr^{4+}/H_2PDC (H_2L)/H_2O/modulator$  was carried out in a Teflon-lined high-throughput autoclave. DMF as solvent or DMF/water mixtures did not yield Zr-UiO-66-PDC, hence other investigations were carried out in water as the solvent. To optimize the reaction conditions, different metal salts as zirconium source were tested ( $Zr(SO_4)_2 \cdot 4H_2O$ ,  $ZrO(NO_3)_2 \cdot xH_2O$ ,  $ZrCl_4$ ,  $ZrOCl_2 \cdot 8H_2O$  and  $Zr(CO_3)_2$ ). Additionally different metal to linker ratios (1:1, 1:2, 1:3) and different modulator (FA = formic acid) to water ratios were investigated (Tab. S2.1. to Tab. S2.5.). With all metal sources Zr-UiO-66-PDC could be obtained, albeit with different crystallinity, using similar formic acid to water ratios ( $\approx 90\%$  FA) and metal to linker ratios (1:2). For all syntheses, the reaction time was set to 24 h and the reaction temperature to  $120^\circ C$ . Figure S2.1. shows the PXRD pattern of Zr-UiO-66-PDC products obtained employing the optimized reaction conditions with different Zr-salts. Since the synthesis of Zr-UiO-66-PDC with  $ZrOCl_2$  showed the product of highest crystallinity, this reaction was further optimized in Pyrex tubes regarding synthesis time (1 – 4 h) and M:H<sub>2</sub>L ratios. The temperature was set to  $120^\circ C$  and the metal to linker ratios 1:1 and 1:2 were used. According to the PXRD data highly crystalline products are already obtained after 1 h and 3 h using a molar ratio of M : L = 1:2 and 1:1, respectively (Fig. S2.2.). For further investigations a molar ratio M:L = of 1:1 was chosen.

**Table S2.1.** Reaction parameters of the HT-assisted synthesis optimisation of Zr-UiO-66-PDC (M = metal source, L = H<sub>2</sub>PDC, HCOOH = formic acid). The red box indicates the optimized reaction parameters for the synthesis of Zr-UiO-66-PDC with  $Zr(SO_4)_2 \cdot 4H_2O$  as metal source.

M : L	Metal source	M / mg	H <sub>2</sub> PDC / mg	H <sub>2</sub> O / $\mu$ L	HCOOH / $\mu$ L
1 : 3	$Zr(SO_4)_2 \cdot 4H_2O$	35.5	50.1	450	550
1 : 3	$Zr(SO_4)_2 \cdot 4H_2O$	35.5	50.1	400	600
1 : 3	$Zr(SO_4)_2 \cdot 4H_2O$	35.5	50.1	350	650
1 : 3	$Zr(SO_4)_2 \cdot 4H_2O$	35.5	50.1	300	700
1 : 3	$Zr(SO_4)_2 \cdot 4H_2O$	35.5	50.1	250	750
1 : 3	$Zr(SO_4)_2 \cdot 4H_2O$	35.5	50.1	200	800
1 : 3	$Zr(SO_4)_2 \cdot 4H_2O$	35.5	50.1	150	850
1 : 3	$Zr(SO_4)_2 \cdot 4H_2O$	35.5	50.1	100	900
1 : 3	$Zr(SO_4)_2 \cdot 4H_2O$	35.5	50.1	50	950
1 : 2	$Zr(SO_4)_2 \cdot 4H_2O$	35.5	33.4	450	550
1 : 2	$Zr(SO_4)_2 \cdot 4H_2O$	35.5	33.4	400	600
1 : 2	$Zr(SO_4)_2 \cdot 4H_2O$	35.5	33.4	350	650
1 : 2	$Zr(SO_4)_2 \cdot 4H_2O$	35.5	33.4	300	700
1 : 2	$Zr(SO_4)_2 \cdot 4H_2O$	35.5	33.4	250	750
1 : 2	$Zr(SO_4)_2 \cdot 4H_2O$	35.5	33.4	200	800
1 : 2	$Zr(SO_4)_2 \cdot 4H_2O$	35.5	33.4	150	850
1 : 2	$Zr(SO_4)_2 \cdot 4H_2O$	35.5	33.4	100	900
1 : 2	$Zr(SO_4)_2 \cdot 4H_2O$	35.5	33.4	50	950
1 : 1	$Zr(SO_4)_2 \cdot 4H_2O$	35.5	16.7	600	400
1 : 1	$Zr(SO_4)_2 \cdot 4H_2O$	35.5	16.7	500	500
1 : 1	$Zr(SO_4)_2 \cdot 4H_2O$	35.5	16.7	250	750

## Anhang

**Table S2.2.** Reaction parameters of the HT-assisted synthesis of Zr-UiO-66-PDC (M = metal source, L = H<sub>2</sub>PDC, HCOOH = formic acid). The red box indicates the optimized reaction parameters for the synthesis of Zr-UiO-66-PDC with ZrOCl<sub>2</sub>·8H<sub>2</sub>O as metal source.

M : L	Metal source	M / g	H <sub>2</sub> PDC / g	H <sub>2</sub> O / μL	HCOOH / μL
1 : 2	ZrOCl <sub>2</sub> ·8H <sub>2</sub> O	0.0322	0.0334	900	100
1 : 2	ZrOCl <sub>2</sub> ·8H <sub>2</sub> O	0.0322	0.0334	800	200
1 : 2	ZrOCl <sub>2</sub> ·8H <sub>2</sub> O	0.0322	0.0334	700	300
1 : 2	ZrOCl <sub>2</sub> ·8H <sub>2</sub> O	0.0322	0.0334	600	400
1 : 2	ZrOCl <sub>2</sub> ·8H <sub>2</sub> O	0.0322	0.0334	500	500
1 : 2	ZrOCl <sub>2</sub> ·8H <sub>2</sub> O	0.0322	0.0334	400	600
1 : 2	ZrOCl <sub>2</sub> ·8H <sub>2</sub> O	0.0322	0.0334	350	650
1 : 2	ZrOCl <sub>2</sub> ·8H <sub>2</sub> O	0.0322	0.0334	300	700
1 : 2	ZrOCl <sub>2</sub> ·8H <sub>2</sub> O	0.0322	0.0334	200	800
1 : 2	ZrOCl <sub>2</sub> ·8H <sub>2</sub> O	0.0322	0.0334	150	850
1 : 2	ZrOCl <sub>2</sub> ·8H <sub>2</sub> O	0.0322	0.0334	100	900
1 : 2	ZrOCl <sub>2</sub> ·8H <sub>2</sub> O	0.0322	0.0334	50	950
1 : 1	ZrOCl <sub>2</sub> ·8H <sub>2</sub> O	0.0322	0.0167	350	650
1 : 1	ZrOCl <sub>2</sub> ·8H <sub>2</sub> O	0.0322	0.0167	300	700
1 : 1	ZrOCl <sub>2</sub> ·8H <sub>2</sub> O	0.0322	0.0167	200	800
1 : 1	ZrOCl <sub>2</sub> ·8H <sub>2</sub> O	0.0322	0.0167	150	850
1 : 1	ZrOCl <sub>2</sub> ·8H <sub>2</sub> O	0.0322	0.0167	100	900
1 : 1	ZrOCl <sub>2</sub> ·8H <sub>2</sub> O	0.0322	0.0167	50	950

**Table S2.3.** Reaction parameters of the HT-assisted synthesis of Zr-UiO-66-PDC (M = metal source, L = H<sub>2</sub>PDC, HCOOH = formic acid). The red box indicates the optimized reaction parameters for the synthesis of Zr-UiO-66-PDC with ZrCl<sub>4</sub> as metal source.

M : L	Metal source	M / g	H <sub>2</sub> PDC / g	H <sub>2</sub> O / μL	HCOOH / μL
1 : 2	ZrCl <sub>4</sub>	0.0233	0.0334	350	650
1 : 2	ZrCl <sub>4</sub>	0.0233	0.0334	300	700
1 : 2	ZrCl <sub>4</sub>	0.0233	0.0334	200	800
1 : 2	ZrCl <sub>4</sub>	0.0233	0.0334	150	850
1 : 2	ZrCl <sub>4</sub>	0.0233	0.0334	100	900
1 : 2	ZrCl <sub>4</sub>	0.0233	0.0334	50	950

**Table S2.4.** Reaction parameters of the HT-assisted synthesis of Zr-UiO-66-PDC (M = metal source, L = H<sub>2</sub>PDC, HCOOH = formic acid). The red box indicates the optimized reaction parameters for the synthesis of Zr-UiO-66-PDC with Zr(CO<sub>3</sub>)<sub>2</sub> as metal source.

M : L	Metal source	M / g	H <sub>2</sub> PDC / g	H <sub>2</sub> O / $\mu$ L	HCOOH / $\mu$ L
1 : 2	Zr(CO <sub>3</sub> ) <sub>2</sub>	0.0211	0.0334	350	650
1 : 2	Zr(CO <sub>3</sub> ) <sub>2</sub>	0.0211	0.0334	300	700
1 : 2	Zr(CO <sub>3</sub> ) <sub>2</sub>	0.0211	0.0334	200	800
1 : 2	Zr(CO <sub>3</sub> ) <sub>2</sub>	0.0211	0.0334	150	850
1 : 2	Zr(CO <sub>3</sub> ) <sub>2</sub>	0.0211	0.0334	100	900
1 : 2	Zr(CO <sub>3</sub> ) <sub>2</sub>	0.0211	0.0334	50	950
1 : 1	Zr(CO <sub>3</sub> ) <sub>2</sub>	0.0211	0.0167	350	650
1 : 1	Zr(CO <sub>3</sub> ) <sub>2</sub>	0.0211	0.0167	300	700
1 : 1	Zr(CO <sub>3</sub> ) <sub>2</sub>	0.0211	0.0167	200	800
1 : 1	Zr(CO <sub>3</sub> ) <sub>2</sub>	0.0211	0.0167	150	850
1 : 1	Zr(CO <sub>3</sub> ) <sub>2</sub>	0.0211	0.0167	100	900
1 : 1	Zr(CO <sub>3</sub> ) <sub>2</sub>	0.0211	0.0167	50	950

**Table S2.5.** Reaction parameters of the HT-assisted synthesis of Zr-UiO-66-PDC (M = metal source, L = H<sub>2</sub>PDC, HCOOH = formic acid). The red box indicates the optimized reaction parameters for the synthesis of Zr-UiO-66-PDC with ZrO(NO<sub>3</sub>)<sub>2</sub>·xH<sub>2</sub>O as metal source.

M : L	Metal source	M / g	H <sub>2</sub> PDC / g	H <sub>2</sub> O / $\mu$ L	HCOOH / $\mu$ L
1 : 2	ZrO(NO <sub>3</sub> ) <sub>2</sub> ·xH <sub>2</sub> O	0.0231	0.0334	350	650
1 : 2	ZrO(NO <sub>3</sub> ) <sub>2</sub> ·xH <sub>2</sub> O	0.0231	0.0334	300	700
1 : 2	ZrO(NO <sub>3</sub> ) <sub>2</sub> ·xH <sub>2</sub> O	0.0231	0.0334	200	800
1 : 2	ZrO(NO <sub>3</sub> ) <sub>2</sub> ·xH <sub>2</sub> O	0.0231	0.0334	150	850
1 : 2	ZrO(NO <sub>3</sub> ) <sub>2</sub> ·xH <sub>2</sub> O	0.0231	0.0334	100	900
1 : 2	ZrO(NO <sub>3</sub> ) <sub>2</sub> ·xH <sub>2</sub> O	0.0231	0.0334	50	950

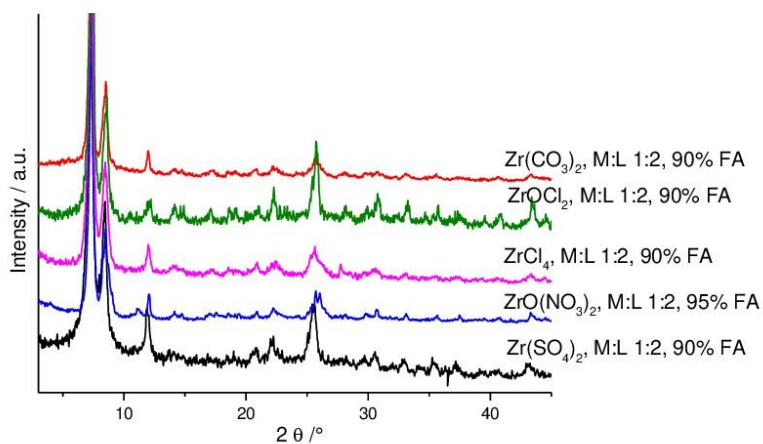


**Fig. S2.1.** PXRD patterns of the Zr-UiO-66-PDC products obtained using different Zr-salts and the respectively optimized reaction conditions (CuK $\alpha_1$  radiation).

**Table S2.6.** Reaction time optimization of the optimized synthesis conditions for Zr-UiO-66-PDC with  $\text{ZrOCl}_2$  varied in Pyrex tubes (M = metal source, L =  $\text{H}_2\text{PDC}$ ,  $\text{HCOOH}$  = formic acid). The red box shows the optimized reaction parameters for the synthesis of Zr-UiO-66-PDC.

M : L	Metal source	M / g	$\text{H}_2\text{PDC}$ / g	$\text{H}_2\text{O}$ / $\mu\text{L}$	$\text{HCOOH}$ / $\mu\text{L}$	T / $^\circ\text{C}$	t / h
1 : 1	$\text{ZrOCl}_2 \cdot 8\text{H}_2\text{O}$	0.0856	0.044	300	2700	120	1
1 : 1	$\text{ZrOCl}_2 \cdot 8\text{H}_2\text{O}$	0.0856	0.044	300	2700	120	2
1 : 1	$\text{ZrOCl}_2 \cdot 8\text{H}_2\text{O}$	0.0856	0.044	300	2700	120	3
1 : 1	$\text{ZrOCl}_2 \cdot 8\text{H}_2\text{O}$	0.0856	0.044	300	2700	120	4
1 : 2	$\text{ZrOCl}_2 \cdot 8\text{H}_2\text{O}$	0.0856	0.088	300	2700	120	1
1 : 2	$\text{ZrOCl}_2 \cdot 8\text{H}_2\text{O}$	0.0856	0.088	300	2700	120	2
1 : 2	$\text{ZrOCl}_2 \cdot 8\text{H}_2\text{O}$	0.0856	0.088	300	2700	120	3
1 : 2	$\text{ZrOCl}_2 \cdot 8\text{H}_2\text{O}$	0.0856	0.088	300	2700	120	4

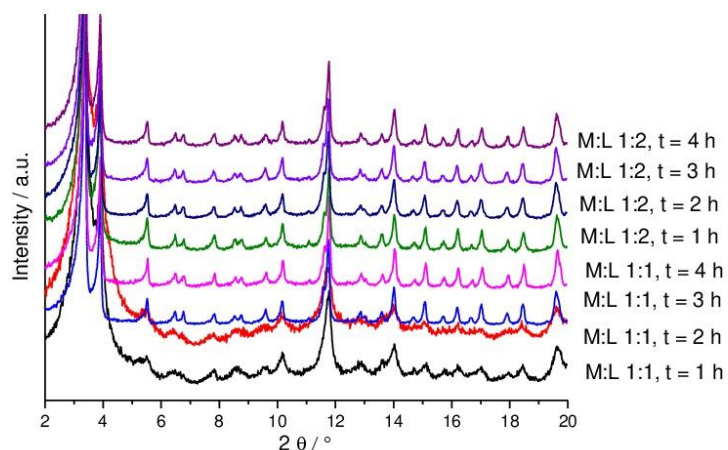


**Fig. S2.2.** PXRD patterns of the Zr-UiO-66-PDC products obtained using  $\text{ZrOCl}_2 \cdot 8\text{H}_2\text{O}$  as Zr-salt, formic acid as modulator with two different metal to linker ratios and temperatures from one to four hours ( $\text{MoK}\alpha_1$  radiation).



### S3 Discovery, Optimization and Synthesis of Hf-UiO-66-PDC

The systematic investigation of the synthesis of Zr-UiO-66-PDC showed that the product could not be obtained in DMF or DMF/solvent mixtures. Thus for Hf-UiO-66-PDC every reaction was carried out in water with HfCl<sub>4</sub> as metal salt. In the high throughput investigation different metal to linker ratios (2:1, 1:1, 1:2), different modulators (formic acid, acetic acid and hydrochloric acid) and different water to modulator ratios were tested. (Table S3.1. to Table S.3.3.). The reaction time was 24 h and the reaction temperature was 120 °C for every reaction. The optimized metal to linker ratio is 1:1 with similar water to modulator ratios for all different modulators. PXRD pattern of the optimized reactions are shown in Fig.S.3.1. Reaction time and temperature optimization were carried out with the optimized synthesis utilising acetic acid as modulator in pyrex tubes (Table S3.4.), the PXRD patterns are shown in Fig S.3.2.

**Table S3.1.** Reaction parameters of the HT-assisted synthesis of Hf-UiO-66-PDC (M = metal source, L = H<sub>2</sub>PDC, HCOOH = formic acid). The red box indicates the optimized reaction parameters for the synthesis of Hf-UiO-66-PDC with formic acid as modulator.

M : L	Metal source	M / g	H <sub>2</sub> PDC / g	H <sub>2</sub> O / $\mu$ L	HCOOH / $\mu$ L
1 : 2	HfCl <sub>4</sub>	0.0320	0.0334	1000	0
1 : 2	HfCl <sub>4</sub>	0.0320	0.0334	900	100
1 : 2	HfCl <sub>4</sub>	0.0320	0.0334	800	200
1 : 2	HfCl <sub>4</sub>	0.0320	0.0334	700	300
1 : 2	HfCl <sub>4</sub>	0.0320	0.0334	600	400
1 : 2	HfCl <sub>4</sub>	0.0320	0.0334	500	500
1 : 2	HfCl <sub>4</sub>	0.0320	0.0334	400	600
1 : 2	HfCl <sub>4</sub>	0.0320	0.0334	300	700
1 : 2	HfCl <sub>4</sub>	0.0320	0.0334	200	800
1 : 2	HfCl <sub>4</sub>	0.0320	0.0334	100	900
1 : 2	HfCl <sub>4</sub>	0.0320	0.0334	0	1000
1 : 1	HfCl <sub>4</sub>	0.0320	0.0167	1000	0
1 : 1	HfCl <sub>4</sub>	0.0320	0.0167	900	100
1 : 1	HfCl <sub>4</sub>	0.0320	0.0167	800	200
1 : 1	HfCl <sub>4</sub>	0.0320	0.0167	700	300
1 : 1	HfCl <sub>4</sub>	0.0320	0.0167	600	400
1 : 1	HfCl <sub>4</sub>	0.0320	0.0167	500	500
1 : 1	HfCl <sub>4</sub>	0.0320	0.0167	400	600
1 : 1	HfCl <sub>4</sub>	0.0320	0.0167	300	700
1 : 1	HfCl <sub>4</sub>	0.0320	0.0167	200	800
1 : 1	HfCl <sub>4</sub>	0.0320	0.0167	100	900
1 : 1	HfCl <sub>4</sub>	0.0320	0.0167	0	1000
2 : 1	HfCl <sub>4</sub>	0.0641	0.0167	1000	0
2 : 1	HfCl <sub>4</sub>	0.0641	0.0167	900	100
2 : 1	HfCl <sub>4</sub>	0.0641	0.0167	800	200
2 : 1	HfCl <sub>4</sub>	0.0641	0.0167	700	300
2 : 1	HfCl <sub>4</sub>	0.0641	0.0167	600	400
2 : 1	HfCl <sub>4</sub>	0.0641	0.0167	500	500
2 : 1	HfCl <sub>4</sub>	0.0641	0.0167	400	600
2 : 1	HfCl <sub>4</sub>	0.0641	0.0167	300	700
2 : 1	HfCl <sub>4</sub>	0.0641	0.0167	200	800

## Anhang

2 : 1	HfCl <sub>4</sub>	0.0641	0.0167	100	900
2 : 1	HfCl <sub>4</sub>	0.0641	0.0167	0	1000

**Table S3.2.** Reaction parameters of the HT-assisted synthesis of Hf-UiO-66-PDC (M = metal source, L = H<sub>2</sub>PDC, CH<sub>3</sub>COOH = acetic acid). The red box indicates the optimized reaction parameters for the synthesis of Hf-UiO-66-PDC with acetic acid as modulator.

M : L	Metal source	M / g	H <sub>2</sub> PDC / g	H <sub>2</sub> O / $\mu$ L	CH <sub>3</sub> COOH / $\mu$ L
1 : 2	HfCl <sub>4</sub>	0.0320	0.0334	1000	0
1 : 2	HfCl <sub>4</sub>	0.0320	0.0334	900	100
1 : 2	HfCl <sub>4</sub>	0.0320	0.0334	800	200
1 : 2	HfCl <sub>4</sub>	0.0320	0.0334	700	300
1 : 2	HfCl <sub>4</sub>	0.0320	0.0334	600	400
1 : 2	HfCl <sub>4</sub>	0.0320	0.0334	500	500
1 : 2	HfCl <sub>4</sub>	0.0320	0.0334	400	600
1 : 2	HfCl <sub>4</sub>	0.0320	0.0334	300	700
1 : 2	HfCl <sub>4</sub>	0.0320	0.0334	200	800
1 : 2	HfCl <sub>4</sub>	0.0320	0.0334	100	900
1 : 2	HfCl <sub>4</sub>	0.0320	0.0334	0	1000
1 : 1	HfCl <sub>4</sub>	0.0320	0.0167	1000	0
1 : 1	HfCl <sub>4</sub>	0.0320	0.0167	900	100
1 : 1	HfCl <sub>4</sub>	0.0320	0.0167	800	200
1 : 1	HfCl <sub>4</sub>	0.0320	0.0167	700	300
1 : 1	HfCl <sub>4</sub>	0.0320	0.0167	600	400
1 : 1	HfCl <sub>4</sub>	0.0320	0.0167	500	500
1 : 1	HfCl <sub>4</sub>	0.0320	0.0167	400	600
1 : 1	HfCl <sub>4</sub>	0.0320	0.0167	300	700
1 : 1	HfCl <sub>4</sub>	0.0320	0.0167	200	800
1 : 1	HfCl <sub>4</sub>	0.0320	0.0167	100	900
1 : 1	HfCl <sub>4</sub>	0.0320	0.0167	0	1000
2 : 1	HfCl <sub>4</sub>	0.0641	0.0167	1000	0
2 : 1	HfCl <sub>4</sub>	0.0641	0.0167	900	100
2 : 1	HfCl <sub>4</sub>	0.0641	0.0167	800	200
2 : 1	HfCl <sub>4</sub>	0.0641	0.0167	700	300
2 : 1	HfCl <sub>4</sub>	0.0641	0.0167	600	400
2 : 1	HfCl <sub>4</sub>	0.0641	0.0167	500	500
2 : 1	HfCl <sub>4</sub>	0.0641	0.0167	400	600
2 : 1	HfCl <sub>4</sub>	0.0641	0.0167	300	700
2 : 1	HfCl <sub>4</sub>	0.0641	0.0167	200	800
2 : 1	HfCl <sub>4</sub>	0.0641	0.0167	100	900
2 : 1	HfCl <sub>4</sub>	0.0641	0.0167	0	1000

## Anhang

**Table S3.3.** Reaction parameters of the HT-assisted synthesis of Hf-UiO-66-PDC (M = metal source, L = H<sub>2</sub>PDC, HCl = hydrochloric acid). The red box indicates the optimized reaction parameters for the synthesis of Hf-UiO-66-PDC with HCl as modulator.

M : L	Metal source	M / g	H <sub>2</sub> PDC / g	H <sub>2</sub> O / $\mu$ L	HCl / $\mu$ L
1 : 2	HfCl <sub>4</sub>	0.0320	0.0334	1000	0
1 : 2	HfCl <sub>4</sub>	0.0320	0.0334	900	100
1 : 2	HfCl <sub>4</sub>	0.0320	0.0334	800	200
1 : 2	HfCl <sub>4</sub>	0.0320	0.0334	700	300
1 : 2	HfCl <sub>4</sub>	0.0320	0.0334	600	400
1 : 2	HfCl <sub>4</sub>	0.0320	0.0334	500	500
1 : 2	HfCl <sub>4</sub>	0.0320	0.0334	400	600
1 : 2	HfCl <sub>4</sub>	0.0320	0.0334	300	700
1 : 2	HfCl <sub>4</sub>	0.0320	0.0334	200	800
1 : 2	HfCl <sub>4</sub>	0.0320	0.0334	100	900
1 : 2	HfCl <sub>4</sub>	0.0320	0.0334	0	1000
1 : 1	HfCl <sub>4</sub>	0.0320	0.0167	1000	0
1 : 1	HfCl <sub>4</sub>	0.0320	0.0167	900	100
1 : 1	HfCl <sub>4</sub>	0.0320	0.0167	800	200
1 : 1	HfCl <sub>4</sub>	0.0320	0.0167	700	300
1 : 1	HfCl <sub>4</sub>	0.0320	0.0167	600	400
1 : 1	HfCl <sub>4</sub>	0.0320	0.0167	500	500
1 : 1	HfCl <sub>4</sub>	0.0320	0.0167	400	600
1 : 1	HfCl <sub>4</sub>	0.0320	0.0167	300	700
1 : 1	HfCl <sub>4</sub>	0.0320	0.0167	200	800
1 : 1	HfCl <sub>4</sub>	0.0320	0.0167	100	900
1 : 1	HfCl <sub>4</sub>	0.0320	0.0167	0	1000
2 : 1	HfCl <sub>4</sub>	0.0641	0.0167	1000	0
2 : 1	HfCl <sub>4</sub>	0.0641	0.0167	900	100
2 : 1	HfCl <sub>4</sub>	0.0641	0.0167	800	200
2 : 1	HfCl <sub>4</sub>	0.0641	0.0167	700	300
2 : 1	HfCl <sub>4</sub>	0.0641	0.0167	600	400
2 : 1	HfCl <sub>4</sub>	0.0641	0.0167	500	500
2 : 1	HfCl <sub>4</sub>	0.0641	0.0167	400	600
2 : 1	HfCl <sub>4</sub>	0.0641	0.0167	300	700
2 : 1	HfCl <sub>4</sub>	0.0641	0.0167	200	800
2 : 1	HfCl <sub>4</sub>	0.0641	0.0167	100	900
2 : 1	HfCl <sub>4</sub>	0.0641	0.0167	0	1000

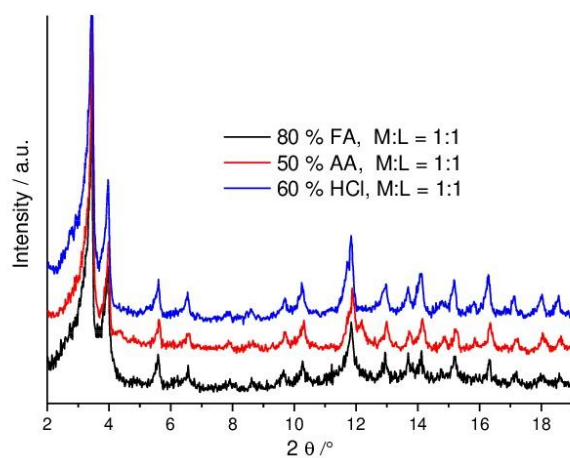


**Fig. S3.1.** PXRD patterns of the Hf-UiO-66-PDC products obtained using different modulators and the respectively optimized reaction conditions (MoK $\alpha_1$  radiation).

**Table S.3.4.** Reaction time and temperature optimization for the synthesis of Hf-UiO-66-PDC with acetic acid as modulator varied in Pyrex tubes (M = metal source, L = H<sub>2</sub>PDC, AA = acetic acid). The red box shows the optimized reaction parameter for the synthesis of Hf-UiO-66-PDC.

M : L	Metal source	M / g	H <sub>2</sub> PDC / g	H <sub>2</sub> O / $\mu$ L	AA / $\mu$ L	T / °C	t / min
1 : 1	HfCl <sub>4</sub>	0.096	0.0501	1500	1500	100	20
1 : 1	HfCl <sub>4</sub>	0.096	0.0501	1500	1500	100	60
1 : 1	HfCl <sub>4</sub>	0.096	0.0501	1500	1500	100	80
1 : 1	HfCl <sub>4</sub>	0.096	0.0501	1500	1500	120	20
1 : 1	HfCl <sub>4</sub>	0.096	0.0501	1500	1500	120	40
1 : 1	HfCl <sub>4</sub>	0.096	0.0501	1500	1500	120	60

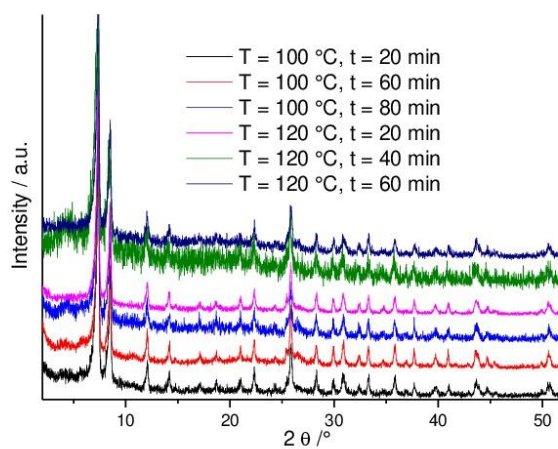


**Fig. S3.2.** PXRD patterns of the Hf-UiO-66-PDC products obtained using acetic acid as modulator, different reaction temperatures (100 and 120 °C) and reactions times (20 to 60 min) (CuK $\alpha_1$  radiation).

#### S4 Discovery, Optimization and Synthesis of Ce-UiO-66-PDC

The reaction time of the synthesis of Ce-UiO-66-PDC was optimized in Pyrex tubes with a reaction temperature of 90 °C (Table S4.1.), the powder patterns are shown in Fig S.4.1.

**Table S4.1.** Reaction parameters of reaction time optimization of the synthesis of Ce-UiO-66-PDC (M = metal source, L = H<sub>2</sub>PDC, HNO<sub>3</sub> = conc. nitric acid). The red box shows the optimized reaction parameters for the synthesis of Ce-UiO-66-PDC.

M : L	Metal source	M / g	H <sub>2</sub> PDC / g	H <sub>2</sub> O / $\mu$ L	HNO <sub>3</sub> / $\mu$ L	t / min
1 : 1	(NH <sub>4</sub> ) <sub>2</sub> [Ce(NO <sub>3</sub> ) <sub>6</sub> ]	0.660	0.167	3000	500	15
1 : 1	(NH <sub>4</sub> ) <sub>2</sub> [Ce(NO <sub>3</sub> ) <sub>6</sub> ]	0.660	0.167	3000	500	30
1 : 1	(NH <sub>4</sub> ) <sub>2</sub> [Ce(NO <sub>3</sub> ) <sub>6</sub> ]	0.660	0.167	3000	500	45
1 : 1	(NH <sub>4</sub> ) <sub>2</sub> [Ce(NO <sub>3</sub> ) <sub>6</sub> ]	0.660	0.167	3000	500	60

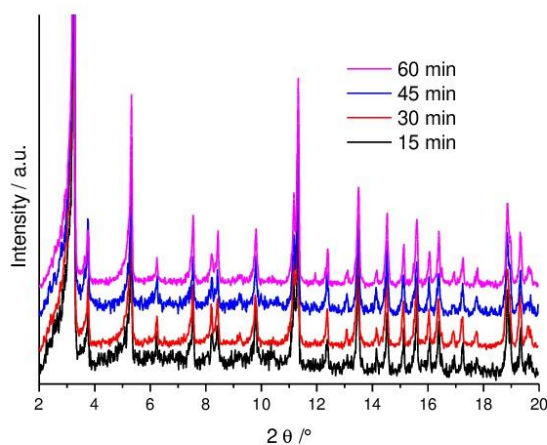


**Fig. S4.1.** PXRD patterns of the Ce-UiO-66-PDC products obtained using (NH<sub>4</sub>)<sub>2</sub>[Ce(NO<sub>3</sub>)<sub>6</sub>] as metal source, conc. nitric acid as modulator and different reactions times (15 to 60 min) (MoK $\alpha$ 1 radiation).

## S5 Structural Analysis of M-UiO-66-PDC (M = Zr, Ce, Hf)

### S5.1 Details of the Rietveld Refinement using fixed occupancies of the linker

Laboratory powder X-ray diffraction data were collected in transmission geometry using a Stoe Stadi P diffractometer fitted with a Cu  $K_{\alpha 1}$  tube radiation source and a Mythen detector. All stages of the refinement were performed using the routines of TOPAS-Academic V5.<sup>1</sup>

For the refinement of the PXRD pattern of **Zr-UiO-66-PDC**, the structure of Zr-UiO-66-BDC was directly used, only accounting for the fractional occupation of the lateral atoms by nitrogen. Moreover the total occupancy for the atoms forming the linker molecule was fixed to 83.3 % being in agreement with five linker molecules per cluster as observed in the TG experiments. It is noted that due to the presence of guest molecules in the MOF, which are modeled as ordered atoms, the occupancy of the linkers cannot be freely refined. The results show that the structural model can describe the data.

For **Ce-UiO-66-PDC**, the pattern is in agreement with the cubic symmetry of the UiO-66 framework. Thus, a starting model for the refinement was developed by replacing the Zr atoms in UiO-66-BDC by Ce atoms and defining the lateral atoms of the aromatic ring as partially occupied by carbon (75 %) and nitrogen atoms (25%). Subsequently this model was fully refined by Rietveld methods. The overall occupancy of the linker molecules was fixed to 1, being in agreement with the results of the TG experiments. Similarly the model for **Hf-UiO-66-PDC** was generated, replacing Zr by Hf atoms. However, the overall occupancy for the linker molecules was fixed to 66 %, being in agreement with the results of the TG experiments. The additional broad peaks are due to the presence of **reo** domains in the particles and were ignored for the refinement. Residual electron density inside the pores was attributed to oxygen atoms representing guest molecules in all these structures. The results show that the structural model can describe the data.

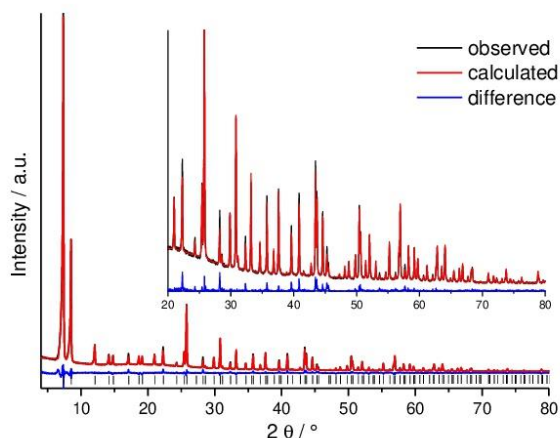


**Fig. S5.1.** Rietveld plot for the final refinement of Zr-UiO-66-PDC using a fixed occupancy factor for the linker molecule. Black line gives the experimental data, red line the calculated fit and the blue line is the difference curve. Black bars indicate the Bragg reflection positions.

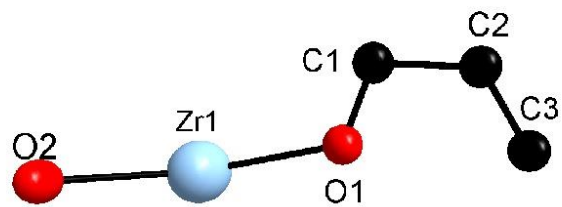


**Fig. S5.2.** Asymmetric unit of Zr-UiO-66-PDC. Oxygen atoms representing water molecules are omitted for clarity.

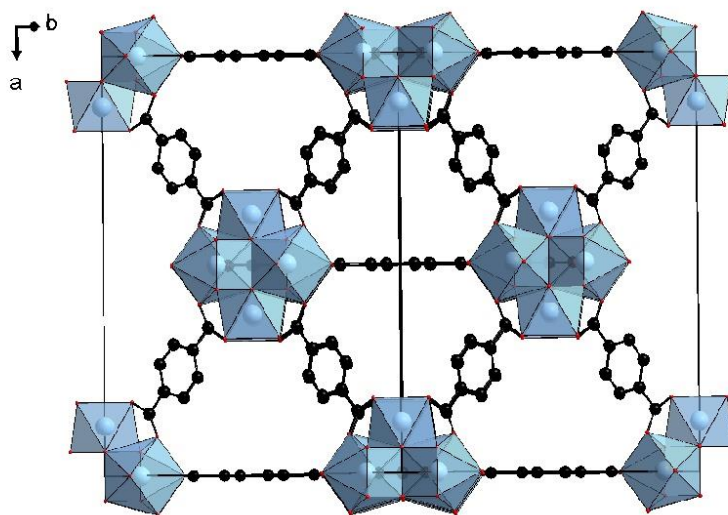


**Fig. S5.3.** Unit cell of Zr-UiO-66-PDC. Oxygen atoms representing water molecules are omitted for clarity.



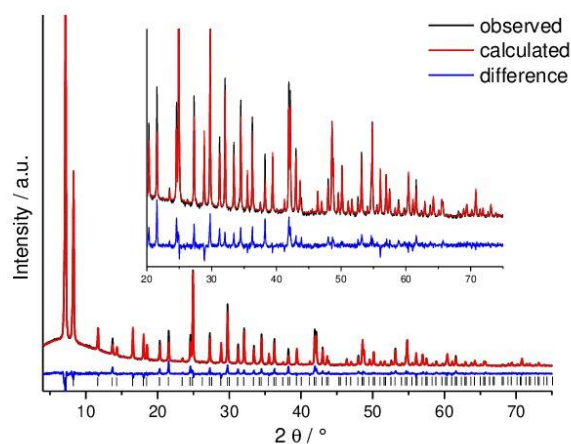


**Fig. S5.4.** Rietveld plot for the final refinement of Ce-UiO-66-PDC using a fixed occupancy factor for the linker molecule. Black line gives the experimental data, red line the calculated fit and the blue line is the difference curve. Black bars indicate the Bragg reflection positions.

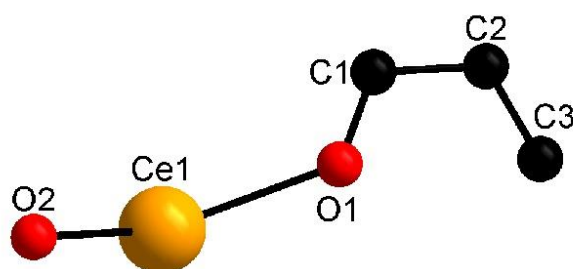


**Fig. S5.5.** Asymmetric unit of Ce-UiO-66-PDC. Oxygen atoms representing water molecules are omitted for clarity.

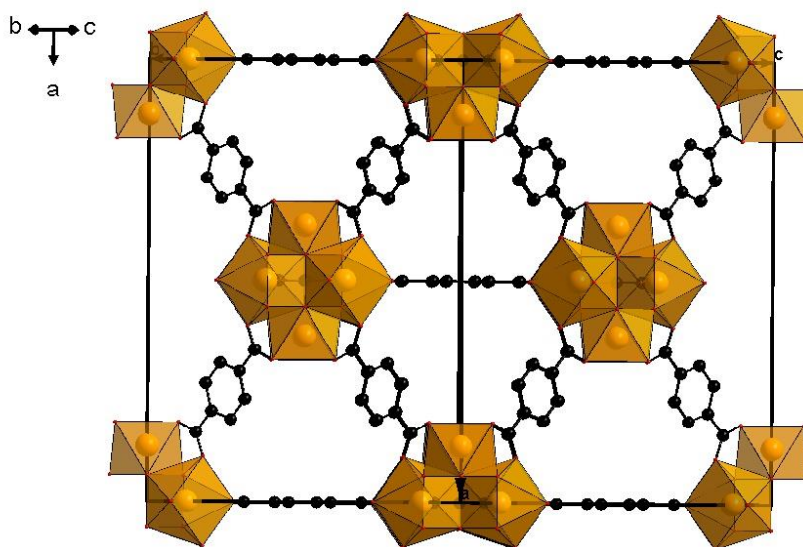


**Fig. S5.6.** Unit cell of Ce-UiO-66-PDC. Oxygen atoms representing water molecules are omitted for clarity.

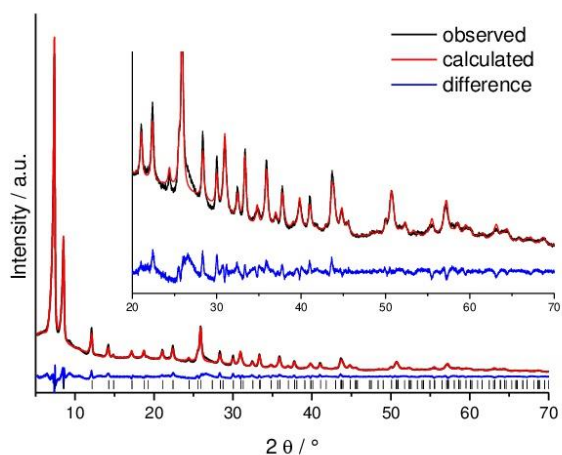


**Fig. S5.7.** Rietveld plot for the final refinement of Hf-UiO-66-PDC using a fixed occupancy factor for the linker molecule. Black line gives the experimental data, red line the calculated fit and the blue line is the difference curve. Black bars indicate the Bragg reflection positions.

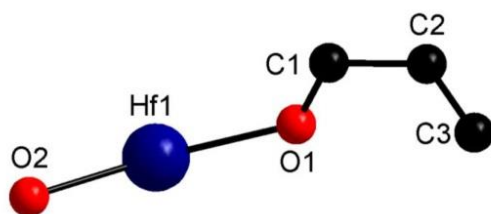


**Fig. S5.8.** Asymmetric unit of Hf-UiO-66-PDC. Oxygen atoms representing water molecules are omitted for clarity.

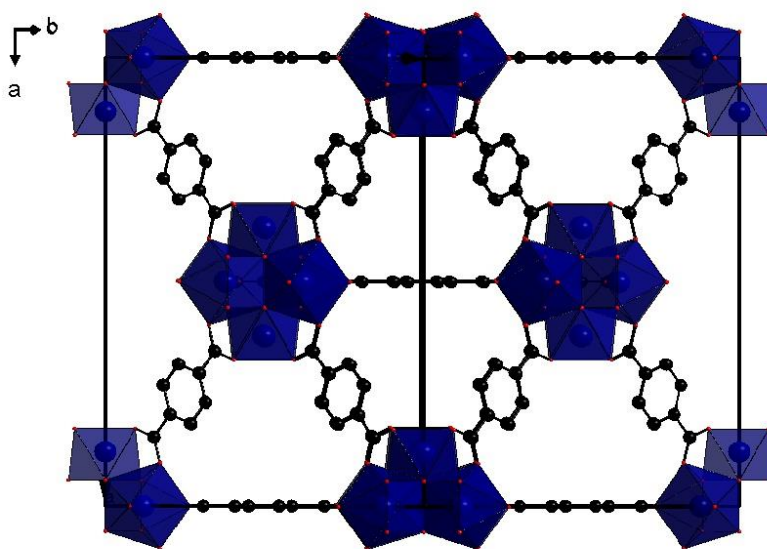


**Fig. S5.9.** Unit cell of Hf-UiO-66-PDC. Oxygen atoms representing water molecules are omitted for clarity.

## Anhang

**Table S5.1.** Crystallographic data for M-UiO-66-PDC (M = Zr, Ce, Hf).

Compound	Zr-UiO-66-PDC	Ce-UiO-66-PDC	Hf-UiO-66-PDC
Space Group	<i>Fm-3m</i>	<i>Fm-3m</i>	<i>Fm-3m</i>
Crystal System	Cubic	Cubic	Cubic
a / Å	20.6819(1)	21.4579(2)	20.5847(8)
b / Å	20.6819(1)	21.4579(2)	20.5847(8)
c / Å	20.6819(1)	21.4579(2)	20.5847(8)
$\alpha$ / °	90	90	90
$\beta$ / °	90	90	90
$\gamma$ / °	90	90	90
V / Å <sup>3</sup>	8846.5(1)	9880.1(3)	8722(1)
Wavelength	Cu K $\alpha$ <sub>1</sub>	Cu K $\alpha$ <sub>1</sub>	Cu K $\alpha$ <sub>1</sub>
R <sub>p</sub> / %	3.6	3.9	3.8
R <sub>wp</sub> / %	4.9	5.6	5.0
GoF	1.3	2.1	2.3
R <sub>Bragg</sub> / %	2.2	5.3	1.9

**Table S5.2.** Comparison of the figures of merit from the Rietveld refinement using the defective model as derived from the results of the other characterisation methods and using a defect-free (ideal) UiO-66-type frameworks.

	Zr-UiO-66-PDC		Hf-UiO-66-PDC	
	defective	ideal	defective	ideal
Ratio M <sup>4+</sup> :Linker	6:5	6:6	6:4	6:6
R <sub>P</sub>	3.6	4.1	3.8	4.4
R <sub>WP</sub>	4.9	5.9	5.0	5.8
GoF	1.3	1.6	2.3	2.7
R <sub>Bragg</sub>	2.2	2.9	1.9	3.0

### S5.2 Zr-UiO-66-PDC Zr K-edge EXAFS data treatment

Preliminary EXAFS data treatment (background subtraction, normalization, averaging) was carried out using the Athena code, while subsequent fitting was made using the Artemis code, both programs being part of Demeter package.<sup>2</sup> The fit was performed in R-space considering  $k^3$ -weighted data. Results of the fit are presented in the Fig. S5.10.

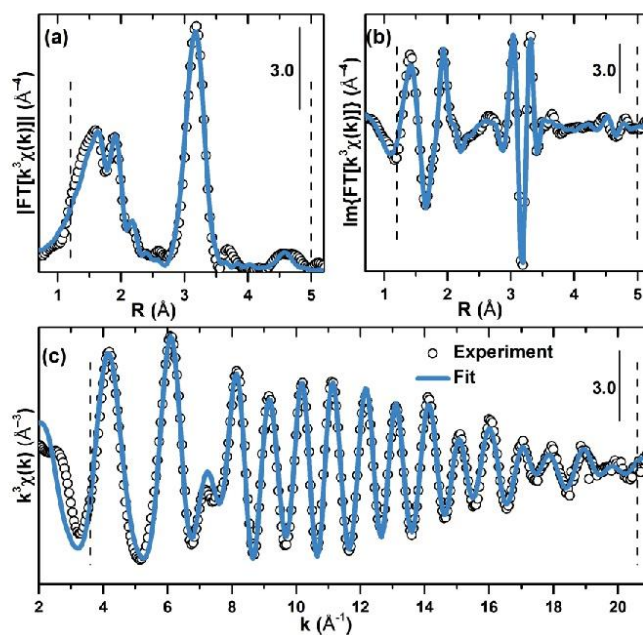


**Fig. S5.10.** Experimental Zr K-edge EXAFS data for Zr-UiO-66-PDC MOF compared to the fit: modulus (a) and imaginary part (b) of the  $k^3$ -weighted phase-uncorrected FT together with the  $k^3\chi(k)$  signal (c) Ranges employed for FT ( $3.7 - 20.6 \text{ \AA}^{-1}$  in  $k$ -space) and fitting ( $1.2 - 5.0 \text{ \AA}$  in  $R$ -space) are shown by the vertical dotted lines on the corresponding panels.

Fitting was performed using the corresponding XRD structure as a model to calculate phase shifts and scattering amplitudes by FEFF6 code.<sup>3</sup> In total 7 scattering paths were included in the fit: single scattering paths formed by  $\mu_3\text{-O}$ , O1, C, Cl, Zr1 and Zr2 atoms and the most intense multiple scattering path formed by O1 and C atoms. 12 fitting parameters were used:

- Energy shift  $\Delta E$  and amplitude reduction factor  $S_0^2$  common for all paths
- Independent elongation/contraction parameters  $\Delta R$  for each of the single-scattering paths apart from Zr2 (5 parameters in total)
- Independent Debye-Waller parameters  $\sigma^2$  for each of the single-scattering paths apart from Zr2 (5 parameters in total).

## Anhang

No additional parameters were introduced to deal with Zr-O1-C and Zr-Zr2 paths. Instead,  $\Delta R$  for these paths were expressed through geometrical relations obtained by solving corresponding triangles and using the parameters already introduced for the single scattering paths:

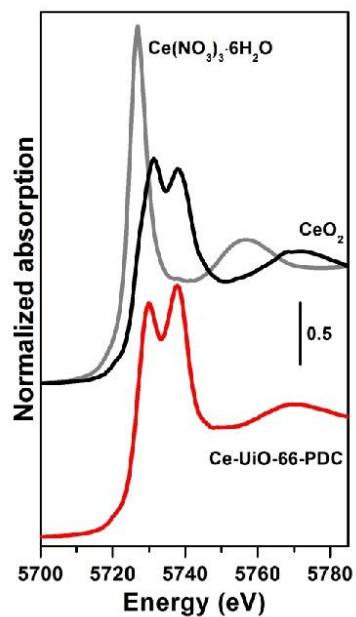
$$\Delta R_{Zr2} = \sqrt{2} \cdot \Delta R_{Zr1}$$
$$\Delta R_{O1-C} = \frac{1}{2}(\Delta R_{O1} + \Delta R_C + (-0.53\Delta R_{O1} + 0.79\Delta R_C))$$

Corresponding Debye-Waller factors were analogously expressed by those of the already parametrized paths:

$$\sigma_{Zr2}^2 = \sigma_{Zr1}^2 \sqrt{\frac{R_{Zr2}}{R_{Zr1}}}$$
$$\sigma_{O1-C}^2 = \sigma_{O1}^2 + \sigma_C^2$$

Besides, degeneracy of Zr-C path was decreased by 17% (from 4 to 3.3) to simulate the missing linker defects, while the degeneracy of Zr-Cl path was set to the remaining 0.7. Indeed, XRD data indicate that each cornerstone is connected in average only by 10 linkers instead of 12, while previous studies report that Cl is likely to fill the coordinative vacancies created by missing linkers.<sup>4</sup>

Based on the adopted model, the fit showed good overall agreement with the experimental EXAFS data and physically reasonable values of the employed parameters. Obtained bond distances are in agreement with the presented XRD data for Zr-UiO-66-PDC MOF and previously published data for standard UiO-66,<sup>5,6</sup> thus complementing the structural characterization of the studied compound.

S5.3 Ce-UiO-66-PDC Ce L<sub>3</sub>-edge XANES spectra

**Fig. S5.11** Ce L<sub>3</sub>-edge XANES spectrum of Ce-UiO-66-PDC MOF compared to Ce(IV) and Ce(III) reference compounds (CeO<sub>2</sub> and Ce(NO<sub>3</sub>)<sub>3</sub>·6H<sub>2</sub>O, respectively), proving the +4 oxidation state of Ce ions in the cornerstones of the MOF. Vertical shift is for the sake of clarity.

**S6 NMR-Spectroscopy**

Samples of M-UiO-66 with M = Zr, Ce and Hf were digested using a NaOD/D<sub>2</sub>O solution and <sup>1</sup>H-NMR spectra were recorded to confirm or exclude the presence of modulator incorporated into the corresponding MOF (Fig.6.1. to Fig.6.3).

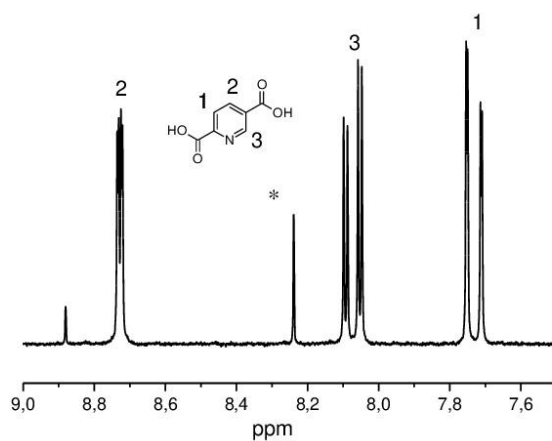


**Fig. S6.1.** <sup>1</sup>H-NMR-spectrum of Zr-UiO-66-PDC dissolved in NaOD/D<sub>2</sub>O. \* indicates a small amount of formate ions (< 0.5 per formula).

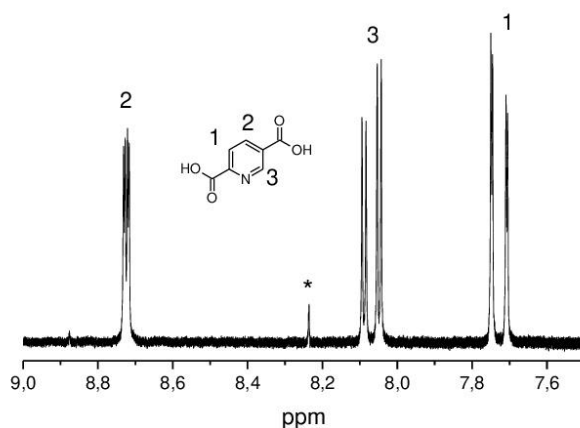


**Fig. S6.2.** <sup>1</sup>H-NMR-spectrum of Ce-UiO-66-PDC dissolved in NaOD/D<sub>2</sub>O. \* indicates a small amount of unknown impurity of about 2%. Since no formic acid was used in the synthesis we exclude the presence of formate ions in the structure of Ce-UiO-66-PDC.



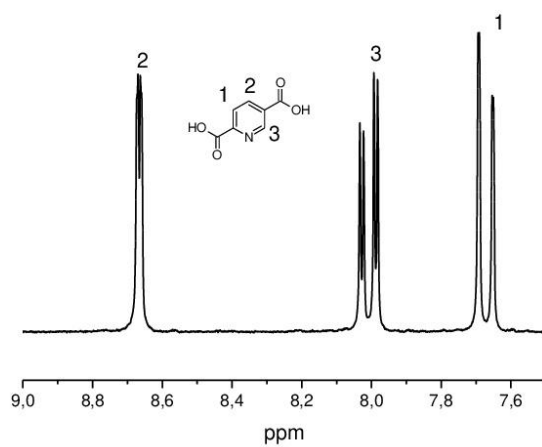


**Fig. S6.3.** <sup>1</sup>H-NMR-spectrum of Hf-UiO-66-PDC dissolved in NaOD/D<sub>2</sub>O shows the absence of modulator in the product.

## S7 Infrared Spectroscopy

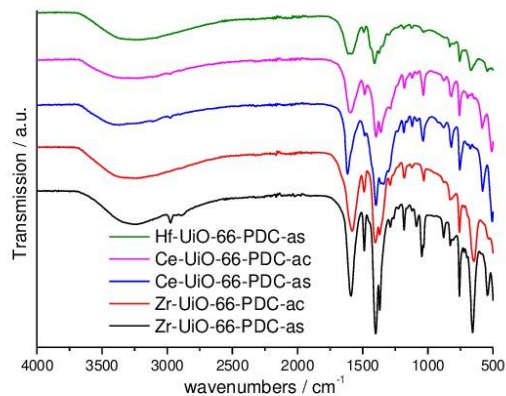


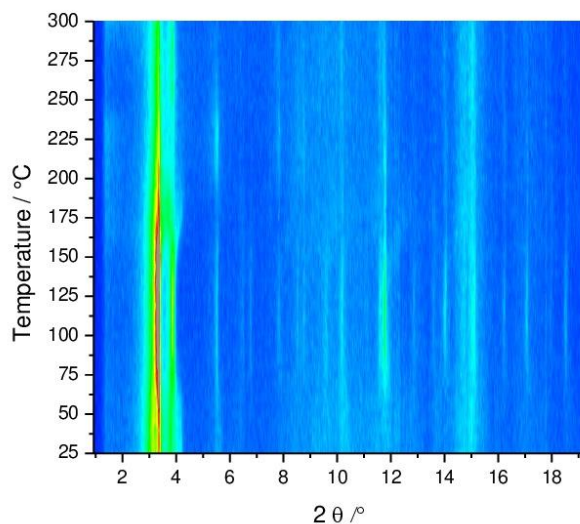
**Fig. S7.1.** FTIR spectra of the as synthesized (as) and the activated (ac) form of M-Uio-66-PDC with M = Zr, Ce, Hf.

**Table S7.1.** Assignment of the bands in the FTIR spectra of as synthesized (as) and the activated (ac) M-Uio-66-PDC with M = Zr, Ce, Hf.

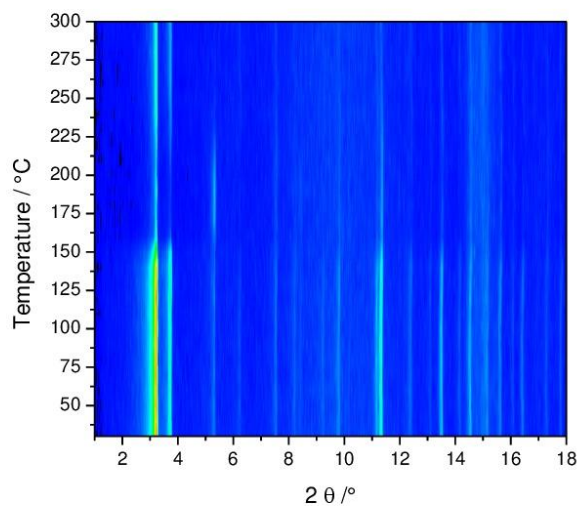
MOF	Wavenumber / $\text{cm}^{-1}$	Intensity	Classification
Zr-Uio-66-PDC-as	2979	w	CH-stretch - $\text{HCOO}^-$
	1590	s	Asymmetric $\text{CO}_2$ -stretch - $\text{PDC}^{2-}$
	1487	m	Symmetric $\text{CO}_2$ -stretch - $\text{PDC}^{2-}$
	752, 659	s, s	2,5-disubstituted Pyridine
Zr-Uio-66-PDC-ac	1584	s	Asymmetric $\text{CO}_2$ -stretch - $\text{PDC}^{2-}$
	1491	m	Symmetric $\text{CO}_2$ -stretch - $\text{PDC}^{2-}$
	752, 650	s, s	2,5-disubstituted Pyridine
Ce-Uio-66-PDC-as	1616	s	Asymmetric $\text{CO}_2$ -stretch - $\text{PDC}^{2-}$
	1484	w	Symmetric $\text{CO}_2$ -stretch - $\text{PDC}^{2-}$
	819, 752	m	2,5-disubstituted Pyridine
Ce-Uio-66-PDC-ac	1594	s	Asymmetric $\text{CO}_2$ -stretch - $\text{PDC}^{2-}$
	1484	m	Symmetric $\text{CO}_2$ -stretch - $\text{PDC}^{2-}$
	820, 758	m, s	2,5-disubstituted Pyridine
Hf-Uio-66-PDC-as	1592	s	Asymmetric $\text{CO}_2$ -stretch - $\text{PDC}^{2-}$
	1487	m	Symmetric $\text{CO}_2$ -stretch - $\text{PDC}^{2-}$
	759, 660	s, s	2,5-disubstituted Pyridine

**S9 Thermal and chemical stability**

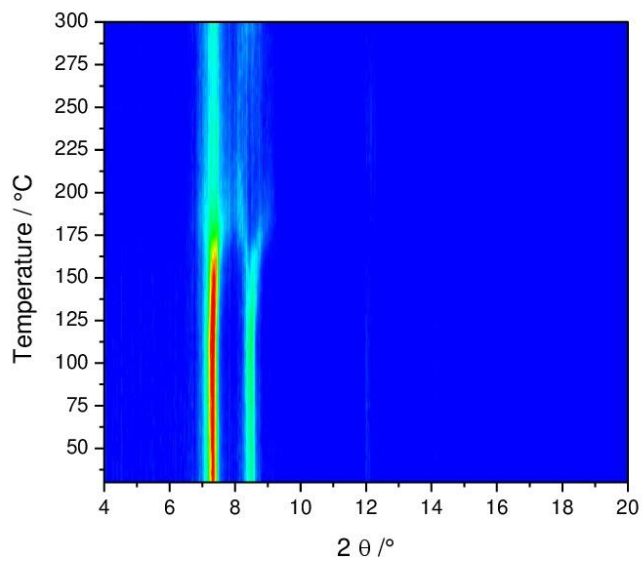
For the temperature dependent PXRD measurements, the samples were prepared in 0.5 mm borosilicate capillaries, which were heated up to 300 °C. A PXRD pattern was measured every 5 °C for five minutes in transmission geometry using Mo  $K_{\alpha 1}$  radiation for Zr- and Ce-UiO-66-PDC. For Hf-UiO-66-PDC Cu  $K_{\alpha 1}$  radiation was used.



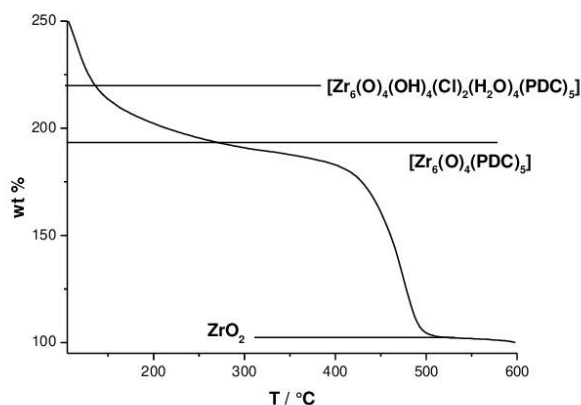
**Fig. S9.1.** Results of the temperature dependent PXRD investigation of Zr-UiO-66-PDC. The compound is thermally stable up to approximately 220°C.



**Fig. S9.2.** Results of the temperature dependent PXRD investigation of Ce-UiO-66-PDC. The compound is thermally stable up to approximately 150°C.



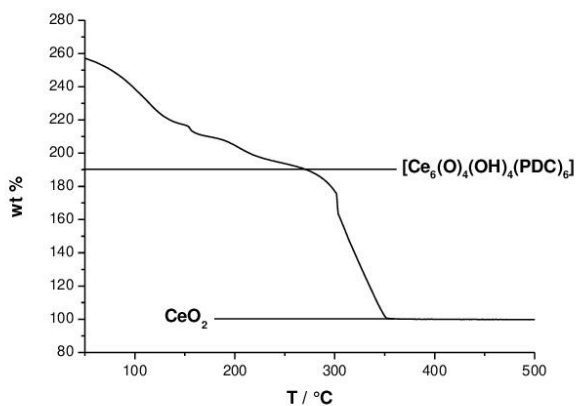
**Fig. S9.3.** Results of the temperature dependent PXRD investigation of Hf-UiO-66-PDC. The compound is thermally stable up to approximately 150°C.



**Fig. S9.4.** TGA plot for Zr-UiO-66-PDC. The MOF shows a relatively high first weight loss event occurring up on dehydration. Zr-UiO-66-PDC is stable up to 350 °C.

**Table S9.1.** Comparison of the thermogravimetric analysis of Zr-UiO-66-PDC and the associated mass loss.

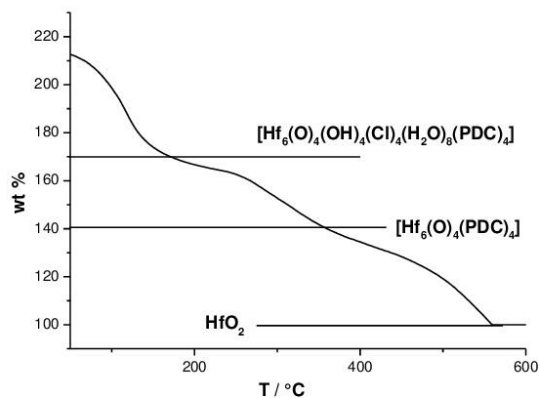
Sum formula of postulated product	T / °C	Theoretical wt %	Measured wt %
Zr-UiO-66-PDC			
[Zr <sub>6</sub> (O) <sub>4</sub> (OH) <sub>4</sub> (Cl) <sub>2</sub> (H <sub>2</sub> O) <sub>4</sub> (PDC) <sub>5</sub> ]	135	220	220
[Zr <sub>6</sub> (O) <sub>4</sub> (PDC) <sub>5</sub> ]	260	194	194
6·ZrO <sub>2</sub>	520	100	100



**Fig. S9.5.** TGA plot for Ce-UiO-66-PDC. The MOF shows a relatively high first weight loss event occurring up on dehydration. Ce-UiO-66-PDC is stable up to 210 °C.

**Table S9.2.** Comparison of the thermogravimetric analysis of Ce-UiO-66-PDC and the associated mass loss.

Sum formula of postulated product Ce-UiO-66-PDC	T / °C	Theoretical wt %	Measured wt %
$[\text{Ce}_6(\text{O})_4(\text{OH})_4(\text{PDC})_6]$	200	190	190
$6 \cdot \text{CeO}_2$	360	100	100

**Fig. S9.6.** TGA plot for Hf-UiO-66-PDC. The MOF shows a relatively high first weight loss event occurring up on dehydration. Hf-UiO-66-PDC is stable up to 220 °C.**Table S9.3.** Comparison of the thermogravimetric analysis of Hf-UiO-66-PDC and the associated mass loss.

Sum formula of postulated product Hf-UiO-66-PDC	T / °C	Theoretical wt %	Measured wt %
$[\text{Hf}_6(\text{O})_4(\text{OH})_4(\text{Cl})_4(\text{H}_2\text{O})_8(\text{PDC})_4]$	170	170	170
$[\text{Hf}_6(\text{O})_4(\text{PDC})_4]$	350	141	141
$6 \cdot \text{HfO}_2$	560	100	100

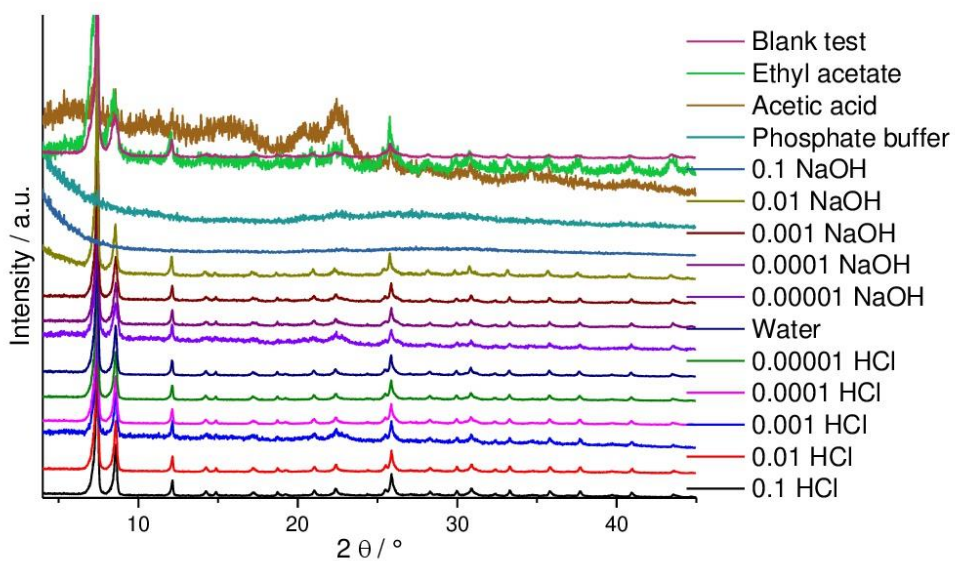


**Fig. S9.7.** PXRD patterns of Zr-UiO-66-PDC after stirring 25 mg in 1ml of aqueous solutions with different pH-values (different concentrations of HCl and NaOH) for 24 h.

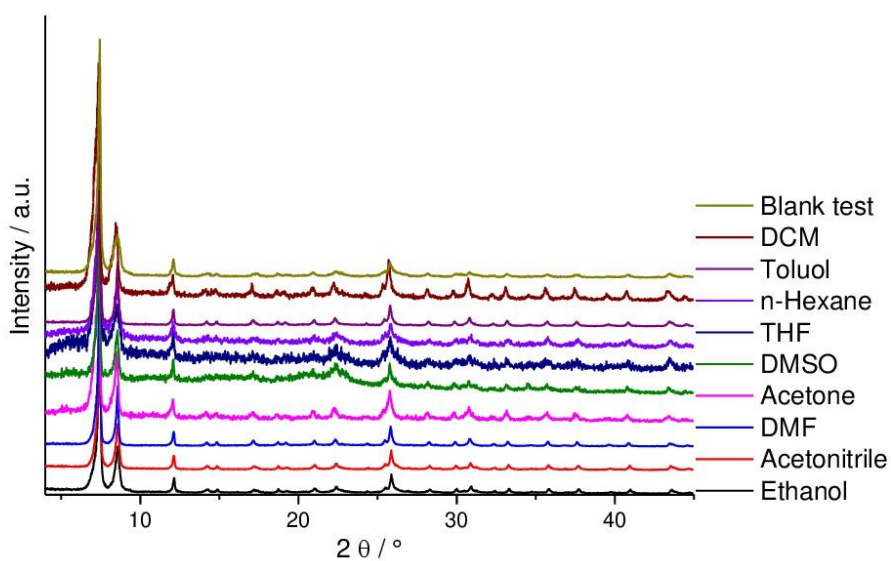


**Fig. S9.8.** PXRD patterns of Zr-UiO-66-PDC after stirring in different organic solvents for 24 h.

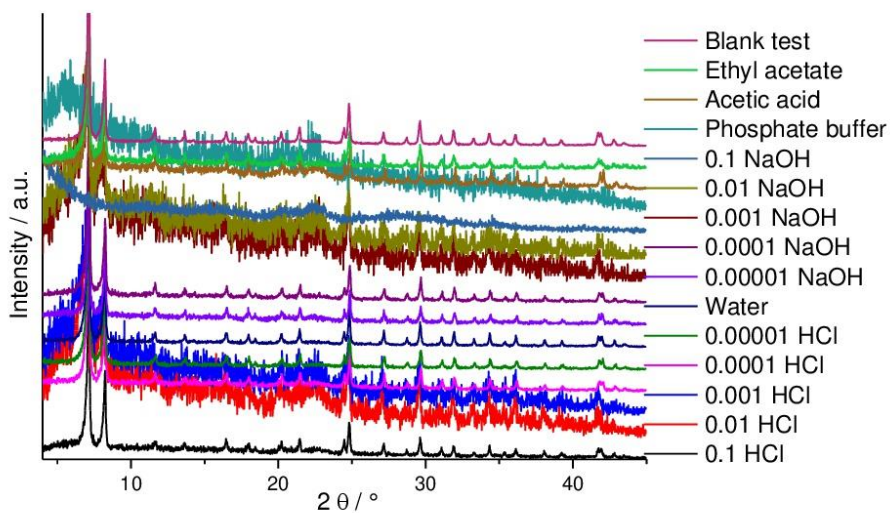


**Fig. S9.9.** PXRD patterns of Ce-UiO-66-PDC after stirring in aqueous solutions with different pH-values due to different concentrations of HCl and NaOH for 24 h.

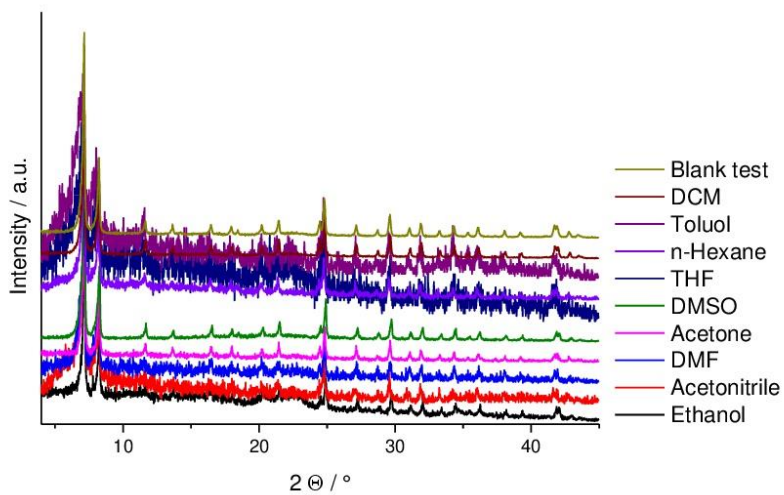


**Fig. S9.10.** PXRD patterns of Ce-UiO-66-PDC after stirring in different organic solvents for 24 h.



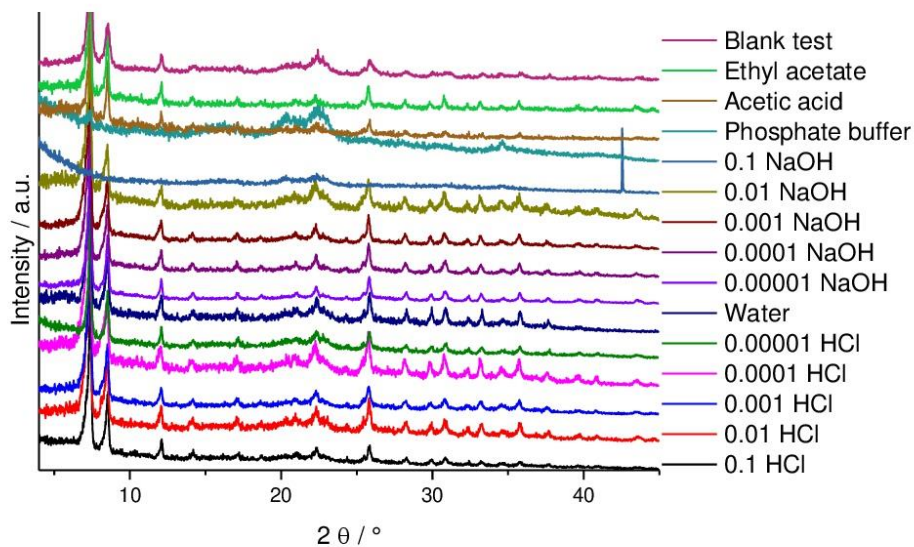


**Fig. S9.11.** PXRD patterns of Hf-UiO-66-PDC after stirring in aqueous solutions with different pH- values due to different concentrations of HCl and NaOH for 24 h.

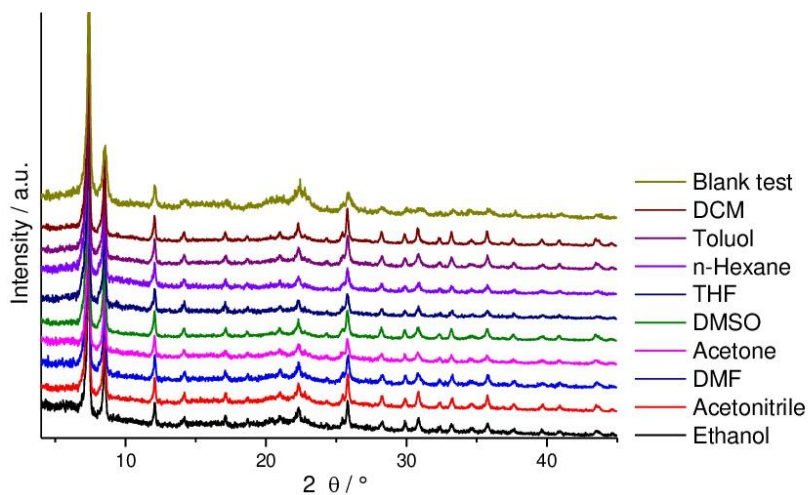


**Fig. S9.12.** PXRD patterns of Hf-UiO-66-PDC after stirring in different organic solvents for 24 h.

## S10 Luminescence Measurements

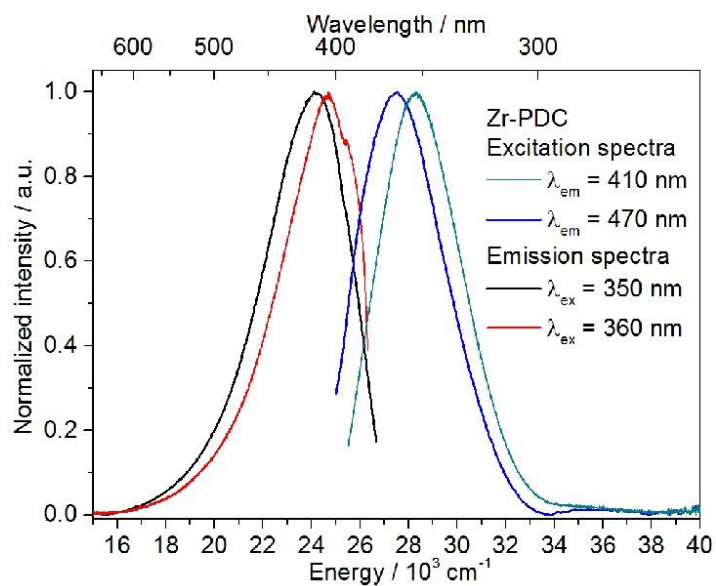
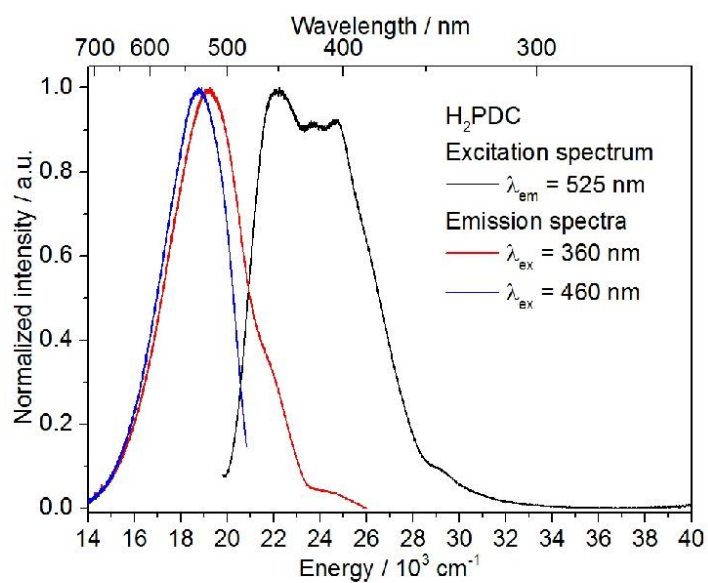


Fig. S10.1. Emission and excitation spectra of Zr-UiO-66-PDC.

Fig. S10.2. Emission and excitation spectra of H<sub>2</sub>PDC.

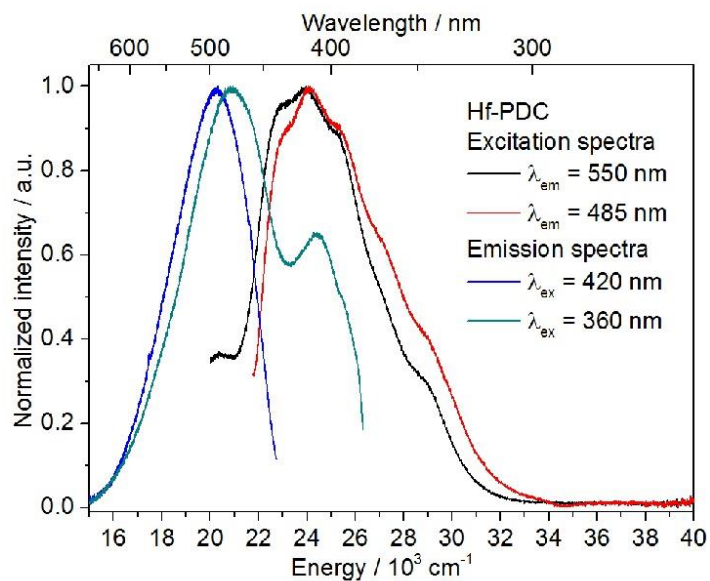


Fig. S10.3. Emission and excitation spectra of Hf-UiO-66-PDC.

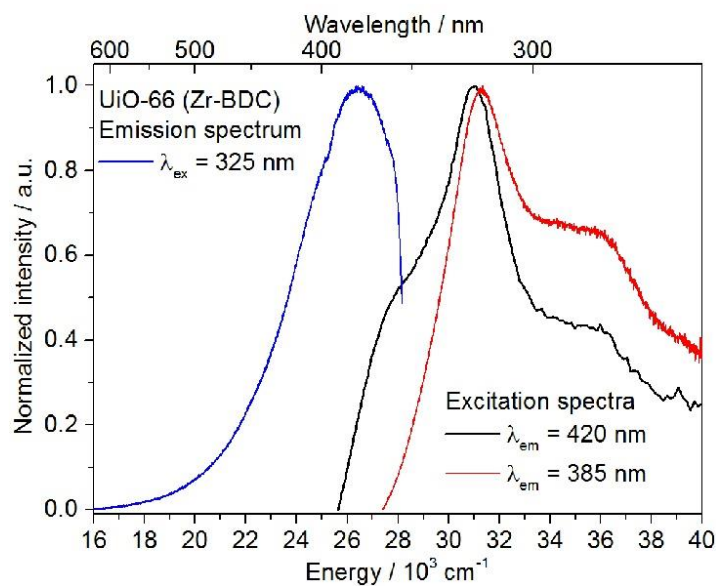
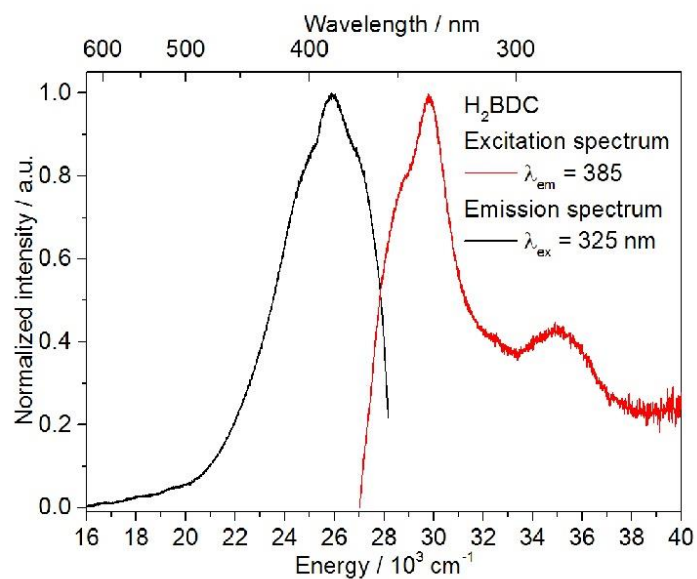
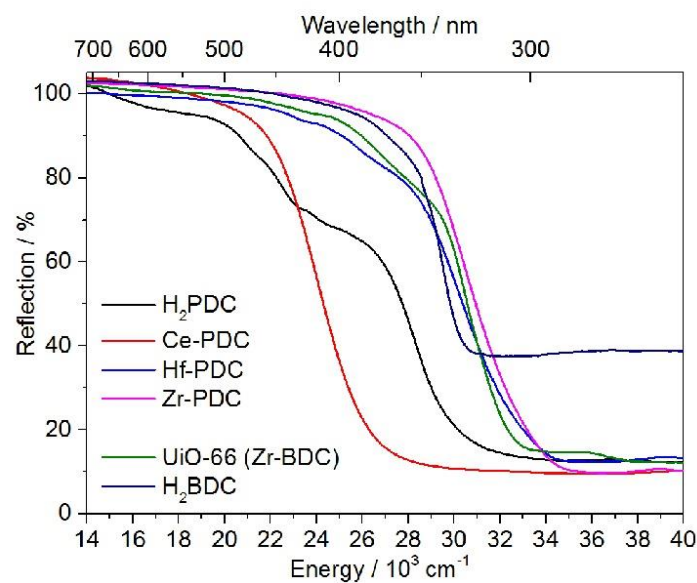


Fig. S10.4. Emission and excitation spectra of Zr-UiO-66-BDC.



**Fig. S10.5.** Emission and excitation spectra of H<sub>2</sub>BDC.



**Fig. S10.6.** Reflection spectra of H<sub>2</sub>PDC, Ce-UiO-66-PDC, Hf-UiO-66-PDC, Zr-UiO-66-PDC, Zr-UiO-66-BDC and H<sub>2</sub>BDC, diluted with BaSO<sub>4</sub>.

### S11 M-UiO-66-PDC (M = Zr, Ce, Hf): Sorption Experiments

M-UiO-66-PDC (M = Zr, Ce, Hf) was activated for sorption measurements by heating the sample at 120 °C under dynamic vacuum overnight. All three compounds are porous towards N<sub>2</sub> and CO<sub>2</sub> at -196 °C and 25 °C respectively (Fig. S11.1. and Fig. S11.3., Tab. S11.1.). The PXRD patterns before and after the activation procedure show no changes with the exclusion of Hf-UiO-66-PDC, which is not stable at this activation condition (Fig. S11.2.).

**Tab. S11.1.:** The specific surface area ( $a_{s,BET}$ ) and the micropore volume ( $V_{mic.}$ ) (left) based on nitrogen adsorption and the total CO<sub>2</sub> uptake with the corresponding pressure (right) of M-UiO-66-PDC with M = Zr, Ce, Hf and the corresponding UiO-66-BDC compounds.

MOF	$a_{s,BET}$ / m <sup>2</sup> g <sup>-1</sup>	$a_{s,BET}$ / m <sup>2</sup> mmol <sup>-1</sup>	$V_{mic.}$ / cm <sup>3</sup> g <sup>-1</sup>	Capacity / mg g <sup>-1</sup>	Capacity / mmol <sup>-1</sup>	p / bar
Zr-UiO-66-PDC	1376	2267	0.54	200	330	1
Zr-UiO-66-BDC <sup>[7],[8]</sup>	1105	---	---	240	---	18
Ce-UiO-66-PDC	768	1505	0.24	100	196	1
Ce-UiO-66-BDC <sup>[9]</sup>	1282	---	0.50	---	---	---
Hf-UiO-66-PDC	383	823	0.18	---	---	---
Hf-UiO-66-BDC <sup>[10]</sup>	358 - 749	---	0.15 - 0.35	---	---	---

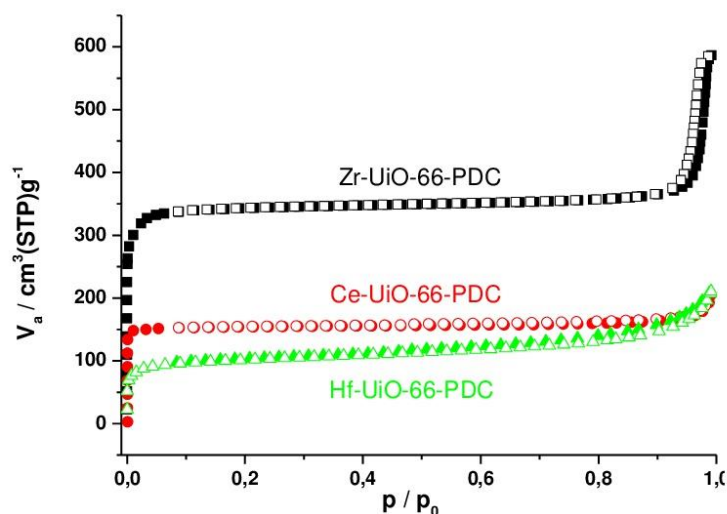


**Fig. S11.1.** N<sub>2</sub>-adsorption and desorption isotherms for M-UiO-66-PDC with M = Zr, Ce, Hf measured at -196 °C.

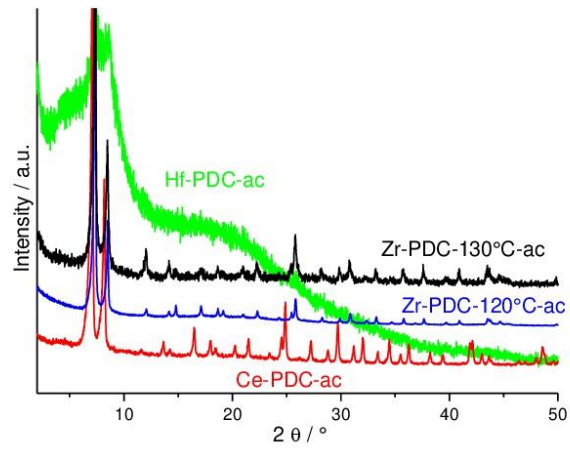


**Fig. S11.2.** PXRD patterns ( $\lambda = \text{Cu K}\alpha_1$ ) of M-UiO-66-PDC with M = Zr, Ce, Hf after activation and after  $\text{N}_2$  sorption experiment.

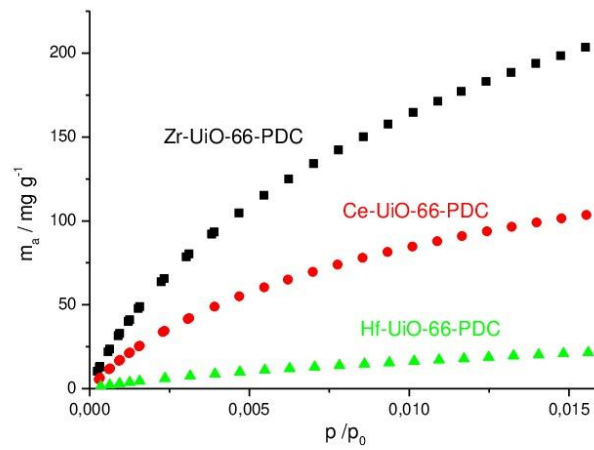


**Fig. S11.3.** CO<sub>2</sub>-adsorption isotherms of M-UiO-66-PDC with M = Zr, Ce, Hf measured at 25 °C.

## Anhang

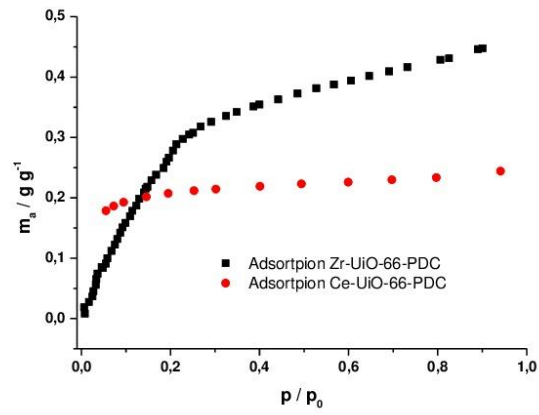


**Fig. S11.4.** H<sub>2</sub>O-adsorption isotherms of M-UiO-66-PDC with M = Zr and Ce measured at 25 °C.

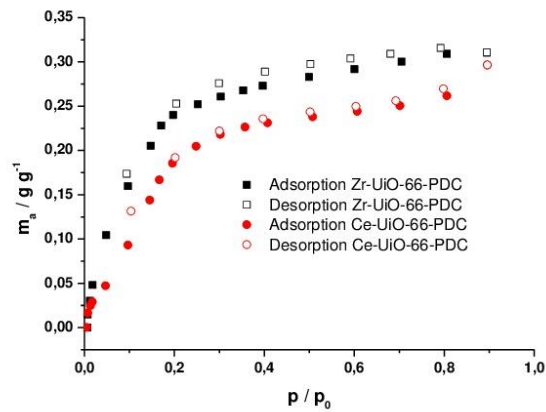


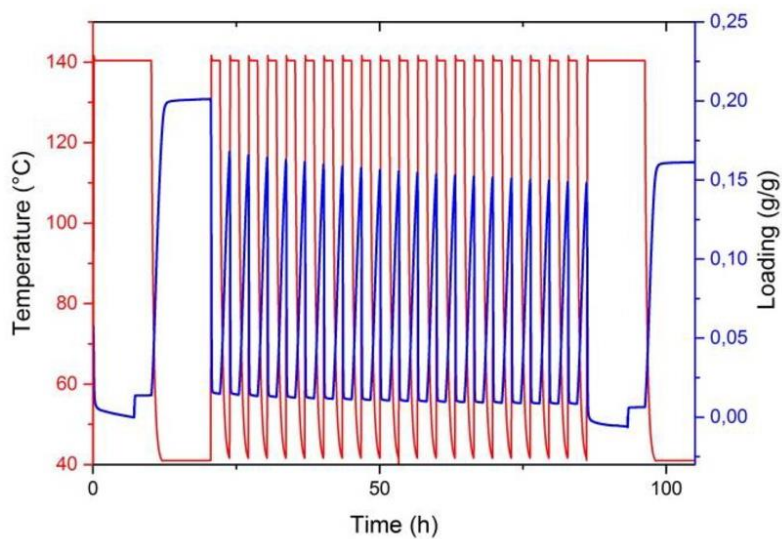
**Fig. S11.5.** MeOH-adsorption and desorption isotherms of M-UiO-66-PDC with M = Zr and Ce measured at 25 °C.

## Anhang

**Tab. S11.2.:** The H<sub>2</sub>O (left) and MeOH (right) uptake with the corresponding pressure of M-UiO-66-PDC with M = Zr and Ce and the corresponding UiO-66-BDC compounds.

MOF	H <sub>2</sub> O			MeOH		
	Capacity / g g <sup>-1</sup>	Capacity / g mmol <sup>-1</sup>	$\alpha$	Capacity / g g <sup>-1</sup>	Capacity / g mmol <sup>-1</sup>	$\alpha$
Zr-UiO-66- PDC	0.34	0.56	0.01 - 0.2	0.31	0.51	0.2
Zr-UiO-66- BDC <sup>[11]</sup>	0.40	---	0.4	---	---	---
Zr-UiO-66- BDC-NH <sub>2</sub> <sup>[11]</sup>	0.34	---	0.25	---	---	---
Ce-UiO-66- PDC	0.23	0.45	0.1	0.30	0.59	0.2



**S12 Cycling water vapor sorption experiments**

**Fig. S12.1:** Thermogravimetric adsorption/desorption cycling experiments for 20 cycles of Ce-Uio-66-PDC. Long segments at the beginning and at the end of each experiment were conducted to determine the equilibrium loading of the sample. Ce-Uio-66-PDC shows nearly no loss of dry mass, the degradation is visible in loss of uptake capacity, from 0.20 g/g to 0.16 g/g (20 %). This larger degradation could also be due to the applied desorption temperature of 140 °C and the low thermal stability of Ce-Uio-66-PDC.

## S13 In situ DRIFTS measurements

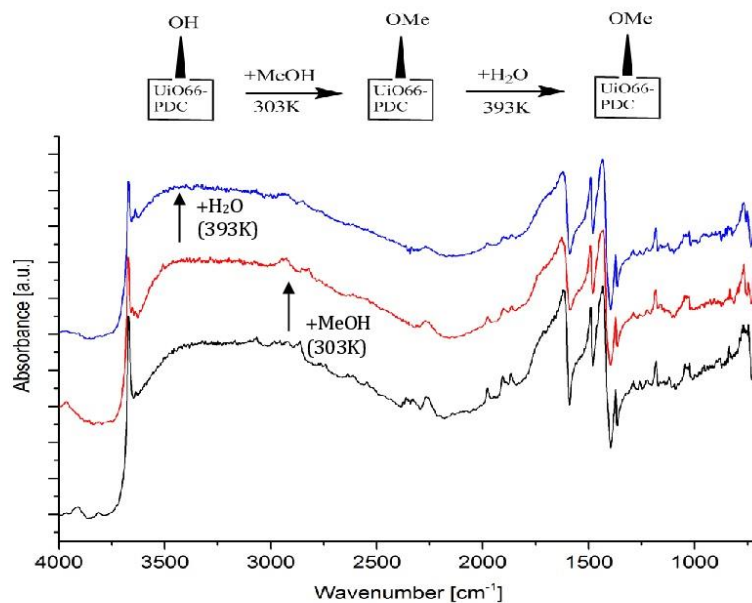


**Fig.S13.1:** Comparison of UiO-66-PDC treatments. Black: UiO-66-PDC; Red: Treatment with methanol wetted gas stream at 303K for 15 minutes; Blue: Treatment with humidified nitrogen stream at 393K for 30 min to investigate if back exchange of methoxy groups to hydroxyl groups occurs. All spectra were recorded under dry N<sub>2</sub> (after reaching equilibrium) at 303K and are shown with a shift in the y-axis for better comparison. No back exchange from the methoxy group through the hydroxyl group could be observed.

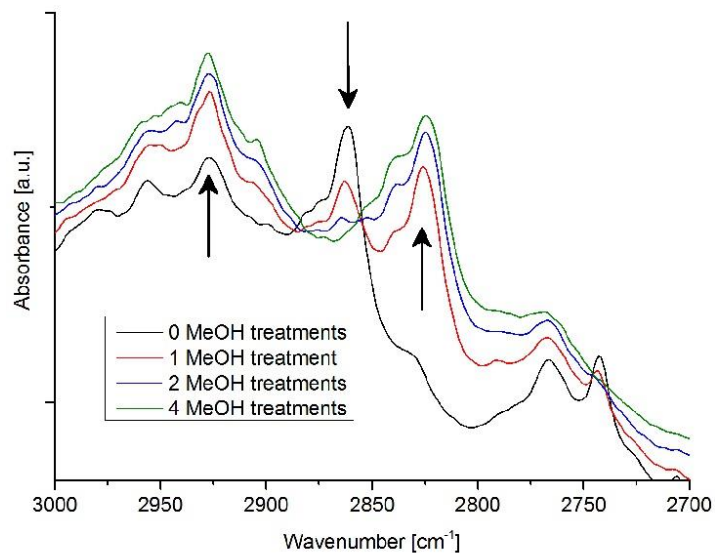


**Fig. S13.2:** In situ DRIFTS measurements. Measurement at 393 K under N<sub>2</sub> gas atmosphere with a flow rate of 100 ml/min. The sample of Zr-UiO-66-PDC was subjected 5 times to a nitrogen stream mixed with MeOH for 30 seconds. For this, the N<sub>2</sub> stream was passed through a MeOH bath (298 K) with a bubble diffusor. After each treatment the sample was treated with dry N<sub>2</sub> until equilibrium and the spectrum was recorded. Arrows indicate the bands that are due to vibrations of the -CH<sub>3</sub> group of methanol (increase at 2927 and 2824 cm<sup>-1</sup>) and the bridging OH group (decrease at 2861 cm<sup>-1</sup>).<sup>12</sup>

**S14 References**

1. A. Topas Academics 4.2; Coelho Software: Brisbane, **2007**.
2. B. Ravel and M. Newville, ATHENA, ARTEMIS, HEPHAESTUS: data analysis for X-ray absorption spectroscopy using IFEFFIT, *J. Synchrotron Rad.*, 2005, **12**.
3. J.J. Rehr and R.C. Albers, *Rev. Mod. Phys.*, 2000, **72**.
4. G.C. Shearer, S. Chavan, J. Ethiraj, J.G. Vitillo, S. Svelle, U. Olsbye, C. Lamberti, S. Bordiga, and K.P. Lillerud, *Chem. Mater.*, 2014, **26**.
5. L. Valenzano, B. Civalleri, S. Chavan, S. Bordiga, M.H. Nilsen, S. Jakobsen, K.P. Lillerud, and C. Lamberti, *Chem. Mater.*, 2011, **23**.
6. S. Øien, D. Wragg, H. Reinsch, S. Svelle, S. Bordiga, C. Lamberti, and K.P. Lillerud, *Cryst. Growth Des.*, 2014, **14**.
7. G. C. Shearer, S. Chavan, J. Ethiraj, J. G. Vitillo, S. Svelle, U. Olsbye, C. Lamberti, S. Bordiga and K. P. Lillerud, *Chem. Mater.*, 2014, **26**.
8. K. Sumida, D. L. Rogow, J. A. Mason, T. M. McDonald, E. D. Bloch, Z. R. Herm, T.-H. Bae, J. R. Long, *Chem. Rev.*, 2012, **112**.
9. M. Lammert, M. T. Wharmby, S. Smolders, B. Bueken, A. Lieb, K. A. Lomachenko, D. D. Vos and N. Stock, *Chem Commun*, 2015, **51**.
10. M. J. Cliffe, W. Wan, X. Zou, P. A. Chater, A. K. Kleppe, M. G. Tucker, H. Wilhelm, N. P. Funnell, F.-X. Coudert and A. L. Goodwin, *Nat. Commun.*, 2014, **5**.
11. F. Jeremias, V. Lozan, S. K. Henninger, C. Janiak, *Dalton Trans.*, 2013, **45**.
12. D. Yang, V. Bernales, T. Islamoglu, O. K. Farha, J. T. Hupp, C. J. Cramer, L. Gagliardi and B. C. Gates, *J. Am. Chem. Soc.*, 2016, **138**.

**7.2 Water-based synthesis and characterization of a new Zr-MOF with a unique inorganic building unit**

**Supporting Information**

**Water-based synthesis and characterization of a  
new Zr-MOF with a unique inorganic building  
unit**

*Steve Waitschat<sup>a</sup>, Helge Reinsch<sup>a</sup> and Norbert Stock<sup>a</sup>*

*<sup>a</sup> Institute für Anorganische Chemie, Christian-Albrechts-Universität,  
Max-Eyth-Straße 2, D 24118 Kiel, Germany*

Prof. Dr. Norbert Stock, Tel.: +49-431-880-1675, Fax: +49-431-880-1775,  
Email: [stock@ac.uni-kiel.de](mailto:stock@ac.uni-kiel.de)

**Table of Contents**

<b>S1</b>	<b>Methods and Reagents</b>
<b>S2</b>	<b>Synthesis and Characterization of the Linker H<sub>2</sub>PzDC</b>
<b>S3</b>	<b>Discovery, Optimization and Synthesis of CAU-22</b>
<b>S4</b>	<b>Structural Analysis of CAU-22: Details of Rietveld refinement; Structure; Crystallographic Tables</b>
<b>S5</b>	<b>Thermal &amp; Elemental Analysis</b>
<b>S6</b>	<b>IR Spectroscopy</b>
<b>S7</b>	<b>NMR Spectroscopy</b>
<b>S8</b>	<b>SEM and EDX Investigation</b>
<b>S9</b>	<b>N<sub>2</sub> and water Sorption Experiments</b>
<b>S10</b>	<b>References</b>

### S1 Methods and Reagents

Initial characterization was performed using a Stoe Stadi P X-ray diffractometer equipped with a  $\theta$ -stage, in transmission geometry using Mo  $K_{\alpha 1}$  radiation and with data collected by a Mythen detector. Powder X-ray diffraction (PXRD) patterns for structure determination were measured using a Stoe Stadi P diffractometer in transmission geometry using Cu  $K_{\alpha 1}$  radiation and with data collected using a Mythen detector. Infrared spectra were recorded on a Bruker ALPHA-P A220/D-01 FTIR spectrometer fitted with an ATR unit, over the spectral range of 4000-40  $\text{cm}^{-1}$ . Thermogravimetric analysis was carried out using a NETSCH STA 429 CD analyzer with a heating rate of 4  $\text{K min}^{-1}$  and under flowing air (flow rate 75  $\text{ml min}^{-1}$ ). Elemental analysis was performed using a EuroVector EuroEA elemental analyzer. NMR spectroscopy was performed using a Bruker DRX 500 spectrometer. Micrographs were recorded using a scanning electron microscope, Zeiss Ultra Plus with FE-gun. Sorption isotherms were measured at  $-196^\circ\text{C}$  for  $\text{N}_2$  and  $25^\circ\text{C}$  for  $\text{H}_2\text{O}$  with a BELSORP-max apparatus (BEL Japan Inc.).

**Table S1.1.** List of reagents used in the synthesis and their suppliers.

Reagent	Supplier	Reagent	Supplier
$\text{Zr}(\text{SO}_4)_2 \cdot 4\text{H}_2\text{O}$	ABCR	Formic acid	Alfa Aesar
$\text{ZrOCl}_2 \cdot 8\text{H}_2\text{O}$	ABCR	Ethanol	Walter CMP
$\text{ZrCl}_4$	ABCR		
$\text{ZrO}(\text{NO}_3)_2 \cdot x\text{H}_2\text{O}$	ABCR		

2,5-pyrazine-dicarboxylic acid ( $\text{H}_2\text{PzDC}$ ) was synthesized following the method reported by Schut.<sup>1</sup>

**Table S1.2.** List of reagents and suppliers used in the synthesis of the linker  $\text{H}_2\text{PzDC}$ .

Reagent	Supplier	Reagent	Supplier
2,5-Dimethylpyrazine	TCI	Pyridine	Grüssing
Selenium dioxid	Merck-Schuchart	Ammonia	VWR
		Hydrochloric acid	VWR

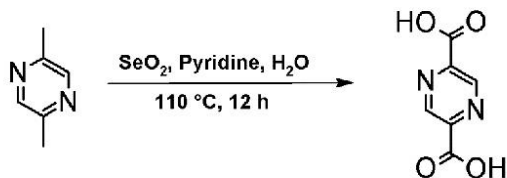
## Anhang

Table S1.3 Summary of some Zr-MOFs, their inorganic building unit, their connectivity and the theoretical formula.

MOF	IBU	Connect	idealized formula	Ref.
DUT-52	$[\text{Zr}_6\text{O}_4(\text{OH})_4(\text{COO-R})_{12}]$	12-fold	$[\text{Zr}_6\text{O}_4(\text{OH})_4(\text{NDC})_6]$	2
UiO-67	$[\text{Zr}_6\text{O}_4(\text{OH})_4(\text{COO-R})_{12}]$	12-fold	$[\text{Zr}_6\text{O}_4(\text{OH})_4(\text{BPDC})_{12}]$	3
DUT-69	$[\text{Zr}_6\text{O}_4(\text{OH})_4(\text{COO-R})_{10}]$	10-fold	$[\text{Zr}_6\text{O}_4(\text{OH})_4(\text{TDC})_5(\text{Ac})_2]$	4
DUT-67	$[\text{Zr}_6\text{O}_4(\text{OH})_4(\text{COO-R})_8]$	8-fold	$[\text{Zr}_6\text{O}_6(\text{OH})_2(\text{TDC})_4(\text{Ac})_2]$	4
DUT-51	$[\text{Zr}_6\text{O}_4(\text{OH})_4(\text{COO-R})_8]$	8-fold	$[\text{Zr}_6\text{O}_6(\text{OH})_2(\text{DTTDC})_4(\text{BC})_2(\text{DMF})_6]$	5
MOF-841	$[\text{Zr}_6\text{O}_4(\text{OH})_4(\text{COO-R})_8]$	8-fold	$[\text{Zr}_6\text{O}_4(\text{OH})_4(\text{MTB})_2(\text{HCOO})_4(\text{H}_2\text{O})_2]$	6
MOF-545	$[\text{Zr}_6\text{O}_4(\text{OH})_4(\text{COO-R})_8]$	8-fold	$[\text{Zr}_6\text{O}_8(\text{T CPP-H}_2)_2(\text{H}_2\text{O})_8]$	7
PCN-521	$[\text{Zr}_6\text{O}_4(\text{OH})_4(\text{COO-R})_8]$	8-fold	$[\text{Zr}_6(\mu_3\text{-OH})_8(\text{OH})_8(\text{MTBC})_2]$	8
MOF-808	$[\text{Zr}_6\text{O}_4(\text{OH})_4(\text{COO-R})_6]$	6-fold	$[\text{Zr}_6\text{O}_4(\text{OH})_4(\text{BTC})_2(\text{HCOO})_6]$	6
MIL-140	$\{\text{Zr}(\mu_3\text{-O})_3\text{O}_4\}$	---	$[\text{ZrO}(\text{BDC})]$	9

NDC<sup>2-</sup> = 2,6-naphthalenedicarboxylate, BPDC<sup>2-</sup> = 4,4'-biphenyldicarboxylate, TDC<sup>2-</sup> = 2,5-thiophenedicarboxylate, DTTDC<sup>2-</sup> = dithieno-[3,2-b;2',3'-d]-thiophene-2,6-dicarboxylate, BC = benzoate, MTB<sup>4-</sup> = methanetetrayltetrabenzoate, TCPP-H<sub>2</sub> = meso-tetrakis(4-carboxylatephenyl)porphyrin, MTBC<sup>4-</sup> = methanetetrayltetrabiphenyl-4-carboxylate, BTC<sup>3-</sup> = benzenetricarboxylate, BDC<sup>2-</sup> = benzenedicarboxylate.



S2 Synthesis and Characterization of the Linker H<sub>2</sub>PzDC

**Fig. S2.1:** Reaction scheme for the synthesis of 2,5-pyrazine-dicarboxylic acid from 2,5-dimethyl-pyrazine.

The synthesis was carried out according to the literature.<sup>[1]</sup> 25 g SeO<sub>2</sub> were mixed with 100 ml of a 10:1 pyridine-water-mixture and 5 g (46.2 mmol) 2,5-dimethylpyrazine were added under stirring. The reaction mixture was stirred for 12 h at 110 °C. The reaction product was separated by filtration and washed with 15 ml 2 M NH<sub>3</sub> at RT. The filtrate was evaporate under vacuum to a volume of about 30 ml and 10 ml concentrated HCl were added. The solid was filtrated and washed with concentrated HCl and water. The obtained product was an orange/brown powder.

Yield: 4.8 g (62%)

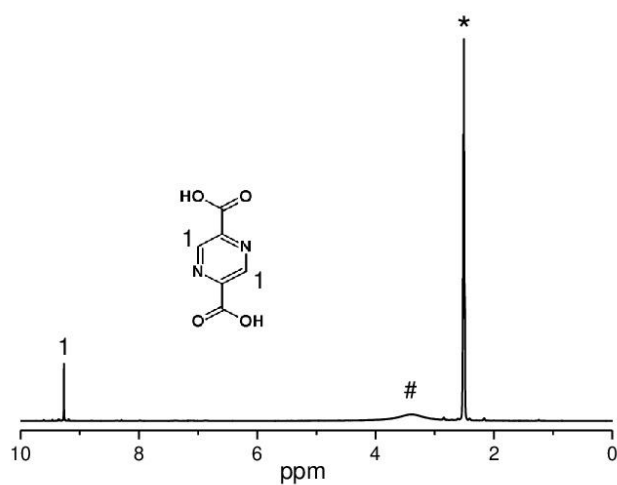


**Fig. S2.2:** <sup>1</sup>H-NMR-spectrum of 2,5-pyrazine-dicarboxylic acid dissolved in (CD<sub>3</sub>)<sub>2</sub>SO (\* signal of (CD<sub>3</sub>)<sub>2</sub>SO and # signal of water).

## Synthesis and Characterization of CAU-22

### S3 Discovery, Optimization and Synthesis of CAU-22

The systematic investigation of the chemical system  $Zr^{4+}/PzDC^{2-}/H_2O/HOOC$  was carried out in a Teflon-lined high-throughput autoclave.<sup>[10]</sup> To optimize the reaction conditions, different zirconium-salts were tested. With  $Zr(SO_4)_2 \cdot 4H_2O$  and  $ZrO(NO_3)_2 \cdot xH_2O$  as starting material no crystalline product was obtained. With  $ZrCl_4$  and  $ZrOCl_2 \cdot 8H_2O$  crystalline products were observed and the employed water/formic acid ratio was further optimized. The optimized reaction conditions are indicated by a red box. For all syntheses, the reaction time was set to 24 h and the reaction temperature to 120 °C.

**Table S3.1.** Reaction parameters of the HT-assisted synthesis of CAU-22. M = metal source, L =  $H_2PzDC$ ,  $HCOOH$  = formic acid. The red box shows the optimized reaction parameter for the synthesis of CAU-22.

Metal source	M / g	$H_2PzDC$ / g	$H_2O$ / $\mu L$	$HCOOH$ / $\mu L$
$Zr(SO_4)_2 \cdot 4H_2O$	0.0533	0.0252	1000	---
$Zr(SO_4)_2 \cdot 4H_2O$	0.0533	0.0252	1500	---
$Zr(SO_4)_2 \cdot 4H_2O$	0.0533	0.0504	1000	---
$Zr(SO_4)_2 \cdot 4H_2O$	0.0533	0.0504	1500	---
$Zr(SO_4)_2 \cdot 4H_2O$	0.1066	0.0252	1000	---
$Zr(SO_4)_2 \cdot 4H_2O$	0.1066	0.0252	1500	---
$Zr(SO_4)_2 \cdot 4H_2O$	0.0355	0.0336	500	500
$Zr(SO_4)_2 \cdot 4H_2O$	0.0355	0.0336	400	600
$Zr(SO_4)_2 \cdot 4H_2O$	0.0355	0.0336	300	700
$Zr(SO_4)_2 \cdot 4H_2O$	0.0355	0.0336	200	800
$Zr(SO_4)_2 \cdot 4H_2O$	0.0355	0.0336	100	900
$Zr(SO_4)_2 \cdot 4H_2O$	0.0355	0.0336	0	1000
$ZrO(NO_3)_2 \cdot xH_2O$	0.0231	0.0336	500	500
$ZrO(NO_3)_2 \cdot xH_2O$	0.0231	0.0336	400	600
$ZrO(NO_3)_2 \cdot xH_2O$	0.0231	0.0336	300	700
$ZrO(NO_3)_2 \cdot xH_2O$	0.0231	0.0336	200	800
$ZrO(NO_3)_2 \cdot xH_2O$	0.0231	0.0336	100	900
$ZrO(NO_3)_2 \cdot xH_2O$	0.0231	0.0336	0	1000
$ZrCl_4$	0.0233	0.0336	1000	0
$ZrCl_4$	0.0233	0.0336	900	100
$ZrCl_4$	0.0233	0.0336	800	200
$ZrCl_4$	0.0233	0.0336	700	300
$ZrCl_4$	0.0233	0.0336	600	400
$ZrCl_4$	0.0233	0.0336	500	500
$ZrCl_4$	0.0233	0.0336	400	600
$ZrCl_4$	0.0233	0.0336	300	700
$ZrCl_4$	0.0233	0.0336	200	800
$ZrCl_4$	0.0233	0.0336	100	900
$ZrCl_4$	0.0233	0.0336	0	1000
$ZrCl_4$	0.0233	0.0168	1000	0
$ZrCl_4$	0.0233	0.0168	900	100
$ZrCl_4$	0.0233	0.0168	800	200

## Anhang

ZrCl <sub>4</sub>	0.0233	0.0168	700	300
ZrCl <sub>4</sub>	0.0233	0.0168	600	400
ZrCl <sub>4</sub>	0.0233	0.0168	500	500
ZrCl <sub>4</sub>	0.0233	0.0168	400	600
ZrCl <sub>4</sub>	0.0233	0.0168	300	700
ZrCl <sub>4</sub>	0.0233	0.0168	200	800
ZrCl <sub>4</sub>	0.0233	0.0168	100	900
ZrCl <sub>4</sub>	0.0233	0.0168	0	1000
ZrOCl <sub>2</sub> ·8H <sub>2</sub> O	0.0322	0.0336	1000	0
ZrOCl <sub>2</sub> ·8H <sub>2</sub> O	0.0322	0.0336	900	100
ZrOCl <sub>2</sub> ·8H <sub>2</sub> O	0.0322	0.0336	800	200
ZrOCl <sub>2</sub> ·8H <sub>2</sub> O	0.0322	0.0336	700	300
ZrOCl <sub>2</sub> ·8H <sub>2</sub> O	0.0322	0.0336	600	400
ZrOCl <sub>2</sub> ·8H <sub>2</sub> O	0.0322	0.0336	500	500
ZrOCl <sub>2</sub> ·8H <sub>2</sub> O	0.0322	0.0336	400	600
ZrOCl <sub>2</sub> ·8H <sub>2</sub> O	0.0322	0.0336	300	700
ZrOCl <sub>2</sub> ·8H <sub>2</sub> O	0.0322	0.0336	200	800
ZrOCl <sub>2</sub> ·8H <sub>2</sub> O	0.0322	0.0336	100	900
ZrOCl <sub>2</sub> ·8H <sub>2</sub> O	0.0322	0.0336	0	1000
ZrOCl <sub>2</sub> ·8H <sub>2</sub> O	0.0322	0.0168	1000	0
ZrOCl <sub>2</sub> ·8H <sub>2</sub> O	0.0322	0.0168	900	100
ZrOCl <sub>2</sub> ·8H <sub>2</sub> O	0.0322	0.0168	800	200
ZrOCl <sub>2</sub> ·8H <sub>2</sub> O	0.0322	0.0168	700	300
ZrOCl <sub>2</sub> ·8H <sub>2</sub> O	0.0322	0.0168	600	400
ZrOCl <sub>2</sub> ·8H <sub>2</sub> O	0.0322	0.0168	500	500
ZrOCl <sub>2</sub> ·8H <sub>2</sub> O	0.0322	0.0168	400	600
ZrOCl <sub>2</sub> ·8H <sub>2</sub> O	0.0322	0.0168	300	700
ZrOCl <sub>2</sub> ·8H <sub>2</sub> O	0.0322	0.0168	200	800
ZrOCl <sub>2</sub> ·8H <sub>2</sub> O	0.0322	0.0168	100	900
ZrOCl <sub>2</sub> ·8H <sub>2</sub> O	0.0322	0.0168	0	1000

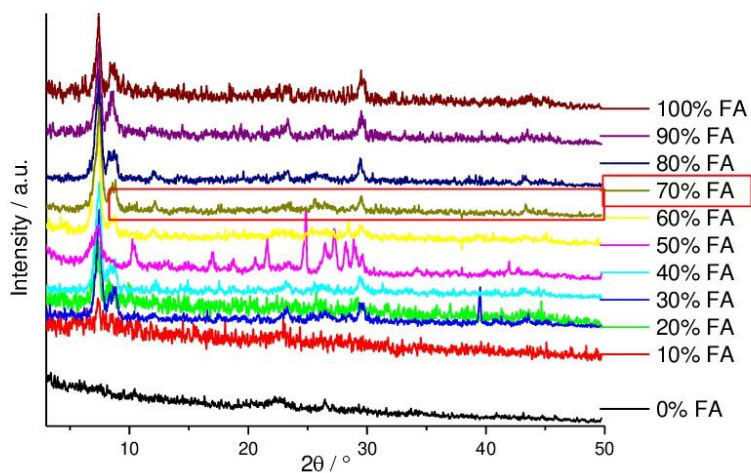


**Fig. S3.1:** PXRD patterns of the products from the high throughput investigation using  $ZrCl_4$  as the metal source. The best PXRD pattern and the optimized formic acid (FA) concentration are indicated by a red box.

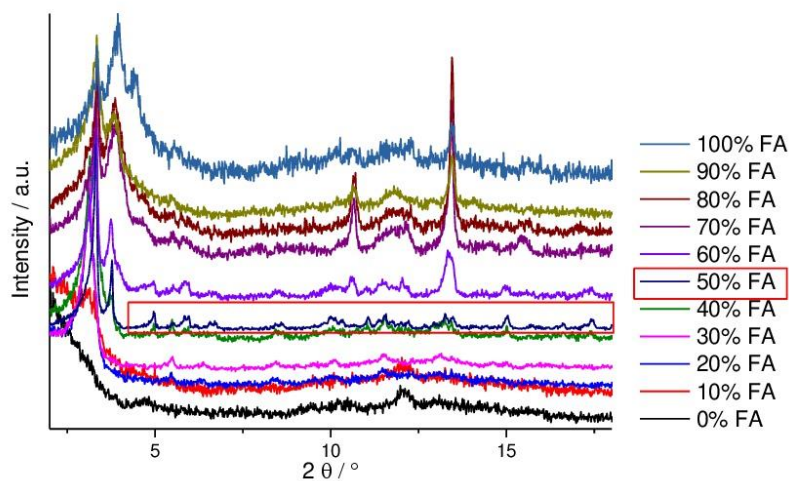


**Fig. S3.2:** PXRD patterns of the products from the high throughput investigation using  $ZrOCl_2 \cdot 8H_2O$  as the metal source. The best PXRD pattern and the optimized formic acid concentration are indicated by a red box.

**Table S3.2.** Optimized reaction parameters of the up-scaled synthesis of CAU-22 in a 25 ml Teflon reactor. The molar ratios were not changed (see Tab. S3.1).

Metal source	M / g	H <sub>2</sub> PzDC / g	H <sub>2</sub> O / $\mu$ L	HCOOH / $\mu$ L	T / $^{\circ}$ C
ZrOCl <sub>2</sub> ·8H <sub>2</sub> O	0.439	0.229	7000	7000	120

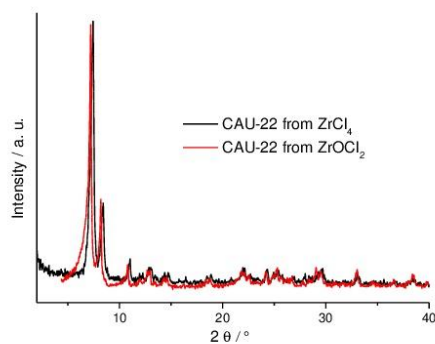


**Fig. S3.3:** PXRD patterns of CAU-22 synthesized with ZrCl<sub>4</sub> (black) and with ZrOCl<sub>2</sub> (red). The red pattern was measured with a wavelength of 0.709 Å but for comparability it was converted to the wavelength of 1.540 Å.

## S4 Structural Analysis of CAU-22

### S4 Details of the Rietveld Refinement

Laboratory powder X-ray diffraction data were collected using a Stoe Stadi P diffractometer fitted with a Cu  $K_{\alpha 1}$  tube radiation source and a Mythen detector, in transmission geometry. All stages of the refinement, including indexing, Pawley fitting and Rietveld refinement were performed using the routines of TOPAS-Academic V5.<sup>[11]</sup> The data was indexed in a monoclinic unit cell ( $a = 21.260(2)$ ,  $b = 14.516(2)$ ,  $c = 8.105(2)$  Å,  $\beta = 84.25(2)^\circ$ ) and found to have systematic absences consistent with the space group  $C2/m$ .

Based on this cell, structure solution was carried out using EXPO2009,<sup>[12]</sup> This initial structural model was completed by inserting the linker molecules and formate ions in suitable positions using Materials Studio.<sup>[13]</sup> Subsequently this model was optimized by force-field calculations (universal force-field) as implemented in Materials Studio and employed as starting point for the Rietveld refinement with TOPAS. Residual electron density inside the framework's cavities was attributed to adsorbed water molecules and therefore attributed to oxygen atoms whose occupancy was also refined. Most atoms were freely refined, however, the position of the atoms of one linker molecule had to be fixed. We assume that this is due to rotational disorder of the pyrazine ring which is difficult to model using PXRD data. The lateral atoms of the other linker molecule were refined with occupancy for carbon exceeding 1 to account for the partial occupation with nitrogen atoms. The refinement converged to sufficient figures of merit ( $R_{WP} = 6.9\%$ ,  $R_{Bragg} = 2.5\%$ ,  $GoF = 2.9$ ) and the plot is shown in Figure S4.1. Some relevant parameters are summarized in Table S4.1. and the asymmetric unit as well as the most relevant distances are shown in Figure S4.2. and S4.3. as well as listed in Table S4.2. Reflections of weak intensity at angles of  $8.8^\circ$  and  $13.6^\circ$  indicate the presence of a small amount of crystalline byproduct. However, upon thermal activation the peak at  $8.8^\circ$  disappears.

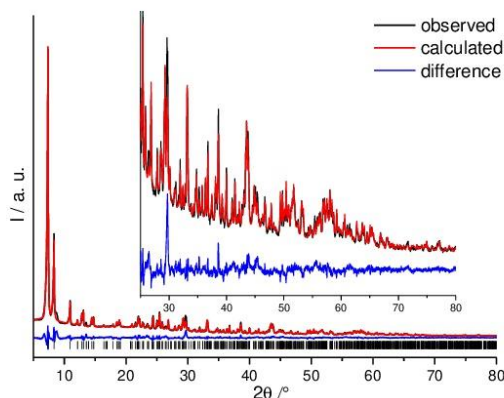


**Figure S4.1.** Rietveld plot for the final refinement of CAU-22. Black line gives the experimental data, red line the calculated fit and the blue line is the difference curve. Black bars indicate the Bragg reflection positions.

**Table S4.1.** Crystallographic data for CAU-22.

Compound	CAU-22
Space Group	<i>C2/m</i>
Crystal System	Monoclinic
<i>a</i> / Å	21.260(2)
<i>b</i> / Å	14.516(2)
<i>c</i> / Å	8.105(2)
$\alpha$ / °	90
$\beta$ / °	84.25(2)
$\gamma$ / °	90
<i>V</i> / Å <sup>3</sup>	2499.6(8)
Wavelength / Å	Cu K $\alpha$ 1
<i>R</i> <sub>p</sub> / %	5.0
<i>R</i> <sub>wp</sub> / %	6.9
GoF	2.9
<i>R</i> <sub>Bragg</sub> / %	2.5

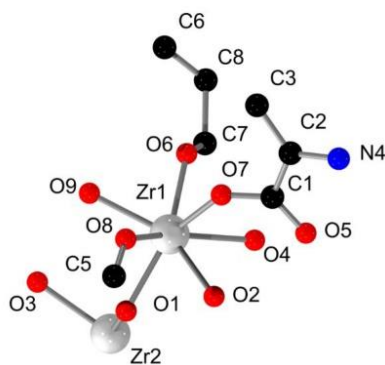


**Figure 4.2.** Asymmetric unit of CAU-22. Oxygen atoms representing water molecules are omitted for clarity. Please note that C6 was refined with occupancy exceeding 1 due to the partial occupation by nitrogen.

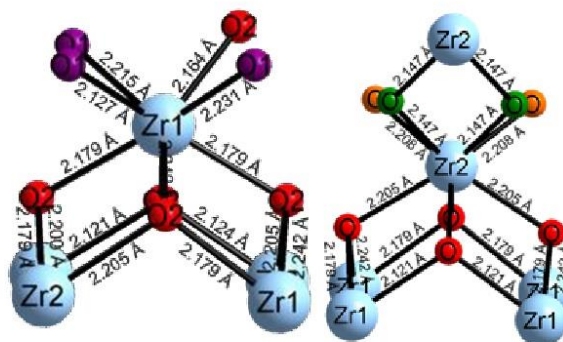


**Figure 4.3.** Left: The coordination sphere of Zr1. Right: The coordination sphere of Zr2.

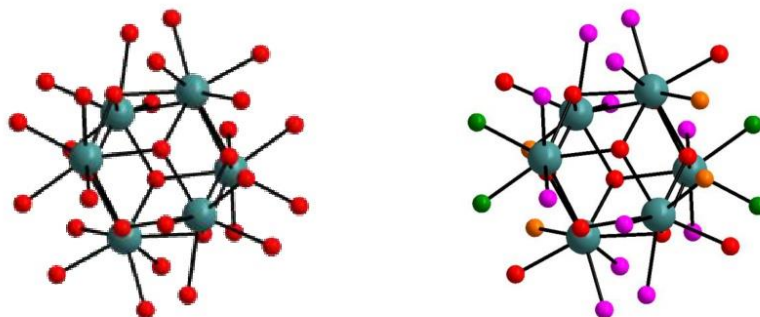


**Figure 4.4.** Left the zirconium cluster  $[\text{Zr}_6(\mu_3\text{-O})_4(\mu_3\text{-OH})_4(\text{OH})_2(\mu_2\text{-OH})_2(\text{H}_2\text{O})_2(\text{HCOO})_2(\text{COO-R})_3]$  of CAU-22. Right: The zirconium cluster with dedicated oxygen atoms.  $[\text{Zr}_6(\mu_3\text{-O})_4(\mu_3\text{-OH})_4(\text{OH})_2(\mu\text{-OH})_2(\text{H}_2\text{O})_2(\text{HCOO})_2(\text{COO-R})_3]$ .

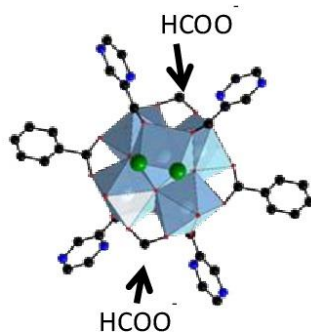


**Figure 4.5.** The 6-fold connected zirconium cluster. The green atoms are the  $\mu\text{-OH}^-$  ions.



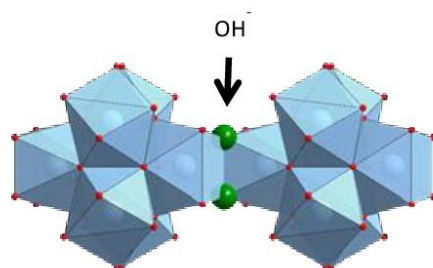


**Figure 4.6.** Two hexanuclear zirconium clusters connected to each other by the  $\mu$ -OH<sup>-</sup> ions.

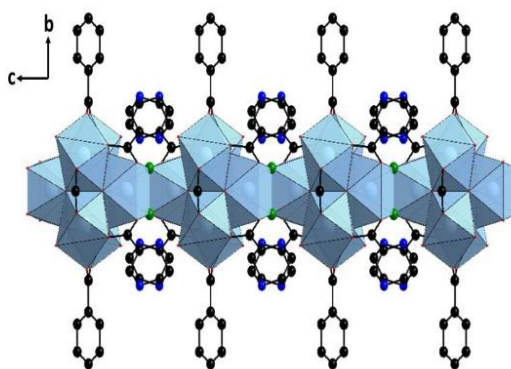


**Figure 4.7.** Four hexanuclear zirconium clusters connected to each other by the  $\mu$ -OH<sup>-</sup> ions. In addition the linker molecules are shown that interconnect the chains.

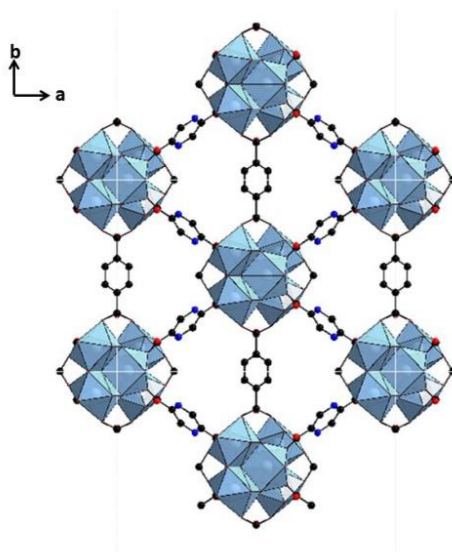


**Figure 4.8.** Structure of CAU-22 viewed along the *c*-axis.

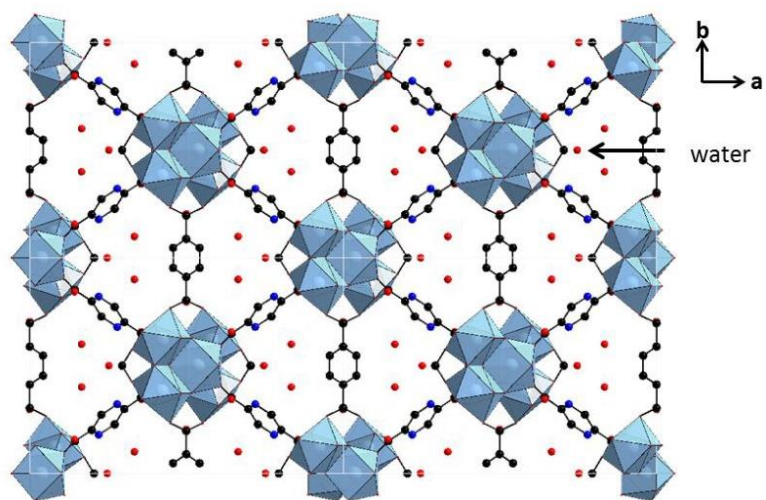


**Figure 4.9.** Structure of CAU-22 viewed along the *c*-axis with water in the pores.

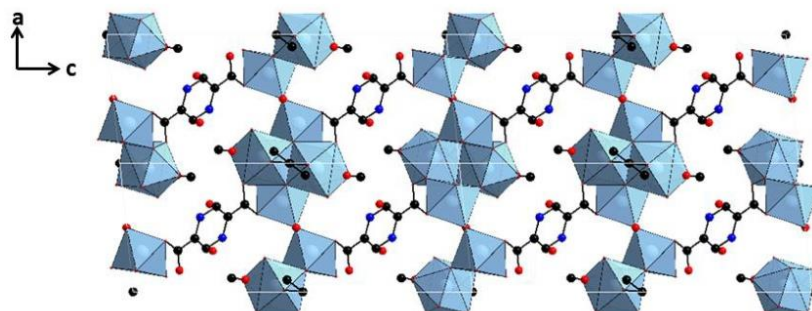


**Figure 4.10.** Structure of CAU-22 viewed along the *b*-axis.

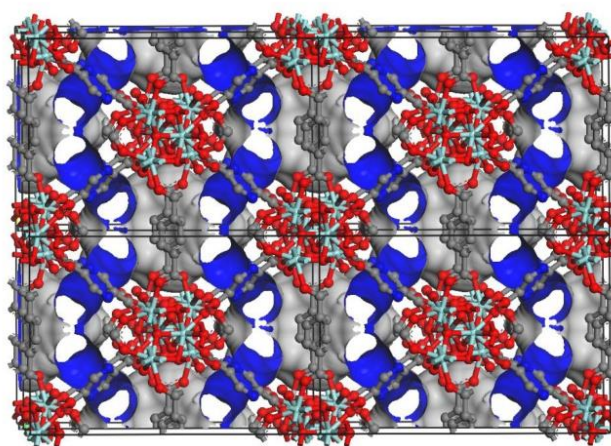


**Fig. 4.11.** Conolloy surface generated with water as probe molecule. Please note that protons are not shown, since the structure is derived from PXRD data.

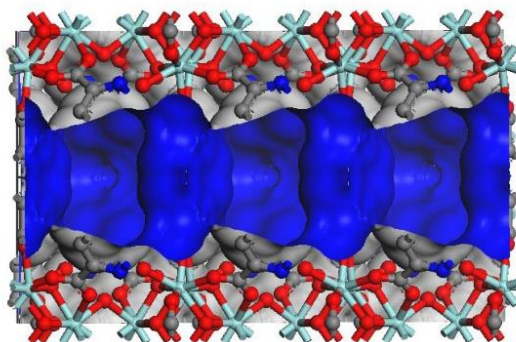


**Fig. 4.12.** Conolloy surface of the channels as seen along  $a$ -axis.

**Table 4.2.** Most important bond lengths observed in the structure of CAU-22 with numbering scheme as in Fig. S4.2. Please note that the positions of the C1, C2, C3 and N4 atoms were fixed and therefore no standard deviation are given for bond length involving these atoms.

Atom 1	Atom 2	Distance / Å	Atom 1	Atom 2	Distance / Å
Zr1	O1	2.121(13)	Zr2	O1	2.124(19)
Zr1	O7	2.127(14)	Zr2	O3	2.147(14)
Zr1	O9	2.164(21)	Zr2	O2	2.199(27)
Zr1	O4	2.179(14)	Zr2	O6	2.231(14)
Zr1	O2	2.179(14)	Zr2	O4	2.242(17)
Zr1	O8	2.215(14)	Zr2	O4	2.205(21)
			Zr2	O5	2.209(12)
O5	C1	1.230(13)	C2	N4	1.4027
O6	C7	1.252(18)	C2	C3	1.4144
O7	C1	1.262(13)	C3	N4	1.4104
O8	C5	1.291(21)	C6	C6	1.363(3)
C1	C2	1.5051	C6	C8	1.368(20)
			C7	C8	1.572(37)

## cif-file of CAU-22

```

data_
_chemical_name_mineral CAU-22
_cell_length_a 21.28954(73)
_cell_length_b 14.55846(52)
_cell_length_c 8.10658(33)
_cell_angle_alpha 90
_cell_angle_beta 84.1730(30)
_cell_angle_gamma 90
_cell_volume 2499.59(16)
_symmetry_space_group_name_H-M C2/M
loop_
_symmetry_equiv_pos_as_xyz
'-x, -y, -z'
'-x, y, -z'
'x, -y, z'
'x, y, z'
'-x+1/2, -y+1/2, -z'
'-x+1/2, y+1/2, -z'
'x+1/2, -y+1/2, z'
'x+1/2, y+1/2, z'
loop_
_atom_site_label
_atom_site_type_symbol
_atom_site_fract_x
_atom_site_fract_y
_atom_site_fract_z
_atom_site_occupancy
_atom_site_B_iso_or_equiv
Zr1 Zr 0.57851(19) 0.61912(28) 0.04052(51) 1 0.25(12)
Zr2 Zr 0.46334(25) 0.5 0.30676(77) 1 0.25(12)
O1 O 0.55665(86) 0.5 0.1858(27) 1 1.94(31)
O2 O 0.6030(13) 0.5 -0.1157(28) 1 1.94(31)
O3 O 0.5 0.5783(16) 0.5 1 1.94(31)
O4 O 0.51662(61) 0.6283(15) -0.1668(21) 1 1.94(31)
O5 O 0.61125(52) 0.59852(87) -0.3969(16) 1 1.94(31)
O6 O 0.55225(60) 0.76629(88) 0.0129(27) 1 1.94(31)
O7 O 0.64326(72) 0.6566(14) -0.1656(16) 1 1.94(31)
O8 O 0.67366(58) 0.57536(94) 0.0968(25) 1 1.94(31)
O9 O 0.6017(11) 0.6853(19) 0.2656(21) 1 1.94(31)
C1 C 0.64462 0.64903 -0.32096 1 1.67(57)
C2 C 0.69773 0.70101 -0.41577 1 1.67(57)
C3 C 0.72860 0.77244 -0.33751 1 1.67(57)
N4 N 0.72018 0.67907 -0.57970 1 1.67(57)
C5 C 0.7051(14) 0.5 0.1058(51) 0.959(65) 1.67(57)
C6 C 0.54239(80) 0.95320(12) 0.0918(24) 1 1.67(57)
C7 C 0.5 0.8036(19) 0 1 1.67(57)
C8 C 0.5 0.9116(17) 0 1.08 1.67(57)
Ow1 O 0.7475(14) 0.5 0.6819(50) 0.999(48) 3.6(11)
Ow2 O 0.5 0.7959(28) 0.5 1.000(51) 3.6(11)
Ow3 O 0.6655(10) 0.9002(19) 0.0938(31) 1.000(45) 3.6(11)

```

**S5 CAU-22: Thermal and Elemental Analysis**

For temperature depended PXRD, the sample was prepared in a 0.5 mm silica-capillary, which was heated up with a heating rate of 50 °C up to 490 °C and a PXRD pattern was measured every 5 °C for five minutes at transmission geometry using Mo  $K\alpha_1$  radiation subsequently.

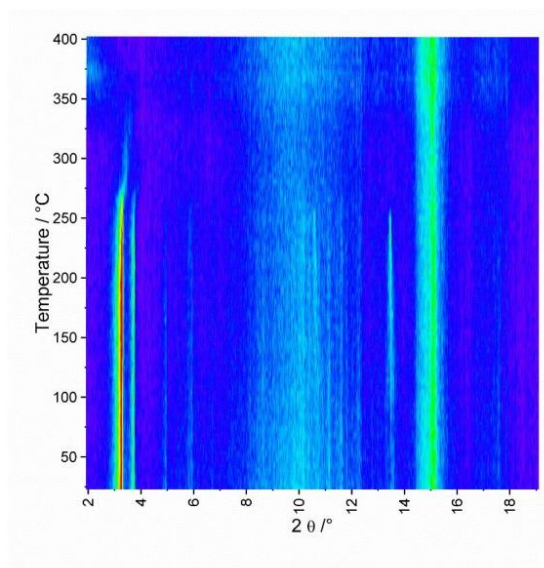


**Fig. S5.1:** Temperature depended PXRD investigation of CAU-22. The compound is thermally stable up to approximately 270°C.

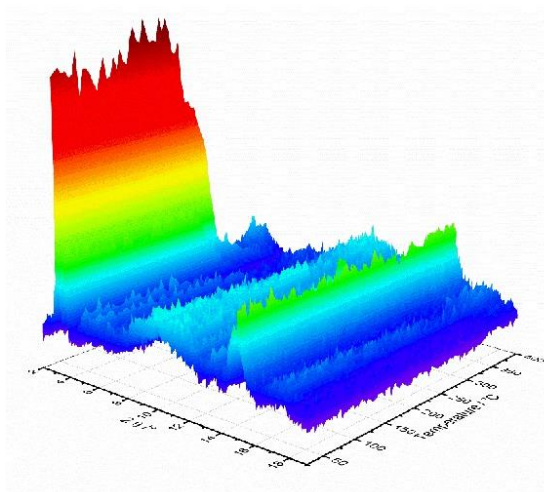


**Fig. S5.2:** 3-D plot of the temperature dependent powder patterns of CAU-22.

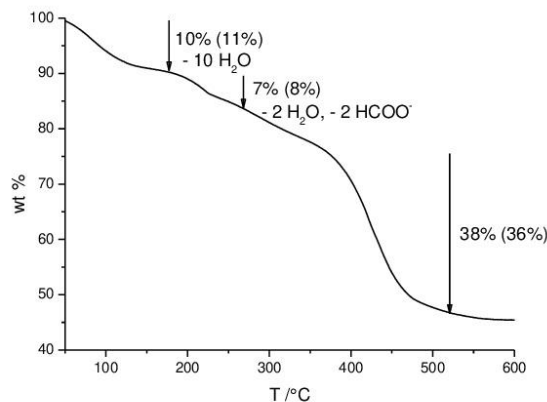


**Figure S5.3.** TGA plot for CAU-22 ( $[\text{Zr}_6(\mu_3\text{-O})_4(\mu_3\text{-OH})_4(\mu\text{-OH})_2(\text{OH})_2(\text{H}_2\text{O})_2(\text{HCOO})_2(\text{PzDC})_3] \cdot 10\text{H}_2\text{O}$ ) showing the weight loss event occurring on dehydration, assigned to the loss of physisorbed water molecules up to 180 °C (10 wt.%; expected 11 wt.%). Up to 270 °C the chemisorbed water and formate ions are removed from the structure (7 wt.%; expected 8%), above this temperature the structure collapses (38 wt.%; expected 36%).

**Table S5.1.** Comparison of the postulated products of the thermogravimetric analysis and the associated mass loss.

Sum formula of postulated product	T / °C	Theoretical wt %	Measured wt %
<b>CAU-22·10H<sub>2</sub>O</b>			
$[\text{Zr}_6(\mu_3\text{-O})_4(\mu_3\text{-OH})_4(\mu_2\text{-OH})_2(\text{OH})_2(\text{H}_2\text{O})_2(\text{HCOO})_2(\text{PzDC})_3] \cdot 10\text{H}_2\text{O}$	25	100	100
$[\text{Zr}_6(\mu_3\text{-O})_4(\mu_3\text{-OH})_4(\mu\text{-OH})_2(\text{OH})_2(\text{H}_2\text{O})_2(\text{HCOO})_2(\text{PzDC})_3]$	180	89	90
$[\text{Zr}_6(\mu_3\text{-O})_4(\mu_3\text{-OH})_4(\mu\text{-OH})_2(\text{OH})_2(\text{PzDC})_3]$	270	81	83
$6 \cdot \text{ZrO}_6$	570	45	45

**Table S5.2.** Results of the elemental analysis of CAU-22 and comparison to the expected values for  $[\text{Zr}_6(\mu_3\text{-O})_4(\mu_3\text{-OH})_4(\mu\text{-OH})_2(\text{OH})_2(\text{H}_2\text{O})_2(\text{HCOO})_2(\text{PzDC})_3] \cdot 20\text{H}_2\text{O}$ .

	C %	H %	N %
CAU-22-ac	14.33	1.72	4.37
Expected	14.18	3.21	4.96

## S6 CAU-22: Infrared Spectroscopy

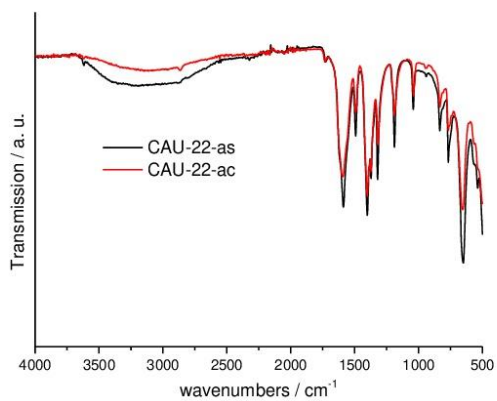


**Figure S6.1.** FTIR spectrum of CAU-22.  $\tilde{\nu}$  ( $\text{cm}^{-1}$ ) = 3267 (b, O-H stretch -  $\text{H}_2\text{O}$ ), 2860 (w, C-H-stretch  $\text{HCOO}^-$ ), 1590 (m, asymmetric  $-\text{CO}_2^-$  stretch -  $\text{PzDC}^{2-}$ ), 1402 (m, symmetric  $\text{CO}_2^-$  stretch -  $\text{PzDC}^{2-}$ ).



**S7 CAU-22: NMR-Spectroscopy**

A sample of CAU-22 was digested for solution  $^1\text{H}$  NMR analysis using a NaOD/D<sub>2</sub>O solution. The spectrum (Fig. S7.1) shows a strong resonance for water ( $\delta = 4.93$  ppm). By comparison with an NMR spectrum of the H<sub>2</sub>PzDC linker and HCOOH, the postulated sum linker to formiate ratio could be verified through integration of the signals.

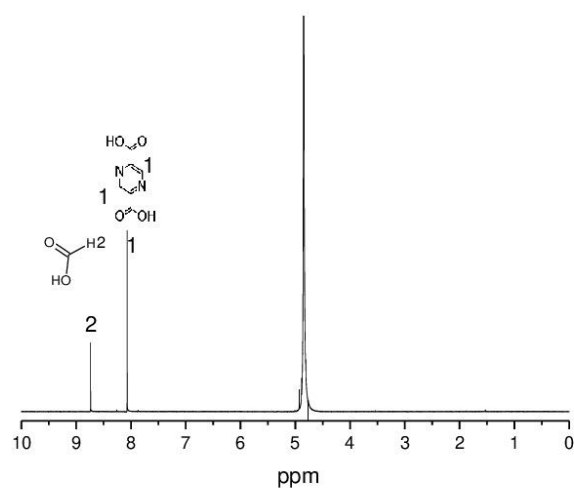


**Figure S7.1.** NMR-spectrum of CAU-22 dissolved in NaOD/D<sub>2</sub>O shows the molar ratio HCOOH : H<sub>2</sub>PzDC of approximately 2 to 3.

S8 CAU-22: SEM and EDX Investigation

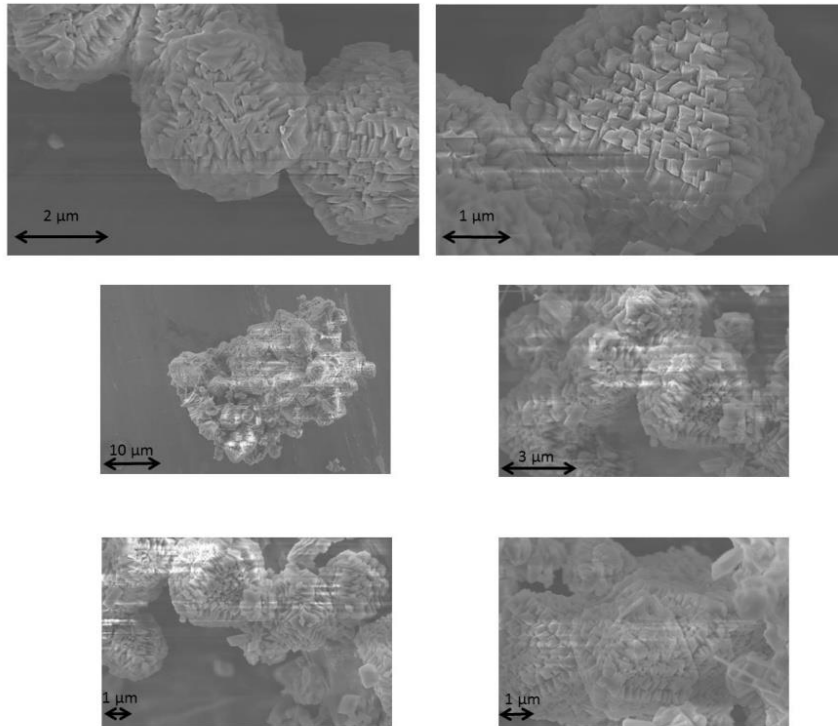


**Figure S3.6.** SEM micrographs of CAU-22.

EDX measurements indicate the absence of chlorine in the samples.

### S9 CAU-22: N<sub>2</sub> and water Sorption Experiments

CAU-22 was activated for sorption measurements by heating the sample to 120 °C under vacuum overnight. CAU-22 is porous towards N<sub>2</sub> and water at -196 °C and 25 °C respectively (Fig. S3.7.1.). The BET surface area was determined to be 276 m<sup>2</sup> g<sup>-1</sup> and the micropore volume to be 0.12 cm<sup>3</sup> g<sup>-1</sup>, based on nitrogen adsorption. The PXRD patterns before and after the activation procedure show no changes (Fig. S6.9.)

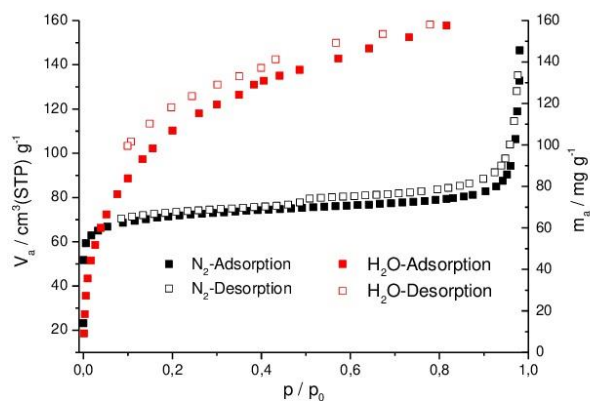


**Figure S9.1.** N<sub>2</sub>- and water-adsorption and desorption isotherms for CAU-22 measured at -196 °C and 25 °C respectively.

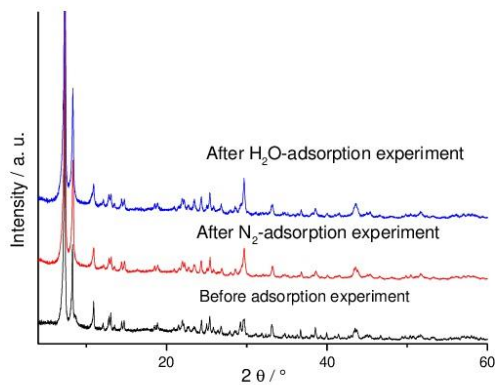


**Figure S9.2.** PXRD patterns ( $\lambda = \text{Cu K}\alpha_1$ ) for CAU-22 before activation and after N<sub>2</sub> and H<sub>2</sub>O sorption experiment.

**S10 References**

1. W. J. Schut, H. I. X. Mager and W. Berends, *Recl. Trav. Chim. Pays-Bas*, 1961, **80**, 391-398.
2. V. Bon, I. Senkowska, M. S. Weiss and S. Kaskel, *CrystEngComm*, 2013, **15**, 9572-9577.
3. A. Schaate, P. Roy, A. Godt, J. Lippke, F. Waltz, M. Wiebcke and P. Behrens, *Chem. Eur. J.*, 2011, **17**, 6643-6651.
4. V. Bon, I. Senkowska, I. A. Baburin and S. Kaskel, *Cryst. Growth Des.*, 2013, **13**, 1231-1237.
5. V. Bon, V. Senkovskyy, I. Senkowska and S. Kaskel, *Chem. Commun.*, 2012, **48**, 8407-8409.
6. H. Furukawa, F. Gándara, Y.-B. Zhang, J. Jiang, W. L. Queen, M. R. Hudson and O. M. Yaghi, *J. Am. Chem. Soc.*, 2014, **136**, 4369-4381.
7. W. Morris, B. Voloskiy, S. Demir, F. Gándara, P. L. McGrier, H. Furukawa, D. Cascio, J. F. Stoddart and O. M. Yaghi, *Inorg. Chem.*, 2012, **51**, 6443-6445.
8. M. Zhang, Y.-P. Chen, M. Bosch, T. Gentle, K. Wang, D. Feng, Z. U. Wang and H.-C. Zhou, *Angew. Chem. Int. Ed.*, 2014, **53**, 815-818.
9. V. Guillerme, F. Ragon, M. Dan-Hardi, T. Devic, M. Vishnuvarthan, B. Campo, A. Vimont, G. Clet, Q. Yang, G. Maurin, G. Férey, A. Vittadini, S. Gross and C. Serre, *Angew. Chem. Int. Ed.*, 2012, **51**, 9267-9271.
10. N. Stock and S. Biswas, *Chem. Rev.*, 2012, **112**, 933-969.
11. Coelho, *TOPAS-Academic v5*, Coelho Software, Brisbane, Australia, 2012.
12. A. Altomare, M. Camalli, C. Cuocci, C. Giacovazzo, A. Moliterni and R. Rizzi, *J. Appl. Crystallogr.*, 2009, **42**, 1197-1202.
13. Materials Studio Version 5.0; Accelrys Inc.: San Diego, **2009**.

**7.3 Direct water-based synthesis and characterization of new Zr/Hf-MOFs with dodecanuclear clusters as IBU**

Electronic Supplementary Material (ESI) for CrystEngComm.  
This journal is © The Royal Society of Chemistry 2018

**Supporting Information**

**Direct water-based synthesis and characterization of  
new Zr/Hf-MOFs with dodecanuclear clusters as IBU**

*Steve Waitschat,<sup>a</sup> Helge Reinsch,<sup>a</sup> Merve Arpacioğlu<sup>a</sup> and Norbert Stock<sup>a</sup>*

*<sup>a</sup> Institute für Anorganische Chemie, Christian-Albrechts-Universität,  
Max-Eyth-Straße 2, D 24118 Kiel, Germany*

Prof. Dr. Norbert Stock, Tel.: +49-431-880-1675, Fax: +49-431-880-1775,  
Email: [stock@ac.uni-kiel.de](mailto:stock@ac.uni-kiel.de)

**Table of Contents**

**S1 Methods and Reagents**

**S2 Synthesis and Characterization of the Linker H<sub>2</sub>APDC**

**S3 Discovery, Optimization and Synthesis of M-CAU-39**

**S4 Structural Analysis of M-CAU-39:  
Details of Rietveld refinement; Structure; Crystallographic  
Tables**

**S5 M-CAU-39: Thermal stability**

**S6 M-CAU-39: IR Spectroscopy**

**S7 M-CAU-39: N<sub>2</sub> Sorption Experiments**

**S8 References**

**S1 Methods and Reagents**

Initial characterization was performed using a Stoe Stadi P X-ray diffractometer equipped with a xy-stage, in transmission geometry using Cu K $\alpha_1$  radiation and with data collected by a Mythen detector. Powder X-Ray Diffraction (PXRD) patterns for structure determination were measured using a Stoe Stadi MP diffractometer in transmission geometry using Cu K $\alpha_1$  radiation and with data collected using a Mythen detector. Infrared spectra were recorded on a Bruker ALPHA-P A220/D-01 FTIR spectrometer equipped with an ATR unit, over the spectral range of 4000-40 cm $^{-1}$ . Thermogravimetric analysis was carried out using a NETZSCH STA 429 CD analyzer with a heating rate of 4 K min $^{-1}$  and under flowing air (flow rate 75 ml min $^{-1}$ ). Sorption isotherms were measured at -196°C for N $_2$  and 25 °C for H $_2$ O with a BELSORP-max apparatus (BEL Japan Inc.).

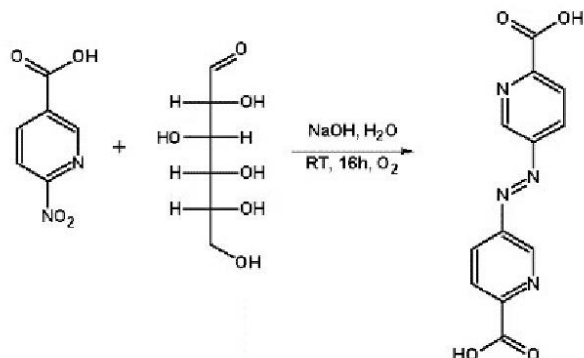
**Table S1.1.** List of reagents used in the synthesis and their suppliers.

Reagent	Supplier	Reagent	Supplier
HfCl $_4$	ABCR	Formic acid	BASF
ZrOCl $_2$ ·8H $_2$ O	ABCR	Acetic acid	VWR
		Hydrochloric acid	Walter CMP
		Ethanol	Walter CMP

4,4'-azopyridine-dicarboxylic acid (H $_2$ APDC) was synthesized following the method reported by Ameerunisha.<sup>1</sup>

**Table S1.2.** List of reagents and suppliers used in the synthesis of the linker H $_2$ APDC.

Reagent	Supplier	Reagent	Supplier
5-Nitrocolinic acid	ABCR	Sodium hydroxide	Grüssing
Hydrochloric acid	VWR	D-Glucose	Grüssing

S2 Synthesis and Characterization of the Linker H<sub>2</sub>APDC

**Fig. S2.1:** Reaction scheme for the synthesis 4,4'-azopyridine-dicarboxylic acid from 5-nitropicolinic acid.

The synthesis was carried out according to the literature.<sup>[1]</sup> 5 g (0.03 mol) 5-nitro-picolinic acid was dissolved in 66 ml H<sub>2</sub>O with 13 g (0.325 mol) NaOH in a 250 ml round bottom flask, the mixture was stirred for 1 h at 60 °C. In this time 27 g D-glucose (0.21 mol) was dissolved in 40 ml H<sub>2</sub>O at approximately 40 °C. The sugar solution was added to the round bottom flask and the whole synthesis mixture was stirred at 60 °C for 3 h. Afterwards the mixture was cooled down to room temperature and was stirred for 16 h while bubbling pressurized air through the solution. Subsequently the product was filtered off, the solid was dissolved in approximately 200 ml H<sub>2</sub>O and precipitated with conc. HCl. The observed red-orange powder was analyzed with <sup>1</sup>H-NMR spectroscopy.

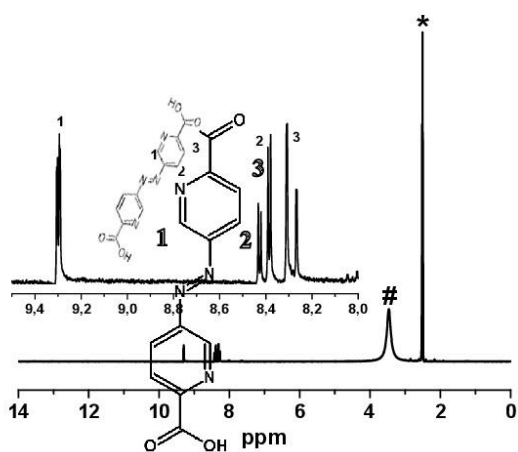


**Fig. S2.2:** <sup>1</sup>H-NMR spectrum of 4,4'-azopyridine-dicarboxylic acid dissolved in (CD<sub>3</sub>)<sub>2</sub>SO (\* signal of (CD<sub>3</sub>)<sub>2</sub>SO and # signal of water).



### Synthesis and Characterization of M-CAU-39

#### S3 Discovery, Optimization and Synthesis of M-CAU-39

The systematic investigation of the chemical system  $M^{4+}/APDC^{2-}$  of M-CAU-39 with  $M = Zr^{4+}$  and  $Hf^{4+}$  was carried out via Pyrex-tubes heated up in an aluminum block. The synthesis conditions of CAU-22<sup>[2]</sup> were initially used and optimized towards the optimized synthesis conditions of CAU-39. Detailed reaction conditions are summarized in Tab. S3.1 and Tab. S3.2. The optimized reaction conditions are indicated by a red box.

**Table S3.1.** Reaction parameters of the synthesis optimisation of Zr-CAU-39.  $M = ZrOCl_2 \cdot 8H_2O$ , The red box shows the optimized reaction parameter for the synthesis of Zr-CAU-39. The metal to linker ratio was fixed to 1:1 for every reaction. Mod = Modulator.

M / g	H <sub>2</sub> APDC / g	H <sub>2</sub> O / $\mu$ L	Modulator	Mod. / $\mu$ L	T / °C	t / min
0.0322	0.0273	400	HCOOH	1600	140	60
0.0322	0.0273	400	HCOOH	1600	140	120
0.0322	0.0273	400	HCOOH	1600	140	180
0.0322	0.0273	400	HCOOH	1600	140	240
0.0322	0.0273	400	CH <sub>3</sub> COOH	1600	140	5
0.0322	0.0273	400	CH <sub>3</sub> COOH	1600	140	10
0.0322	0.0273	400	CH <sub>3</sub> COOH	1600	140	20
0.0322	0.0273	400	CH <sub>3</sub> COOH	1600	140	30
0.0322	0.0273	400	CH <sub>3</sub> COOH	1600	140	40
0.0322	0.0273	400	CH <sub>3</sub> COOH	1600	140	50
0.0322	0.0273	400	CH <sub>3</sub> COOH	1600	140	60
0.0322	0.0273	400	CH <sub>3</sub> COOH	1600	140	70
0.0322	0.0273	400	CH <sub>3</sub> COOH	1600	140	80
0.0322	0.0273	400	CH <sub>3</sub> COOH	1600	140	90
0.0322	0.0273	400	CH <sub>3</sub> COOH	1600	140	100
0.0322	0.0273	400	CH <sub>3</sub> COOH	1600	140	120
0.0322	0.0273	400	CH <sub>3</sub> COOH	1600	140	180
0.0322	0.0273	400	CH <sub>3</sub> COOH	1600	160	5
0.0322	0.0273	400	CH <sub>3</sub> COOH	1600	160	20
0.0322	0.0273	400	CH <sub>3</sub> COOH	1600	160	60
0.0322	0.0273	400	CH <sub>3</sub> COOH	1600	160	120
0.0322	0.0273	400	CH <sub>3</sub> COOH	1600	160	180
0.0161	0.0136	1200	CH <sub>3</sub> COOH	800	140	5
0.0161	0.0136	1200	CH <sub>3</sub> COOH	800	140	10
0.0161	0.0136	1200	CH <sub>3</sub> COOH	800	140	20
0.0161	0.0136	1200	CH <sub>3</sub> COOH	800	140	30
0.0161	0.0136	1200	CH <sub>3</sub> COOH	800	140	40
0.0161	0.0136	1200	CH <sub>3</sub> COOH	800	140	50
0.0322	0.0273	400	C <sub>2</sub> H <sub>5</sub> COOH	1600	140	5
0.0322	0.0273	400	C <sub>2</sub> H <sub>5</sub> COOH	1600	140	10
0.0322	0.0273	400	C <sub>2</sub> H <sub>5</sub> COOH	1600	140	20
0.0322	0.0273	400	C <sub>2</sub> H <sub>5</sub> COOH	1600	140	30
0.0322	0.0273	400	C <sub>2</sub> H <sub>5</sub> COOH	1600	140	40
0.0322	0.0273	400	C <sub>2</sub> H <sub>5</sub> COOH	1600	140	50
0.0322	0.0273	400	C <sub>2</sub> H <sub>5</sub> COOH	1600	140	60
0.0322	0.0273	400	HCl	1600	140	5
0.0322	0.0273	400	HCl	1600	140	10
0.0322	0.0273	400	HCl	1600	140	20
0.0322	0.0273	400	HCl	1600	140	30

## Anhang

0.0322	0.0273	400	HCl	1600	140	40
0.0322	0.0273	400	HCl	1600	140	50
0.0322	0.0273	400	HCl	1600	140	60

**Table S3.2.** Reaction parameters of the synthesis optimisation of Hf-CAU-39. M = HfCl<sub>4</sub>. The red box shows the optimized reaction parameter for the synthesis of Hf-CAU-39. The metal to linker ratio was fixed to 1:1 for every reaction. Mod = Modulator.

M / g	H <sub>2</sub> APDC / g	H <sub>2</sub> O / $\mu$ L	Modulator	Mod. / $\mu$ L	T / °C	t / min
0.0289	0.0136	1600	HCOOH	400	140	5
0.0289	0.0136	1600	HCOOH	400	140	10
0.0289	0.0136	1600	HCOOH	400	140	20
0.0289	0.0136	1600	HCOOH	400	140	30
0.0289	0.0136	1600	HCOOH	400	140	40
0.0289	0.0136	1600	HCOOH	400	140	50
0.0289	0.0136	1600	HCOOH	400	140	60
0.0289	0.0136	1200	HCOOH	800	140	5
0.0289	0.0136	1200	HCOOH	800	140	10
0.0289	0.0136	1200	HCOOH	800	140	20
0.0289	0.0136	1200	HCOOH	800	140	30
0.0289	0.0136	1200	HCOOH	800	140	40
0.0289	0.0136	1200	HCOOH	800	140	50
0.0289	0.0136	1200	HCOOH	800	140	60
0.0289	0.0136	1600	CH <sub>3</sub> COOH	400	140	5
0.0289	0.0136	1600	CH <sub>3</sub> COOH	400	140	10
0.0289	0.0136	1600	CH <sub>3</sub> COOH	400	140	20
0.0289	0.0136	1600	CH <sub>3</sub> COOH	400	160	30
0.0289	0.0136	1600	CH <sub>3</sub> COOH	400	160	40
0.0289	0.0136	1600	CH <sub>3</sub> COOH	400	160	50
0.0289	0.0136	1600	CH <sub>3</sub> COOH	400	160	60
0.0289	0.0136	1200	CH <sub>3</sub> COOH	800	160	5
0.0289	0.0136	1200	CH <sub>3</sub> COOH	800	140	10
0.0289	0.0136	1200	CH <sub>3</sub> COOH	800	140	20
0.0289	0.0136	1200	CH <sub>3</sub> COOH	800	140	30
0.0289	0.0136	1200	CH <sub>3</sub> COOH	800	140	40
0.0289	0.0136	1200	CH <sub>3</sub> COOH	800	140	50
0.0289	0.0136	1200	CH <sub>3</sub> COOH	800	140	60

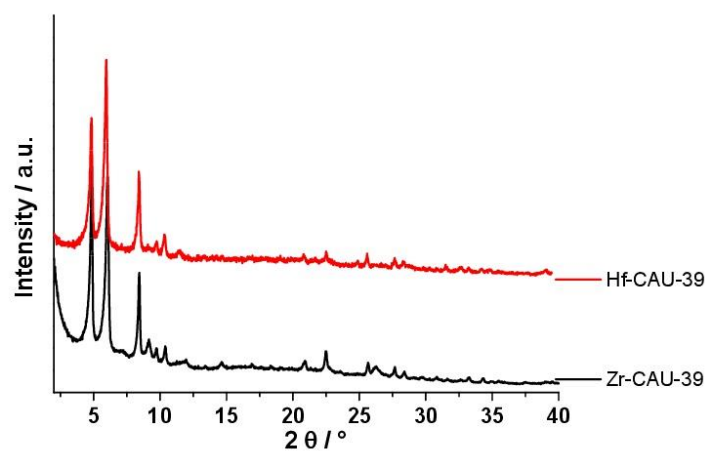


**Fig. S3.1:** PXRD patterns of the obtained M-CAU-39, with M = Zr, Hf from the optimized reaction conditions.

#### S4 Structural Analysis of M-CAU-39

##### S4 Details of the Rietveld Refinement

The PXRD pattern for Hf-CAU-39 was measured in transmission geometry using  $\text{CuK}\alpha_1$  radiation and could be successfully indexed using TOPAS academics<sup>[3]</sup> with a hexagonal cell with extinction conditions suitable for space group  $P6_3/m$ . The space group symmetry thus is lower than the one of the recently reported MOF based on biphenyldicarboxylic acid<sup>[4]</sup> ( $P6_3/mmc$ ). Still, a suitable model was developed by converting the crystal structure of the former compound using the Materials Studio software.<sup>[5]</sup> The crystal structure was converted into a triclinic model in space group  $P1$ , the carboxylate capped clusters were slightly rotated around  $c$  axis and the azo-functionality was manually inserted into this model. Indeed the model exhibited the observed space group symmetry  $P6_3/m$ . It was energetically optimized by force-field calculations using the forcite routine implemented in Materials Studio. Subsequently the model was refined by Rietveld methods. Residual electron density as identified by Fourier synthesis was attributed to partially occupied oxygen atoms, which serve as dummies for any kind of guest molecules. The linker molecule was refined as fragmented rigid body, i.e. two half molecules split at the azo-group. All other atoms were freely refined. The temperature factors were refined as one parameter for all atoms and a preferred orientation along (110) was also taken into account. The final plot is shown in Fig. S4.1. For Zr-CAU-39 the PXRD data proves its isoreticularity and the cell parameters were refined by the Le Bail method. However, the structure could not be refined by Rietveld methods, which we tentatively attribute to a possible stronger stacking disorder which affects the peak intensities.

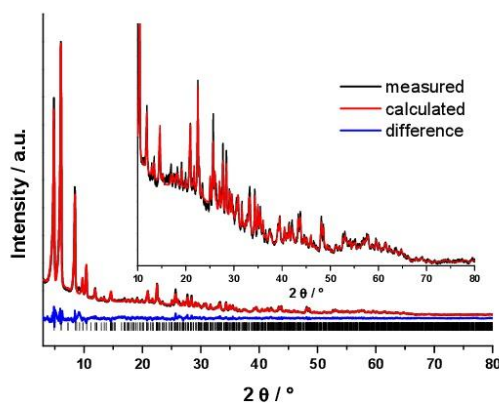


**Figure S4.1.** Rietveld plot for the final refinement of Hf-CAU-39. Black line gives the experimental data, red line the calculated fit and the blue line is the difference curve. Black bars indicate the Bragg reflection positions.

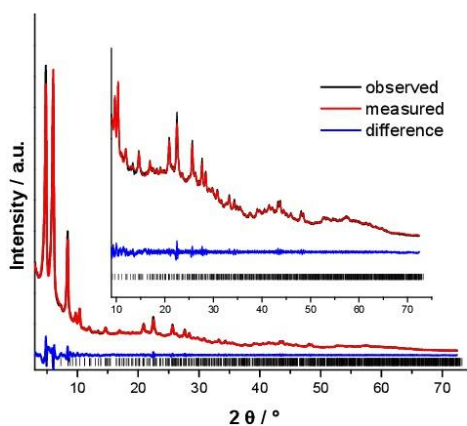


**Figure S4.2.** Le-Bail-Fit of Zr-CAU-39. Black line gives the experimental data, red line the calculated fit and the blue line is the difference curve. Black bars indicate the Bragg reflection positions.

**Table S4.1.** Crystallographic data for M-CAU-39 with M = Hf (Rietfeld refinement) and M = Zr (Le-Bail-Fit).

Compound	Hf-CAU-39	Zr-CAU-39
Space Group	<i>P63/m</i>	<i>P63/m</i>
Crystal System	Hexagonal	Hexagonal
$a / \text{Å}$	20.8436(8)	20.86(2)
$c / \text{Å}$	24.367(2)	24.25(3)
Wavelength / Å	Cu $K_{\alpha 1}$	Cu $K_{\alpha 1}$
$R_p / \%$	3.8	2.2
$R_{wp} / \%$	5.0	3.0
GoF	2.5	4.9

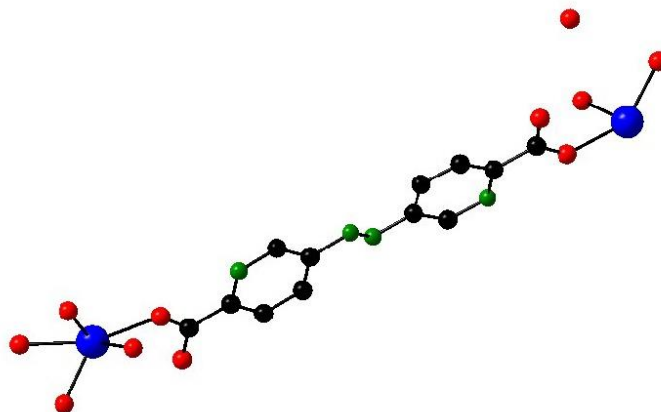


**Figure 4.3.** Asymmetric unit of M-CAU-39. Oxygen atoms representing water molecules are omitted for clarity.

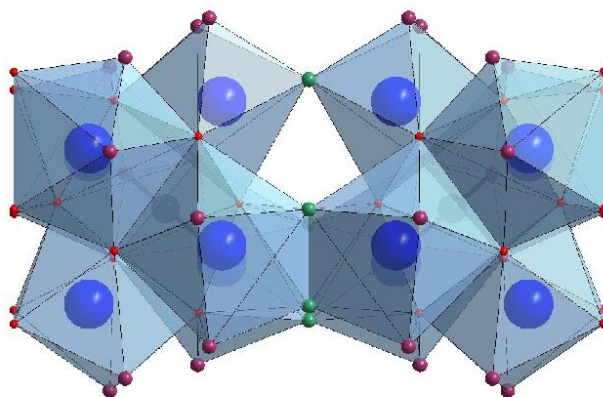


**Figure 4.4** The dodecanuclear MO-cluster observed as IBU in the crystal structure of M-CAU-39. The different oxygen atoms are highlighted according the following composition  $[M_{12}(\mu_3-O)_8(\mu_3-OH)_8(OH)_6(\mu-OH)_6(H_2O)_6(COO-R)_6]$ .

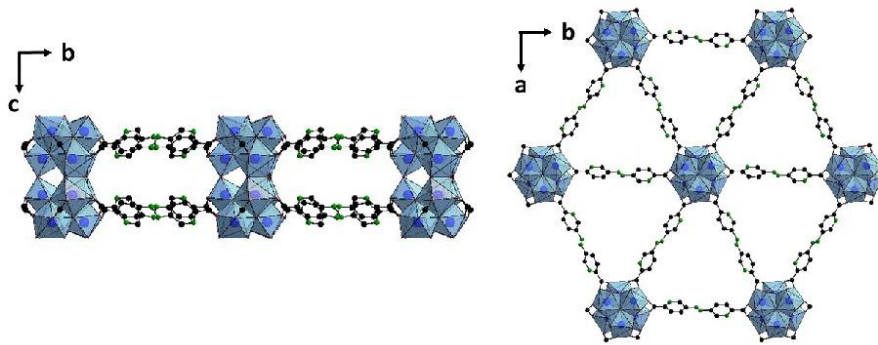


**Figure 4.5.** One layer of M-CAU-39 along the  $a$ -axis (left) and along the  $c$ -axis (right)

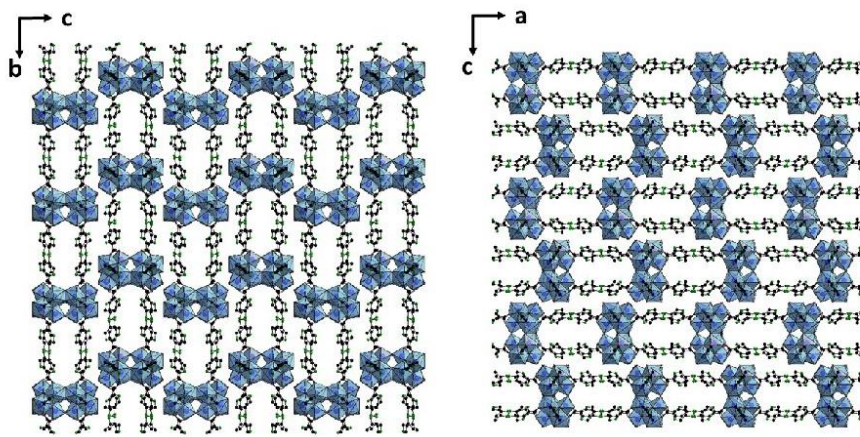


**Figure 4.6.** Multiple-layers of M-CAU-39 indicating an ABA stacking as seen along the  $a$ -axis (left) and along the  $b$ -axis (right).

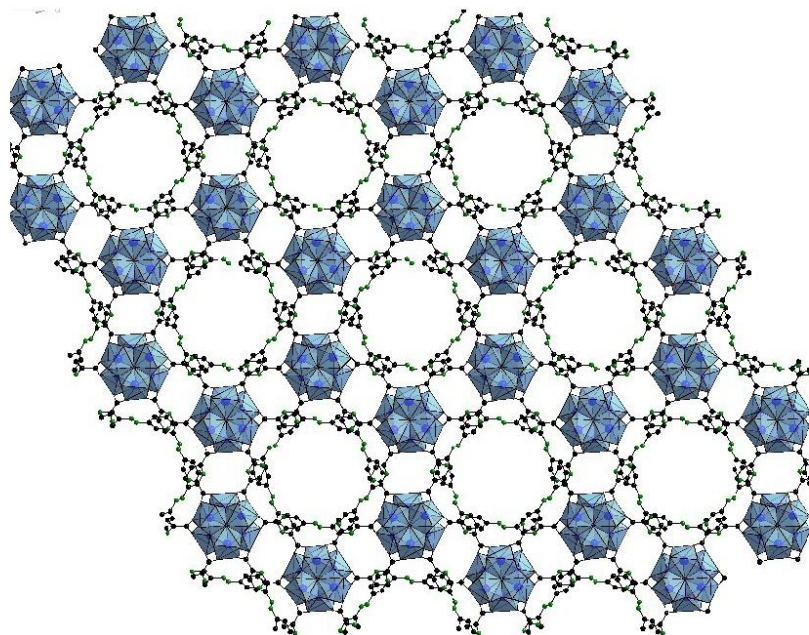


**Figure 4.7.** Structure of M-CAU-39 as seen along the *c*-axis.



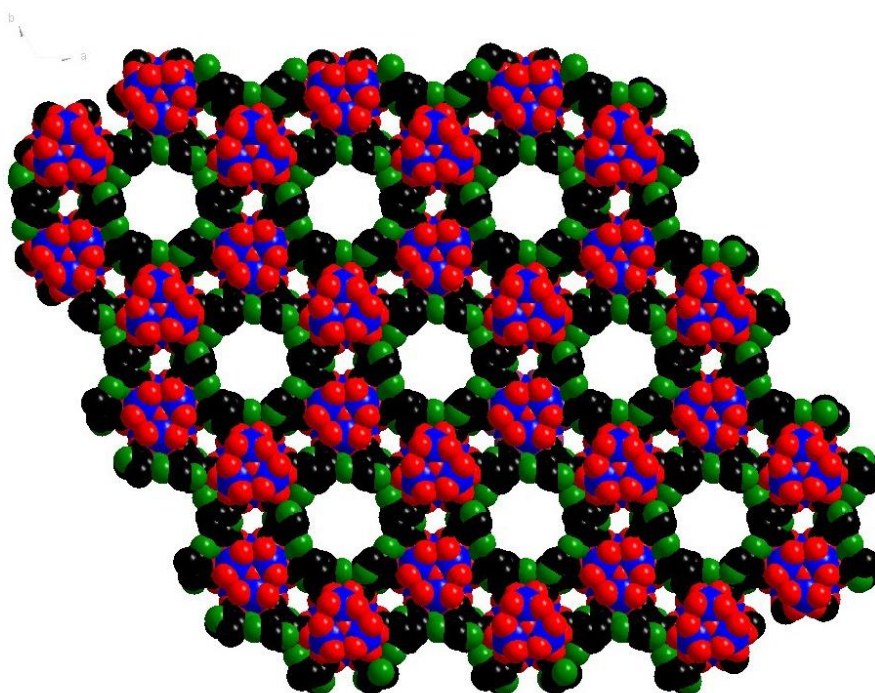


**Figure 4.8.** Structure of M-CAU-39 as seen along the *c*-axis with a space filling model. The pore diameter is approximately 8 Å.

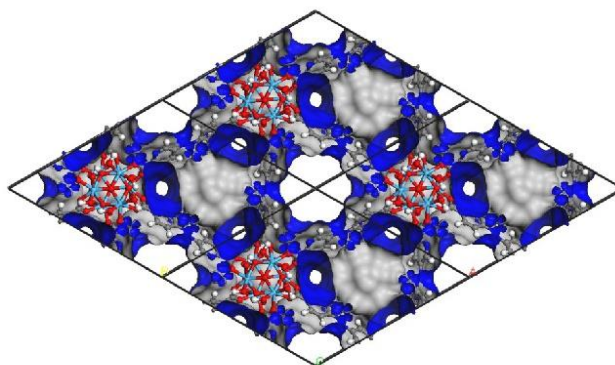


**Fig. 4.9.** Conolly surface area generated with water as probe molecule.

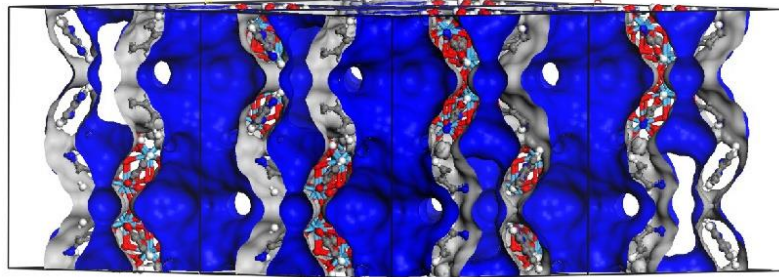


**Fig. 4.10.** Conolly surface area of the channels seen along [1 1 0].

## S5 M-CAU-39: Thermal stability

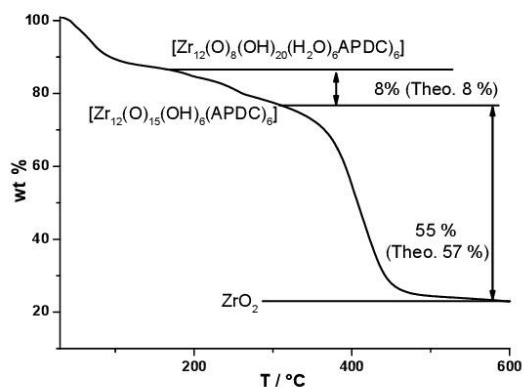


**Figure S5.1.** TGA plot for Zr-CAU-39  $[\text{Zr}_{12}(\text{O})_8(\text{OH})_{20}(\text{H}_2\text{O})_6(\text{APDC})_6] \cdot x$  solvent showing the weight loss event occurring on dehydration, assigned to the loss of physisorbed water molecules up to 170 °C, above this temperature the dehydration of the dodecancluster (8 wt.%, expected 8 %) is observed, above 320 °C the total structure decompose (55 wt.%; expected 57%).

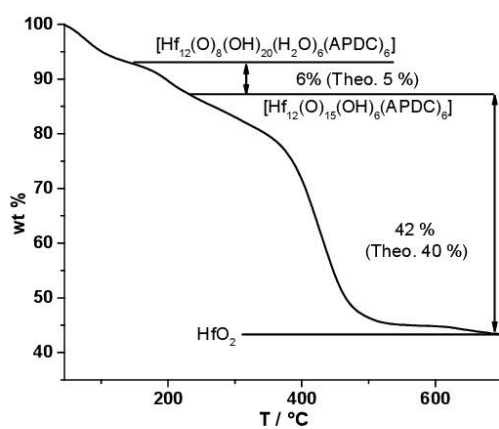


**Figure S5.2.** TGA plot for Hf-CAU-39  $[\text{Hf}_{12}(\text{O})_8(\text{OH})_{20}(\text{H}_2\text{O})_6(\text{APDC})_6] \cdot x$  solvent showing the weight loss event occurring on dehydration, assigned to the loss of physisorbed water molecules up to 170 °C, above this temperature the dehydration of the dodecancluster (6 wt.%, expected 5 %) is observed, above 320 °C the total structure decompose (42 wt.%; expected 40%).

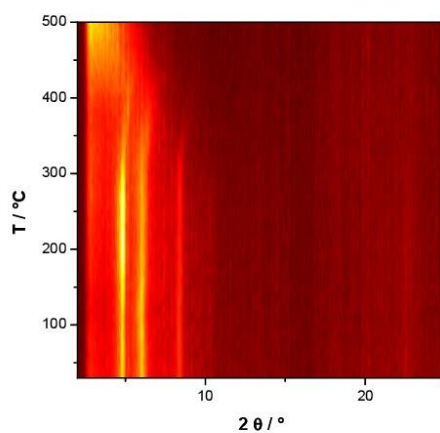


**Figure S5.3.** VT-PXRD measurement of Zr-CAU-39 measured in transmission geometry using Cu K $\alpha$ 1 radiation. The compound is thermally stable up to approximately 350 °C.

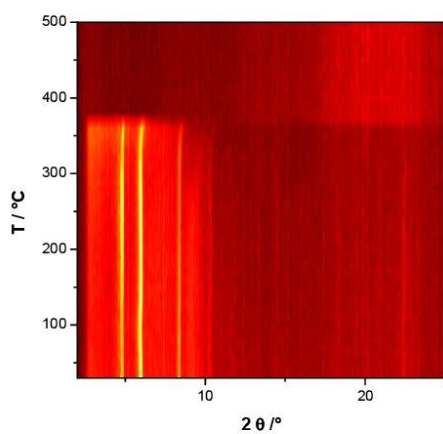


**Figure S5.4.** VT-PXRD measurement of Hf-CAU-39 measured in transmission geometry using Cu K $\alpha$ 1 radiation. The compound is thermally stable up to approximately 375 °C.

## S6 M-CAU-39: Infrared Spectroscopy

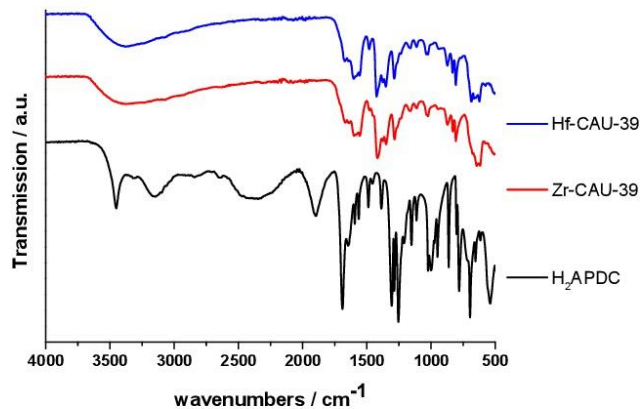


**Figure S6.1.** FTIR spectrum of M-CAU-39 with M = Zr and Hf.

Tab. S6.1 Classification of the vibrations of M-CAU-39 with M = Zr and Hf from the FTIR spectrum.

	Vibration	Intensity	Wavenumber / $\text{cm}^{-1}$
Zr-CAU-39	OH-stretch – $\text{H}_2\text{O}$	b	3434
	Asymmetric $\text{CO}_2^-$ stretch – APDC $^{2-}$	m	1600
	Symmetric $\text{CO}_2^-$ stretch – APDC $^{2-}$	m	1419
Hf-CAU-39	OH-stretch – $\text{H}_2\text{O}$	b	3371
	Asymmetric $\text{CO}_2^-$ stretch – APDC $^{2-}$	m	1604
	Symmetric $\text{CO}_2^-$ stretch – APDC $^{2-}$	m	1436

**S7 M-CAU-39: N<sub>2</sub> Sorption Experiments**

M-CAU-39 with M = Zr and Hf was activated for sorption measurements by heating the sample to 120°C under vacuum overnight. M-CAU -39 is porous towards N<sub>2</sub> at -196 °C (Fig. S7.1).

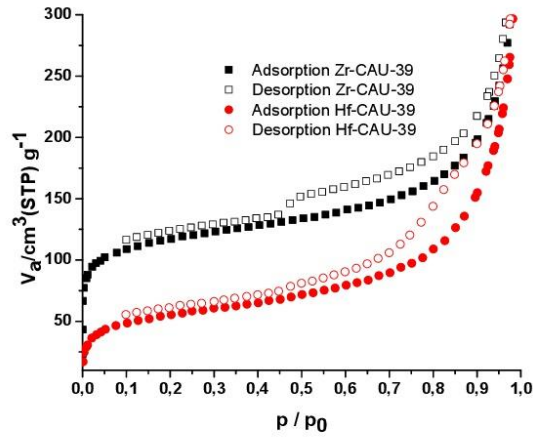


**Figure S7.1.** N<sub>2</sub>-adsorption and desorption isotherms for M-CAU -39 with M = Hf (red) and Zr (black) measured at -196 °C.

Tab. S7.1 The specific surface area ( $a_{s,BET}$ ) and the micropore volume ( $V_{mic}$ ) based on N<sub>2</sub> adsorption of M-CAU -39 with M = Zr and Hf.

	$a_{s,BET} / m^2 \cdot g^{-1}$	$V_{mic} / cm^3 \cdot g^{-1}$
Zr-CAU-39	430	0.21
Hf-CAU-39	200	0.11

**S8**    **References**

1. S. Ameerunisha, P. S. Zacharias, *J. Chem. Soc. Perkin. Trans. 2*, **1995**, 1679 – 1682.
2. S. Waitschat, H. Reinsch, N. Stock, *Chem. Commun.*, **2016**, 52, 12698 - 12701.
3. Coelho, *TOPAS-Academic v5*, Coelho Software, Brisbane, Australia, 2012.
4. M. J. Cliffe, E. Castillo-Martinez, Y. Wu, J. Lee, A. C. Forse, F. C. N. Firth, P. Z. Moghadam, D. Fairen-Jimenez, M. W. Gaultois, J. A. Hill, O. V. Magdysyuk, B. Slater, A. L. Goodwin and C. P. Grey, *J. Am. Chem. Soc.*, 2017, **139 (15)**, 5397 - 5404.
5. Materials Studio Version 5.0; Accelrys Inc.: San Diego, **2009**.

**7.4 Flow-synthesis of carboxylate and phosphonate based metal–organic frameworks under nonsolvothermal reaction conditions**

Electronic Supplementary Material (ESI) for Dalton Transactions.  
This journal is © The Royal Society of Chemistry 2015

**Supporting Information**

**Flow-Synthesis of Carboxylate and Phosphonate  
Based Metal-Organic Frameworks Under Non-  
solvothermal Reaction Conditions**

*Steve Waitschat<sup>a</sup>, Michael T. Wharmby<sup>a,b</sup> and Norbert Stock<sup>a</sup>*

<sup>a</sup> *Institute für Anorganische Chemie, Christian-Albrechts-Universität,  
Max-Eyth-Straße 2, D 24118 Kiel, Germany*

<sup>b</sup> *Diamond Light Source Ltd., Diamond House, Harwell Science and Innovation Campus,  
Didcot, Oxfordshire, OX11 0DE, United Kingdom*

Prof. Dr. Norbert Stock, Tel.: +49-431-880-1675, Fax: +49-431-880-1775,  
Email: [stock@ac.uni-kiel.de](mailto:stock@ac.uni-kiel.de)

Dr Michael. T Wharmby, Tel.: +44-1235-77-8327, Fax: +44-1235-778468,  
Email: [michael.wharmby@diamond.ac.uk](mailto:michael.wharmby@diamond.ac.uk)



**Table of Contents**

<b>S1</b>	<b>Previous Reports of Flow Syntheses</b>
<b>S2</b>	<b>Reagents</b>
<b>S3</b>	<b>Description of the Non-Solvothermal Flow Reactor</b>
<b>S4</b>	<b>Flow Synthesis &amp; Characterization of UiO-66</b>
<b>S4.1</b>	<b>Flow Reactor Synthesis</b>
<b>S4.2</b>	<b>UiO-66: Powder Diffraction Pattern &amp; Pawley Fit</b>
<b>S4.3</b>	<b>UiO-66: Thermal &amp; Elemental Analysis</b>
<b>S4.4</b>	<b>UiO-66: Infrared Spectrum</b>
<b>S4.5</b>	<b>UiO-66: SEM Image</b>
<b>S4.6</b>	<b>UiO-66: N<sub>2</sub> Sorption Experiments</b>
<b>S5</b>	<b>Flow Synthesis &amp; Characterization of CAU-13</b>
<b>S5.1</b>	<b>Flow Reactor Synthesis</b>
<b>S5.2</b>	<b>CAU-13: Pawley Fit</b>
<b>S5.3</b>	<b>CAU-13: Thermal &amp; Elemental Analysis</b>
<b>S5.4</b>	<b>CAU-13: Infrared Spectrum</b>
<b>S5.5</b>	<b>CAU-13: NMR Spectrum</b>
<b>S5.6</b>	<b>CAU-13: SEM Image</b>
<b>S5.7</b>	<b>CAU-13: N<sub>2</sub> Sorption Experiments</b>
<b>S6</b>	<b>Flow Synthesis &amp; Characterization of STA-12(Cd)</b>
<b>S6.1</b>	<b>Flow Reactor Synthesis</b>
<b>S6.2</b>	<b>Structural Analysis of STA-12(Cd): Details of Rietveld refinement; Structure; Crystallographic Tables</b>
<b>S6.3</b>	<b>STA-12(Cd): Thermal &amp; Elemental Analysis</b>
<b>S6.4</b>	<b>STA-12(Cd): Infrared Spectrum</b>
<b>S6.5</b>	<b>STA-12(Cd): NMR Spectrum</b>
<b>S6.5</b>	<b>STA-12(Cd): SEM Image</b>
<b>S6.6</b>	<b>STA-12(Cd): N<sub>2</sub> Sorption Experiments</b>
<b>S7</b>	<b>References</b>

# Anhang

## S1 Previous Reports of Flow Reactor Syntheses

**Table S1.1.** Summary of the published syntheses of Metal-Organic Framework (MOF) compounds in flow reactors and their reaction conditions.

Framework	Metal Source	Linker	Solvent	Temp. / °C	Time / min	Pressure / bar	Reference
HKUST-1	Cu(NO <sub>3</sub> ) <sub>2</sub> ·2.5H <sub>2</sub> O	H <sub>3</sub> BTC	H <sub>2</sub> O/DMF/EtOH	100 - 400	0.0167	250	1
HKUST-1	Cu(NO <sub>3</sub> ) <sub>2</sub> ·6H <sub>2</sub> O	H <sub>3</sub> BTC	EtOH or H <sub>2</sub> O	60 - 160	5	100	2
HKUST-1	Cu(NO <sub>3</sub> ) <sub>2</sub> ·H <sub>2</sub> O	H <sub>3</sub> BTC	DMF/EtOH/H <sub>2</sub> O	90	1 - 12	-	3
HKUST-1	Cu(NO <sub>3</sub> ) <sub>2</sub> ·H <sub>2</sub> O	H <sub>3</sub> BTC	EtOH	200	15	75	4
HKUST-1	Cu(NO <sub>3</sub> ) <sub>2</sub> ·3H <sub>2</sub> O	H <sub>3</sub> BTC	EtOH	140	1 - 10	≤ 20	5
CPO-27(Ni)	Ni(AcO) <sub>2</sub> ·4H <sub>2</sub> O	H <sub>2</sub> DOBDC	H <sub>2</sub> O/DMF	200	0.0167	205	1
MIL-88B(Fe)	FeCl <sub>3</sub> ·6H <sub>2</sub> O	H <sub>2</sub> BDC	DMF/H <sub>2</sub> O	95	4	-	6
MIL-53(Al)	Al(NO <sub>3</sub> ) <sub>3</sub> ·9H <sub>2</sub> O	H <sub>2</sub> BDC	H <sub>2</sub> O	250	20	230	4
UiO-66	ZrCl <sub>4</sub>	H <sub>2</sub> BDC	DMF/HCl	140	15	-	3
UiO-66	ZrCl <sub>4</sub>	H <sub>2</sub> BDC	DMF	130	10	≤ 20	5
UiO-66	ZrCl <sub>4</sub>	H <sub>2</sub> BDC	DMF	120	45	-	This work
UiO-66-NH <sub>2</sub>	ZrCl <sub>4</sub>	H <sub>2</sub> BDC-NH <sub>2</sub>	DMF	100-120	720	-	7
NOTT-400	Sc(SO <sub>3</sub> CF <sub>3</sub> ) <sub>3</sub>	H <sub>4</sub> BPTC	DMF/THF/H <sub>2</sub> O	85	15	≤ 20	5
MOF-5	Zn(NO <sub>3</sub> ) <sub>6</sub> ·H <sub>2</sub> O	H <sub>2</sub> BDC	DMF	120	3	-	3
IRMOF-3	Zn(NO <sub>3</sub> ) <sub>6</sub> ·H <sub>2</sub> O	H <sub>2</sub> BDC-NH <sub>2</sub>	DMF	120	3	-	3
[Ce <sub>5</sub> (BDC) <sub>7.5</sub> (DMF) <sub>4</sub> ]	Ce(NH <sub>4</sub> ) <sub>2</sub> (NO <sub>3</sub> ) <sub>6</sub>	H <sub>2</sub> BDC	DMF	230	0.5	100	8
CAU-13	AlCl <sub>3</sub> ·6H <sub>2</sub> O	H <sub>2</sub> CDC	DMF/AcOH	130	20	-	This work
STA-12(Cd)	Cd(AcO) <sub>2</sub> ·2H <sub>2</sub> O	H <sub>4</sub> L	H <sub>2</sub> O/KOH	70	15	-	This work

\* H<sub>3</sub>BTC - Benzene-1,3,5-tricarboxylic acid; H<sub>2</sub>BDC - Benzene-1,4-dicarboxylic acid; H<sub>2</sub>BDC-NH<sub>2</sub> - 2-aminobenzene-1,4-dicarboxylic acid; H<sub>2</sub>DOBDC - 2,5-dihydroxybenzene-1,4-dicarboxylic acid; H<sub>4</sub>BPTC - Biphenyl-3,3',5,5'-tetracarboxylic acid; H<sub>2</sub>CDC - Cyclohexane-1,4-dicarboxylic acid; H<sub>4</sub>L - N,N'-piperazinebis(methylenephosphonic acid).

## S2 Reagents

**Table S2.1.** List of reagents and suppliers used in the synthesis of inorganic-organic hybrid compounds in the flow reactor

Reagent	Supplier	Reagent	Supplier
Aluminium(III) chloride hexahydrate	Sigma Aldrich	<i>trans</i> -1,4-cyclohexane-dicarboxylic acid	ABCR
Cadmium acetate dihydrate	ABCR	1,4-benzenedicarboxylic acid	Sigma Aldrich
Cobalt(II) acetate tetrahydrate	ABCR	Acetic acid	Alfa Aesar
Nickel(II) acetate tetrahydrate	Alfa Aesar	N,N-dimethylformamide (DMF)	BASF
Zirconium tetrachloride	ABCR	Paraffin	Alfa Aesar
		Potassium hydroxide (pellets)	BAK

N,N'-piperazinebis(methylenephosphonic acid) (**H<sub>4</sub>L**) was synthesised following the method reported by Mowat *et al.*<sup>9</sup>

**Table S2.2.** List of reagents and suppliers used in the synthesis of the linker **H<sub>4</sub>L**.

Reagent	Supplier	Reagent	Supplier
Piperazine	Alfa Aesar	Phosphorous acid	ABCR
Formaldehyde	Alfa Aesar	Hydrochloric acid	Alfa Aesar

### S3 Description of the Non-Solvothermal Flow Reactor

Two configurations of the non-solvothermal flow reactor reported in this work were developed: the first with three syringe pumps (two reagents and one transport medium); the second with two syringe pumps (two reagents) and fitted with an ultrasonic probe. Both configurations are assembled from widely available commodity hardware (Table S3.1).

**Table S3.1.** List of parts & materials used to assemble the flow reactor.

Part	Supplier	Part	Supplier
Syringe pump LA-100	Landgraf Laborsysteme HLL GmbH, Germany	Teflon® tube (ID = 1.6 mm)	Eydam KG, Germany
PEEK/PTFE Y- and X-connectors	TechLab GmbH, Germany	Flangeless Ferules and nuts	Upchurch Scientific, IDEX Health & Science LLC, USA
Stirrer Hotplate	Eydam KG, Germany	Ultrasonic Probe UP-200s	Dr. Hielscher GmbH, Germany



**Figure S3.1.** Photograph of the two syringe pump configuration of the flow reactor including the ultrasonic probe (centre).

In both configurations, solutions of reagents are loaded into syringe pumps. These are then connected through lengths of Teflon® tube to a three-way Y- or four-way X-connector (for the three & four pump configurations respectively). At this point, the two reagents in the system first mix together. In the three-pump configuration, in addition to the two reagent flows, a transport flow is also pumped into the X-connector, which helps to prevent clogging by either increasing the flow rate (when solvents are used as the transport medium) or by forming bubbles of reagent solution (when paraffin is used)

## Anhang

which are isolated from each other and also from the walls of the reactor tube. The molar ratio of reagents mixing in the reactor is a function of the concentrations of the solutions and their relative pumping rates (Eq.S3.1). The residence time of the reagents in the reactor is a function of the total volume of the reactor ( $V_{\Sigma}$ ) and the overall flow rate (Eq.S3.2).

$$mol_n = M_n * 1000 * f_n$$

$$t = \frac{V_{\Sigma}}{\sum_n f_n}$$

**Equation S3.1.** The amount of the  $n^{\text{th}}$  reagent in the flow reactor ( $mol_n$  in  $mol \text{ min}^{-1}$ ) is calculated from the concentration ( $M_n$  in  $mol \text{ dm}^{-3}$ ) and the flow rate ( $f_n$  in  $ml \text{ min}^{-1}$ ).

**Equation S3.2.** Residence time in the flow reactor ( $t$  in  $min$ ) determined by the sum of all flow rates ( $f_n$  in  $ml \text{ min}^{-1}$ ) and the volume of the flow reactor ( $V_{\Sigma}$  in  $ml$ ).

## S4 Flow Synthesis and Characterisation of UiO-66

### S4.1 Flow Reactor Synthesis

For the flow reactor syntheses, zirconium tetrachloride ( $\text{ZrCl}_4$ ) and the linker 1,4-benzenedicarboxylic acid (terephthalic acid,  $\text{H}_2\text{BDC}$ ) were dissolved in *N,N*-dimethylformamide (DMF) to yield two solutions both with concentrations of  $0.1 \text{ mol dm}^{-3}$ . These solutions were then loaded into the syringe pumps and connected to the flow reactor with either two- or three-pump configurations. Typical syntheses in both these configurations are given below.

#### S4.1.1 Typical Three-Pump Configuration

The loaded syringe pumps were connected into a three syringe pump configuration (metal, linker and paraffin) and solutions were injected into a flow reactor ( $V_{\Sigma} = 14.45 \text{ ml}$ ) with flow rates of  $0.040 \text{ ml min}^{-1}$ ,  $0.120 \text{ ml min}^{-1}$  and  $0.161 \text{ ml min}^{-1}$  for the metal, linker and paraffin respectively, giving a molar ratio of reagents of 1:3 ( $\text{ZrCl}_4:\text{H}_2\text{BDC}$ ) total reaction time of 45 mins. During the reaction the flow reactor was kept at a temperature of  $120^\circ\text{C}$ . The reaction product was collected, and separated by filtration and washed sequentially with dichloromethane (DCM) and ethanol.

#### S4.1.2 Typical Two-Pump Configuration

The loaded syringe pumps were connected into a two syringe pump configuration (metal and linker) fitted with an ultrasonic probe to prevent clogging. The solutions were injected into a flow reactor ( $V_{\Sigma} = 16.87 \text{ ml}$ ) with flow rates of  $0.094 \text{ ml min}^{-1}$  and  $0.281 \text{ ml min}^{-1}$  for the metal and linker solutions respectively, giving a total reaction time of 45 mins. During the reaction the flow reactor was kept at a temperature of  $120^\circ\text{C}$  and the ultrasonic probe was set up with a cycle of 0.25 and amplitude of 100 %. The product was collected, and separated by centrifugation and washing with DMF followed by ethanol.

#### S4.1.3 Summary of Flow Reactor Experiments

**Table S4.1.** Summary of the reaction conditions tested for the synthesis of UiO-66 using the flow reactor.

$V_{\Sigma} / \text{ml}$	$\text{ZrCl}_4$ Flowrate / $\text{ml min}^{-1}$	$\text{H}_2\text{BDC}$ Flowrate / $\text{ml min}^{-1}$	Transport <sup>a</sup> Flowrate / $\text{ml min}^{-1}$	Temp. / $^\circ\text{C}$	Time / min	Ultra Sound	
						Cycle	Amplitude
14.45	0.040	0.120	0.161 (Para.)	120	45	-	-
16.83	0.047	0.140	0.187 (DMF)	130	45	-	-
16.87 <sup>b</sup>	0.094	0.281	-	120	45	0.25	100 %
16.80	0.070	0.210	-	120	60	0.25	100 %
16.87	0.094	0.281	-	120	45	-	-
16.80	0.070	0.210	-	120	60	-	-

<sup>a</sup> A transport medium in addition to the reaction solvent, used to prevent clogging of the reactor.

<sup>b</sup> This reaction produced the most crystalline and phase pure UiO-66, which is further analysed in this work. This is equivalent to a reaction ratio of 1:3 ( $\text{ZrCl}_4:\text{H}_2\text{BDC}$ ).

**Table S4.2.** Optimised reaction conditions for the synthesis of UiO-66 using the a three-pump flow reactor, with paraffin as the transport medium, and a two-pump flow reactor fitted with an ultrasonic probe (cycle 0.25, amplitude 100 %).

	ZrCl <sub>4</sub> Flowrate / ml min <sup>-1</sup>	H <sub>2</sub> BDC Flowrate / ml min <sup>-1</sup>	Transport Flowrate / ml min <sup>-1</sup>	Temp. / °C	Time
Three-pump	0.040	0.120	0.161	120	45
Two-pump	0.094	0.281	-	120	45

#### S4.2 UiO-66: Powder Diffraction Pattern & Pawley Fit

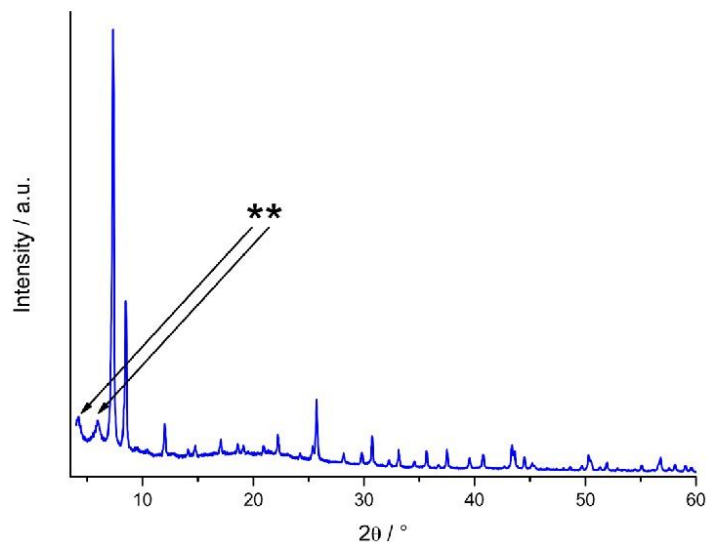


**Figure S4.1.** PXRD pattern of UiO-66 produced in the flow reactor ( $\lambda = \text{Cu K}\alpha$ ). The asterisks indicate two symmetry forbidden reflections, which indicate defect rich regions within the sample.<sup>10</sup>

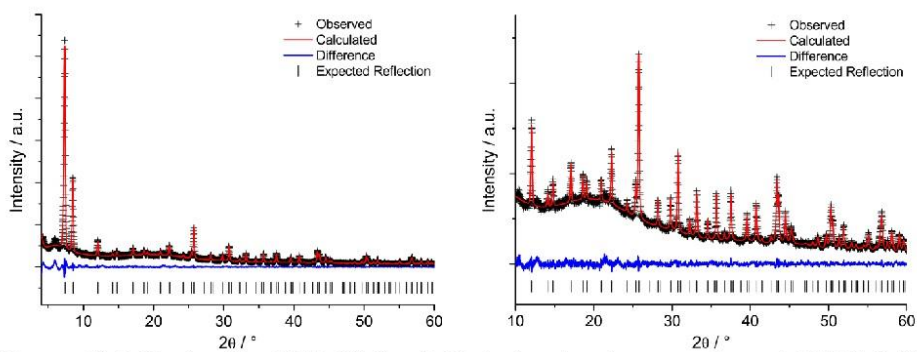


**Figure S4.2.** Pawley fit of UiO-66 ( $\lambda = \text{Cu K}\alpha$ ), showing the range from 4-60°  $2\theta$  (left) and 10-60°  $2\theta$  (right). Final fit to a cubic unit cell in space group  $Fm\bar{3}m$ , with the unit cell parameter  $a = 20.7367(4) \text{ \AA}$ . ( $R_{\text{wp}} = 5.59 \%$ ,  $\chi^2 = 3.644$ ). The determined cell parameter is very similar to the literature value of  $a = 20.7751(2) \text{ \AA}$ .<sup>11</sup>

## S4.3 UiO-66: Thermal &amp; Elemental Analysis

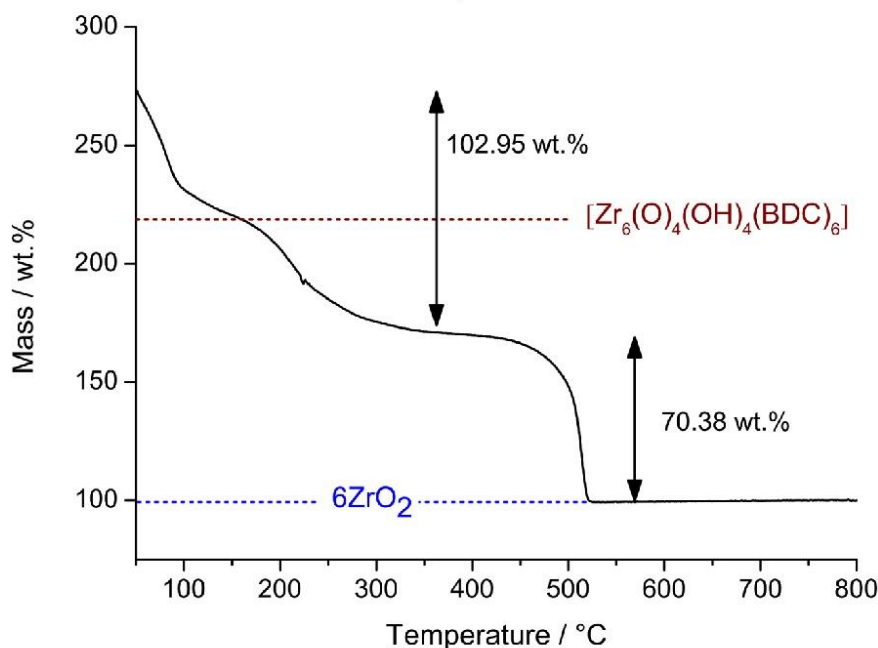


**Figure S4.3.** TGA plot for UiO-66 produced in the flow reactor. The principal weight loss events are indicated, assigned to the loss of solvent molecules (DMF, ethanol water) from the pores and to the collapse of the framework, to yield  $ZrO_2$  as the final product (70.38 wt.%; expected 120 wt.%). The red dashed line represents the expected fractional mass of  $[Zr_6O_4(OH)_4(BDC)_6]$ , calculated from  $ZrO_2$  (blue dashed line); the large difference between expected and observed weight losses indicates there are significant numbers of missing  $BDC^{2-}$  linkers.<sup>12</sup>

**Table S4.3.** Elemental analysis of UiO-66 obtained from the flow reactor compared to the expected values for  $[Zr_6O_4(OH)_4(BDC)_6]$ . It was not possible to identify the exact amount of DMF in the pores and thus there is a large discrepancy in the measured and calculated elemental analysis values.

	C %	H %	N %	S %
Found	27.5	3.2	4.4	0
Expected <sup>a</sup>	34.6	1.7	0	0

<sup>a</sup> Calculated for  $[Zr_6O_4(OH)_4(BDC)_6]$ .

EDX measurements indicate the presence of chlorine in the sample (assumed to be  $Cl^-$  ions, in ratios with  $Zr^{4+}$  of between 1:1 and 2:1 ( $Cl^-:Zr^{4+}$ ), which is consistent with the presence of defect regions within the framework.<sup>12</sup>



#### S4.4 UiO-66: Infrared Spectrum

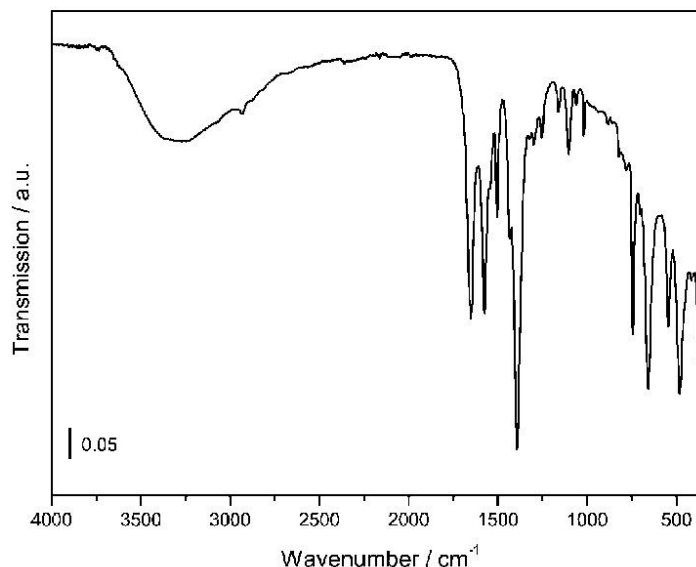


**Figure S4.4.** FTIR spectrum of UiO-66.  $\tilde{\nu}$  (cm<sup>-1</sup>) = 3348 (b, O-H stretch - H<sub>2</sub>O), 1659 (m, C-O stretch - DMF), 1573 (m, asymmetric CO<sub>2</sub><sup>-</sup> stretch - BDC<sup>2-</sup>), 1393 (s, symmetric CO<sub>2</sub><sup>-</sup> stretch - BDC<sup>2-</sup>).

#### S4.5 UiO-66: SEM Image

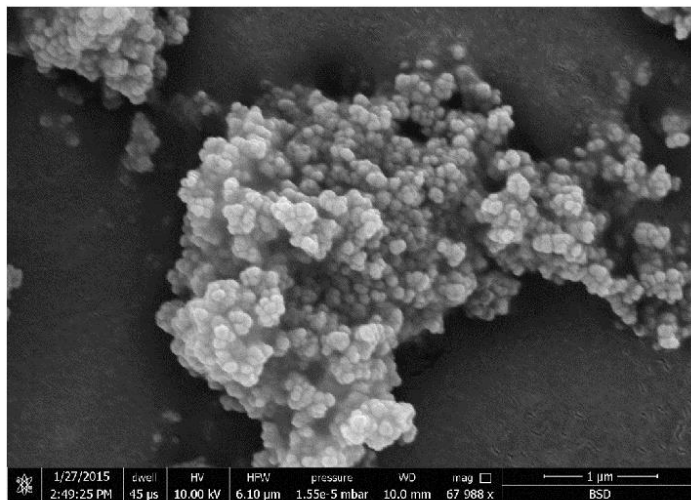


**Figure S4.5.** SEM micrograph of UiO-66 sample produced in the flow reactor. Particles appear to have the shape of small spheres, approximately 100 nm across. The size distribution of the particles is also quite small.

#### S4.6 UiO-66: N<sub>2</sub> Sorption Experiments

For sorption experiments, UiO-66 was activated by heating the sample to 220°C under dynamic vacuum overnight. Samples from both a three-pump configuration (where

paraffin was used as the transport medium) and a two-pump configuration (using the ultrasonic probe) were investigated and both found to be porous though to different degrees (Fig S4.6).

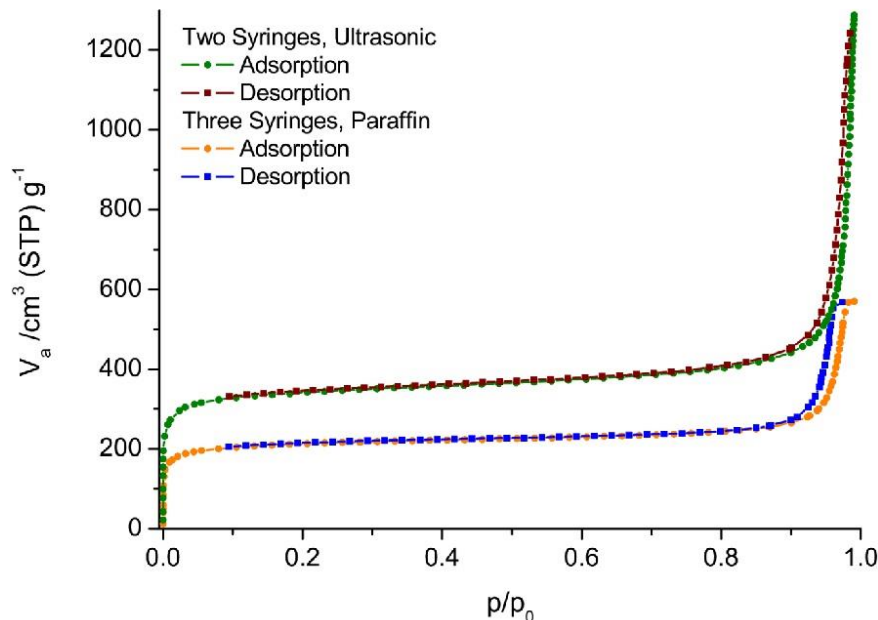


**Figure S4.6.**  $N_2$  adsorption and desorption isotherms measured at 77 K on samples of UiO-66 produced in a two-pump (ultrasonic probe; green & red traces) and three-pump (paraffin transport; orange & blue traces) flow reactor.

**Table S4.4.** BET surface areas and micropore volumes for UiO-66 samples produced using the two-pump (ultrasonic probe) and three-pump (paraffin transport) configurations of the flow reactor.

Flow Reactor Configuration	BET / $m^2 g^{-1}$	Micropore Volume / $cm^3 g^{-1}$
Two-pumps	1263(8)	0.54
Three-pumps	786(5)	0.33

The ideal surface area for a perfect sample of UiO-66 has been calculated as  $1125 m^2 g^{-1}$ .<sup>12</sup> PXRD, TGA, elemental analysis and EDX measurements have indicated that our samples of UiO-66 contain a significant density of defects and thus it is expected that they will show significantly larger surface areas than this ideal value. The three-pump product shows a significantly lower surface area however, which is attributed to the inclusion of residual and hard to remove paraffin within the pore spaces. By comparison, the sample produced from the two-syringe reactor has a BET surface area slightly higher than the expected ideal value. This result is consistent with the presence of defects and is expected.

The sensitivity of the UiO-66 samples to the activation procedure was also investigated. The PXRD patterns of the UiO-66 sample from the two-pump reactor were collected before and after the adsorption experiment. These indicate no significant degradation of the structure on activation (Fig. S4.7).

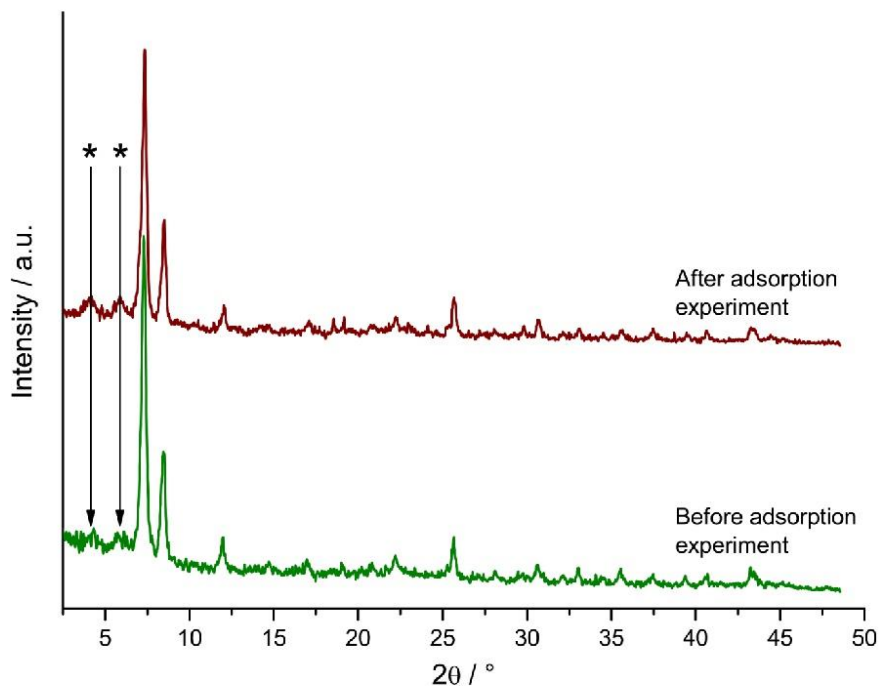


**Figure S4.7.** PXRD patterns ( $\lambda = \text{Cu } K_{\alpha 1}$ ) of UiO-66 produced using the two-pump reactor configuration, before and after activation for the  $\text{N}_2$  sorption experiment. \*s indicate the symmetry forbidden reflections attributed to defect rich regions of the sample.

## S5 Flow Synthesis & Characterisation of CAU-13

### S5.1 Flow Reactor Synthesis

For flow reactor syntheses, aluminium(III) chloride hexahydrate ( $\text{AlCl}_3 \cdot 6\text{H}_2\text{O}$ ) was dissolved in DMF to yield a  $0.5 \text{ mol dm}^{-3}$  solution and loaded into a syringe pump. A second syringe pump was charged with a  $0.5 \text{ mol dm}^{-3}$  solution of the linker, *trans*-1,4-cyclohexanedicarboxylic acid (*trans*- $\text{H}_2\text{CDC}$ ). To this was added acetic acid (AcOH) to give a final ratio of  $\text{H}_2\text{CDC}:\text{AcOH}$  of 1:9. AcOH was used to act as modulator in synthesis.<sup>13</sup>

#### S5.1.1 Typical Two-Pump Synthesis

The loaded syringe pumps were connected into a two syringe pump configuration (metal, linker:AcOH) and injected into a flow reactor ( $V_{\Sigma} = 16.16 \text{ ml}$ ) with equal flow rate for each pump of  $0.404 \text{ ml min}^{-1}$ , giving a molar ratio of the reagents of 1:1 ( $\text{AlCl}_3:\text{H}_2\text{CDC}$ ) and a total reaction time of 20 mins. During the reaction the flow reactor was kept at a temperature of  $130^\circ\text{C}$ . The product was collected and the solid separated by sequential centrifugation and washing with DMF followed by ethanol.

#### S5.1.2 Summary of Flow Reactor Experiments

**Table S5.1.** Summary of reaction conditions tested for the synthesis of CAU-13 using the flow reactor.

$V_{\Sigma} / \text{mL}$	$\text{AlCl}_3$ Flowrate / $\text{ml min}^{-1}$	$\text{H}_2\text{CDC}$ Flowrate / $\text{ml min}^{-1}$	Transport <sup>a</sup> Flowrate / $\text{ml min}^{-1}$	Conc. <sup>b</sup> / $\text{mol dm}^{-3}$	AcOH: $\text{H}_2\text{CDC}$ Ratio	Temp. / $^\circ\text{C}$	Time / min
15.25	0.381	0.381	-	0.1	-	120	20
15.25	0.381	0.381	-	0.1	1:9	120	20
15.25	0.381	0.381	-	0.1	1:9	130	20
15.25	0.381	0.381	-	0.1	1:9	140	20
15.25	0.190	0.190	0.381	0.1	1:9	130	20
15.25	0.127	0.127	0.254	0.1	1:9	130	30
15.25	0.085	0.085	0.169	0.1	1:9	130	45
15.25	0.127	0.254	0.381	0.1	1:9	130	20
15.25	0.085	0.169	0.245	0.1	1:9	130	30
15.25	0.056	0.113	0.169	0.1	1:9	130	45
16.16 <sup>c</sup>	0.404	0.404	-	0.5	1:9	130	20
16.16	0.269	0.269	-	0.5	1:9	130	30
16.16	0.179	0.359	-	0.5	1:9	130	30
16.84	0.421	0.421	-	0.5	1:9	130	20

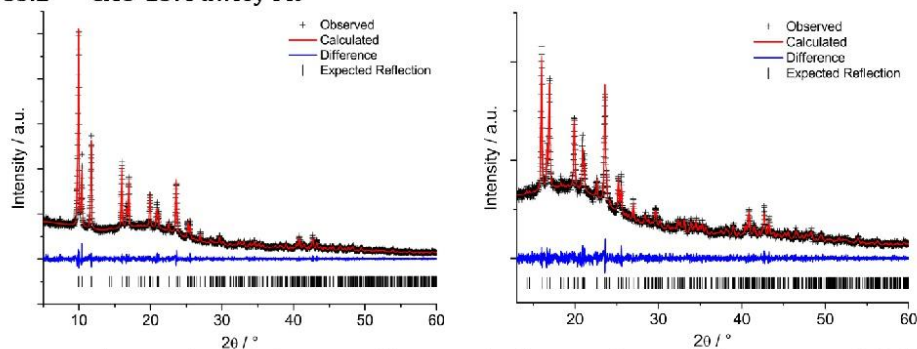
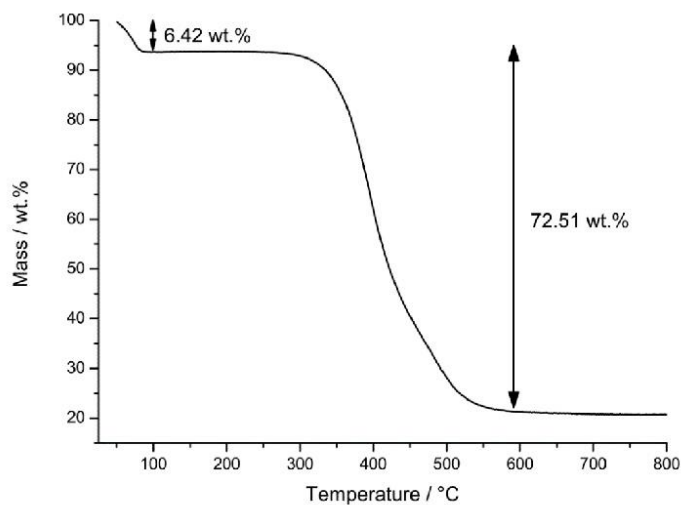
<sup>a</sup> A transport medium in addition to the reaction solvent, used to prevent clogging of the reactor, in this case DMF.

<sup>b</sup> The concentration of the reagent solutions was also investigated, with both syringe pumps have the same concentration.

<sup>c</sup> This reaction produced the most crystalline and phase pure CAU-13, which is further analysed in this work. This is equivalent to a reaction ratio of 1:1 ( $\text{AlCl}_3:\text{H}_2\text{CDC}$ ).

**Table S5.2.** Optimised reaction conditions for the synthesis of CAU-13 using the flow reactor.

AlCl <sub>3</sub> Flowrate / ml min <sup>-1</sup>	H <sub>2</sub> CDC/AcOH Flowrate / ml min <sup>-1</sup>	H <sub>2</sub> CDC:AcOH	Temperature / °C	Time / min
0.404	0.404	1:9	130	20

**S5.2 CAU-13: Pawley Fit****Figure S5.1.** Pawley fit of CAU-13 ( $\lambda = \text{Cu K}\alpha$ ), showing the range from 4-60° 2 $\theta$  (left) and 13-60° 2 $\theta$  (right). Final fit to a triclinic unit cell in space group  $P\bar{1}$ , with unit cell parameters  $a = 6.6111(4) \text{ \AA}$ ,  $b = 9.4498(6) \text{ \AA}$ ,  $c = 9.4652(5) \text{ \AA}$ ,  $\alpha = 107.652(4)^\circ$ ,  $\beta = 107.690(6)^\circ$  and  $\gamma = 93.185(5)^\circ$ . ( $R_{\text{wp}} = 4.71 \%$ ,  $\chi^2 = 1.080$ ). The determined cell parameters are very similar to the literature parameters of  $a = 6.6169(5) \text{ \AA}$ ,  $b = 9.4300(6) \text{ \AA}$ ,  $c = 9.4642(6) \text{ \AA}$ ,  $\alpha = 107.577(3)^\circ$ ,  $\beta = 107.725(7)^\circ$  and  $\gamma = 93.209(5)^\circ$ .<sup>14</sup>**S5.3 CAU-13: Thermal & Elemental Analysis****Figure S5.2.** TGA plot for CAU-13 produced in the flow reactor. The principal weight loss events are indicated, assigned to the loss of one molecule of H<sub>2</sub>O per formula unit from the structure (6.42 wt.%; expected 7.76 wt.%) and collapse of the framework to form Al<sub>2</sub>O<sub>3</sub> (72.51 wt.%; expected 70.28 wt.%).

**Table S5.3.** Elemental analysis of CAU-13 obtained by flow synthesis with the theoretical one ( $[\text{Al}(\text{OH})(\text{C}_8\text{H}_{10}\text{O}_4)] \cdot \text{H}_2\text{O}$ ). The small amount of N found in the flow reactor product is attributed to residual DMF in the structure and this may also account for the discrepancies in the amounts of C and H in the sample.

	C %	H %	N %	S %
Found	40.1	6.2	0.1	0
Expected	41.4	5.6	0.0	0

#### S5.4 CAU-13: Infrared Spectrum

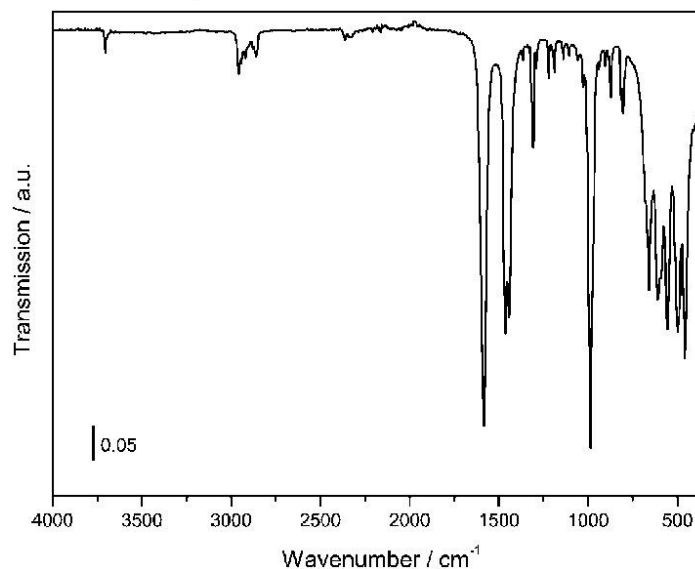


**Figure S5.3.** FTIR spectrum of CAU-13.  $\tilde{\nu}$  ( $\text{cm}^{-1}$ ) = 3704 (m, O-H stretch), 2955 (m, asymmetric C-H stretch -  $\text{cdc}^2$ ), 2842 (m, symmetric C-H stretch -  $\text{cdc}^2$ ), 1587 (s, asymmetric  $\text{CO}_2^-$  stretch -  $\text{cdc}^2$ ), 1456 (s, symmetric  $\text{CO}_2^-$  stretch -  $\text{cdc}^2$ ), 983 (s, C-C stretch,  $\text{cdc}^2$ ).

**S5.5 CAU-13: NMR Spectrum**

A sample of CAU-13 was digested for solution state NMR analysis using a NaOD/D<sub>2</sub>O solution. The spectrum (Fig. S5.4) shows a strong resonance for water ( $\delta = 4.93$  ppm) and several much lower intensity overlapping resonances in the region 0 – 2 ppm (Fig. S5.4 inset). By comparison with an NMR spectrum of the H<sub>2</sub>CDC linker, dissolved in a similar NaOD/D<sub>2</sub>O solution, it is clear that the only organic present is the H<sub>2</sub>CDC and therefore no acetic acid/acetate anions have been incorporated into the structure.

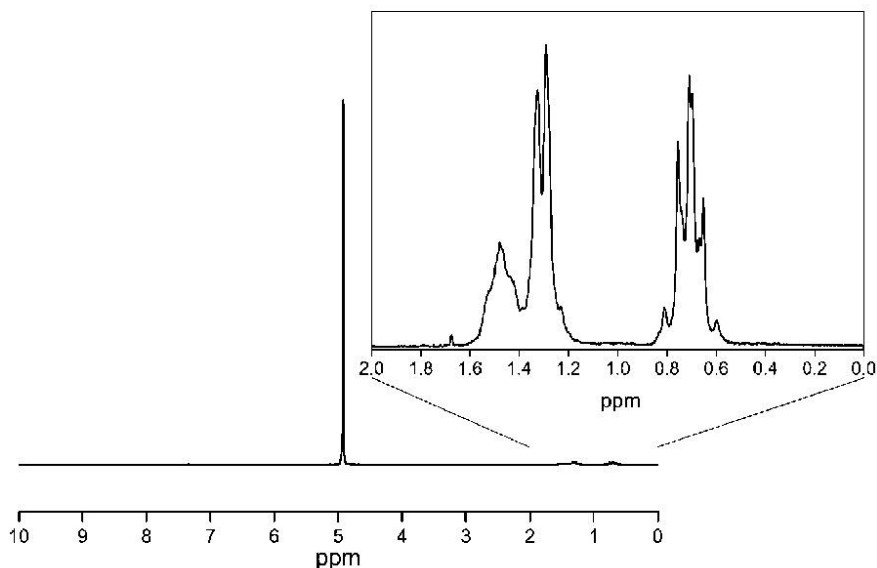


**Figure S5.4.** Solution state NMR spectrum of CAU-13 obtained from the flow reactor in a NaOD/D<sub>2</sub>O solution. Inset shows an enlarged view of the region 0 – 2 ppm.

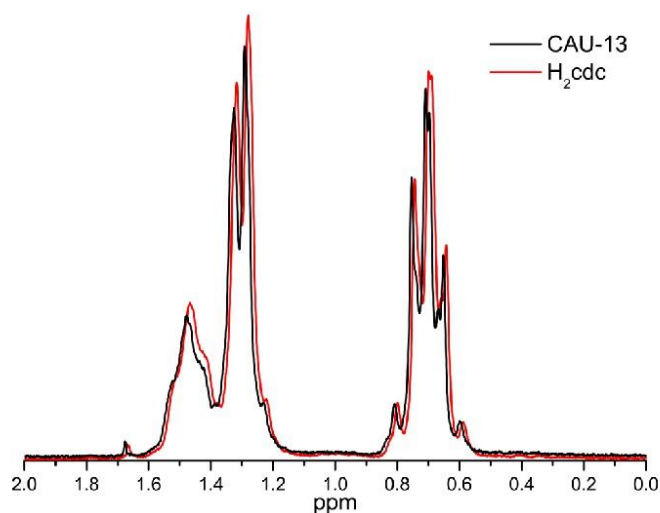


**Figure S5.5.** Solution state NMR spectra of CAU-13 (black) and linker H<sub>2</sub>cdc (red) in the region 0 – 2 ppm. Both spectra were measured in NaOD/D<sub>2</sub>O.

## S5.6 CAU-13: SEM Image

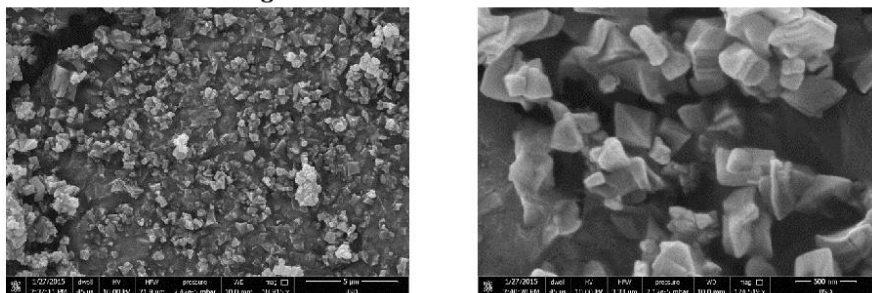


**Figure S5.6.** SEM micrographs of CAU-13 produced with the flow reactor. The image on the right is a higher magnification view of some of the crystals in the field of view of the left hand micrograph. Crystallites at both magnifications exhibit a blocky form, but show no regular shape. At higher magnification it is clear that there is a large distribution of crystallite sizes in the sample.

S5.7 CAU-13: N<sub>2</sub> Sorption Experiments

CAU-13 was activated for sorption measurements by heating the sample to 200°C under dynamic vacuum for 12 hrs. CAU-13 is porous to N<sub>2</sub> at 77 K (Fig. S5.7) and has a BET surface area of 401(6) m<sup>2</sup> g<sup>-1</sup> (calculated over the range  $p/p_0 = 0.037-0.183$ ) and a micropore volume of 0.18 m<sup>3</sup> g<sup>-1</sup> (calculated by the Dubinin-Radushkevitch - D-R-method).<sup>15</sup> These values are slightly higher than those previously reported for CAU-13, but within reasonable sample-to-sample variation (literature: BET - 378 m<sup>2</sup> g<sup>-1</sup>; micropore volume - 0.15 cm<sup>3</sup> g<sup>-1</sup>).<sup>14</sup>

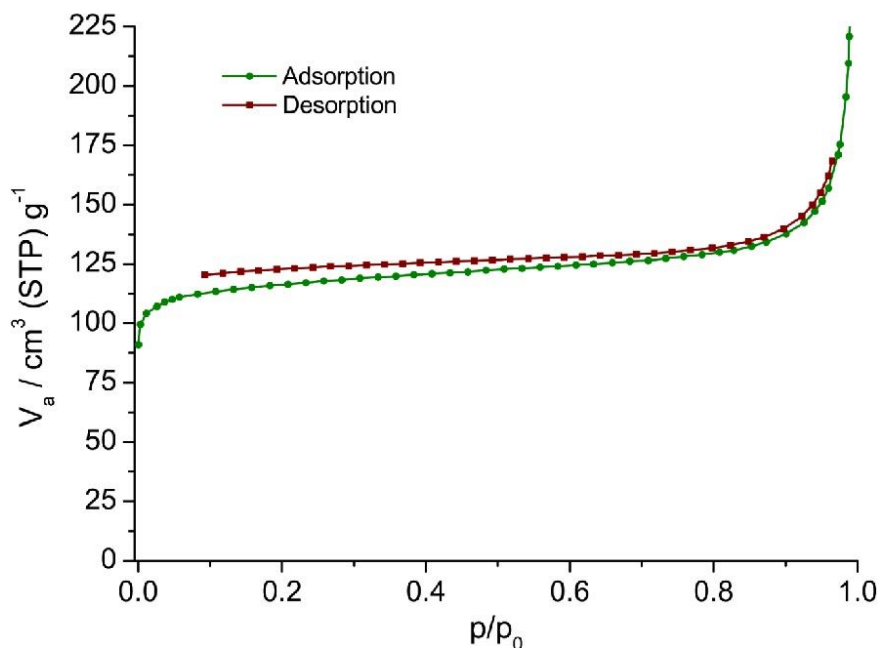


**Figure S5.7.** N<sub>2</sub> adsorption and desorption isotherms for CAU-13, measured at 77 K.



PXRD patterns were collected before and after the activation procedure to confirm that the crystallinity of the sample was unaffected by heating under vacuum (Fig. S.8), although differences were observed due to the flexible nature of the framework.

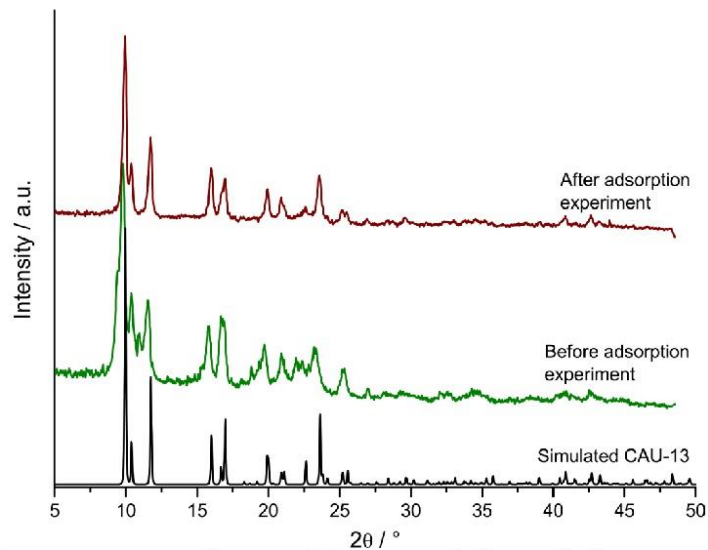


**Figure S5.8.** PXRD patterns ( $\lambda = \text{Cu K}\alpha$ ) for CAU-13 before and after activation for the  $\text{N}_2$  sorption experiment and the theoretical PXRD pattern for CAU-13.<sup>14</sup> The difference in the PXRD pattern is caused by the flexible nature of the framework, which undergoes a breathing transition an adsorption/desorption of guest molecules.

## S6 Flow Synthesis & Characterisation of Reported STA-12 Frameworks and New Compound STA-12(Cd)

### S6.1 Flow Reactor Synthesis

Initial work on the STA-12 family of compounds focused on the preparation of the known Ni<sup>2+</sup> and Co<sup>2+</sup> compounds,<sup>16,17</sup> whilst subsequently a new member of this family of compounds, STA-12(Cd) was prepared. In the initial work, 0.1 mol dm<sup>-3</sup> aqueous solutions of nickel(II) acetate or cobalt(II) acetate were prepared and loaded into a syringe pump which was then connected to a three-pump configured flow reactor. For the synthesis of STA-12(Cd), a 0.1 mol dm<sup>-3</sup> aqueous solution of cadmium(II) acetate was used as the metal source and a two-pump set up was employed.

In all reactions, due to the insolubility of the linker, N,N'-piperazinebis(methylenephosphonic acid) (H<sub>4</sub>L), in water below 120°C, a 0.1 mol dm<sup>-3</sup> solution of the potassium salt of the linker was formed, dissolving solid H<sub>4</sub>L in a solution of potassium hydroxide, in a molar ratio of 1:2 (H<sub>4</sub>L:KOH). This solution was then loaded into a syringe pump and connected to the flow reactor in a three-pump configuration, using paraffin as the transport medium.

#### S6.1.1 Preliminary Studies – Typical Synthesis

The loaded syringe pumps were connected to a flow reactor (V<sub>2</sub> = 14.80 ml) and the solutions were injected with flow rates of 0.987 ml min<sup>-1</sup> : 0.493 ml min<sup>-1</sup> : 1.48 ml min<sup>-1</sup> (metal : H<sub>4</sub>L/KOH : paraffin), to give a molar ratio of reagents of 2:1 (M<sup>2+</sup>:H<sub>4</sub>L), as reported in the literature, and a reaction time of 5 min. Products were collected and paraffin was removed by sequential centrifugation and washing with toluene. The products were isolated by a further sequence of centrifugation and washing with ethanol.

#### S6.1.2 Preliminary Studies – Flow Reactor Experiments

**Table S6.1.** Summary of conditions tested for the synthesis of STA-12(Co) using the three-syringe pump flow reactor.

Flowrate Co(AcO) <sub>2</sub> / ml min <sup>-1</sup>	Flowrate H <sub>4</sub> L/KOH / ml min <sup>-1</sup>	Flowrate Paraffin / ml min <sup>-1</sup>	Temp. / °C	Time / min
0.740	0.740	1.480	50	5
0.987	0.493	1.480	50	5
0.493	0.987	1.480	50	5
1.184	0.296	1.480	50	5
1.316	0.164	1.480	50	5
0.370	0.370	0.740	50	10
0.493	0.247	0.740	50	10
0.247	0.493	0.740	50	10
0.592	0.148	0.740	50	10
0.658	0.082	0.740	50	10
0.247	0.247	0.493	50	15
0.329	0.164	0.493	50	15
0.164	0.329	0.493	50	15
0.394	0.099	0.493	50	15
0.438	0.055	0.493	50	15

## Anhang

0.740	0.740	1.480	70	5
0.987	0.493	1.480	70	5
0.493	0.987	1.480	70	5
1.184	0.296	1.480	70	5
1.316	0.164	1.480	70	5
0.370	0.370	0.740	70	10
0.493	0.247	0.740	70	10
0.247	0.493	0.740	70	10
0.592	0.148	0.740	70	10
0.658	0.082	0.740	70	10
0.247	0.247	0.493	70	15
0.329	0.164	0.493	70	15
0.164 <sup>a</sup>	0.329	0.493	70	15
0.394	0.099	0.493	50	15
0.438	0.055	0.493	50	15

<sup>a</sup> This reaction produced the most crystalline and phase pure STA-12(Co), which is further analysed in this work. This is equivalent to a reaction ratio of 1:2:4 (Co(AcO)<sub>2</sub>:H<sub>4</sub>L:KOH).

**Table S6.2.** Summary of conditions tested for the synthesis of STA-12(Ni) using the three-syringe pump flow reactor.

Flowrate Ni(AcO) <sub>2</sub> / ml min <sup>-1</sup>	Flowrate H <sub>4</sub> L/KOH / ml min <sup>-1</sup>	Flowrate Paraffin / ml min <sup>-1</sup>	Temp. / °C	Time / min
0.740	0.740	1.480	70	5
0.987	0.493	1.480	70	5
0.493	0.987	1.480	70	5
1.184	0.296	1.480	70	5
0.370	0.370	0.740	70	10
0.493	0.247	0.740	70	10
0.247	0.493	0.740	70	10
0.592	0.148	0.740	70	10
0.247	0.247	0.493	70	15
0.329	0.164	0.493	70	15
0.164	0.329	0.493	70	15
0.394	0.099	0.493	70	15
0.123 <sup>a</sup>	0.123	0.247	70	30
0.082	0.164	0.247	70	30

<sup>a</sup> This reaction produced the most crystalline and phase pure STA-12(Ni), which is further analysed in this work. This is equivalent to a reaction ratio of 1:1:2 (Ni(AcO)<sub>2</sub>:H<sub>4</sub>L:KOH).

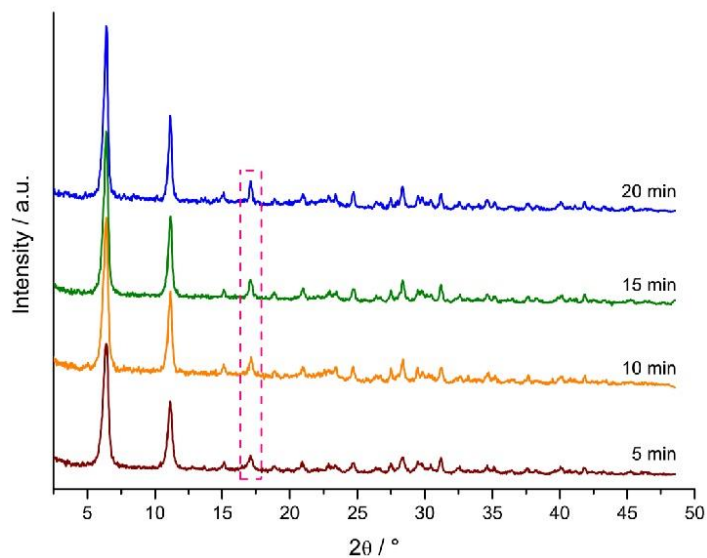
### S6.1.3 Synthesis of STA-12(Cd)

A syringe charged with a 0.1 mol dm<sup>-3</sup> aqueous solution of cadmium(II) acetate was connected to a two pump configured flow reactor (V<sub>Σ</sub> = 14.80 ml). The pumping rates of the pumps were set such that the ratio of reagents was 1:1:2 (Cd(AcO)<sub>2</sub>:H<sub>4</sub>L:KOH). For this synthesis, the reactor was heated to 70°C. Different pumping rates were used to give different reaction times (summarised in Table S6.3). The product was collected and separated by a sequence of centrifugation and washing with water and then ethanol.

**Table S6.3.** Flowrates of individual pumps and overall flowrate for different reaction time syntheses of STA-12(Cd). Reactions performed at 70°C

Cd(AcO) <sub>2</sub> Flowrate / ml min <sup>-1</sup>	H <sub>4</sub> L/KOH Flowrate / ml min <sup>-1</sup>	Total Flowrate / ml min <sup>-1</sup>	Reaction Time / min
1.48	1.48	2.96	5
0.74	0.74	1.48	10
0.49	0.49	0.98	15
0.37	0.37	0.74	20

Powder X-ray diffraction (PXRD) patterns of the products obtained after a reaction time of 5, 10, 15 and 20 min (Fig. S6.1) demonstrate that STA-12(Cd) may be obtained in pure form and with good crystallinity after just 5 minutes; a reaction time of 2 min yielded insufficient solids to collect a PXRD pattern. With increasing reaction times, the peaks appear narrower and more well-defined (for example the (140) reflection, highlighted in the dashed box) and furthermore, it becomes possible to resolve features at higher angles. The observations indicate that using our flow reactor set-up we are able to follow the growth and increase in long-range order of crystallites.

**Figure S6.1.** Laboratory PXRD patterns ( $\lambda = \text{Cu K}\alpha$ ) of samples of STA-12(Cd) prepared in the flow reactor with reaction times increasing from 5 to 20 minutes. Dashed box indicates the (140) reflection, which narrows with increasing reaction time, indicating an increase in particle size.

## S6.2 Structural Analysis of STA-12(Cd)

### S6.2.1 Details of the Rietveld Refinement

Laboratory powder X-ray diffraction data were collected using a Stoe StadiP diffractometer fitted with a Cu  $K_{\alpha 1}$  tube radiation source and a Mythen detector, in a transmission geometry. All stages of the refinement, including indexing, Pawley fitting and Rietveld refinement were performed using the routines of TOPAS-Academic V5.<sup>18</sup> The data were indexed with a metrically trigonal/hexagonal unit cell ( $a = b = 27.4134 \text{ \AA}$ ,  $c = 6.7264 \text{ \AA}$ ,  $GOF = 49.77$ ) and found to have systematic absences consistent with the space group  $R\bar{3}$ . STA-12 has been reported in the space group  $R\bar{3}$  and thus this space group was selected for the subsequent Pawley fit. The cell refined to  $a = b = 27.4087(11) \text{ \AA}$ ,  $c = 6.7275(3) \text{ \AA}$  in this space group, with an  $R_{wp} = 5.61 \%$  and  $\chi^2 = 1.145$ .

A Rietveld refinement was then performed using the structure of as-prepared STA-12(Mn) as a starting model<sup>17</sup> and the background, profile and unit cell parameters from the Pawley fit. Bonding restraints were applied to the octahedral Cd-O, Cd-O100 and Cd-N distances (all  $2.35 \text{ \AA}$ ); tetrahedral P-O and P-C distances ( $1.51 \text{ \AA}$  and  $1.85 \text{ \AA}$  respectively); and the C-C and C-N bonds ( $1.53 \text{ \AA}$  and  $1.51 \text{ \AA}$ ,  $1.53 \text{ \AA}$ ). Additionally, through-space restraints were applied to the linker N...N, C...C (diagonal, cross-ring) and C...C (2nd neighbor) ( $2.91 \text{ \AA}$ ,  $2.91 \text{ \AA}$  and  $2.48 \text{ \AA}$  respectively). The framework was fully refined, whilst the positions of the O atoms representing physisorbed water molecules in the channel were left unaltered from the  $Mn^{2+}$  structure. The channel O atoms were then removed and new positions were identified by Fourier mapping, revealing four sites. The occupancies and positions of these sites were then refined against the data, with an additional anti-bumping restraint applied to ensure O atoms remained at chemically reasonable separations ( $2.5 \text{ \AA}$ ). Further cycles of refinement were performed with the framework and a final fit to the data of  $R_{wp} = 6.43 \%$  and  $\chi^2 = 1.302$  was achieved. Rietveld plots for the final refinement are given in Fig. S6.2 and the final structural model viewed is shown in Fig. S6.3. Full crystallographic details are given in Table S6.4.

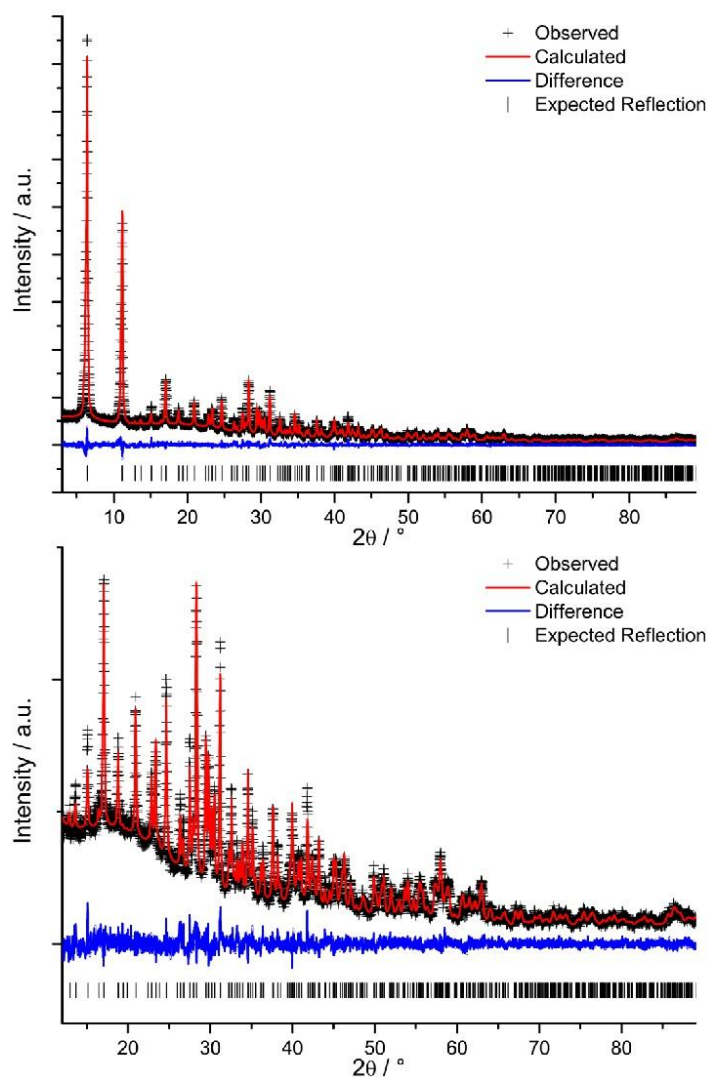


**Figure S6.2.** Rietveld plots for the final refinement of STA-12(Cd) showing the ranges 3-90°  $2\theta$  (top) and 12-90°  $2\theta$  (bottom). (Data collected using a laboratory Stoe Stadi P diffractometer fitted with a Cu  $K_{\alpha 1}$  tube radiation source).

## S6.2.2 Structure of STA-12(Cd)

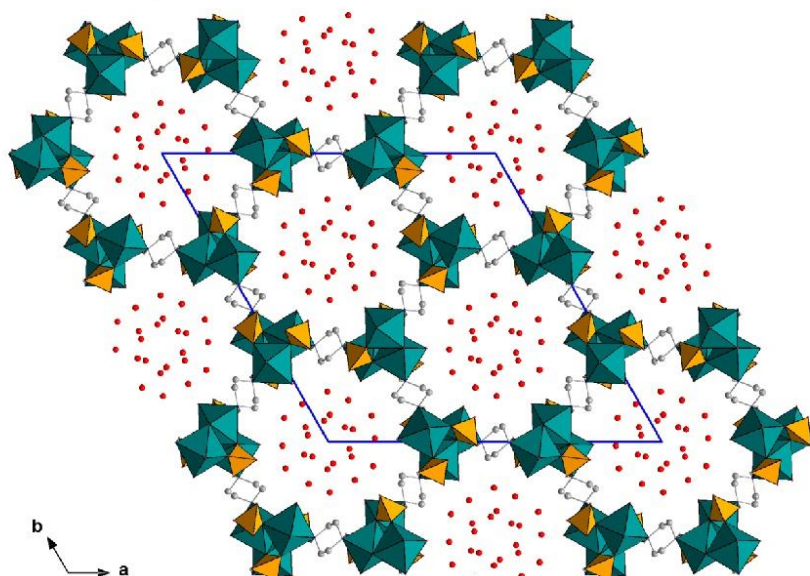


**Figure S6.3.** Structure of as-prepared STA-12(Cd), showing the honeycomb arrangement of heaxagonal unidirectional channels. Edge-sharing  $\text{CdO}_5\text{N}$  octahedra are bridged together by  $\text{PO}_3\text{C}$  phosphonate tetrahedra to form helical metal-phosphonate chains parallel to the  $c$ -axis. Chains are linked through piperaziny groups, bonded to the phosphonate groups, which also coordinatively bond to the  $\text{Cd}^{2+}$  ions through their N atoms. ( $\text{CdO}_5\text{N}$  octahedra – turquoise;  $\text{PO}_3\text{C}$  tetrahedra – orange; C – gray spheres; water molecules (represented as O atoms) – red spheres).

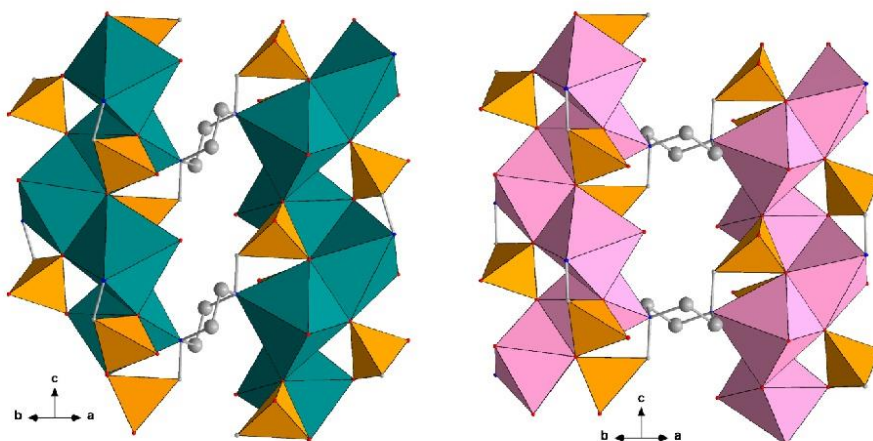


**Figure S6.4.** Structures of the chains of STA-12(Cd) (left) and STA-12(Mn) (right).<sup>17</sup> Both compounds have similar edge-sharing helical chains, however due to the greater radius of  $\text{Cd}^{2+}$  ( $\text{Cd}^{2+}$ : 1.10 Å;  $\text{Mn}^{2+}$ : 0.96 Å)<sup>19</sup>, the piperaziny groups are forced to lie parallel to the chains.

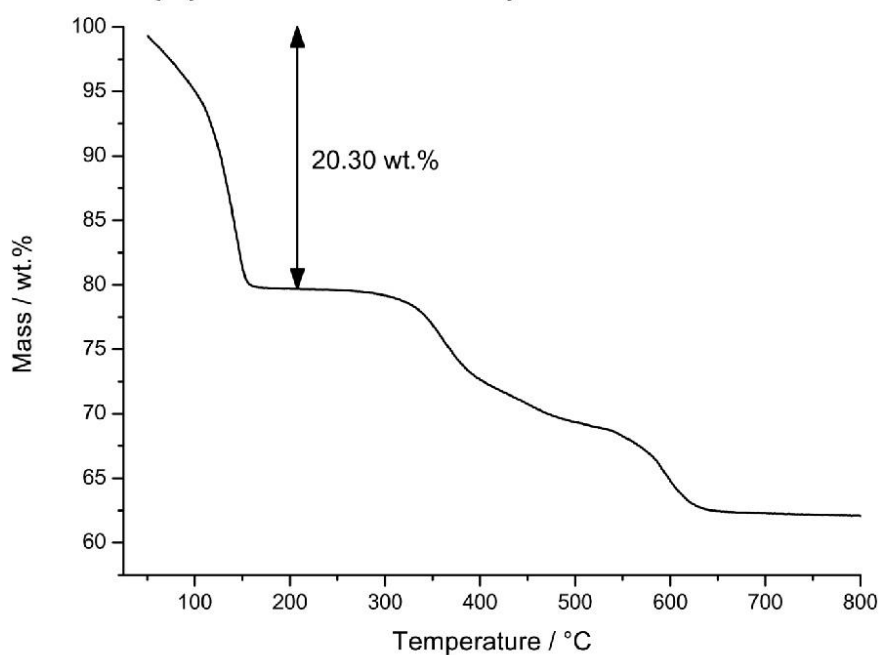
## S6.2.3 Table of Crystallographic Data for STA-12(Cd)

Table S6.4. Crystallographic data for STA-12(Cd).

Compound	STA-12(Cd)
Empirical Formula	$[\text{Cd}_2(\text{H}_2\text{O})_2(\text{C}_6\text{H}_{12}\text{N}_2\text{O}_6\text{P}_2)] \cdot 5.52\text{H}_2\text{O}$
Moiety (refined, no H)	$\text{CdC}_3\text{NO}_{6.76}\text{P}$
Moiety Formula Weight	301.63
Calculated Density (no H) / $\text{g cm}^{-3}$	2.060
Space Group	$R\bar{3}$
Cell Setting	Trigonal
$a / \text{\AA}$	27.4100(8)
$c / \text{\AA}$	6.7279(2)
$V / \text{\AA}^3$	4377.5(3)
Z	18
Diffractometer	Stoe Stadi P
Temperature / K	298
Wavelength / $\text{\AA}$	Cu $K_{\alpha 1}$
No. Reflections	778
No. Atoms	14
No. Restraints	21
$R_p$	0.0493
$R_{wp}$	0.0643
$\chi^2$	1.302
$R_{\text{Bragg}}$	0.0156



## S6.3 STA-12(Cd): Thermal &amp; Elemental Analysis



**Figure S6.5.** TGA Plot for STA-12(Cd) showing the principal weight loss event occurring on dehydration, assigned to the loss of both physisorbed and chemisorbed water molecules (14.9 wt.%; expected 15.4 wt.%). The dehydrated structure is stable to 315°C, above which temperature the structure collapses.

**Table S6.5.** Elementary analysis of STA-12(Cd) compared to the expected values for the theoretical compound of  $[\text{Cd}_2(\text{H}_2\text{O})_2(\text{C}_6\text{H}_{12}\text{N}_2\text{P}_2\text{O}_6)] \cdot 5\text{H}_2\text{O}$ .

	<b>C %</b>	<b>H %</b>	<b>N %</b>
<b>Found</b>	12.1	4.1	4.9
<b>Expected</b>	11.9	4.3	4.6

EDX measurements indicate a  $\text{Cd}^{2+}:\text{P}$  ratio of 1:1, which is in good agreement with the proposed composition of  $[\text{Cd}_2(\text{H}_2\text{O})_2(\text{C}_6\text{H}_{12}\text{N}_2\text{P}_2\text{O}_6)] \cdot 5\text{H}_2\text{O}$ .

## S6.4 STA-12(Cd): Infrared Spectrum

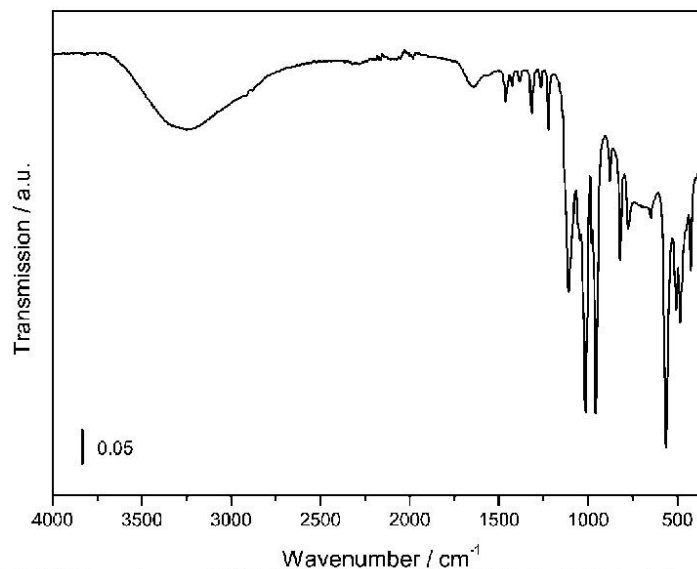


**Figure S6.6.** FTIR spectrum of STA-12(Cd).  $\tilde{\nu}$  ( $\text{cm}^{-1}$ ) = 3280 (b, O-H stretch -  $\text{H}_2\text{O}$ ), 1465 (w, asymmetric  $\text{CH}_2$  deformation - piperazine), 1377 (w, symmetric  $\text{CH}_2$  deformation - piperazine), 1102 (s, asymmetric P-O), 958 (s, symmetric. P-O).

## S6.5 STA-12(Cd): SEM Image

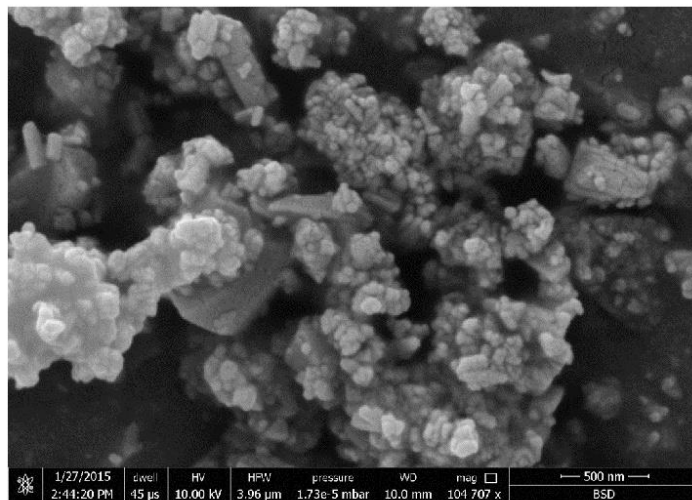


**Figure S6.7.** SEM micrograph of STA-12(Cd) produced using the flow reactor. Particles show no distinct form.

### S6.6 STA-12(Cd): N<sub>2</sub> Sorption Experiments

STA-12(Cd) was activated for sorption measurements by heating the sample to 200°C under vacuum overnight. STA-12(Cd) is porous to N<sub>2</sub> at 77 K (Fig. S6.8) with a BET surface area (calculated over the range  $p/p_0 = 0.033-0.239$ ) was determined to be 134(2) m<sup>2</sup> g<sup>-1</sup> and the micropore volume 0.08 cm<sup>3</sup> g<sup>-1</sup> (calculated by the Dubinin-Radushkevitch - D-R - method).<sup>15</sup> These values are significantly lower than for other members of the STA-12 family and even allowing for the greater mass of the Cd<sup>2+</sup> cation, the micropore uptake calculated by the D-R method ( $N_0 = 2.29(1)$  mmol g<sup>-1</sup> is approximately 25 % less than expected. This indicates that there is some degree of pore blocking or an amorphous second phase in the analysed sample, possibly X-ray amorphous cadmium hydroxide. The lower N<sub>2</sub> porosity is not attributed to a collapse of the framework during activation, since PXRD patterns before and after the activation procedure show no changes (Fig. S6.9.)

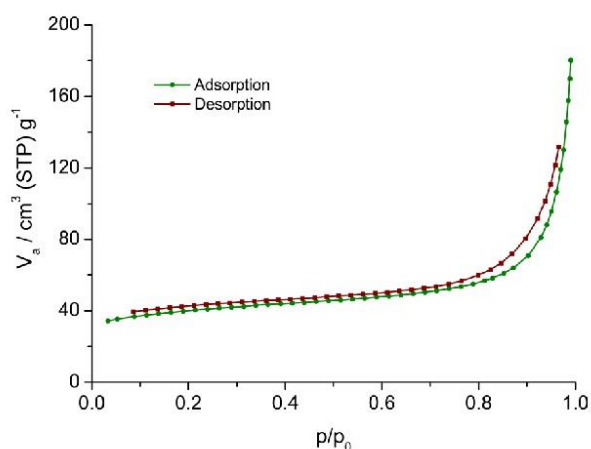


**Figure S6.8.** N<sub>2</sub> adsorption and desorption isotherms for STA-12(Cd) measured at 77 K.

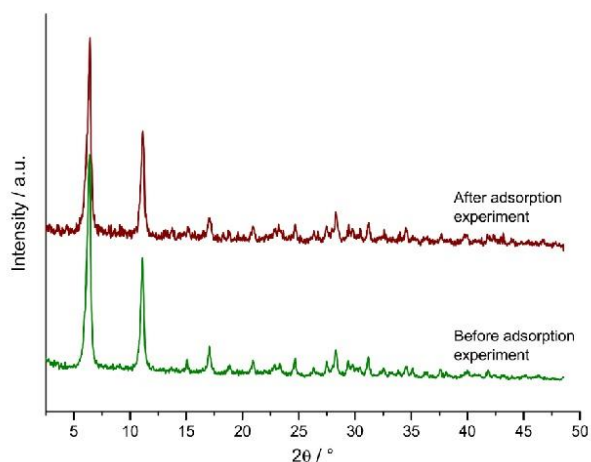


**Figure S6.9.** PXRD patterns ( $\lambda = \text{Cu } K_{\alpha 1}$ ) for STA-12(Cd) before and after activation for the N<sub>2</sub> sorption experiment.

**S7 References**

- 1 M. Gimeno-Fabra, A. S. Munn, L. A. Stevens, T. C. Drage, D. M. Grant, R. J. Kashtiban, J. Sloan, E. Lester and R. I. Walton, *Chem. Commun.*, 2012, **48**, 10642–10644.
- 2 K.-J. Kim, Y. J. Li, P. B. Kreider, C.-H. Chang, N. Wannemacher, P. K. Thallapally and H.-G. Ahn, *Chem. Commun.*, 2013, **49**, 11518–11520.
- 3 M. Faustini, J. Kim, G.-Y. Jeong, J. Y. Kim, H. R. Moon, W.-S. Ahn and D.-P. Kim, *J. Am. Chem. Soc.*, 2013, **135**, 14619–14626.
- 4 P. A. Bayliss, I. A. Ibarra, E. Perez, S. Yang, C. C. Tang, M. Poliakoff and M. Schroder, *Green Chem.*, 2014, **16**, 3796–3802.
- 5 M. Rubio-Martinez, M. P. Batten, A. Polyzos, K.-C. Carey, J. I. Mardel, K.-S. Lim and M. R. Hill, *Sci. Rep.*, 2014, **4**.
- 6 L. Paseta, B. Seoane, D. Julve, V. Sebastián, C. Téllez and J. Coronas, *ACS Appl. Mater. Interfaces*, 2013, **5**, 9405–9410.
- 7 P. M. Schoenecker, G. A. Belancik, B. E. Grabicka and K. S. Walton, *AIChE J.*, 2013, **59**, 1255–1262.
- 8 L. D'Arras, C. Sassoey, L. Rozes, C. Sanchez, J. Marrot, S. Marre and C. Aymonier, *New J. Chem.*, 2014, **38**, 1477–1483.
- 9 J. P. S. Mowat, J. A. Groves, M. T. Wharmby, S. R. Miller, Y. Li, P. Lightfoot and P. A. Wright, *J. Solid State Chem.*, 2009, **182**, 2769–2778.
- 10 M. J. Cliffe, W. Wan, X. Zou, P. A. Chater, A. K. Kleppe, M. G. Tucker, H. Wilhelm, N. P. Funnell, F.-X. Coudert and A. L. Goodwin, *Nat Commun*, 2014, **5**, 4176.
- 11 L. Valenzano, B. Civalieri, S. Chavan, S. Bordiga, M. H. Nilsen, S. Jakobsen, K. P. Lillerud and C. Lamberti, *Chem. Mater.*, 2011, **23**, 1700–1718.
- 12 G. C. Shearer, S. Chavan, J. Ethiraj, J. G. Vitillo, S. Svelle, U. Olsbye, C. Lamberti, S. Bordiga and K. P. Lillerud, *Chem. Mater.*, 2014, **26**, 4068–4071.
- 13 A. Schaate, P. Roy, A. Godt, J. Lippke, F. Waltz, M. Wiebcke and P. Behrens, *Chem. – Eur. J.*, 2011, **17**, 6643–6651.
- 14 F. Niekel, M. Ackermann, P. Guerrier, A. Rothkirch and N. Stock, *Inorg. Chem.*, 2013, **52**, 8699–8705.
- 15 F. Rouquerol, J. Rouquerol and K. S. W. Sing, *Adsorption by Powders and Porous Solids: Principles, Methodology and Applications*, Academic Press, 1998.
- 16 J. A. Groves, S. R. Miller, S. J. Warrender, C. Mellot-Draznieks, P. Lightfoot and P. A. Wright, *Chem. Commun.*, 2006, 3305–3307.
- 17 M. T. Wharmby, G. M. Pearce, J. P. S. Mowat, J. M. Griffin, S. E. Ashbrook, P. A. Wright, L.-H. Schilling, A. Lieb, N. Stock, S. Chavan, S. Bordiga, E. Garcia, G. D. Pirngruber, M. Vreeke and L. Gora, *Microporous Mesoporous Mater.*, 2012, **157**, 3–17.
- 18 A. Coelho, *TOPAS-Academic v5*, Coelho Software, Brisbane, Australia, 2012.
- 19 R. D. Shannon, *Acta Crystallogr. Sect. A*, 1976, **32**, 751–767.

**7.5 Nanoscale Synthesis of Two Porphyrin-Based MOFs with Gallium and Indium**

**Supporting Information**

**Nanoscale Synthesis of two Porphyrin-based MOFs  
with Gallium and Indium**

*Timo Rhauderwiek,<sup>a</sup> Steve Waitschat,<sup>a</sup> Stefan Wutke,<sup>b</sup> Helge Reinsch,<sup>c</sup> Thomas Bein,<sup>b</sup> Norbert Stock<sup>a,\*</sup>*

<sup>a</sup> Institute of Inorganic Chemistry, Christian-Albrechts-Universität, Max-Eyth Straße 2, D-24118 Kiel, Germany

<sup>b</sup> Department of Chemistry and Center for NanoScience (CeNS), University of Munich (LMU), Butenandtstraße 5-13, D-81377 Munich, Germany

<sup>c</sup> Department of Chemistry, University of Oslo, N-0371 Oslo, Norway

- 1. Synthesis of H<sub>6</sub>TCPP**
- 2. High-throughput investigation of Ga- and In-PMOF**
- 3. Pawley-fits and crystallographic data of Ga-PMOF-cf, In-PMOF-cf and In-PMOF-bs-us**
- 4. Sorption properties and PXRD patterns of the activated samples**
- 5. TG investigations and PXRD patterns of the decomposition products**
- 6. IR spectroscopy of Ga- and In-PMOF-bs-th**
- 7. DLS and SEM investigations**
- 8. Literature**

**1. Synthesis of H<sub>6</sub>TCPP.** The synthesis of H<sub>6</sub>TCPP was carried out following the procedures described in the literature.<sup>1-3</sup> Pyrrole (14.01 mL, 202.5 mmol) and 4-formylbenzoic acid (30.40 g, 202.5 mmol) in 750 mL propionic acid were heated under reflux for 2 h. Afterwards the reaction mixture was cooled down to RT and poured into 1000 mL of MeOH and stirred for 30 min in an ice bath. The resulting precipitate was filtered and washed several times with MeOH until the filtrate was clear. Subsequently, the product was washed with 200 mL warm distilled water and dried at 70 °C in a drying oven.

Elemental analysis of H<sub>6</sub>TCPP: calc (%): C 72.9, H 3.8, N 7.1, found (%): C 71.3, H 4.3, N 6.9. The small difference between the calculated and observed values is due to impurities caused by solvent molecules used in the synthesis. These impurities were also observed in the <sup>1</sup>H-NMR measurements.

<sup>1</sup>H-NMR (Figure S1), (500 MHz, DMSO-d<sub>6</sub>): δ= 8.86 (s, 8H, H-1); 8.39 (d, 8H, H-2); 8.33 (d, 8H, H-3); 3.35 (s, 2H, H<sub>2</sub>O); 2.50 (s, 6H, DMSO); 2.22 (q, 2H, propionic acid); 1.00 (t, 3H, propionic acid) ppm.

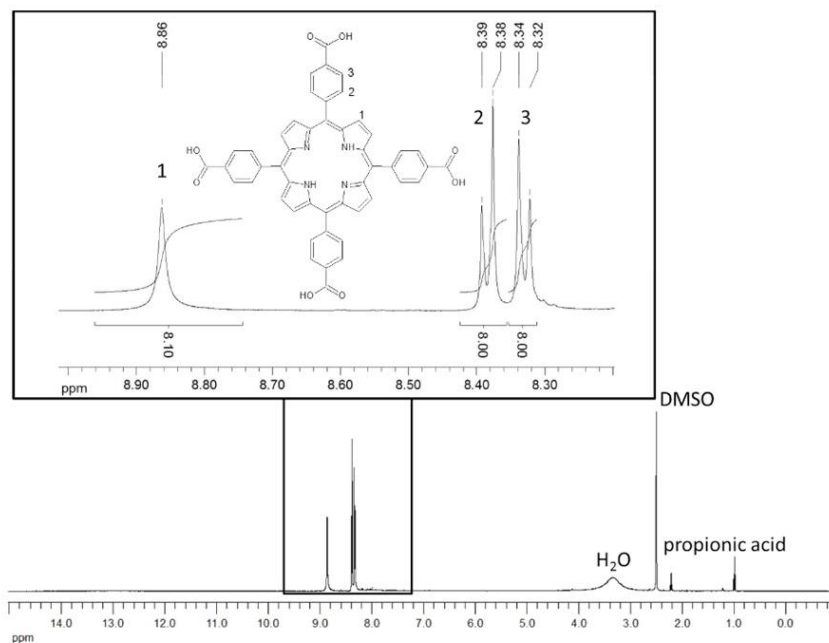


**Figure S1.**  $^1\text{H-NMR}$  spectrum of the synthesized  $\text{H}_6\text{TCPP}$  linker.

**2. High-throughput investigation of Ga- and In-PMOF-bs-th**

The crystallinity of Ga- and In-PMOF depends strongly on the water : DMF ratio. With a large amount of water or linker : metal ratios > 1 : 5, no crystalline products are observed.

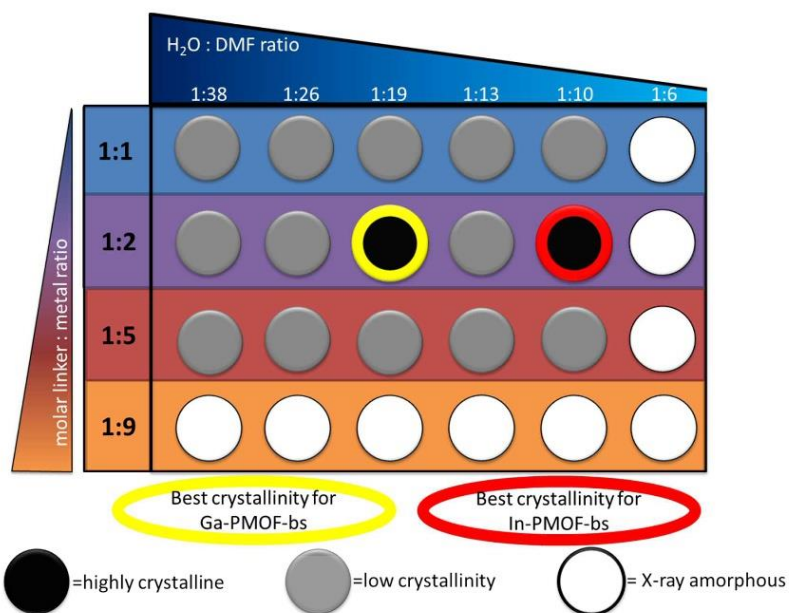


**Figure S2.** Schematic illustration of HT-experiments that led to the resulting Ga- and In-PMOF-bs-th. Water : DMF ratios are given in vol %.



### 3. Pawley fits and crystallographic data of In-PMOF-bs-us, Ga-PMOF-cf and In-PMOF-cf

The Pawley fits show that all measured samples show no additional crystalline impurities.

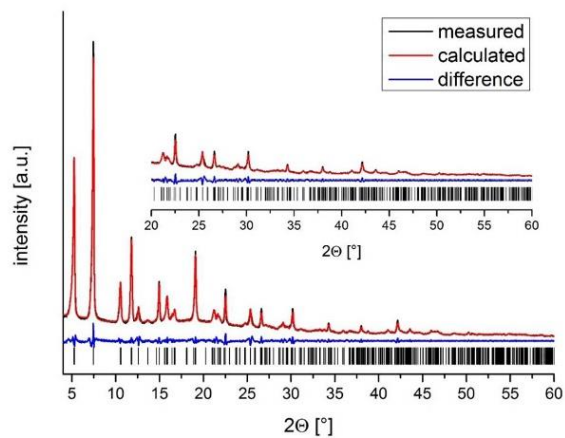


**Figure S3.** Result of the Pawley fit of In-PMOF-bs-us.

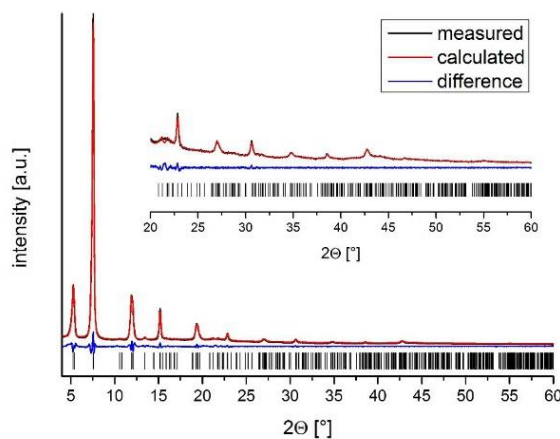


**Figure S4.** Result of the Pawley fit of Ga-PMOF-cf.

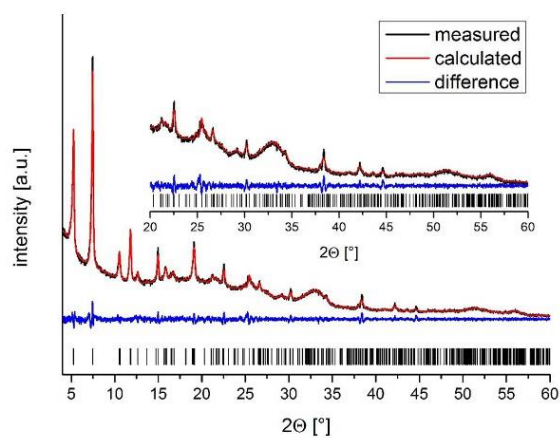


**Figure S5.** Result of the Pawley fit of In-PMOF-cf.

**Table S1.** Refined crystallographic parameters of In-PMOF-bs-th, -bs-us and -cf and Ga-PMOF-bs-th, -bs-us in comparison.

	SG	a [Å]	b [Å]	c [Å]	GOF	$R_{wp}$
In-PMOF-bs-th	<i>Cmmm</i>	33.432(2)	7.152(1)	16.7181(9)	1.6	5.7
In-PMOF-bs-us	<i>Cmmm</i>	33.351(2)	7.1742(5)	16.786(1)	1.0	5.0
In-PMOF-cf	<i>Cmmm</i>	33.283(8)	7.151(2)	16.793(4)	1.1	3.6
Ga-PMOF-bs-th	<i>Cmmm</i>	32.950(4)	6.700(2)	16.556(2)	2.4	6.5
Ga-PMOF-cf	<i>Cmmm</i>	32.652(8)	6.716(4)	16.739(4)	2.1	5.5

#### 4. Sorption properties and PXRD patterns of the activated samples

Figure S6 shows the CO<sub>2</sub>-sorption isotherm (298.15 K,  $p_{\max} = 1$  bar) of Ga- and In-PMOF-bs-th in mol mol<sup>-1</sup> and wt%. Figure S7 and S8 show the N<sub>2</sub>-Sorpton isothermes of In-PMOF-bs-us and Ga-PMOF-cf (120 °C). The hysteresis at  $p/p_0$  of 0.8 is due to the small particle size of this samples of about 65 nm and indicates textural porosity between the nanoparticles.

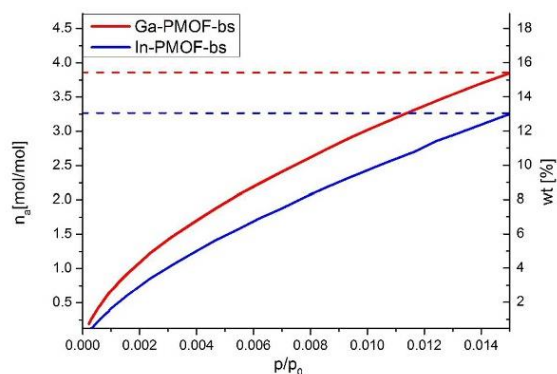


**Figure S6.** CO<sub>2</sub>-sorption isotherm of Ga- and In-PMOF obtained from the batch synthesis measured at 298.15 K up to 1 bar.

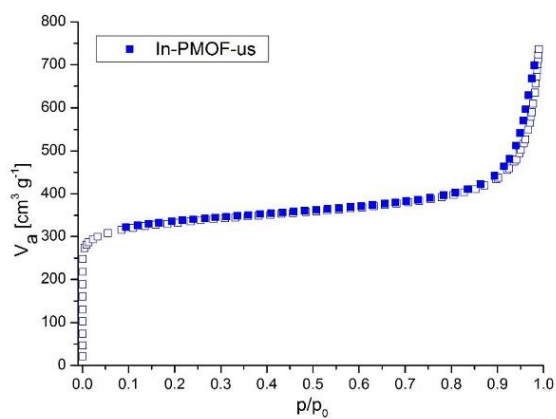


**Figure S7.** N<sub>2</sub>-sorption isotherm of In-PMOF-bs-us measured at 77 K. Filled squares represent the adsorption and empty squares show desorption.

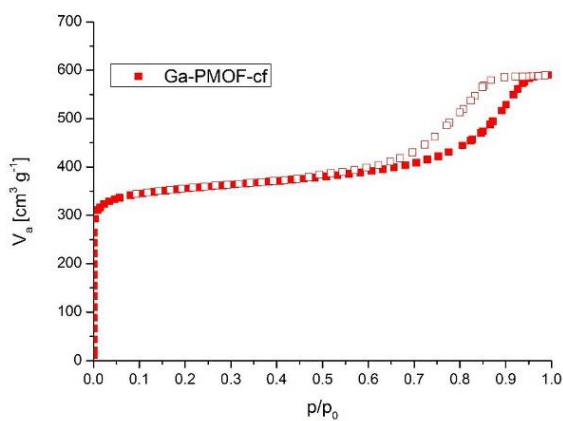


**Figure S8.** N<sub>2</sub>-sorption isotherm of Ga-PMOF-cf (120 °C) measured at 77 K. Filled squares represent the adsorption and empty squares show desorption.

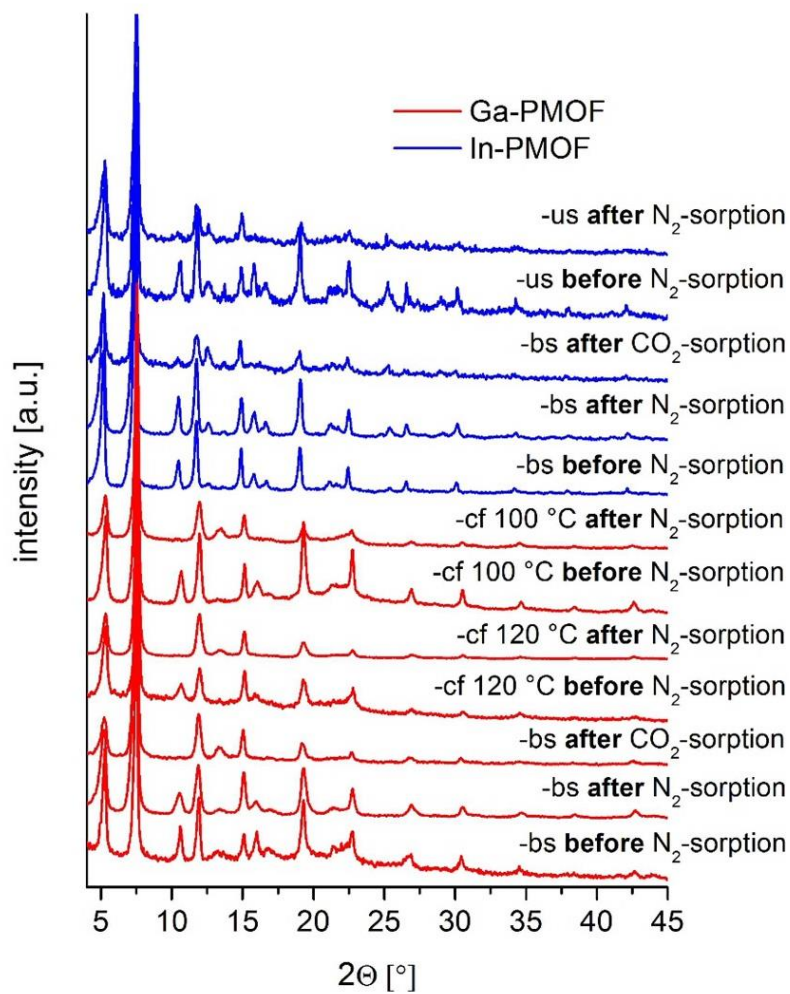


**Figure S9.** PXRD patterns of all measured samples before and after the individual sorption experiments.

**5. TG investigations and PXRD patterns of the decomposition products**

The TG measurements of the as-synthesized samples show slightly different amounts of solvent molecules in the pores (Figs. S11, S13, S14). After activation at 140 °C at  $10^{-2}$  kPa the DMF molecules can be removed and just small amounts of physisorbed water remains in the pores (Fig. S10 and S12). The decomposition products of the Ga- and In-PMOFs are  $\text{Ga}_2\text{O}_3$  and  $\text{In}_2\text{O}_3$ , which was shown by PXRD measurements (Fig. S15).

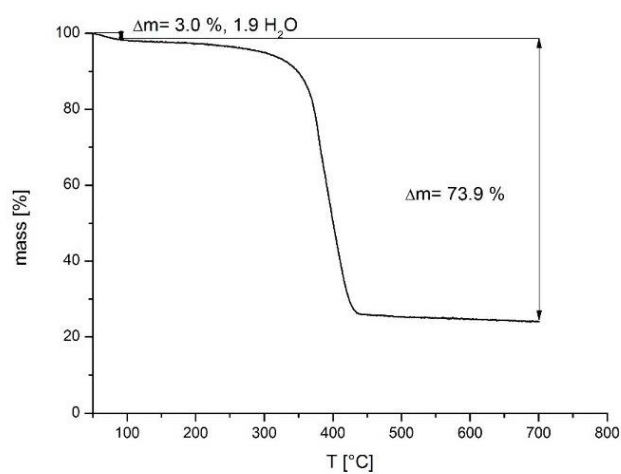


**Figure S10.** Thermogravimetric curve of an activated sample of In-PMOF-bs-th (140 °C,  $10^{-2}$  kPa). The measurement reveals a molar linker : metal : H<sub>2</sub>O ratio of 1 : 1.9 : 1.9.

## Anhang

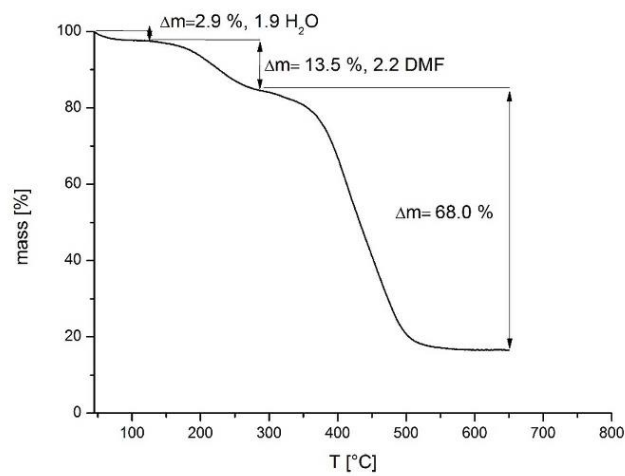


**Figure S11.** Thermogravimetric curve of an as-synthesized sample of Ga-PMOF-bs-th. The measurement reveals a molar linker : metal : H<sub>2</sub>O : DMF ratio of 1 : 1.8 : 1.9 : 2.2.

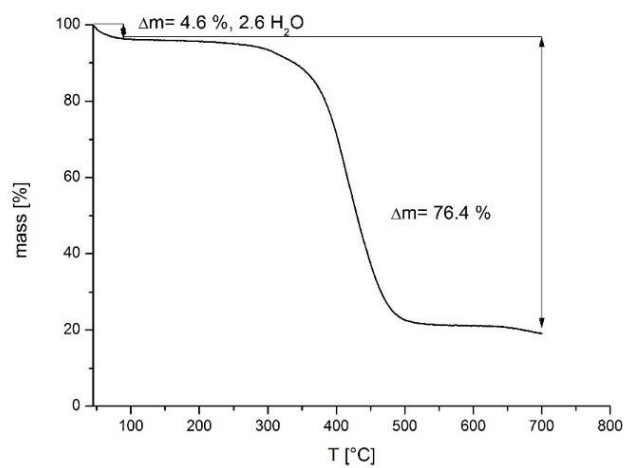


**Figure S12.** Thermogravimetric curve of an activated samples of Ga-PMOF-bs-th (140 °C, 10<sup>-2</sup> kPa). The measurement reveals a molar linker : metal : H<sub>2</sub>O ratio of 1 : 2.1 : 2.6.

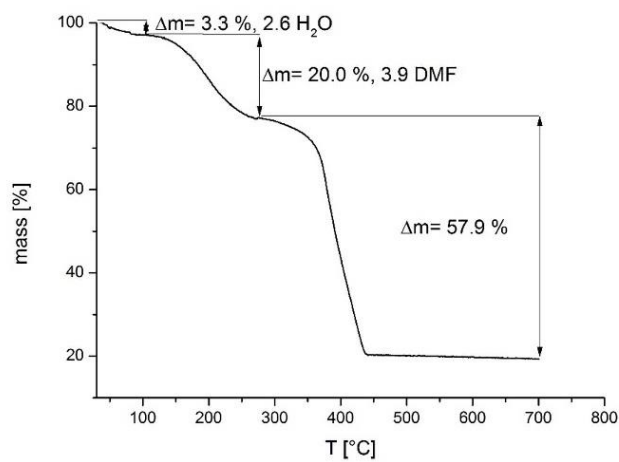


**Figure S13.** Thermogravimetric curve of an as-synthesized sample of In-PMOF-bs-us. The measurement reveals a molar linker : metal : H<sub>2</sub>O : DMF ratio of 1 : 2.0 : 2.6 : 3.9.

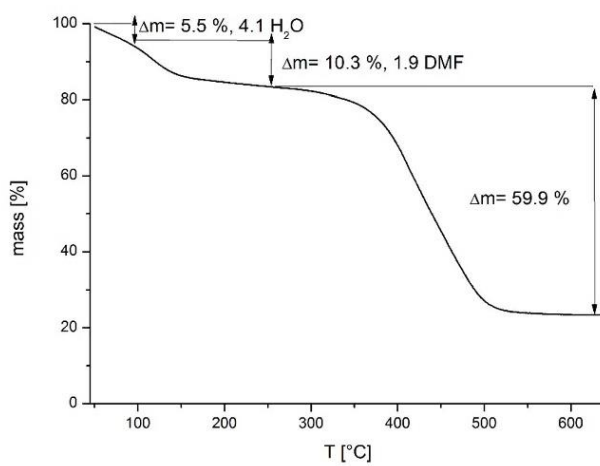


**Figure S14.** Thermogravimetric curve of an as-synthesized sample of Ga-PMOF-cf (120 °C). The measurement reveals a molar linker : metal : H<sub>2</sub>O : DMF ratio of 1 : 2.0 : 1.9 : 4.1.



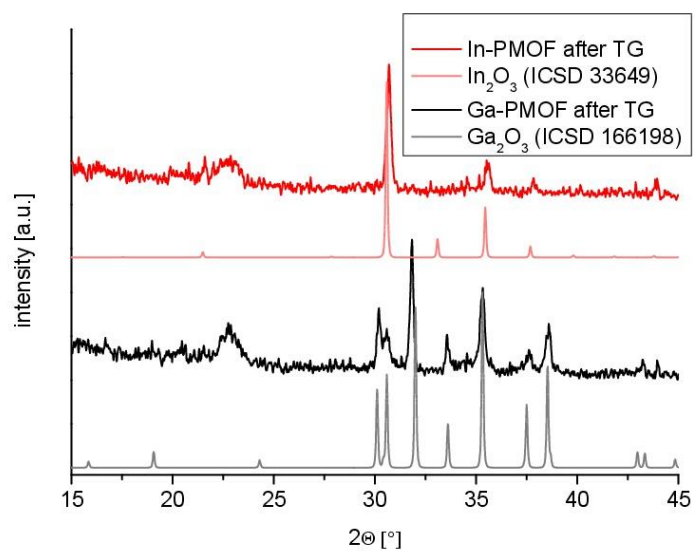


**Figure S15.** PXRD patterns of the decomposition products of Ga-PMOF (black) and In-PMOF (red) after thermogravimetric measurements up to 700 °C. The simulated PXRD patterns of  $\text{In}_2\text{O}_3$  and  $\text{Ga}_2\text{O}_3$  are also presented for comparison.

## 6. IR spectroscopy of Ga- and In-PMOF-bs-th

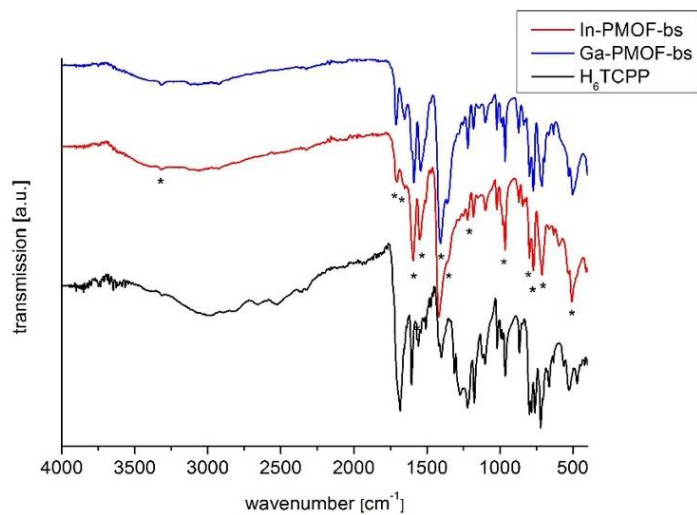


**Figure S16.** IR-spectra of as-synthesized samples of Ga- (blue) and In-PMOF-bs-th (red). For comparison the IR-spectrum of the linker H<sub>6</sub>TCPP (black) is also presented. The black stars mark the selected bands commented in Table S2.

## Anhang

**Table S2.** Assignment of the vibrations in the IR-spectra of Ga- and In-PMOF-bs-th as-synthesized. Red numbers indicate slight impurities with DMF or linker, black numbers represent vibrations of the corresponding MOF.<sup>4,5</sup>

Vibration	Ga-PMOF-bs-th $\tilde{\nu}$ IR [cm <sup>-1</sup> ]	In-PMOF-bs-th $\tilde{\nu}$ IR [cm <sup>-1</sup> ]	H <sub>6</sub> TCPP $\tilde{\nu}$ IR [cm <sup>-1</sup> ] <sup>1-3</sup>
$\nu$ NH (pyrrole)	3320	3318	3315
$\nu$ CO (DMF)	1709	1711	
$\nu_{as}$ CO (COOH (H <sub>6</sub> TCPP))	1652	1652	1684
$\nu_{as}$ CO (COO)	1594	1587	
$\nu$ C=C (arom.)	1550	1542	1558
$\nu_s$ CO (COO)	1417	1409	
$\nu$ C-N (pyrrole)	1362	1362	1399
$\delta$ O-H (COOH (H <sub>6</sub> TCPP))	1222	1219	1222/ 1173
$\delta$ C-H, N-H (pyrrole), neighboring H	961	964	962
$\gamma$ C-H (1,4-subst.)	796	799	798
$\delta$ C-H, N-H (pyrrole), neighboring H	766	768	757
$\gamma$ C-H (out of plane)	708	714	717
$\delta$ C=C (skeleton)	504	506	525

## 7. DLS and SEM measurements

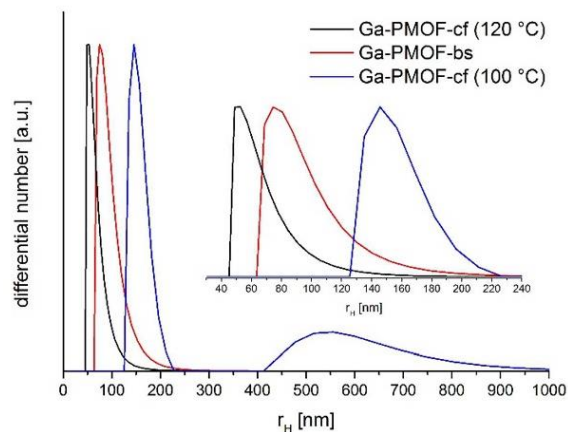


**Figure S17.** Results of the DLS measurements of as-synthesized samples of the Ga-PMOFs by number distribution. Ga-PMOF-cf (120 °C) is shown in black, Ga-PMOF-bs-th in red and Ga-PMOF-cf (100 °C) in blue. The small fraction of larger particle sizes of Ga-PMOF-cf (100 °C) is caused by agglomeration during the DLS measurement.

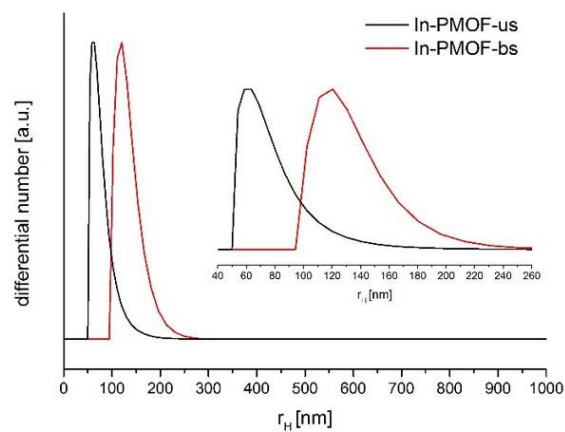


**Figure S18.** Results of the DLS measurements of as-synthesized samples of the In-PMOFs by number distribution. In-PMOF-bs-us is shown in black and In-PMOF-bs-th in red.

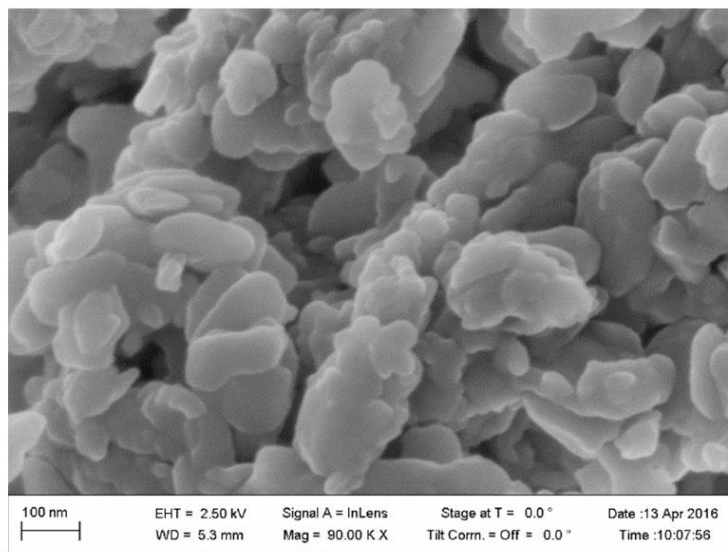


**Figure S19.** SEM image of Ga-PMOF-bs-th.

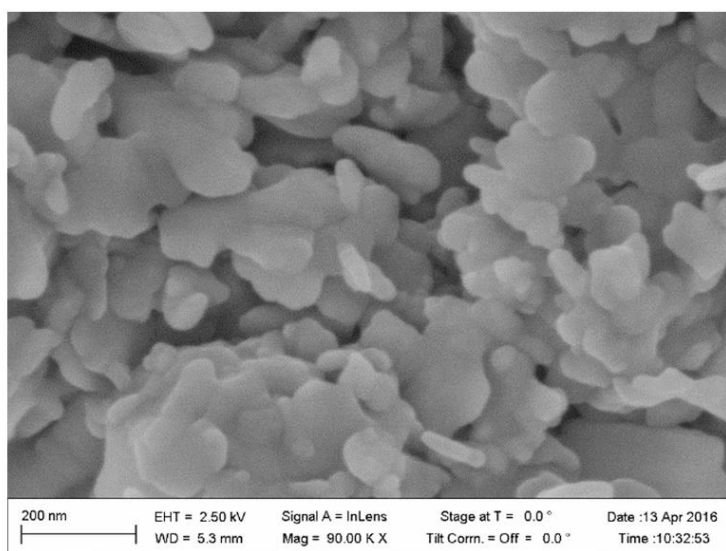


**Figure S20.** SEM image of In-PMOF-bs-th.

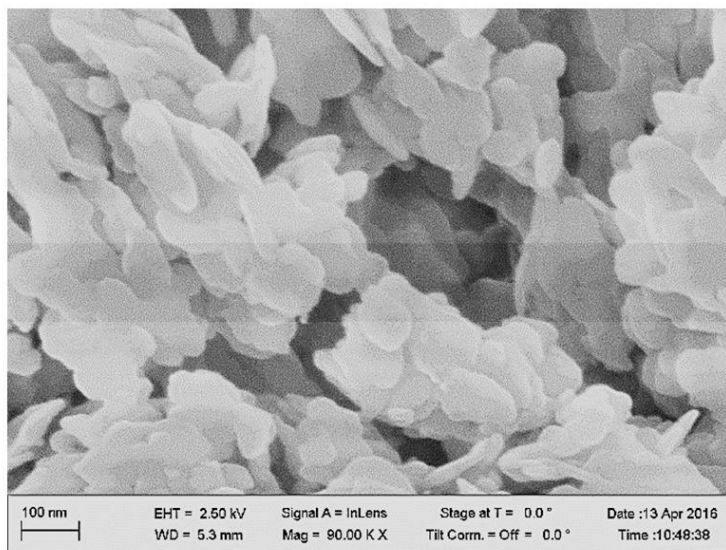


**Figure S21.** SEM image of In-PMOF-bs-us.

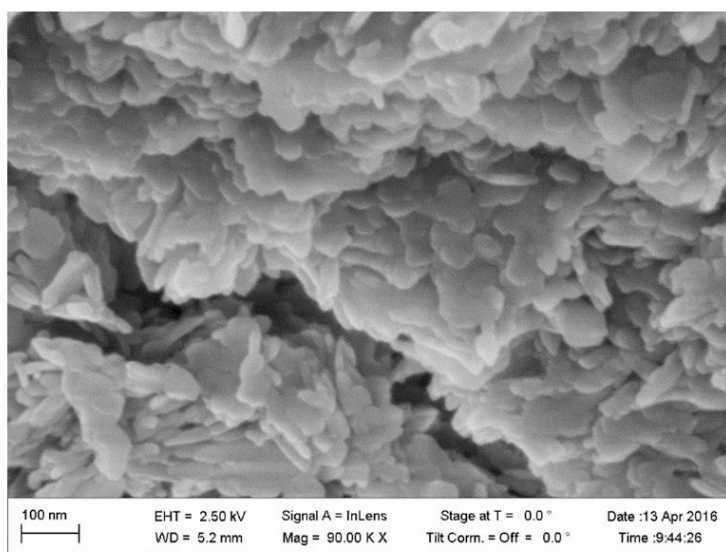


**Figure S22.** SEM image of Ga-PMOF-cf (100 °C).

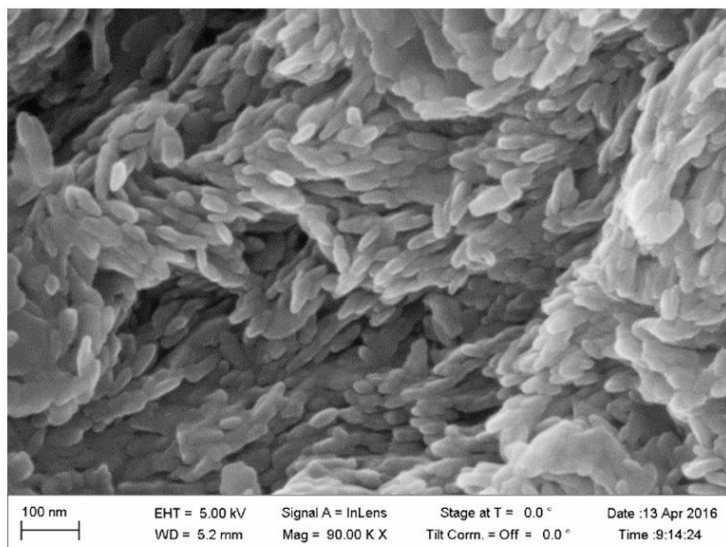


**Figure S23.** SEM image of Ga-PMOF-cf. (120 °C).

#### 8. Literature

- (1) Jeong, E.-Y.; Ansari, M. B.; Mo, Y.-H.; Park, S.-E., *J. Hazard. Mater.* **2011**, *185*, 1311-1317.
- (2) Harada, A.; Yamaguchi, H.; Okamoto, K.; Fukushima, H.; Shiotsuki, K.; Kamachi, M., *Photochem. Photobiol.* **1999**, *70*, 298-302.
- (3) Garcia, G.; Sol, V.; Lamarche, F.; Granet, R.; Guilloton, M.; Champavier, Y.; Krausz, P., *Bioorg. Med. Chem. Lett.* **2006**, *16*, 3188-3192.
- (4) Socrates, G., *Infrared and Raman Characteristic Group Frequencies: Tables and Charts.* Wiley: **2004**.
- (5) Hesse, M.; Meier, H.; Zeeh, B., *Spektroskopische Methoden in der organischen Chemie.* Thieme: **2005**.

**7.6 A Facile “Green” Route for Scalable Batch Production and Continuous Synthesis of Zirconium MOFs**

*Eur. J. Inorg. Chem.* **2016** · ISSN 1099–0682

**SUPPORTING INFORMATION**

**DOI:** 10.1002/ejic.201600295

**Title:** A Facile “Green” Route for Scalable Batch Production and Continuous Synthesis of Zirconium MOFs

**Author(s):** Helge Reinsch,\* Steve Waitschat, Sachin M. Chavan, Karl Petter Lillerud, Norbert Stock\*



**Preliminary test reactions**

Initially we evaluated the opportunity to obtain the MOF zirconium fumarate employing only the linker molecule fumaric acid, zirconium sulfate and water under stirring and reflux. Since the desired product could not be obtained, we changed the Zr-source to  $\text{ZrOCl}_2 \cdot 8\text{H}_2\text{O}$ , albeit this results in risks for corrosion in synthesis scale up. Employing only water as solvent, mostly gels were obtained after heating, similarly to the results of the synthesis using  $\text{ZrCl}_4$  (references 24 and 26 in the manuscript). The PXRD patterns of the product obtained in this manner only showed very few and broad reflections, indicating that no well-ordered crystalline MOFs could be obtained. Adding formic acid to the synthesis mixture, which is known to act as modulating reagent in the synthesis of Zr-MOFs, drastically increased the crystallinity of the products. The amount of modulator was varied in high-throughput experiments fixing the concentration of linker and  $\text{Zr}^{4+}$  ions to 0.2 m, respectively, and it was observed that three crystalline products can be obtained under these conditions. Using water/formic acid mixtures with composition 0%/100% yielded a weakly crystalline product with not yet identified structure and composition (Fig. S1). Employing mixtures with 33%/67% composition resulted in the formation of a crystalline but yet unreported compound. We identified this as a mixed linker MOF with the approximate composition  $[\text{Zr}_6\text{O}_4(\text{OH})_6(\text{O}_2\text{C}-\text{C}_2\text{H}_2-\text{CO}_2)_4(\text{O}_2\text{CH})_2(\text{H}_2\text{O})_2]$  containing fumarate and formate anions. A very similar compound was already obtained using uranium (Fig. S2).<sup>1</sup> However, up-scaling of the reaction was not yet possible and thus we were not able to fully characterize this compound, although a tentative Rietveld refinement could be conducted. Employing mixtures with 50%/50% solvent composition yielded the pure zirconium fumarate at 90 °C, but initial attempts to obtain the MOF under reflux conditions indicated that impurities of the mixed-linker-MOF are formed under these conditions. Thus the solvent system was changed to water/acetic acid mixtures which allowed for the synthesis of pure compounds as described in the manuscript.

## Anhang

Table S1: Observed elemental atom ratios of the title compounds as detected by EDX spectroscopy.

MOF	Zr-Fum	Zr-Mes	UiO-66-(OH) <sub>2</sub>	MOF-808	DUT-67
	no chloride	Zr:Cl=14:1	no chloride traces of Na	Zr:Cl=6:1	no chloride

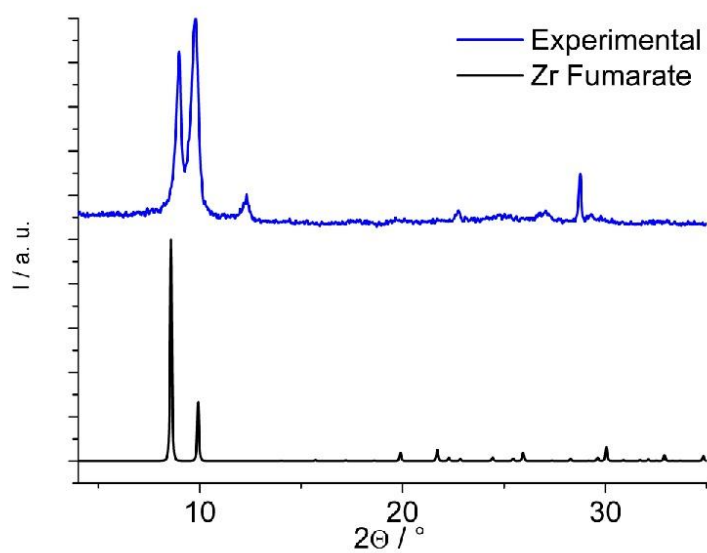


Figure S1: Simulated PXRD pattern of zirconium fumarate and experimental pattern of the unknown product obtained in pure formic acid. Reaction conditions are: 42 mg (0.36 mmol) fumaric acid, 140 mg (44 mmol)  $\text{ZrOCl}_2 \cdot 8\text{H}_2\text{O}$  and 1.5 mL formic acid were heated under stirring for one hour at 98 °C.

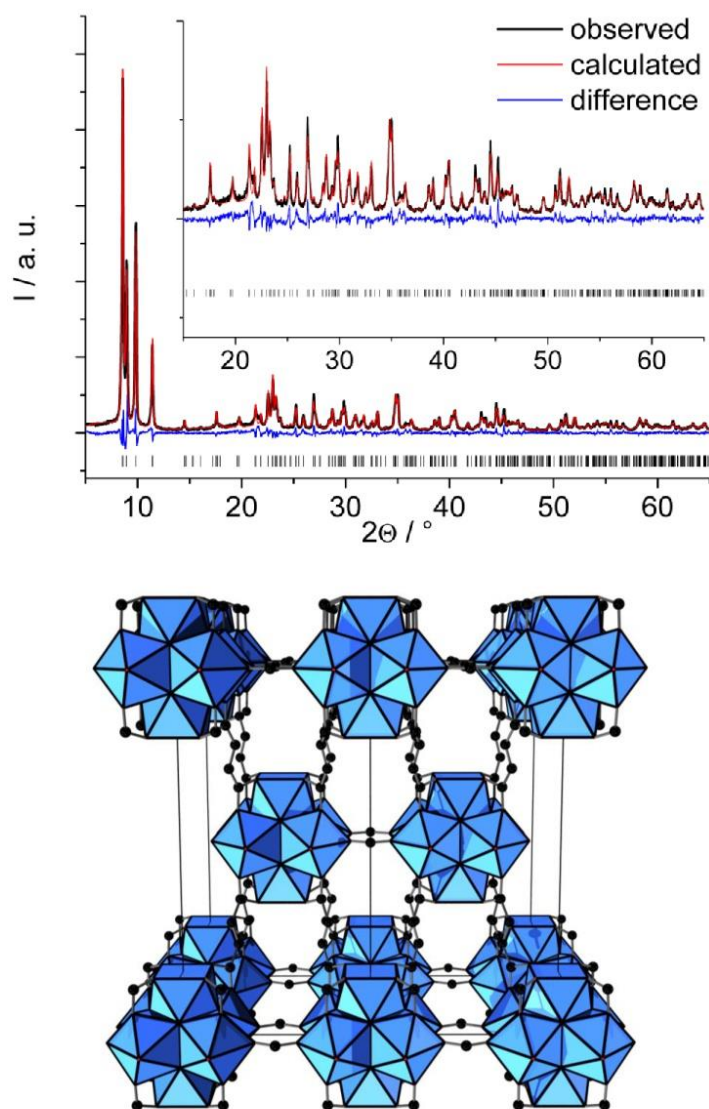


Figure S2: Rietveld plot and framework structure for the mixed linker zirconium fumarate/formate with the idealized composition  $[\text{Zr}_6\text{O}_4(\text{OH})_6(\text{O}_2\text{C}-\text{C}_2\text{H}_2-\text{CO}_2)_4(\text{O}_2\text{CH})_2(\text{H}_2\text{O})_2] \cdot \text{Guests}$ . Reaction conditions are: 42 mg (0.36 mmol) fumaric acid, 140 mg (44 mmol)  $\text{ZrOCl}_2 \cdot 8\text{H}_2\text{O}$ , 0.5 mL  $\text{H}_2\text{O}$  and 1 mL formic acid were heated under stirring for one hour at 98 °C.

## Anhang

The structure model was obtained after cell parameter adjustment of the reported uranium MOF to the indexed cell parameters, replacement of uranium atoms by zirconium atoms and subsequent structure optimization via force field methods.<sup>2</sup> In order to obtain a reasonable model matching with the observed cell parameters, the connectivity of the framework had to be lowered from 10 fumarates ions coordinating in the uranium MOF to 8 fumarates ions coordinating in the zirconium MOF. The maximum space group symmetry found in this energetically optimized model (*Immm*, in agreement with the observed extinction conditions) was imposed on the model. Residual electron density was assigned to partially occupied oxygen atoms, serving as dummy atoms for guest molecules. Since scale up of the reaction was not straight-forward, a complete characterization of the compound was not yet possible. Therefore the refinement must be considered as tentative, mainly proving the framework connectivity. The figures of merit are  $R_{WP} = 12.5\%$ ,  $R_{Bragg} = 2.8\%$  and  $GoF = 2.2$ .

```
data_
_chemical_name_mineral "ZrFormateFumarate"
_cell_length_a 10.08217(54)
_cell_length_b 12.06289(72)
_cell_length_c 19.7550(11)
_cell_angle_alpha 90
_cell_angle_beta 90
_cell_angle_gamma 90
_cell_volume 2402.60(23)
_symmetry_space_group_name_H-M IMMM
loop_
_atom_site_label
_atom_site_type_symbol
_atom_site_symmetry_multiplicity
_atom_site_fract_x
_atom_site_fract_y
_atom_site_fract_z
_atom_site_occupancy
_atom_site_B_iso_or_equiv
Zr1 Zr 0 0.17379(51) 0.14786(48) 0 1 0.92(23)
Zr2 Zr 0 0 0 0.12348(31) 1 0.92(23)
O1 O 0 0.7714(21) 0.2045(18) 0.09801(48) 1 2.79(34)
O2 O 0 0.8623(13) 0.1210(12) 0.17854(95) 1 2.79(34)
O3 O 0 0.6103(12) 0.1158(15) 0 1 2.79(34)
O4 O 0 0.8238(29) 0.6647(20) 0 1 2.79(34)
O5 O 0 0 0.8491(25) 0.9376(12) 1 2.79(34)
O6 O 0 0.1845(24) 0 0.9291(12) 1 2.79(34)
C1 C 0 0.7742(16) 0.1870(17) 0.16009(75) 1 8.0(12)
C2 C 0 0.7330(33) 0.7374(19) 0.21734(80) 1 8.0(12)
C3 C 0 0 0.6615(33) 0.5 1 8.0(12)
Og1 O 0 0.7451(39) 0.5 0.1015(24) 0.774(49) 8.0(16)
Og2 O 0 0.5 0 0.8722(41) 0.858(54) 8.0(16)
Og3 O 0 0.5 0 0.7722(37) 0.897(63) 8.0(16)
Og4 O 0 0.5 0 0.3452(48) 0.633(59) 8.0(16)
Og5 O 0 0.5 0.5 0.1874(71) 0.425(59) 8.0(16)
Og6 O 0 0 0.9479(81) 0.4051(40) 0.401(40) 8.0(16)
```

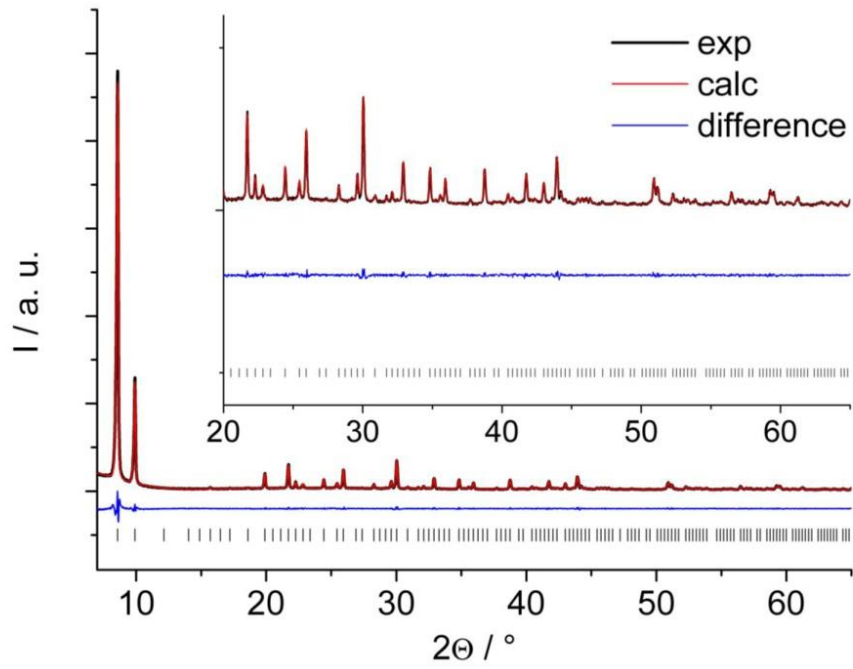


Figure S3: Pawley fit for the structure-less unit cell refinement of zirconium fumarate. Black line are the measured data, red line the calculated fit, blue line gives the difference curve. Vertical bars mark the allowed Bragg reflection position.

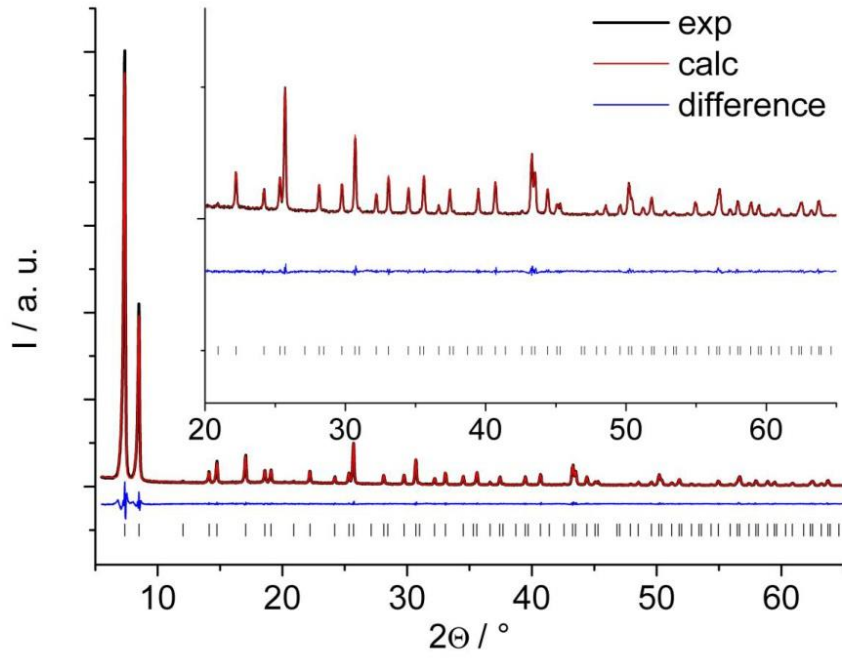


Figure S4: Pawley fit for the structure-less unit cell refinement of UiO-66(OH)<sub>2</sub>. Black line are the measured data, red line the calculated fit, blue line gives the difference curve. Vertical bars mark the allowed Bragg reflection position.

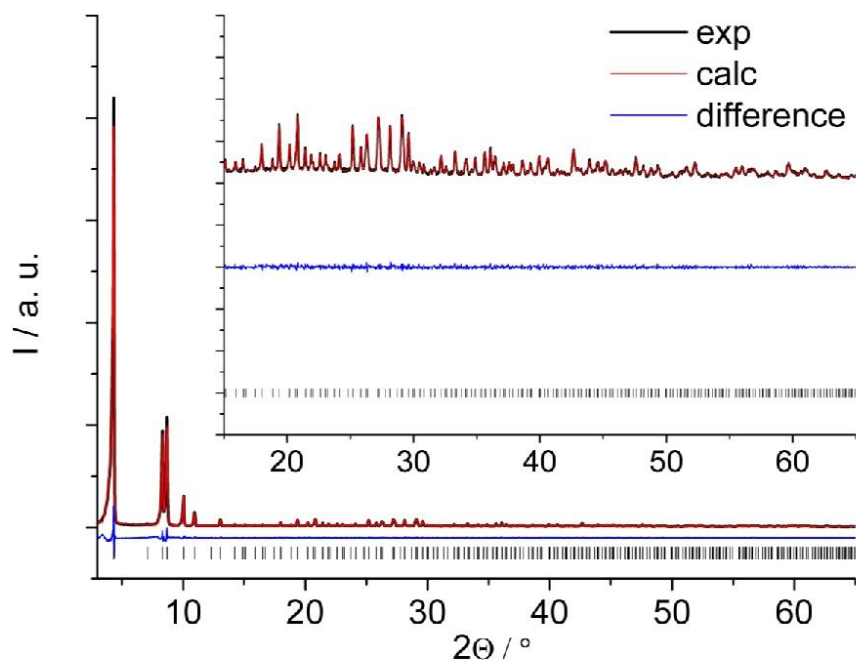


Figure S5: Pawley fit for the structure-less unit cell refinement of MOF-808. Black line are the measured data, red line the calculated fit, blue line gives the difference curve. Vertical bars mark the allowed Bragg reflection position.

**Details on the Rietveld refinements:**

For the refinement of DUT-67, the reported crystal structure was taken as starting model. During the course of the refinement it was observed that no residual electron density could be located inside the dodecahedral cavities. Instead substantial electron density was localized in the octahedral cavities and attributed to three different partially occupied oxygen atoms which serve as dummies for any guest molecules. All atoms could be freely refined using only distance restraints. The \*.cif file is given below.

```

data_
_chemical_name_mineral DUT-67
_cell_length_a 38.83935(58)
_cell_length_b 38.83935(58)
_cell_length_c 38.83935(58)
_cell_angle_alpha 90
_cell_angle_beta 90
_cell_angle_gamma 90
_cell_volume 58589.0(26)
_symmetry_space_group_name_H-M Fm-3m
loop_
_atom_site_label
_atom_site_type_symbol
_atom_site_fract_x
_atom_site_fract_y
_atom_site_fract_z
_atom_site_occupancy
_atom_site_B_iso_or_equiv
Zr1 Zr 0.217310(93) 0.282690(93) 0.04567(12) 1 2.91(11)
Zr2 Zr 0.20480(13) 0.20480(13) 0 1 2.91(11)
S1 S 0.25068(34) 0.10982(23) 0.10982(23) 1 2.91(11)
C1 C 0.22900(39) 0.15624(32) 0.05367(35) 1 2.91(11)
C2 C 0.22076(37) 0.12700(34) 0.07982(32) 1 2.91(11)
C3 C 0.19237(39) 0.10462(37) 0.07906(32) 1 2.91(11)
O1 O 0.20335(28) 0.15767(26) 0.03374(25) 1 2.91(11)
O2 O 0.22924(33) 0.22924(33) 0.04315(55) 1 2.91(11)
O3 O 0.16681(24) 0.25862(29) 0.06298(28) 1 2.91(11)
O4 O 0.21930(40) 0.28070(40) 0.10328(40) 1 2.91(11)
O5 O 0.17714(34) 0.32286(34) 0.02988(65) 1 2.91(11)
O6 O 0.23850(48) 0.30515(54) 0 1 2.91(11)
Og1 O 0.6589(13) 0.1589(13) 0.3268(21) 0.333(19) 2.91(11)
Og2 O 0.71589(35) 0.28411(35) -0.12935(68) 1.000(23) 2.91(11)
Og3 O 0.67620(51) 0.73296(82) 0.67620(51) 0.840(21) 2.91(11)

```



## Anhang

For the refinement of zirconium mesaconate, the reported crystal structure of UiO-66 was taken as the starting model for force-field calculations using Materials Studio. Replacement of the terephthalate linker molecules by mesaconate linker molecules lead to a hypothetical crystal structure with  $Fm-3$  space group symmetry. Subsequent optimization of this model with cell parameters fixed to the indexed values gave the starting model for Rietveld refinement. Residual electron density was assigned to partially occupied oxygen atoms which serve as dummy atoms for any guest molecules. All atoms could be freely refined using only distance restrains. The \*.cif file is given below.

```
data_
_chemical_name_mineral zirconium mesaconate
_cell_length_a 17.78043(22)
_cell_length_b 17.78043(22)
_cell_length_c 17.78043(22)
_cell_angle_alpha 90
_cell_angle_beta 90
_cell_angle_gamma 90
_cell_volume 5621.17(21)
_symmetry_space_group_name_H-M FM-3
loop_
_atom_site_label
_atom_site_type_symbol
_atom_site_fract_x
_atom_site_fract_y
_atom_site_fract_z
_atom_site_occupancy
_atom_site_B_iso_or_equiv
Zr1 Zr 0.13925(19) 0 0 1 5.04(14)
O1 O 0.07694(45) 0.07694(45) 0.07694(45) 1 5.04(14)
O2 O 0.12037(35) 0 -0.18250(61) 1 5.04(14)
O3 O 0.21764(56) 0 -0.09033(36) 1 5.04(14)
C1 C 0.18720(50) 0 -0.15429(47) 1 5.04(14)
C2 C 0.24858(60) 0 -0.21297(46) 1 5.04(14)
C3 C 0.3239(20) 0 -0.1714(10) 0.5 5.04(14)
Og1 O 0.6677(10) 0.1677(10) 0.6677(10) 0.397(14) 5.04(14)
Og2 O 0 0 0.5579(37) 0.200(19) 5.04(14)
Og3 O 0.4010(21) 0 0.9010(21) 0.250(15) 5.04(14)
Og4 O 0.25 0.25 0.75 0.105(38) 5.04(14)
```

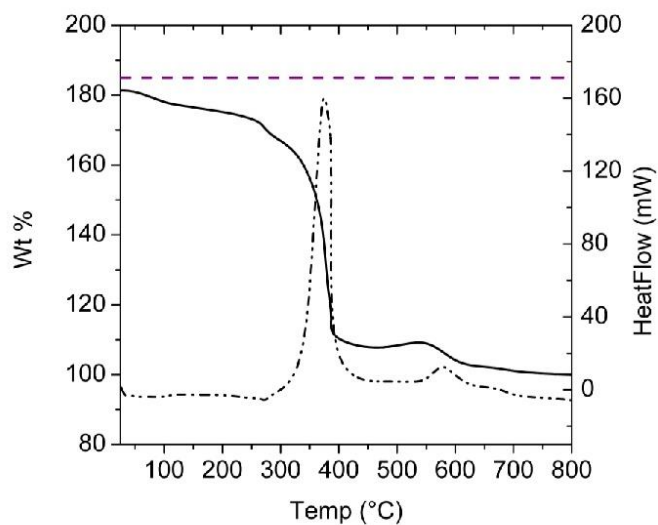


Figure S6: TG curve for zirconium fumarate (black line) with heat flow (dashed/dotted line) and the expected plateau (dashed purple line) for the idealized ratio Zr : linker 6 : 6.

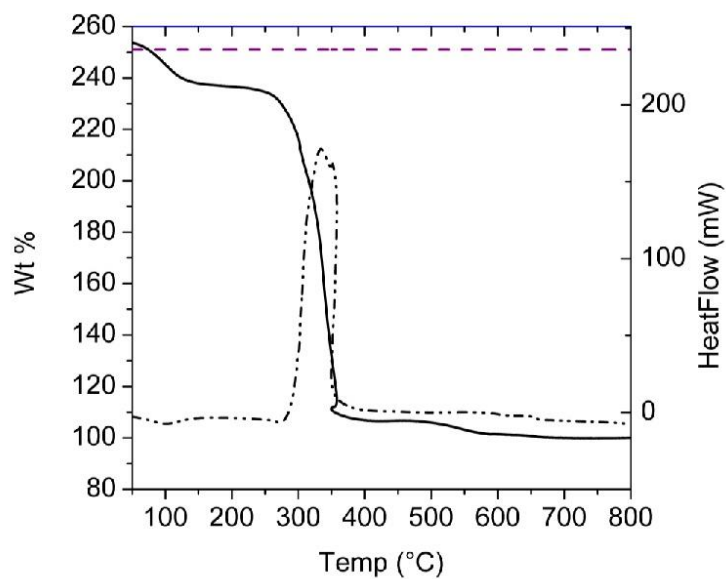


Figure S7: TG curve for UiO-66-(OH)<sub>2</sub> (black line) with heat flow (dashed/dotted line) and the expected plateau (dashed purple line) for the idealized ratio Zr : linker 6 : 6.

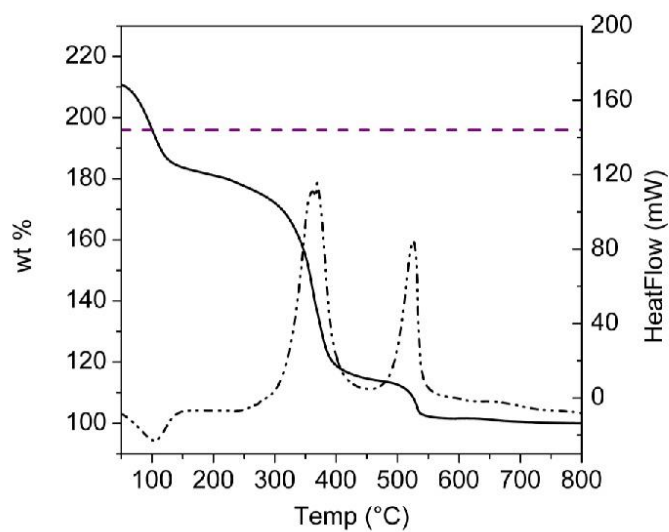


Figure S8: TG curve for zirconium mesaconate (black line) with heat flow (dashed/dotted line) and the expected plateau (dashed purple line) for the idealized ratio Zr : linker 6 : 6.

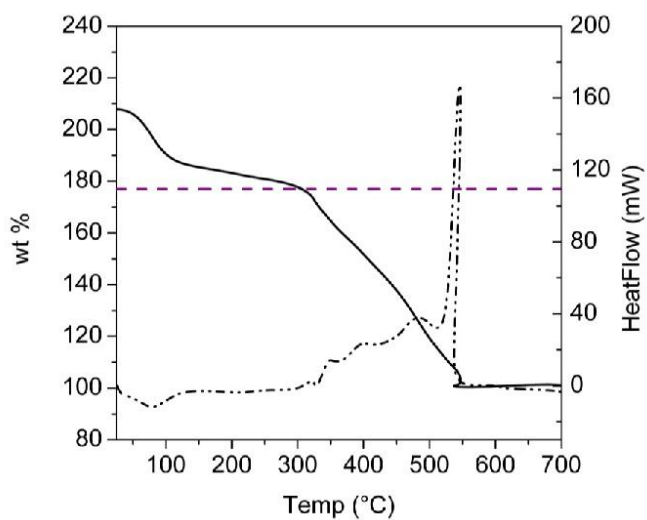


Figure S9: TG curve for MOF-808 (black line) with heat flow (dashed/dotted line) and the expected plateau (dashed purple line) for the idealized ratio Zr : linker 6 : 2.

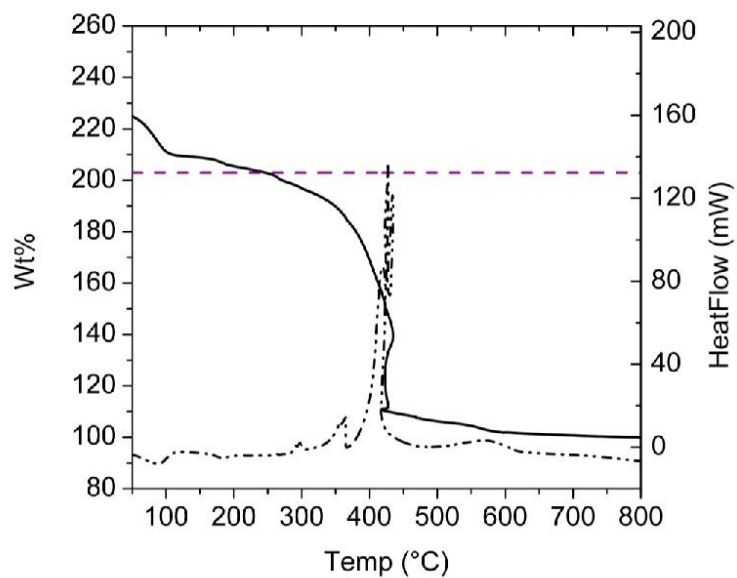


Figure S10: TG curve for DUT-67 (black line) with heat flow (dashed/dotted line) and the expected plateau (dashed purple line) for the idealized ratio Zr : linker 6 : 4.

**Description of the Flow Reactor**

In this work a flow reactor was developed that allows us to carry out reactions below the boiling point of the solvent. It is utilizing a magnetic membrane pump and Teflon tubes. Three aluminum plates were rolled into cylinders with different diameter, wrapped with Teflon tube and placed inside each other. Thus three interleaved cylinders wrapped with tubes of approximately 50 m Teflon tube each, connected to each other by PTFE-connectors, represent the reactor. This reactor part was placed in a conventional convection oven for heating. To mix the starting slurry a magnetic stirrer was used.

**Table S3.** List of parts & materials used to assemble the flow reactor and supplier.

Part	Supplier
Magnetic membrane pump Delta0730	ProMinent
Teflon tube (ID = 4 mm)	Fluortechnik Deutschland
Tube connector	Eydam
Heating Oven UF55	Memmert
Magnetic stirrer	Eydam
Al perforated Plate	Adolf Richter
Al Base Plate	Adolf Richter



Figure S11: Set up of the flow reactor.

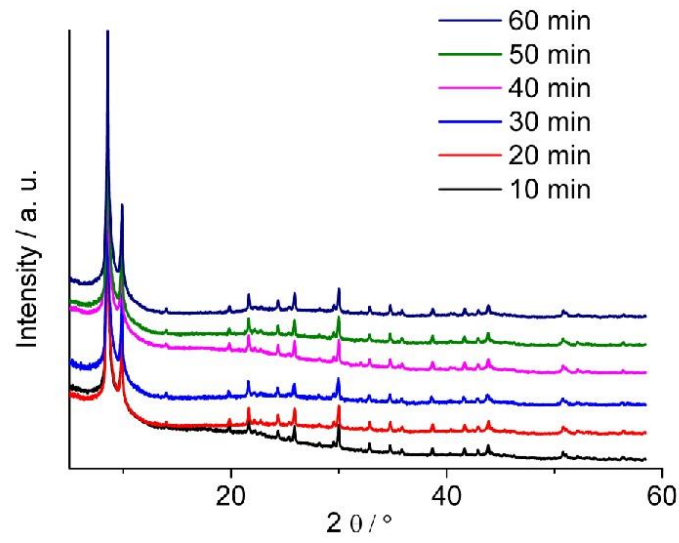


Figure S12: PXRD patterns of zirconium fumarate prepared in Pyrex tubes for ten to sixty minutes reaction time.

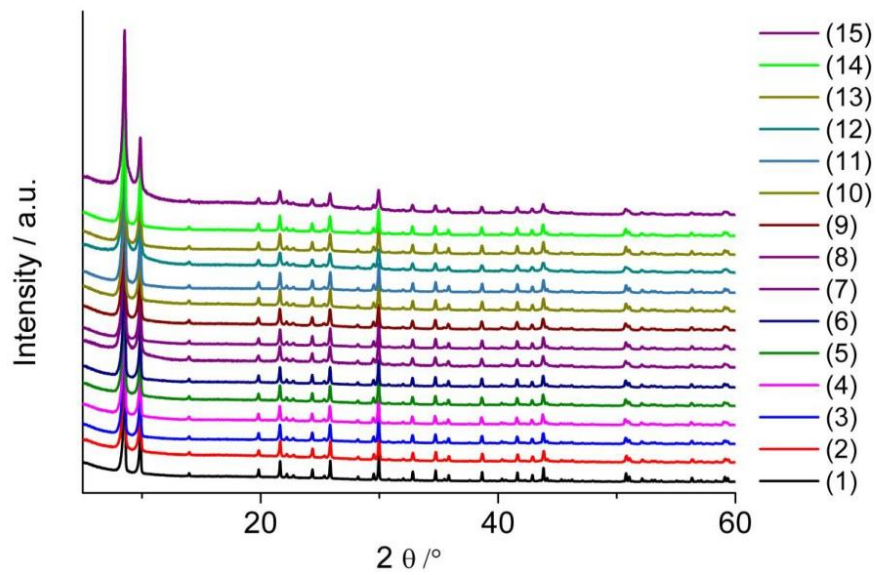


Figure S13: PXRD patterns of all 15 zirconium fumarate fractions prepared in the flow reactor with the respective number of fraction.

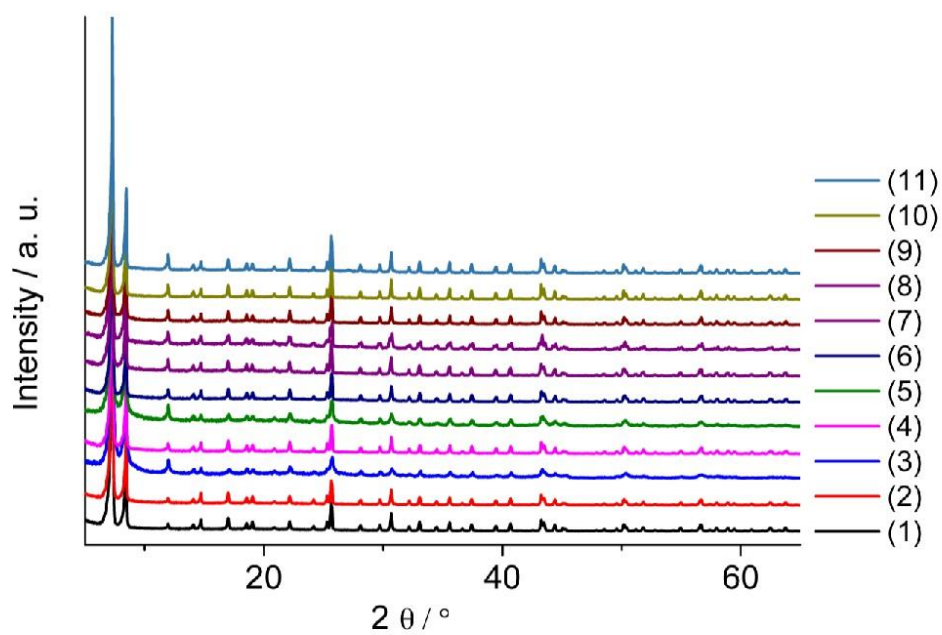


Figure S14: PXRD patterns of all 11 UiO-66-NH<sub>2</sub> fractions prepared in the flow reactor with the respective number of fraction.

<sup>1</sup> C. Falaise, C. Volkringer, T. Loiseau, *Cryst. Growth Des.* 2013, 13, 3225–3231.

<sup>2</sup> Materials Studio Version 5.0, Accelrys Inc., San Diego, CA, 2009.

**8. Quellenverzeichnis**

- 1 G. Ertl, *Angew. Chem.*, 1990, **102**, 1258–1266.
- 2 F. Harbor, 1908, Patent:DE235421.
- 3 P. B. Venuto and E. T. J. Habib, *Fluid catalytic cracking with zeolite catalysts*, USA, 1979.
- 4 J. L. C. Rowsell and O. M. Yaghi, *Microporous Mesoporous Mater.*, 2004, **73**, 3–14.
- 5 S. R. Batten, N. R. Champness, X.-M. Chen, J. Garcia-Martinez, S. Kitagawa, L. Öhrström, M. O’Keeffe, M. Paik Suh and J. Reedijk, *Pure Appl. Chem.*, 2013, **85(8)**.
- 6 J. H. Cavka, S. Jakobsen, U. Olsbye, N. Guillou, C. Lamberti, S. Bordiga and K. P. Lillerud, *J. Am. Chem. Soc.*, 2008, **130**, 13850–13851.
- 7 S. Smolders, A. Struyf, H. Reinsch, B. Bueken, T. Rhauderwiek, L. Mintrop, P. Kurz, N. Stock and D. E. De Vos, *Chem. Commun.*, 2018, **54**, 876–879.
- 8 N. Heidenreich, A. Lieb, N. Stock and H. Reinsch, *Dalton Trans.*, 2018, **47**, 215–223.
- 9 H. Reinsch, T. Homburg, N. Heidenreich, D. Fröhlich, S. Henninger, M. Wark and N. Stock, *Chem. - Eur. J.*, 2018, **24**, 2173–2181.
- 10 H. Reinsch, M. Feyand, T. Ahnfeldt and N. Stock, *Dalton Trans.*, 2012, **41**, 4164.
- 11 B. Cai, P. Yang, J.-W. Dai and J.-Z. Wu, *CrystEngComm*, 2011, **13**, 985–991.
- 12 R. Plessius, R. Kromhout, A. L. D. Ramos, M. Ferbinteanu, M. C. Mittelmeijer-Hazeleger, R. Krishna, G. Rothenberg and S. Tanase, *Chem. - Eur. J.*, 2014, **20**, 7922–7925.
- 13 M. Lammert, C. Glišmann, H. Reinsch and N. Stock, *Cryst. Growth Des.*, 2017, **17**, 1125–1131.
- 14 B. Bueken, F. Vermoortele, D. E. P. Vanpoucke, H. Reinsch, C.-C. Tsou, P. Valvekens, T. De Baerdemaeker, R. Ameloot, C. E. A. Kirschhock, V. Van Speybroeck, J. M. Mayer and D. De Vos, *Angew. Chem.*, 2015, **127**, 14118–14123.
- 15 H. Assi, G. Mouchaham, N. Steunou, T. Devic and C. Serre, *Chem Soc Rev*, 2017, **46**, 3431 - 3452.
- 16 H. L. Nguyen, *New J Chem*, 2017, **41**, 14030 - 14043.
- 17 H. Reinsch, M. Krüger, J. Wack, J. Senker, F. Salles, G. Maurin and N. Stock, *Microporous Mesoporous Mater.*, 2012, **157**, 50–55.
- 18 F. Niekel, M. Ackermann, P. Guerrier, A. Rothkirch and N. Stock, *Inorg. Chem.*, 2013, **52**, 8699–8705.
- 19 G. Férey, C. Mellot-Draznieks, C. Serre, F. Millange, J. Dutour, S. Surblé and I. Margiolaki, *Science*, 2005, **309**, 2040–2042.
- 20 P. Horcajada, H. Chevreau, D. Heurtaux, F. Benyettou, F. Salles, T. Devic, A. Garcia-Marquez, C. Yu, H. Lavarard, C. L. Dutson, E. Magnier, G. Maurin, E. Elkaïm and C. Serre, *Chem. Commun.*, 2014, **50**, 6872.
- 21 K.-S. Lin, A. K. Adhikari, C.-N. Ku, C.-L. Chiang and H. Kuo, *Int. J. Hydrog. Energy*, 2012, **37**, 13865–13871.
- 22 S. R. Miller, E. Alvarez, L. Fradcourt, T. Devic, S. Wuttke, P. S. Wheatley, N. Steunou, C. Bonhomme, C. Gervais, D. Laurencin, R. E. Morris, A. Vimont, M. Daturi, P. Horcajada and C. Serre, *Chem. Commun.*, 2013, **49**, 7773.
- 23 D. Saha, T. Maity and S. Koner, *Eur. J. Inorg. Chem.*, 2015, **2015**, 1053–1064.
- 24 L. J. Wang, H. Deng, H. Furukawa, F. Gándara, K. E. Cordova, D. Peri and O. M. Yaghi, *Inorg. Chem.*, 2014, **53**, 5881–5883.
- 25 L. Hu, X.-M. Lin, J.-T. Mo, J. Lin, H.-L. Gan, X.-L. Yang and Y.-P. Cai, *Inorg. Chem.*, 2017, **56**, 4289–4295.
- 26 M. Servati Gargari, V. Stilinović, A. Bauzá, A. Frontera, P. McArdle, D. Van Derveer, S. W. Ng and G. Mahmoudi, *Chem. - Eur. J.*, 2015, **21**, 17951–17958.
- 27 A. K. Inge, M. Köppen, J. Su, M. Feyand, H. Xu, X. Zou, M. O’Keeffe and N. Stock, *J. Am. Chem. Soc.*, 2016, **138**, 1970–1976.



- 28 M. Köppen, O. Beyer, S. Wuttke, U. Lüning and N. Stock, *Dalton Trans.*, 2017, **46**, 8658–8663.
- 29 A. M. Rasero-Almansa, M. Iglesias and F. Sánchez, *RSC Adv*, 2016, **6**, 106790–106797.
- 30 M. Lammert, C. Glißmann and N. Stock, *Dalton Trans.*, 2017, **46**, 2425–2429.
- 31 M. Taddei, F. Costantino, F. Marmottini, A. Comotti, P. Sozzani and R. Vivani, *Chem Commun*, 2014, **50**, 14831–14834.
- 32 T. Rhauderwiek, H. Zhao, P. Hirschle, M. Döblinger, B. Bueken, H. Reinsch, D. De Vos, S. Wuttke, U. Kolb and N. Stock, *Chem. Sci.*, 2018, **8**, 5467 - 5478.
- 33 A. Mietrach, T. W. T. Muesmann, J. Christoffers and M. S. Wickleder, *Eur. J. Inorg. Chem.*, 2009, **2009**, 5328–5334.
- 34 G. Zhang, G. Wei, Z. Liu, S. R. J. Oliver and H. Fei, *Chem. Mater.*, 2016, **28**, 6276–6281.
- 35 G. Mouchaham, L. Cooper, N. Guillou, C. Martineau, E. Elkaim, S. Bourrelly, P. L. Llewellyn, C. Allain, G. Clavier, C. Serre and T. Devic, *Angew. Chem.*, 2015, **127**, 13495–13499.
- 36 G. Wißmann, A. Schaate, S. Lilienthal, I. Bremer, A. M. Schneider and P. Behrens, *Microporous Mesoporous Mater.*, 2012, **152**, 64–70.
- 37 B. Bueken, F. Vermoortele, M. J. Cliffe, M. T. Wharmby, D. Foucher, J. Wieme, L. Vanduyfhuys, C. Martineau, N. Stock, F. Taulelle, V. Van Speybroeck, A. L. Goodwin and D. De Vos, *Chem. - Eur. J.*, 2016, **22**, 3264–3267.
- 38 H. Reinsch, S. Waitschat and N. Stock, *Dalton Trans.*, 2013, **42**, 4840.
- 39 R. Banerjee, H. Furukawa, D. Britt, C. Knobler, M. O’Keeffe and O. M. Yaghi, *J. Am. Chem. Soc.*, 2009, **131**, 3875–3877.
- 40 L. J. Murray, M. Dincă and J. R. Long, *Chem. Soc. Rev.*, 2009, **38**, 1294.
- 41 J.-R. Li, R. J. Kuppler and H.-C. Zhou, *Chem. Soc. Rev.*, 2009, **38**, 1477.
- 42 F. Jeremias, D. Fröhlich, C. Janiak and S. K. Henninger, *RSC Adv.*, 2014, **4**, 24073.
- 43 A. Corma, H. García and F. X. Llabrés i Xamena, *Chem. Rev.*, 2010, **110**, 4606–4655.
- 44 Q. Hu, J. Yu, M. Liu, A. Liu, Z. Dou and Y. Yang, *J. Med. Chem.*, 2014, **57**, 5679–5685.
- 45 M. Ibrahim, R. Sabouni and G. A. Hussein, *Curr. Med. Chem.*, 2017, **24**, 193–214.
- 46 N. Stock, *Chem. Ing. Tech.*, 2010, **82**, 1039–1047.
- 47 N. Stock, *Microporous Mesoporous Mater.*, 2010, **129**, 287–295.
- 48 S. Bauer and N. Stock, *Chem. Unserer Zeit*, 2007, **41**, 390–398.
- 49 H. Reinsch, M. A. van der Veen, B. Gil, B. Marszalek, T. Verbiest, D. de Vos and N. Stock, *Chem. Mater.*, 2013, **25**, 17–26.
- 50 S. Waitschat, D. Fröhlich, H. Reinsch, H. Terraschke, K. A. Lomachenko, C. Lamberti, H. Kummer, T. Helling, M. Baumgartner, S. Henninger and N. Stock, *Dalton Trans.*, 2018, **47**, 1062–1070.
- 51 F. Rouquerol, J. Rouquerol and K. S. W. Sing, *Adsorption by powders and porous solids: principles, methodology, and applications*, Academic Press, San Diego, 1999.
- 52 Á. Piñeiro, P. Brocos, A. Amigo, J. Gracia-Fadrique and M. Guadalupe Lemus, *Langmuir*, 2001, **17**, 4261–4266.
- 53 P. L. Llewellyn, F. Rodriguez-Reinoso, J. Rouquerol and N. Seaton, *Stud. Surf. Sci. Catal.*, 2007, **160**, 49.
- 54 A. Galarneau, F. Villemot, J. Rodriguez, F. Fajula and B. Coasne, *Langmuir*, 2014, **30**, 13266–13274.
- 55 O. Šolcová, L. Matějová and P. Schneider, *Appl. Catal. Gen.*, 2006, **313**, 167–176.
- 56 M. Thommes, K. Kaneko, A. V. Neimark, J. P. Olivier, F. Rodriguez-Reinoso, J. Rouquerol and K. S. W. Sing, *Pure Appl. Chem.*, DOI:10.1515/pac-2014-1117.
- 57 D. Fröhlich, S. K. Henninger and C. Janiak, *Dalton Trans*, 2014, **43**, 15300–15304.
- 58 E. Wiberg and N. Wiberg, *Lehrbuch der anorganischen Chemie*, Walter de Gruyter & Co., Berlin, New York, 102nd edn., 2007.
- 59 R. W. G. Wyckoff, *Crystal structures*, Interscience Publisher, New York, 2d ed., 1963.

## Quellenverzeichnis

- 60 R. G. Pearson, *J. Am. Chem. Soc.*, 1963, **85**, 3533–3539.
- 61 G. Kickelbick and U. Schubert, *Chem. Ber.*, 1997, **130**, 473–478.
- 62 G. Kickelbick and U. Schubert, *J. Chem. Soc. Dalton Trans.*, 1999, 1301–1306.
- 63 G. Kickelbick, D. Holzinger, C. Brick, G. Trimmel and E. Moons, *Chem. Mater.*, 2002, **14**, 4382–4389.
- 64 M. Puchberger, F. R. Kogler, M. Jupa, S. Gross, H. Fric, G. Kickelbick and U. Schubert, *Eur. J. Inorg. Chem.*, 2006, **2006**, 3283–3293.
- 65 P. Piszczek, A. Radtke, A. Wojtczak, T. Muzioł and J. Chojnacki, *Polyhedron*, 2009, **28**, 279–285.
- 66 T. J. Boyle, L. A. M. Ottley and M. A. Rodriguez, *Polyhedron*, 2005, **24**, 1727–1738.
- 67 P. Walther, M. Puchberger, F. R. Kogler, K. Schwarz and U. Schubert, *Phys. Chem. Chem. Phys.*, 2009, **11**, 3607.
- 68 C. Artner, M. Czakler and U. Schubert, *Inorganica Chim. Acta*, 2015, **432**, 208–212.
- 69 T. Xu, X. Hou, Y. Wang, J. Zhang, J. Zhang and B. Liu, *Dalton Trans.*, 2017, **46**, 10185–10188.
- 70 B. Moraru, G. Kickelbick and U. Schubert, *Eur. J. Inorg. Chem.*, 2001, **2001**, 1295–1301.
- 71 Y. Bai, Y. Dou, L.-H. Xie, W. Rutledge, J.-R. Li and H.-C. Zhou, *Chem Soc Rev*, 2016, **45**, 2327–2367.
- 72 Z. Hu and D. Zhao, *Dalton Trans.*, 2015, **44**, 19018–19040.
- 73 S. Biswas and P. Van Der Voort, *Eur. J. Inorg. Chem.*, 2013, **2013**, 2154–2160.
- 74 S. Biswas, J. Zhang, Z. Li, Y.-Y. Liu, M. Grzywa, L. Sun, D. Volkmer and P. Van Der Voort, *Dalton Trans.*, 2013, **42**, 4730.
- 75 A. Schaate, S. Dühnen, G. Platz, S. Lilienthal, A. M. Schneider and P. Behrens, *Eur. J. Inorg. Chem.*, 2012, **2012**, 790–796.
- 76 A. A. Barkhordarian and C. J. Kepert, *J Mater Chem A*, 2017, **5**, 5612–5618.
- 77 V. Bon, I. Senkovska, I. A. Baburin and S. Kaskel, *Cryst. Growth Des.*, 2013, **13**, 1231–1237.
- 78 V. Bon, I. Senkovska, M. S. Weiss and S. Kaskel, *CrystEngComm*, 2013, **15**, 9572.
- 79 H. Reinsch, I. Stassen, B. Bueken, A. Lieb, R. Ameloot and D. De Vos, *CrystEngComm*, 2015, **17**, 331–337.
- 80 A. A. Bezrukov, K. W. Törnroos, E. Le Roux and P. D. C. Dietzel, *Chem. Commun.*, 2018, **54**, 2735–2738.
- 81 P. Ji, K. Manna, Z. Lin, X. Feng, A. Urban, Y. Song and W. Lin, *J. Am. Chem. Soc.*, 2017, **139**, 7004–7011.
- 82 R. Dai, F. Peng, P. Ji, K. Lu, C. Wang, J. Sun and W. Lin, *Inorg. Chem.*, 2017, **56**, 8128–8134.
- 83 S. Waitschat, H. Reinsch, M. Arpacioğlu and N. Stock, *CrystEngComm*, 2018, DOI:10.1039/C8CE00949J.
- 84 S. Waitschat, H. Reinsch and N. Stock, *Chem Commun*, 2016, **52**, 12698–12701.
- 85 S. Leubner, *Aktuelle Arbeiten Promotion 2018*, .
- 86 V. Guillermin, F. Ragon, M. Dan-Hardi, T. Devic, M. Vishnuvarthan, B. Campo, A. Vimont, G. Clet, Q. Yang, G. Maurin, G. Férey, A. Vittadini, S. Gross and C. Serre, *Angew. Chem. Int. Ed.*, 2012, **51**, 9267–9271.
- 87 L. Cooper, N. Guillou, C. Martineau, E. Elkaim, F. Taulelle, C. Serre and T. Devic, *Eur. J. Inorg. Chem.*, 2014, **2014**, 6281–6289.
- 88 D. Feng, H.-L. Jiang, Y.-P. Chen, Z.-Y. Gu, Z. Wei and H.-C. Zhou, *Inorg. Chem.*, 2013, **52**, 12661–12667.
- 89 C. Serre, F. Millange, C. Thouvenot, M. Nogues, G. Marsolier, D. Louër and G. Férey, *J. Am. Chem. Soc.*, 2002, **124**, 13519–13526.
- 90 S. S.-Y. Chui, S. M.-F. Lo, J. P. Charmant, A. G. Orpen and I. D. Williams, *Science*, 1999, **283**, 1148–1150.

- 91 K. S. Park, Z. Ni, A. P. Côté, J. Y. Choi, R. Huang, F. J. Uribe-Romo, H. K. Chae, M. O’Keeffe and O. M. Yaghi, *Proc. Natl. Acad. Sci.*, 2006, **103**, 10186–10191.
- 92 L. Chen, J. Ou, H. Wang, Z. Liu, M. Ye and H. Zou, *ACS Appl. Mater. Interfaces*, 2016, **8**, 20292–20300.
- 93 Z. Wang, Y. Huang, J. Yang, Y. Li, Q. Zhuang and J. Gu, *Dalton Trans*, 2017, **46**, 7414 - 7420.
- 94 M. J. Cliffe, E. Castillo-Martinez, Y. Wu, J. Lee, A. C. Forse, F. C. N. Firth, P. Z. Moghadam, D. Fairen-Jimenez, M. W. Gaultois, J. A. Hill, O. V. Magdysyuk, B. Slater, A. L. Goodwin and C. P. Grey, *J. Am. Chem. Soc.*, 2017, **139(15)**, 5397 - 5404.
- 95 N. Stock and S. Biswas, *Chem. Rev.*, 2012, **112**, 933–969.
- 96 M. Gaab, N. Trukhan, S. Maurer, R. Gummaraju and U. Müller, *Microporous Mesoporous Mater.*, 2012, **157**, 131–136.
- 97 L. Garzón-Tovar, A. Carné-Sánchez, C. Carbonell, I. Imaz and D. MasPOCH, *J Mater Chem A*, 2015, **3**, 20819–20826.
- 98 T. Zhao, F. Jeremias, I. Boldog, B. Nguyen, S. K. Henninger and C. Janiak, *Dalton Trans*, 2015, **44**, 16791–16801.
- 99 H. Chevreau, A. Permyakova, F. Nouar, P. Fabry, C. Livage, F. Ragon, A. Garcia-Marquez, T. Devic, N. Steunou, C. Serre and P. Horcajada, *CrystEngComm*, 2016, **18**, 4094–4101.
- 100 D. Cattaneo, S. J. Warrender, M. J. Duncan, R. Castledine, N. Parkinson, I. Haley and R. E. Morris, *Dalton Trans*, 2016, **45**, 618–629.
- 101 D. Lenzen, P. Bendix, H. Reinsch, D. Fröhlich, H. Kummer, M. Möllers, P. P. C. Hügenell, R. Gläser, S. Henninger and N. Stock, *Adv. Mater.*, 2018, **30**, 1705869.
- 102 A. Garcia Marquez, P. Horcajada, D. Grosso, G. Ferey, C. Serre, C. Sanchez and C. Boissiere, *Chem. Commun.*, 2013, **49**, 3848.
- 103 A. Carné-Sánchez, I. Imaz, M. Cano-Sarabia and D. MasPOCH, *Nat. Chem.*, 2013, **5**, 203–211.
- 104 D. Crawford, J. Casaban, R. Haydon, N. Giri, T. McNally and S. L. James, *Chem Sci*, 2015, **6**, 1645–1649.
- 105 B. P. Mason, K. E. Price, J. L. Steinbacher, A. R. Bogdan and D. T. McQuade, *Chem. Rev.*, 2007, **107**, 2300–2318.
- 106 J. Puigmartí-Luis, *Chem Soc Rev*, 2014, **43**, 2253–2271.
- 107 S. Waitschat, M. T. Wharmby and N. Stock, *Dalton Trans*, 2015, **44**, 11235–11240.
- 108 C. Csajági, B. Borcsek, K. Niesz, I. Kovács, Z. Székelyhidi, Z. Bajkó, L. Üрге and F. Darvas, *Org. Lett.*, 2008, **10**, 1589–1592.
- 109 D. V. R. Kumar, A. A. Kulkarni and B. L. V. Prasad, *Colloids Surf. Physicochem. Eng. Asp.*, 2014, **443**, 149–155.
- 110 H. Wang, H. Nakamura, M. Uehara, M. Miyazaki and H. Maeda, *Chem. Commun.*, 2002, 1462–1463.
- 111 M. Gimeno-Fabra, A. S. Munn, L. A. Stevens, T. C. Drage, D. M. Grant, R. J. Kashtiban, J. Sloan, E. Lester and R. I. Walton, *Chem. Commun.*, 2012, **48**, 10642.
- 112 M. P. Batten, M. Rubio-Martinez, T. Hadley, K.-C. Carey, K.-S. Lim, A. Polyzos and M. R. Hill, *Curr. Opin. Chem. Eng.*, 2015, **8**, 55–59.
- 113 P. W. Dunne, A. S. Munn, C. L. Starkey, T. A. Huddle and E. H. Lester, *Philos. Trans. R. Soc. Math. Phys. Eng. Sci.*, 2015, **373**, 20150015.
- 114 J. Zhang, C. Gong, X. Zeng and J. Xie, *Coord. Chem. Rev.*, 2016, **324**, 39–53.
- 115 P. W. Dunne, E. Lester and R. I. Walton, *React Chem Eng*, 2016, **1**, 352–360.
- 116 M. Rubio-Martinez, M. P. Batten, A. Polyzos, K.-C. Carey, J. I. Mardel, K.-S. Lim and M. R. Hill, *Sci. Rep.*, 2014, **4**.
- 117 K.-J. Kim, Y. J. Li, P. B. Kreider, C.-H. Chang, N. Wannemacher, P. K. Thallapally and H.-G. Ahn, *Chem. Commun.*, 2013, **49**, 11518.

## Quellenverzeichnis

- 118 L. Paseta, B. Seoane, D. Julve, V. Sebastián, C. Téllez and J. Coronas, *ACS Appl. Mater. Interfaces*, 2013, **5**, 9405–9410.
- 119 M. Taddei, D. A. Steitz, J. A. van Bokhoven and M. Ranocchiari, *Chem. - Eur. J.*, 2016, **22**, 3245–3249.
- 120 M. Rubio-Martinez, T. D. Hadley, M. P. Batten, K. Constanti-Carey, T. Barton, D. Marley, A. Mönch, K.-S. Lim and M. R. Hill, *ChemSusChem*, 2016, **9**, 938–941.
- 121 R. Ameloot, F. Vermoortele, W. Vanhove, M. B. J. Roeffaers, B. F. Sels and D. E. De Vos, *Nat. Chem.*, 2011, **3**, 382–387.
- 122 L. D'Arras, C. Sassoie, L. Rozes, C. Sanchez, J. Marrot, S. Marre and C. Aymonier, *New J. Chem.*, 2014, **38**, 1477.
- 123 M. Faustini, J. Kim, G.-Y. Jeong, J. Y. Kim, H. R. Moon, W.-S. Ahn and D.-P. Kim, *J. Am. Chem. Soc.*, 2013, **135**, 14619–14626.
- 124 P. A. Bayliss, I. A. Ibarra, E. Pérez, S. Yang, C. C. Tang, M. Poliakoff and M. Schröder, *Green Chem.*, 2014, **16**, 3796.
- 125 G. H. Albuquerque, R. C. Fitzmorris, M. Ahmadi, N. Wannemacher, P. K. Thallapally, B. P. McGrail and G. S. Herman, *CrystEngComm*, 2015, **17**, 5502–5510.
- 126 H.-S. Choi, S.-J. Lee, Y.-S. Bae, S.-J. Choung, S. H. Im and J. Kim, *Chem. Eng. J.*, 2015, **266**, 56–63.
- 127 A. S. Munn, P. W. Dunne, S. V. Y. Tang and E. H. Lester, *Chem Commun*, 2015, **51**, 12811–12814.
- 128 G.-Y. Jeong, R. Ricco, K. Liang, J. Ludwig, J.-O. Kim, P. Falcaro and D.-P. Kim, *Chem. Mater.*, 2015, **27**, 7903–7909.
- 129 H. Reinsch, S. Waitschat, S. M. Chavan, K. P. Lillerud and N. Stock, *Eur. J. Inorg. Chem.*, 2016, **2016**, 4490–4498.
- 130 T. Rhauderwiek, S. Waitschat, S. Wuttke, H. Reinsch, T. Bein and N. Stock, *Inorg. Chem.*, 2016, **55**, 5312–5319.
- 131 S. Tai, W. Zhang, J. Zhang, G. Luo, Y. Jia, M. Deng and Y. Ling, *Microporous Mesoporous Mater.*, 2016, **220**, 148–154.
- 132 A. Polyzoidis, T. Altenburg, M. Schwarzer, S. Loebbecke and S. Kaskel, *Chem. Eng. J.*, 2016, **283**, 971–977.
- 133 C. McKinsty, R. J. Cathcart, E. J. Cussen, A. J. Fletcher, S. V. Patwardhan and J. Sefcik, *Chem. Eng. J.*, 2016, **285**, 718–725.
- 134 S. R. Jambovane, S. K. Nune, R. T. Kelly, B. P. McGrail, Z. Wang, M. I. Nandasiri, S. Katipamula, C. Trader and H. T. Schaef, *Sci. Rep.*, 2016, **6**.
- 135 L. Garzón-Tovar, M. Cano-Sarabia, A. Carné-Sánchez, C. Carbonell, I. Imaz and D. Maspocho, *React Chem Eng*, 2016, **1**, 533–539.
- 136 D. Balzar, N. Audebrand, M. R. Daymond, A. Fitch, A. Hewat, J. I. Langford, A. Le Bail, D. Louër, O. Masson, C. N. McCowan, N. C. Popa, P. W. Stephens and B. H. Toby, *J. Appl. Crystallogr.*, 2004, **37**, 911–924.

## 9. Publikationsliste und Konferenzbeiträge

### Publikationsliste:

1. H. Reinsch, S. Waitschat, N. Stock, *Dalton Trans.*, **2013**, 42, 4840.
2. S. Waitschat, M. T. Wharmby, N. Stock, *Dalton Trans.*, **2015**, 44, 11235.
3. T. Rhauderwiek, S. Waitschat, S. Wuttke, H. Reinsch, T. Bein, N. Stock, *Inorg. Chem.*, **2016**, 55, 5312.
4. H. Reinsch, S. Waitschat, S. M. Chavan, K. P. Lillerud, N. Stock, *Eur. J. Inorg. Chem.*, **2016**, 27, 4490.
5. S. Waitschat, H. Reinsch, N. Stock, *Chem. Commun.*, **2016**, 52, 12698.
6. S. Waitschat, D. Fröhlich, H. Reinsch, H. Terraschke, K. A. Lomachenko, C. Lamberti, H. Kummer, T. Helling, M. Baumgartner, S. Henninger, N. Stock, *Dalton Trans.*, **2018**.
7. H. Reinsch, D. Fröhlich, S. Waitschat, S. Chavan, K. -P. Lillerud, S. Henninger, N. Stock, *React. Chem. Eng.*, **2018**, 3, 365 - 370.
8. S. Waitschat, H. Reinsch, M. Arpacioğlu, N. Stock, *CrystEngComm*, **2018**, 10.1039/C8CE00949J.

### Konferenzbeiträge Vorträge:

1. S. Waitschat; Metal-Organic Frameworks with Nitrogen containing Heterocycles and zirconium; AC-Kolloquium, 2018; Kiel, D.
2. S. Waitschat, H. Reinsch, N. Stock; *Continuous flow synthesis of Zr-MOFs with UiO-66 framework structure leading to high space time and real time yields*; Norddeutsches Doktorandenkolloquium 2016; Hamburg, D.

### Konferenzbeiträge Poster:

1. S. Waitschat, D. Fröhlich, H. Reinsch, S. Henninger, N. Stock, *Modification of the water sorption properties of MOFs by hydrophilisation*; 2<sup>st</sup> European Conference on Metal-Organic Frameworks and Porous Polymers 2017; Delft, NL.
2. S. Waitschat, D. Fröhlich, H. Reinsch, S. Henninger, N. Stock; *Synthesis and characterization of two new Zr-MOF based on nitrogen containing heterocycles and possible application in heat transformation*, Deutsche Zeolith-Tagung 2017, Frankfurt, D.
3. S. Waitschat, D. Fröhlich, H. Reinsch, S. Henninger, K. P. Lillerud, N. Stock; *Optimization of synthesis conditions for UiO-66-COOH towards industrial scale and continuous production*, Deutsche Zeolith-tagung 2016, Gießen, D.
4. S. Waitschat, M. T. Wharmby, N. Stock, *Continuous flow-synthesis of carboxylate and phosphonate based metal-organic frameworks under non-solvothermal reaction conditions*; 1<sup>st</sup> European Conference on Metal-Organic Frameworks and Porous Polymers 2015; Potsdam, D.
5. S. Waitschat, M. T. Wharmby, N. Stock, *Continuous flow-synthesis of carboxylate and phosphonate based metal-organic frameworks under non-solvothermal reaction conditions*; Deutsche Zeolith-Tagung 2015; Oldenburg, D.
6. S. Waitschat, M. T. Wharmby, N. Stock, *Continuous flow-synthesis of carboxylate and phosphonate based metal-organic frameworks under non-solvothermal reaction conditions*; Live Science Tagung 2014; Kiel, D.

**Eidesstattliche Erklärung**

Hiermit versichere ich Steve Waitschat an Eides statt, dass ich die hier vorliegende Dissertation selbständig – abgesehen von der wissenschaftlichen Betreuung durch meinen Doktorvater Prof. Dr. Norbert Stock – und nur unter Verwendung der angegebenen Hilfsmittel, angefertigt habe. Diese Dissertation wird ausschließlich an dieser Stelle zur Promotion vorgelegt. Teile der Arbeit wurden in den genannten Journalen als wissenschaftliche Beiträge bereits veröffentlicht oder wurden zur Veröffentlichung eingereicht. Ich erkläre hiermit, dass ich noch keinen Promotionsversuch unternommen habe und dass die Arbeit unter Einhaltung der Regeln guter wissenschaftlicher Praxis der Deutschen Forschungsgesellschaft entstanden ist.

Ostenfeld, 24.08.2018

## Lebenslauf

### Persönliche Angaben:

Steve Waitschat  
Geburtsdatum: 29.12.1986 in Salzwedel  
Familienstand: ledig  
Staatsangehörigkeit: deutsch



---

### Ausbildung:

- 04/2015 – 10/2018  
Christian-Albrechts Universität zu Kiel  
Promotion im Fachbereich Chemie  
Titel Doktorarbeit: „Entdeckung & Syntheseoptimierung von Zr-MOFs: Hochdurchsatzuntersuchungen und Synthesen in Flussreaktoren“
- 05/2013 – 03/2015  
Christian-Albrechts-Universität zu Kiel  
Fachrichtung: Wirtschaftschemie  
Abschluss: Master of Science (2.0)  
Titel Masterarbeit: „Synthese von Metal-organischen Gerüstverbindungen in einem Durchflussreaktor“
- 10/2008 – 04/2013  
Christian-Albrechts-Universität zu Kiel  
Fachrichtung: Wirtschaftschemie  
Abschluss: Bachelor of Science (2.7)  
Titel Bachelorarbeit: „Synthese und Charakterisierung von porösen Gerüstverbindungen mit CAU-10 Topologie“
- 10/2007 – 09/2008  
Christian-Albrechts-Universität zu Kiel  
Fachrichtung: Wirtschaftsingenieur
- 10/2006 – 06/2007  
Hindenburgkaserne Munster  
Grundwehrdienst (Munitionskanonier)
- 09/1999 – 07/2006  
Friedrich-Ludwig-Jahn Gymnasium Salzwedel  
Abschluss: Abitur (2.3)

---

### Praxiserfahrung:

- 04/2012 – 10/2012  
Industriepraktikum, Lufa-ITL GmbH, Kiel  
Schwerpunkt: Controlling in der organischen Analytik
-

## Lebenslauf

### Kenntnisse:

- Sprachen: Englisch (verhandlungssicher)
- EDV: Microsoft Office (sehr gut), Origin (sehr gut), Topas (gut)
- Chemische Synthesen: organische wie anorganische Synthesen, im speziellen: Flussreaktoren und Solvothermale Hochdurchsatzmethoden
- Charakterisierungsmethoden: Gassorption , IR- und NMR-Spektroskopie, Röntgenbeugung, Thermogravimetrie,
- Rheologie und Kolloidchemie
- Organisation und Finanzierung von Konferenzen (Frühjahrssymposium 2016, Norddeutsches Doktorandenkolloquium 2017, Deutsche Zeolith Tagung 2018)

---

### Studienbegleitende Tätigkeiten:

- Schüler- und Studentennachhilfe in Mathematik, Chemie und Physik
- Assistent in chemischen Nebenfachpraktika
- Tutor für Chemie für Mediziner

---

### Ehrenamtliche Tätigkeiten:

- Seid 04/2017 HFM FFW Ostenfeld
- 02/2012 – 04/2016 Kassenwart des JungChemikerForum Kiel
- 06/2015 – 05/2016 Finanzvorstand des Wi.-Chem. Kiel e.V.
- 09/2015 – 09/2016 Bundesvorstand JungChemikerForum

---

### Ehrungen:

- 07/2015 Jahrespreis für besondere wissenschaftliche Leistung und Engagement des Fördervereins der Mathematischen-Naturwissenschaftlichen Fakultät

---

### Freizeitaktivitäten:

- Meine Familie und der Hund
- Literatur
- Wrestling

Kiel, 24.08.2018



Steve Waitschat